Near-Infrared GaAs-on-SiN Photonic Integration Platform Based on Micro-Transfer-Printing

Jeroen Goyvaerts

Doctoral dissertation submitted to obtain the academic degree of
Doctor of Photonics Engineering

Supervisors

Prof. Roel Baets, PhD - Prof. Günther Roelkens, PhD

Department of Information Technology
Faculty of Engineering and Architecture, Ghent University

October 2021

GHENT
UNIVERSITY

Acknowledgements

I can remember the week in January 2016 as if it were yesterday. I applied on Monday morning, had a joint call with Roel and Günther on Thursday. Some doubts were creeping in from my side, but then I received a Friday evening mail from Roel, saying: 'if you want it, it is yours!'. As soon as I read that email, the doubts disappeared, and I was off on a new adventure!

Fast forward to 2021, and the journey is over! To work in such a large research group, along with so many bright students and professors is truly a privilege. For that, I must thank Roel first and foremost. He is patient zero of the photonics-bug. But he is not alone, with Günther leading the precious Transfer-Printing efforts, Dries the novel material integration, Geert on lasers, Wim on everything-design related, Bart on Terahertz/mode-locked lasers, Stephane on Raman/quantum, Peter on some other stuff that makes my head hurt. And they are all supported by a great team, on which I was able to rely on: thank you Ilse, Ilse, Kristien, Peter, Bert, Jasper, Michael, Mike, Kamal, Eva and the entire gang.

Onto the body of work, I want to thank my two co-promotors, Günther Roelkens and Roel Baets once again, for both for their guidance, their ideas, their tenacity and their feedback that have made this body of work into the bundle of pages you are holding or scrolling through. Their insights are so sharp, they cut like a hot knife through butter. It can be intimidating, but it is helpful and betters the work of their students. They always keep you on your toes. Thank you Roel for your help on the sensor and the VCSEL and thank you Günther for your help on the PDs and the VCSEL. The next person I want to thank is Sulakshna Kumari. She was my predecessor on VCSEL-on-SiN$_x$ integration, she became my colleague in transfer-printing and she will be a lifelong friend.

I have been one of the lucky few to have shared their research efforts with several colleagues. By far the most meaningful collaboration has been with the opto-electronics group of Chalmers Technical University, of Gothenburg, Sweden. Professor Anders Larsson and professor Johan Gustavsson form the backbone of more than 3 decades of VCSEL expertise. They, and their team, form the pinnacle of VCSEL development. I have been lucky to work in some form or shape with

What did he say? Exactly what I needed to hear: "Oh?! So you are the only PhD student who is having a hard time? That's cute!" And he was right, complaining gets you nowhere. Thank you for pointing me back into the right direction :) !

A special thanks goes to my dear Pakistani friend Abdul, the unofficial sage of the group. I have fond memories of your teachings, but maybe even more so of our less academic discussions on life. When I was in doubt, I could always go to for advice. Even more important was your indirect help in getting my next job through the silicon nitride crash course that you organized. I am very grateful for this. I hope I at least payed you back a little in the form of being your driver's teacher :D!

I also want to say another thanks to 2016 team of students with whom I have started together and have shared some PhD memories along the way. While most people find good friends during a PhD, few people can ever do PhD with one of their lifelong friends. Kristof, thanks for all the laughs, the good times and sharing of the bad times! Then there is Camiel, one of the funniest guys around and another chameleon as well. I dare you to try to give him an assignment which he can't do ... And Lukas, one of the other cleanroom magicians and just an amazing engineer. It is unfortunate we did not have a larger overlap in topics. Bahawal, the best of us, with an iron determination and great ambition. And Alessio, one of my close companions from the office and someone on which everybody could count upon. Xiaoning, whenever I felt down, I just had to look at the gas-sensor setup in the cleanroom and I could find you there, day or night, tinkering away relentlessly. You sure inspired me to not ever give up! Try everything and then some more!

Beyond the photonic group, I want to thank my friends and family for taking my mind of the thesis at times. I have had some great laughs and moments outside the academic bubble, which I believe are necessary to keep your mind clear. I also want to thank my parents from the bottom of my heart. I have had it far easier than most, with all the support that they have given me over the years. And I am glad that I can finally return them the favor with an actual graduation ceremony I hope (sorry for the previous times)! Also, a special thank you to my grand-mother. She has always taken a great interest into the education of all her grand-children, providing delicious cookies over the years. The real reason for starting the PhD was that I didn't want my supply of cookies to dry out... Thank god the flow of cookies never stopped, or else these pages would be blank!

And finally, and most importantly, I absolutely need to thank Karen. For over twelve years we share our lives; long before the start of this PhD and hopefully for long after as well. The pursuit of the PhD would have been that much harder without your support, your various proofreading efforts, your care and your love. Your presence elevated the bad days, while amplifying the good days! For all of that, I am deeply grateful. And now, onto our next adventure!

Fall 2021
Jeroen Goyvaerts

Contents

List of Figures

List of Tables

List of Acronyms

A

ADF	Add-Drop Filter
AFM	Atomic Force Microscopy
AlAs	Aluminium Arsenide
AlGaAs	Aluminium Gallium Arsenide
APF	All-Pass Filter
AWG	Arbitrary Waveform Generator (depending on context)
AWG	Arrayed Waveguide Grating (depending on context)

B

BCB	Benzocyclobutene
BOX	Buried Oxide

C

CMOS	Complementary Metal Oxide Semiconductor
CW	Continuous Wave

D

DBR	Distributed Bragg Reflector
DFB	Distributed Feedback Laser
DVS-BCB	Divinylsiloxane - Benzocyclobutene

E

EEL	Edge-Emitting Laser
EIC	Electronic Integrated Circuit
ER	Extinction Ratio

F

FDTD	Finite Difference Time Domain
FP	Fabry-Pérot
FOM	Figure of Merit
FSR	Free Spectral Range

G

GaAs	Gallium Arsenide
GC	Grating Coupler

H

HCG	High Contrast Grating

I

ICP   Inductively Coupled Plasma
InAlP   Indium Aluminium Phosphide
InGaP   Indium Gallium Phosphide
InP   Indium Phosphide
IPA   Iso-Propylalcohol

L

LCG   Low Contrast Grating
LD   Laser Diode
LED   Light Emitting Diode
LiDAR   Light Detection And Ranging
LIV   Light-Current-Voltage
LOD   Limit of Detection
LPCVD   Low Pressure Chemical Vapor Deposition

M

MCG   Medium Contrast Grating
MOB   Micro Optical Bench
MPW   Multi-Project Wafer
MSM   Metal-Semiconductor-Metal
MRR   MicroRing Resonator
MQW   Multiple Quantum Well
MZI   Mach-Zehnder Interferometer

N

NIR   Near Infra-Red

O

OOK	On-Off-Keying
OSA	Optical Spectrum Analyzer

P

PD	Photodetector
PECVD	Plasma Enhanced Chemical Vapor Deposition
PIC	Photonic Integrated Circuit
PR	Photoresist

R

RIE	Reactive Ion Etching
RIU	Refractive Index Units

S

SiP	Silicon Photonics
SMSR	Side Mode Suppression Ratio
SOA	Semiconductor Optical Amplifier
SOI	Silicon on Insulator

T

TE	Transverse Electric
TM	Transverse Magnetic
TMM	Transfer Matrix Method
TOF	Time-of-Flight
TOX	Top Oxide Cladding
TRL	Technology Readiness Level

U

(μ)TP   (micro-)Transfer-Printing

V

VCSEL   Vertical Cavity Surface Emitting Laser
VCSIL   Vertical Cavity Silicon (Nitride) Integrated Laser
VIS   Visble (light spectrum)
VOC   Volatile Organic Compounds

W

WDM   Wavelength Division Multiplexing

Samenvatting

In dit werk wordt er onderzoek uitgevoerd naar de integratie van gallium arsenide opto-elektronische componenten op een silicium-nitride golfgeleider platform voor het nabije infrarood golflengtegebied door middel van transfer-printing.

Gedurende de laatste twintig jaar is het domein van geïntegreerde fotonische schakelingen enorm gegroeid. Tot dusver wordt de markt gedomineerd door applicaties in informatietechnologie, waar licht wordt gebruikt om informatie te verzenden binnen en tussen datacentra. Normaliter worden hiervoor silicium of indiumfosfide gebaseerde fotonische schakelingen gebruikt. Omwille van een groeiende maturiteit in deze industrie, wordt er geleidelijk aan gekeken naar applicatiedomeinen die tot op heden niet compatibel zijn geweest met de bovenvermelde platformen. Het zichtbaar en het nabije infrarood spectrum, dat tussen 400 nm en $\sim$ 1000 nm ligt, is interessant voor biologische toepassingen en microscopie. Echter, onder 1200 nm absorberen de silicium golfgeleiders het licht, wat dit materiaal niet langer geschikt maakt. Er moet dus worden overgeschakeld naar een nieuw platform, zoals siliciumnitride, dat transparant is boven een golflengte van 400 nm. Bovendien heeft siliciumnitride een lagere brekingsindex dan silicium, wat leidt tot een lager brekingsindex contrast met het omliggend oxide en lagere propagatie verliezen. Het nadeel van siliciumnitride fotonica is het gebrek aan actieve functionaliteit. Zo is er geen lichtbron gebaseerd op siliciumnitride, en ook niet op silicium. Maar silicium golfgeleiders kunnen wel gebruik maken van gedopeerd silicium voor het maken van modulatoren, of het groeien van germanium-op-silicium voor detectoren. Dit is een gebrek bij siliciumnitride fotonica en om deze functionaliteit te kunnen integreren, moet er gekeken worden naar het heterogeen integreren van andere materialen bovenop het siliciumnitride golfgeleider platform.

Dit onderzoekswerk tracht het bovenstaande te bereiken door gebruik te maken van de relatief nieuwe transferprint (TP) integratietechnologie. Deze technologie combineert het beste van de reeds bestaande flip-chip integratietechniek en de waferbindingstechniek. De voordelen zijn veelvuldig, met (1) een hoge doorvoer van componenten door middel van het wafer-compatibele aspect van de technologie, (2) de mogelijkheid voor pre-integratie testen van de componenten, (3) gemakkelijke invoer in CMOS fabrieken door middel van de scheiding in procestechnieken door het III-V materiaal te definiëren op het III-V substraat voor de transferprinting stap, (4) het kost-effectieve gebruik van het duurdere III-V materiaal ten opzichte
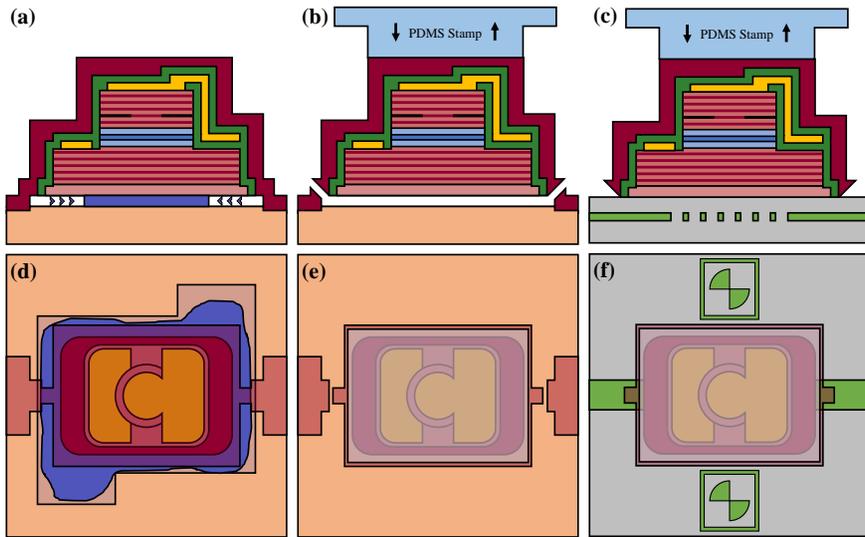
Figuur 1: Conceptueel overzicht van de relevante transferprint integratie stappen van een GaAs VCSEL. De bovenste rij toont een cross-sectie overzicht, en de onderste rij toont een bovenaanzicht van: (a & d) de natte onderets van de VCSEL om deze quasi vrijstaand te maken, (b & e) de component na de opneem stap, (c & f) het printen van de VCSEL op een siliciumnitride golfgeleider.

van waferbinding en substraat-verwijderingstechnieken en (5) de mogelijkheid om verschillende nieuwe materialen te integreren op eenzelfde substraat. Een conceptueel overzicht met de meest relevante stappen is weergegeven in Figuur 1. Microscoopafbeeldingen zijn terug te vinden in Figuur 2 voor de transferprint integratie van een VCSEL. Kortom, de transferprint techniek is een interessante kandidaat om het probleem van opto-elektronische functionaliteit op silicium en siliciumnitride golfgeleider platformen aan te gaan.

Met siliciumnitride golfgeleiders is het nabije infrarood gebied geopend voor applicaties die gebruik maken van fotonische schakelingen. Biologische weefsels kunnen hierdoor onderzocht worden, want het nabije infrarood gebied heeft een lage absorptie van water waardoor het gewenste signaal beter doorkomt. Hierdoor kunnen kleine veranderingen in de brekingsindex van waterige monsters, zoals de aanwezigheid van virussen, antistoffen of een andere stof, effectief gedetecteerd worden. Meer specifiek focussen wij ons op het 850 nm golflengte domein, omwille van de brede kennis aan fabricage technieken voor hoge efficiëntie VCSELs bij deze golflengte. Hierbij steunen we op het onderzoek van deze VCSELs voor applicaties in informatietechnologie bij dezelfde golflengte. Bijgevolg staat het gallium arsenide (GaAs) materiaalplatform centraal in het onderzoek naar de integratie van de opto-elektronische componenten op siliciumnitride. Een overzicht van de onderzochte componenten is terug te vinden in Figuur 3. Daar zijn een metaal-
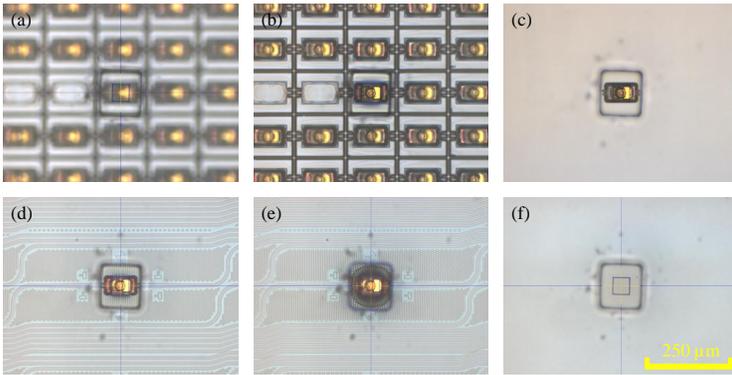
Figuur 2: Microscoop afbeeldingen van de transferprint technologie: (a) component identificatie op het III-V substraat, (b) de aanrakingsstap tussen de PDMS stempel en de component, (c) het opnemen van de component door de stempel, (d) het aligneren van de component ten opzichte van de alignatie-markers op de fotonische schakeling, (e) het printen van de component op het golfgeleider circuit na de alignatie, (f) het geleidelijk weghalen van de stempel waardoor de component achterblijft op het nieuwe substraat.

halfgeleider-metaal (MSM) fotodetector, een PIN fotodetector en een neerwaarts stralende VCSEL te zien.
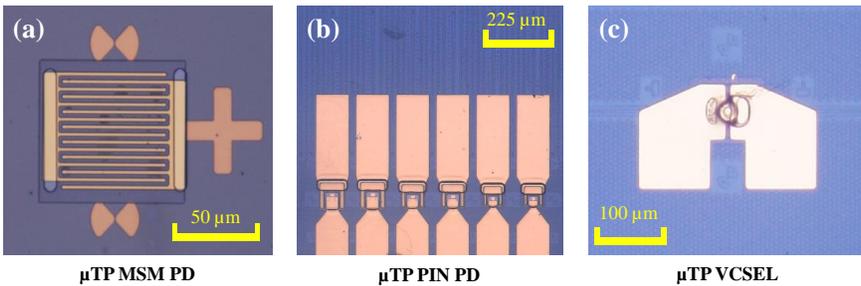
Figuur 3: De componenten die zijn getransferprint in dit onderzoekswerk: (a) een hoge snelheid metaal-halfgeleider-metaal fotodetector met ineen geschakelde vingercontacten, (b) een golfgeleider gekoppelde PIN fotodetector met een hoge responsiviteit en (c) een golfgeleider gekoppelde, neerwaarts stralende VCSEL laser die als kleinbandige, afstembare laser kan gebruikt worden voor bio-gerelateerde sensor applicaties.
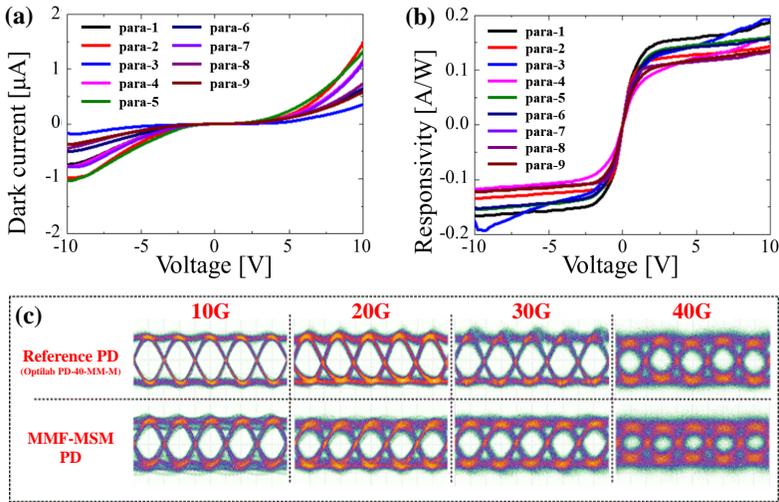
Figuur 4: De karakterisatie van de grote-oppervlakte MSM fotodetector: (a) de donkerstroom van de detector, (b) de responsiviteit van de detector en (c) de betrouwbare hoge snelheid data detectie tot 40 Gbit per seconde.

Een transferprint compatibele metaal-halfgeleider-metaal (MSM) PD

De metaal-halfgeleider-metaal fotodetector is een plenaire, hoge snelheidsdetector. Wij demonstreren de transferprint integratie techniek op een grote-oppervlakte detector die koppelt met multimodale lichtvezels, en een klein-oppervlakte detector die koppelt met een siliciumnitride golfgeleider. De combinatie van beide groottes opent mogelijkheden in het applicatiedomein van fotonische tussencircuits die de communicatie tussen verschillende elektronische schakelingen kan voorzien met lichtkanalen. De communicatie tussen elektronische schakelingen op eenzelfde tussencircuit kunnen gefaciliteerd worden door de siliciumnitride golfgeleiders met de golfgeleider-gekoppelde kleine-oppervlakte detectoren. De communicatie tussen verschillende tussencircuits kan voorzien worden door een grotere lichtvezel, waarvan het licht koppelt met de grote-oppervlakte detector variant.

De fotodetectoren zijn gegroeid op een hoge aluminium concentratie AlGaAs laag, en ze zijn vervolgens getransferprint op siliciumnitride golfgeleiders en hoge weerstand silicium substraten. De karakterisatie van de grote-oppervlakte detector is terug te vinden in Figuur 4. Gemiddeld genomen is de donkerstroom respectievelijk 22.0 nA en 7.2 nA en de responsiviteit 0.17 A/W en 0.10 AW, voor de grote-oppervlakte en de kleine-oppervlakte detectoren. Een bandbreedte van meer dan 19 GHz is opgemeten voor de grote-oppervlakte detectoren. Hiermee zijn hogesnelheidsschakelingen gemaakt die hoeveelheden data tot 40 Gbit per seconde betrouwbaar kunnen opmeten.
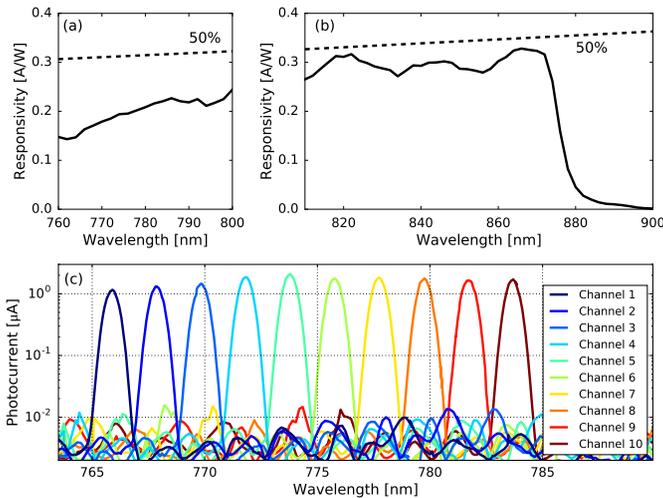
Figuur 5: De karakterisatie van een getransferprinte fotodetector, met een golfgeleider gerefereerde responsiviteit weergegeven in (a) rondom 780 nm en in (b) rondom 850 nm. (c) toont de fotostroom van verschillende detectoren die getransferprint zijn op de uitkoppelingskanalen van een spectrometer geïntegreerd op een siliciumnitride chip.

Een transferprint compatibele PIN PD

Een PIN fotodetector is geïntegreerd met dezelfde transferpint technologie. Deze detector verbeterd de lage snelheids prestaties ten opzichte van de MSM detector. De PIN detector is gegroeid op een InAlP laag. Vanuit het transferprint perspectief is dit de meest geschikte laag voor verscheidene proces-gerelateerde eigenschappen. Echter, het is niet triviaal om deze laag defect vrij te groeien. De dikkere absorptie laag van de PIN PD draagt bij tot een verbeterde responsiviteit ten opzichte van het licht in de golfgeleider. Deze waarden zijn weergegeven in Figuur 5-(a & b). De detectoren hebben een lage donkerstroom met een gemiddelde waarde van 10 pA. In dit schema is de diffractie koppelaar een belangrijk tussenstuk dat bijdraagt tot de efficientie en responsiviteit.

Er is ook een demonstratie aangetoond van het parallel printen van meerdere detectoren in één enkele stap. Deze detectoren werden geprint op de diffractie koppelaars van de uitgangskanalen van een geïntegreerde spectrometer op het siliciumnitride golfgeleider platform. De detectoren werden geprint in paren van 7 om de spectrometer te karakteriseren. De resultaten zijn terug te vinden in Figuur 5-(c). Een externe, afstembare laser werd gebruikt om de spectrometer met detectoren op te meten. Er zijn geen indicaties dat de hoge integratie-dichtheid nadelige effecten zou hebben op de overspraak tussen de kanalen. De detectoren zijn excellente kandidaten voor volledig geïntegreerde sensoren omwille van het breedbandige werkingsregime in het nabije infrarood golflengte gebied.
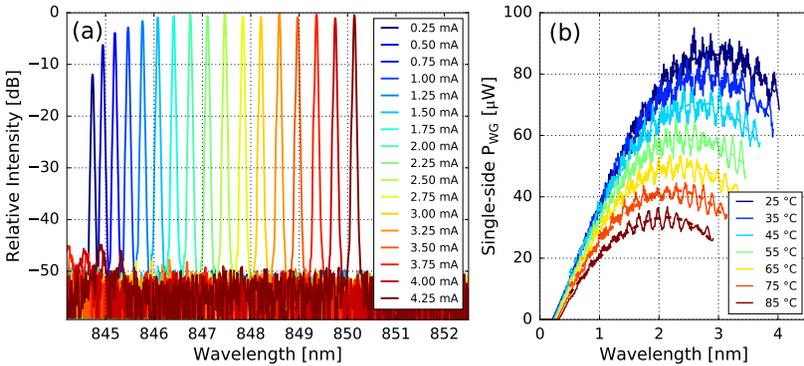
Figuur 6: Enkele karakterisatie parameters van een golfgeleider gekoppelde, neerwaarts stralende VCSEL: (a) de afstembare golflengte capabiliteit van de VCSEL, opgemeten in de golfgeleider, (b) de thermische stabiliteit van een golfgeleider gekoppelde VCSEL.

Een transferprint compatibele VCSEL lichtbron

De getransferprinte VCSEL is ontwikkeld in samenwerking met de opto-elektronische groep uit Chalmers Technische Universiteit van Göteborg, Zweden. Het project is een verderzetting van een eerdere demonstratie op basis van waferbindingtechnieken. De gekozen aanpak voor de transfer-print compatibele VCSEL maakt gebruik van een neerwaarts stralende VCSEL laser die koppelt met de siliciumnitride golfgeleider door middel van een diffractie koppelaar. Het design van de VCSEL lekt licht opwaarts, waardoor de structuren op het III-V substraat kunnen getest worden voor redenen van proces controle.

De drempelstroom van de VCSELs varieert tussen 0.10 en 0.35 mA, afhankelijk van de grootte van het apertuur van de VCSEL. De golflengte van de VCSEL kan afgestemd worden door middel van het variëren van de VCSEL-stroom, zoals aangetoond in Figuur 6. Hiermee wordt een bereik van 4 to 5 nm behaald, wat een kleinbandig afstembare laser vormt. De diffractie koppelaar verbetert de onderdrukking van hogere orde modes van de VCSEL met ongeveer 5 tot 10 dB. Met de huidige strategie zijn de VCSELs met een apertuur tussen 4 & 5 µm diegene met het hoogste vermogen en toch goede hogere orde onderdrukking (> 35 dB). De enkelzijdige koppelingsefficiëntie ligt boven 10 %, met een dubbelzijdige koppelingsefficiëntie boven 20 %. Door het transferprinten stijgt de thermische weerstand, waardoor de thermische golflengte afstemming sneller wordt bereikt en dat bij een lager vermogen. Hierdoor is de VCSEL ideaal geschikt voor applicaties die een laag vermogen vereisen zoals wearable sensoren. De breedte van de afstemming halveert met een scan snelheid van 1 MHz. Voor biologische toepassingen is een scansnelheid ver boven de specificaties vereist voor brekingsindex sensoren. De grootte van het golfgeleider gekoppeld vermogen is dusdanig groot dat meer dan 1000 sensoren in parallel kunnen gescand worden met één enkele VCSEL, samen met de PIN detectoren die eerder vermeld zijn.
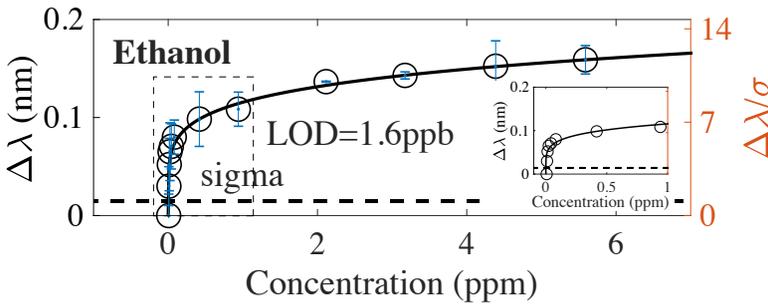
Figuur 7: Ethanol gas concentratiedetectie met een hoog sensitieve, kleinbandige MZI brekingsindex gas sensor. De detectielimiet is 1.6 ppb voor ethanol.

Een kleinbandige brekingsindex sensor

Het nabije infrarood golflengte bereik is een ideale kandidaat voor brekingsindex sensoren die verschillende geprefereerde stoffen kunnen detecteren op basis van applicatie gerichte coating lagen. De gedemonstreerde VCSEL en PIN PD vormen hoge prestatie bouwblokken voor een geminiaturiseerde sensor. Omwille van deze redenen is een nieuwe kijk genomen op een golfgeleider signaal overdrager die compatibel is met de bouwblokken. Een Mach-Zehnder interferometer (MZI) is gekozen als de kandidaat met de hoogste flexibiliteit naar design en sensitiviteit toe. De werking van deze sensor is aangetoond met een op zweet gebaseerde ionenconcentratie, die in het relevante millimolar concentratieniveau kan gedetecteerd worden. Een tweede applicatie omvat vluchtige organische stoffen die lokaal binden aan een mesoporeuze silicium oxide laag, ontwikkeld aan de technische universiteit van Wenen. Een voorbeeld van een ethanol concentratiemeting is weergegeven in Figuur 7. De gedemonstreerde brekingsindexs sensoren tonen een betere sensitiviteit en detectielimiet dan equivalente Raman spectroscopische sensoren.

Besluit

In dit doctoraatsonderzoek is de transferprint technologie ontwikkeld en toegepast voor de heterogene integratie van GaAs gebaseerde opto-elektronische schakelingen op siliciumnitride golfgeleider circuits. Wij demonstreren de golfgeleider gekoppelde werking van detectoren en VCSELs, samen met een demonstratie van een hoog sensitieve, applicatie-gerichte gas sensor. Deze componenten vormen de bouwstenen voor de volgende generatie geminiaturiseerde brekingsindex sensoren in het nabije golflengte gebied.

Summary

This work pursues the micro-transfer print integration of GaAs opto-electronic onto silicon nitride waveguide circuits for the near-infrared wavelength region.

Over the past two decades, the field of integrated photonics has grown tremendously. So far, the market is dominated by telecom and datacom applications in the c-band wavelength range and usually adopts silicon photonics or indium phosphide photonics. As the technology is maturing, new opportunities are arising outside of the traditional wavelength range. For wavelengths below 1.2 μm, silicon can no longer perform effective guiding of the light due to increased absorption. Hence, a wider bandgap material such as silicon nitride (SiN_x) is used for wavelengths ranging from 400 nm up to 3500 nm. Moreover, with the low index contrast of silicon nitride, the propagation losses can be significantly lower than for silicon. The downside of SiN_x photonic circuits is the lack of integrated active components. The lack of light source integration is similar for both Si and SiN_x due to the lack of a direct bandgap feature. However, silicon photonics can use doped Si structures for modulators and strained germanium for modulators and detectors. In contrast, silicon nitride photonics has to rely on novel material integration to obtain similar functionalities on the PIC.

In this work we investigate the novel method of micro-transfer-printing (μTP) to achieve the goal of functional integration of active components on top of SiN_x waveguides. This technique aims to combine the best of flip-chip and wafer-bonding based integrations. The TP-technique offers (1) a high throughput capability via the wafer-scale process, (2) the capability to do pre-testing on the III-V substrate for process control monitoring, (3) easy applicability with the separation of the III-V processing from the PIC wafer, (4) cost-effective handling of the expensive III-V material and (5) smooth integration of several different materials onto a single target substrate. A conceptual overview of the key processing steps is shown in Figure 8, with a visualization of those steps in Figure 9. The technique is an interesting candidate to solve the problem of opto-electronic integrated circuits.

With SiN_x, the near-infrared (NIR) wavelength range opens up the capability to probe biological tissues in a wavelength range of reduced water absorption. This allows for effective detection of changes of the refractive index of liquids due to the presence of specific analytes. The 850 nm region was chosen due to the expertise of fabricating high efficiency VCSELs in the datacom market. Therefore, this work
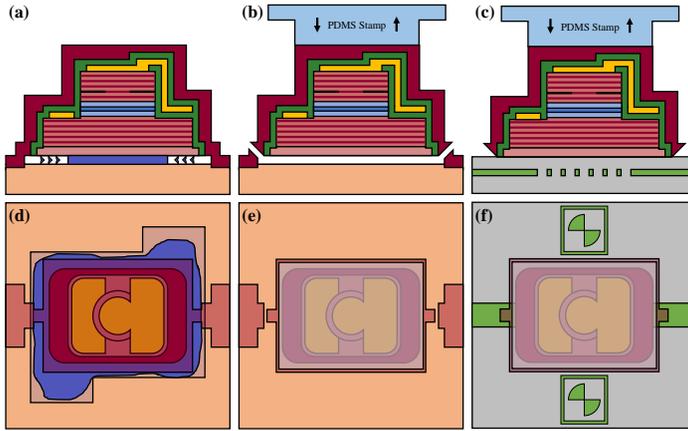
Figure 8: Concept of the micro-transfer-print method for a 850 nm VCSEL. The top row illustrates a cross-sectional overview, while the bottom row shows a top-down view of the relevant processing steps: (a & d) the underetch of the release layer, (b & e) the device after pick-up, (c & f) the printing of the device on the SiN_x waveguide of the PIC.

investigates GaAs as the material system for the development of the transfer-printing efforts. An overview of the investigated components is demonstrated in Figure 10. It showcases a metal-semiconductor-metal photodetector, a PIN photodetector and a bottom emitting VCSEL.
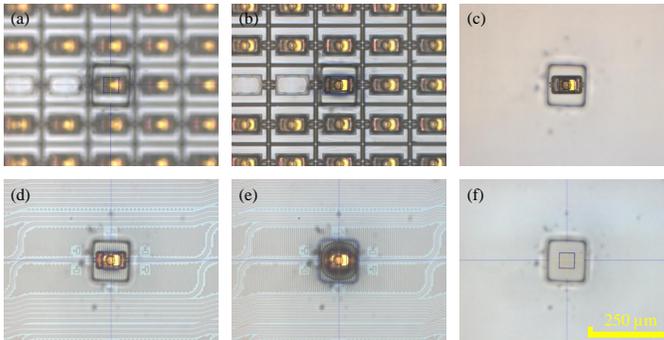
Figure 9: Microscope images of the TP-steps of a VCSEL: (a) coupon identification, (b) touch-down of the PDMS stamp onto the device, (c) device pick-up, (d) alignment of the device with respect to PIC, (e) printing of the device onto the PIC, (f) peeling off the PDMS stamp, with the coupon remaining on the PIC.
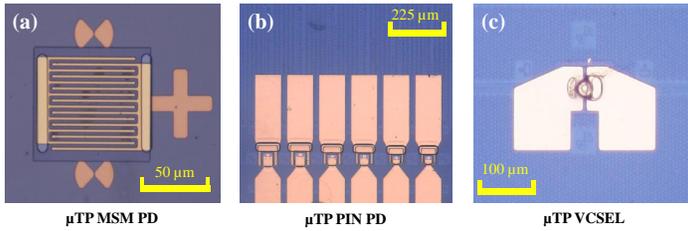
Figure 10: The micro-transfer-printed devices investigated in this work: (a) a high-speed metal-semiconductor-metal photodetector with interdigitated finger contacts, (b) a waveguide-coupled p-i-n photodetector with high responsivity and (c) a waveguide-coupled, bottom-emitting VCSEL as a narrow tunable laser for bio-sensing applications.

Transfer-printed Metal-Semiconductor-Metal PD

The metal-semiconductor-metal photodetector is a high-speed, planar detector. We demonstrated the transfer-printing capabilities of a large area (fiber-interfacing) and small area (waveguide-coupled) MSM PDs. Combining both opens up opportunities for a photonic interposer application, where intra-die communication is facilitated by a SiN_x waveguide and waveguide-coupled PD. Inter-die communication with large multi-mode fibers can be detected with the large area MSM PD.

The photodetector was grown on a high-aluminium AlGaAs release layer, with devices printed on SiN_x waveguides and high-resistivity silicon substrates. Figure 11 summarizes the device characteristics of the large area MSM PD. On average, dark current values were 22 nA and 7.2 nA for the larger and smaller PDs, respectively. Similarly, the responsivity was 0.17 A/W and 0.1 A/W for both PDs. A bandwidth of more than 19 GHz was measured. With this, high speed data rate transmission can be achieved, with open-eye diagrams observed at 40 Gbit/s.
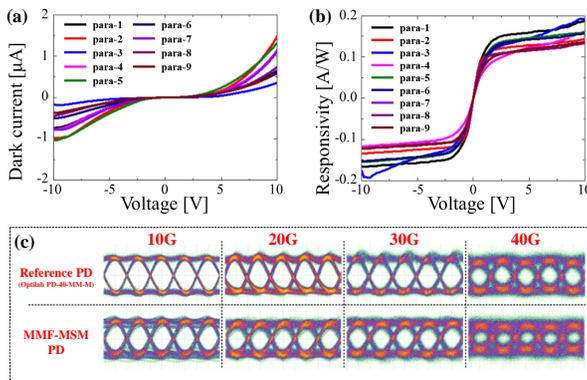
Figure 11: Device performance of the large area MSM PD: (a) the device dark current, (b) the device responsivity and (c) the high speed detection up to 40 Gbit/s, staying below the forward error correction limit.
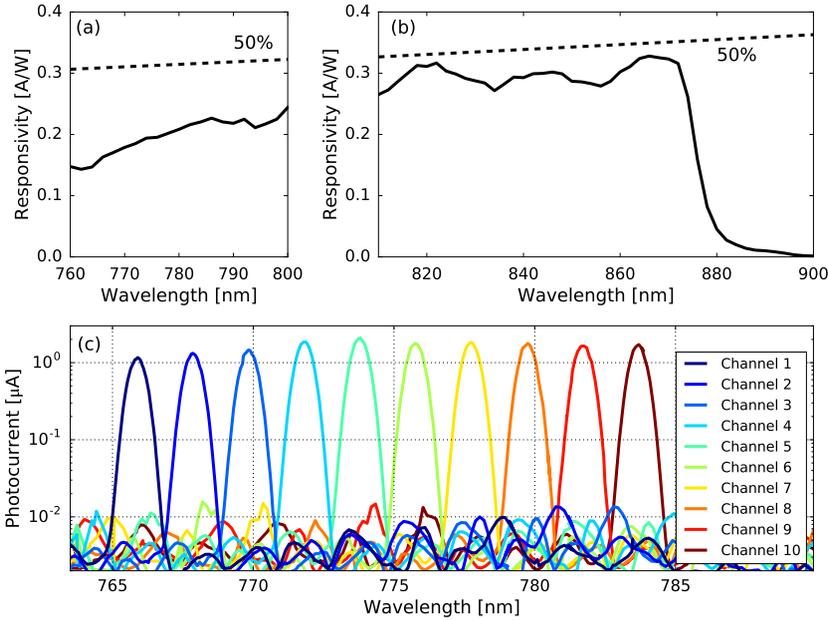
Figure 12: Characterization of transfer-printed PIN photodetectors, with the waveguide-referred responsivity shown around (a) 780 nm and (b) 850 nm. (c) Photo-current of several array-printed PDs on the GC output channels of an arrayed waveguide grating spectrometer.

Transfer-printed PIN PD

A PIN PD integration is also demonstrated to improve the static device performance of the MSM PD. For the PIN PD, an InAlP layer is used as the sacrificial layer. This is the best layer system for GaAs devices, although it is not trivial to grow defect free.

The thick absorption layer of the PIN PD contributes to an improved waveguide referred responsivity as plotted in Figure 12. The devices have a low intrinsic dark current at an average of 10 pA. Moreover, with the improved grating coupler design, more light is diffracted upwards. This results in increased responsivity.

A demonstration is made for high throughput array printing on an on-chip arrayed waveguide grating as a spectrometer. Sets of 7 PDs are printed and characterized for the PD response. Figure 12-(c) shows the PD photocurrent measured with a tunable laser. There are no indications of increased cross-talk with the PDs integrated on the PIC. Due to their broad wavelength operations, the PDs are excellent candidates for on-chip integrated sensors in the entire NIR wavelength range.
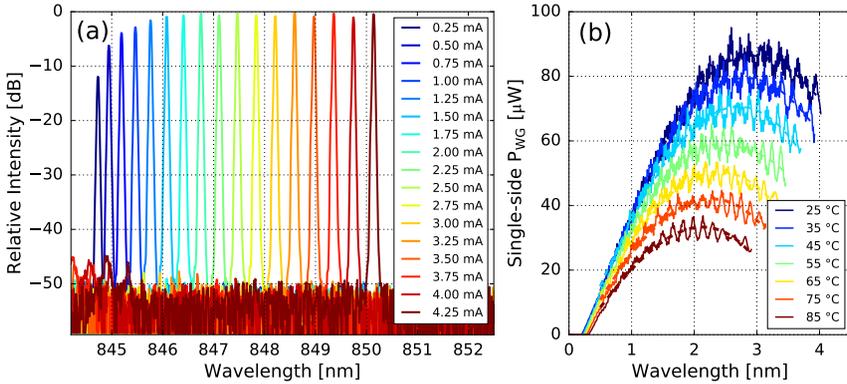
Figure 13: Characterization of transfer-printed, waveguide-coupled bottom-emitting VCSELs on a SiN$_x$ PIC: (a) the VCSEL wavelength tuning with low power dissipation, (b) the high-temperature performance of the waveguide-coupled VCSELs.

Transfer-printed VCSEL

The transfer-printed VCSELs were developed in collaboration with the Opto-electronic Group of Chalmers Technical University Sweden. The project is a continuation of an earlier wafer-bonded demonstration. The approach of the transfer-printed VCSEL is a bottom emitting device that illuminates a medium index contrast, second order diffraction grating in the silicon nitride waveguide layer. The chosen approach allows for a fraction of the light to leak out of the top-side DBR. With this feature, we can test structures on the source substrate for process control purposes.

The devices have a lasing threshold in the 0.10 to 0.35 mA range, depending on the size of the oxide-defined aperture. Through current biasing, the wavelength is tuned over a range of approximately 4.5 nm, as can be seen in Figure 13. With the oxide-silicon substrate and BCB cladding, the thermal resistance increases. As a result, the thermal roll-over occurs in the 8-10-12 mW power dissipation range, depending on the apertures of 3-4-5 μm. This limits the on-chip optical power, but results in low-power consuming lasers that can tune mode hop free over several nanometers. The tuning range is maintained over 10 kHz, with a 3dB signal reduction at approximately 1 MHz. The lasers can interrogate and sample refractive sensors at speeds far exceeding the specification for biological applications.

The SiN$_x$ VCSEL diffraction gratings improve the suppression of the next higher order modes by approximately 5 to 10 dB. In the current approach, the oxide apertures between 4 and 5 μm combine the highest waveguide-coupled power with excellent single-mode characteristics (>35 dB suppression). Overall, a single-side waveguide coupling efficiency of over 10% is observed, with more than 20% double-side coupling efficiency.
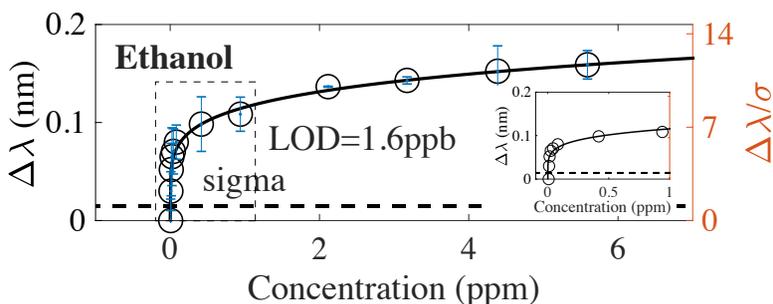
Figure 14: Ethanol concentration measurement on a highly sensitive, narrowband MZI refractive index gas sensor. The demonstrated LOD is 1.6 ppb for this specific analyte.

Refractive index sensor

The NIR wavelength range is an ideal candidate for on-chip refractive index sensors that can detect various analytes based on the applied coating. The demonstrated VCSEL and PIN PD are attractive building blocks for a compact, integrated sensor. Therefore, a refined approach is taken to a waveguide based transducer for narrow wavelength laser interrogation. A Mach-Zehnder Interferometer (MZI) design with extremely high sensitivity is chosen to detect sweat-based ions in the millimolar range relevant for health sensing. A second application is tested, where a mesoporous silica oxide coating, developed at TU Vienna, is used to detect several volatile organic compounds. An example of ethanol sensing is illustrated in Figure 14. The demonstrated sensor showed performances exceeding that of equivalent Raman-based sensors, with limits of detection in the low to mid parts-per-billion range.

Conclusions

In this dissertation, the transfer-printing method is studied and implemented for heterogeneous integration of GaAs opto-electronic components on a silicon nitride photonic circuit. We demonstrated the waveguide-based integration of detectors, VCSELs and highly sensitive waveguide sensors. These components are expected to form the building blocks for the next generation on-chip refractive sensors in the near infrared wavelength range.

1

Introduction to integrated photonics

1.1 Silicon and silicon nitride integrated photonics

Integrated photonics is the field of making integrated optical circuits on CMOS compatible wafers. By leveraging the tools from the CMOS industry, advanced CMOS nodes are available for high-resolution patterning and dense integration of optical circuits on chip [1]. On top of this, a route to high-volume production is feasible. There are many waveguide systems, such as silicon-on-insulator (SOI), silicon nitride (SiN_x)-on-insulator, germanium-on-silicon and others that can benefit from this proposition. Figure 1.1 shows that InP offerings with integrated lasers have so far been the dominant player in the field of optical transceivers. Silicon photonics is however catching up at a compound annual growth rate of 44.5%.

PIC revenues for InP and SiPh-based transceivers

	2018	2019	2020	2021	2022	2023	2024	CAGR
■ InP	$4,086	$3,934	$5,011	$6,784	$9,750	$11,907	$14,756	23.9%
■ SiPh	$455	$484	$740	$1,154	$1,966	$2,822	$4,144	44.5%
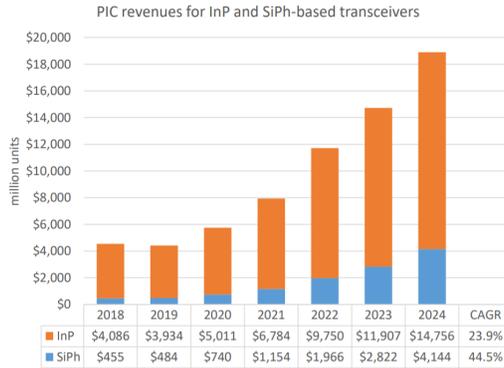
Figure 1.1: Yole development forecast on PIC revenues for optical transceivers [2].

For each of these platforms, the light is confined inside a high refractive index core layer and surrounded by lower refractive index cladding layers, often silicon oxide (SiO_x). The index contrast between core and cladding is a measure for the achievable integration density. The index contrast of SiN_x-to-SiO_x is lower than for SOI, leading to a lower integration density. But there are advantages to SiN_x, such as the broader transparency window from 400 nm to 4 μm. SiN_x also has a lower thermo-optic coefficient compared to silicon, which is an advantage for thermal stability but a disadvantage for power-efficient thermal phase shifters. Higher on-chip powers can be achieved as well with SiN_x versus Si, where two-photon absorption is the limiting factor. The material can be deposited through low-pressure chemical vapor deposition (LPCVD) or plasma-enhanced chemical vapor deposition (PECVD). LPCVD is the more stable configuration, has a higher refractive index and lower losses for the infrared wavelength spectrum. PECVD has a higher transparency window, leading to lower losses at shorter wavelengths. PECVD nitride is also a low-temperature deposition process, thus compatible with CMOS back-end processing.

Due to these various advantages, the SiN_x photonic integration field is expected to grow. From the same report [2], a prediction is made that the SiN_x PIC market will double over the next four years to $10M revenue by 2024. In Europe alone various commercial offerings are becoming available, each with their own advantages: (i) imec's PECVD biopix_300 nm platform has a 300nm thick nitride. It is processed on 200 mm wafers and can achieve 150 nm feature sizes, while integrating heaters and exposing waveguides. (ii) Lionix, with their TriPlex platform, aims for a different approach with a lower mode confinement and allowing for lower waveguide losses. (iii) Ligentec's LPCVD Thick SiN_x or CNM-IMB's LPCVD nitride offering [3, 4] can handle high power, nonlinear super-continuum generation, while achieving very dense on-chip integration.
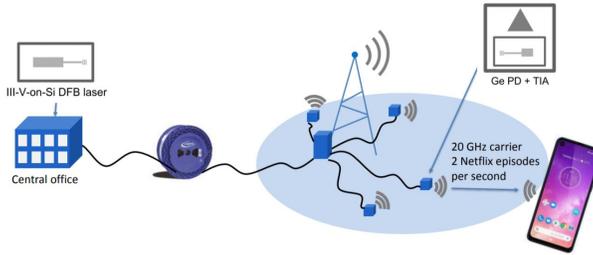
Figure 1.2: Radio (5G) signal - over - optical (carrier), reproduced from [8].

1.1.1 Telecom & datacom

The main driver in the field of integrated photonics has been telecommunications (telecom), where information is sent and received through cities and countries via the vast optical long-haul fiber network. The more recent addition has been data communications (datacom), where information is shared within and between large data centers. The large demand of streaming services and online videos leads to an explosion of data traffic in these data centers. This is expected to rise even further with 4K and 8K formats, virtual streaming, Ultra-HD video streaming, self-driving cars, etc. Luxtura, Intel, Lumentum, Infinera and others are making high-speed transceivers to service those needs [5–7].

The next big market driver are 5G base stations, where silicon photonics can play a major role in servicing with digital transceivers as in the case of a data center or by using a radio-over-fiber approach. In such products, the RF signal is encoded on an optical carrier and then transmitted over an optical fiber towards the 5G base stations. At the base station, a high-speed photodetector captures the signal and the signal is amplified and transmitted [8].

1.1.2 LiDAR

In the quest for self-driving cars, Light Detection and Ranging (LiDAR) has become an interesting tool to achieve computer-vision with accurate depth measurements. Currently, non-integrated LiDAR systems are bulky and expensive at $\sim$ \$10k per unit. So far, they have consisted of movable or rotating parts to achieve a wider field of view. On-chip solid state LiDAR can offer benefits of size reduction, lower cost ($\leq$ \$500) and lower maintenance by using all-optical beam steering techniques, e.g. phased arrays. Several companies are developing such LiDAR products or are already offering similar products: Aeva optics backed by Volkswagen [9]; MIT-Darpa; Xenomatix [10]; AMS [11] with their VCSEL-based lidar systems;

Luminar; Blackmore Sensors; and Analytics backed by BMW iVentures. Others, like SensePhotonics [12], have a different LiDAR architecture, using thousands of miniaturized integrated light sources, as will be discussed in chapter 4.

1.1.3 Sensing

Besides the current transceiver products and upcoming 5G and LiDAR chips, PICs for optical sensing form another branch of applications that are slowly gaining traction in various different fields.

Refractive Index Sensing

Refractive index sensing uses light-matter interaction and has proven to be an extremely sensitive method to detect all kinds of matter interactions. The introduction of new PIC-technology modules can expose the waveguide to air by locally removing the SiO_x, and thus allowing for a direct interface between the waveguide and the to-be-detected analyte. Refractive index sensors using Mach-Zehnder interferometers have been used to detect antibodies in blood and urea [13–15], or particles in gasses [16]. The light sources used in such applications are either broadband emitters, or tunable lasers. In the case of a broadband light source, arrayed waveguide gratings (AWG) are commonly used as an interrogator. A recent review compares the latest trends in label-free biosensing with on-chip micro-fluidic functionality for low-cost healthcare [15]. Other instances include refractive index based optical microphones and pressure sensors based on the photo-elastic effect [17].

Absorption spectroscopy

Absorption spectroscopy, as the name implies, looks at how much light of each wavelength is being absorbed by a compound. One option to investigate a wavelength region of interest is to use a broadband emitter, which covers the spectral region with an on-chip interrogator for spectral analysis. Another option is using a tunable laser to scan the different parts of the spectrum step-by-step.

With over 400 million people suffering from diabetes, easy and continuous glucose monitoring can be a game changer in managing the disease. Optical glucose sensors have a longer lifespan, which is a key advantage over chemical based sensors. Glucose has a strong interaction with infrared light in the wavelength range between 1500 nm and 2200 nm, with different companies pursuing various subsections of the spectrum [18, 19]. Besides glucose, there are many other relevant parameters to be measured in human blood, such as lactates for monitoring muscle condition, and sepsis control [19].
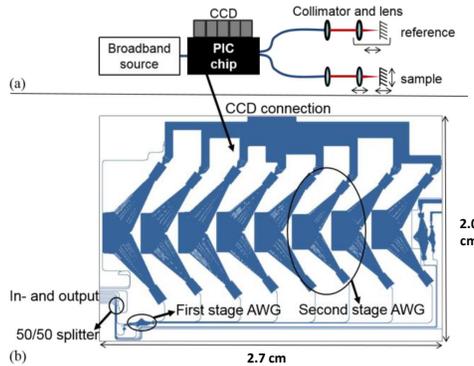
Figure 1.3: OCT-system with on-chip interferometer and interrogator, as currently developed by Lionix-AMC [26].

Raman spectroscopy

Each material or molecule has low-energy vibrational and rotational modes that can be probed by inelastic scattering of light in Raman spectroscopy. An incoming pump light source excites the molecule to a virtual state, after which it falls back to a different state with a different energy level with respect to the first one. The process of inelastic scattering is faint, but it scales inversely proportional to the fourth power of the wavelength. Hence, it is interesting to use light sources close to the visible spectrum, often at 785 nm on a SiN_x platform. The generated Raman spectrum is broadband in nature. Demonstrations over the last years include spontaneous Raman spectroscopy on-chip [20], and surface enhanced Raman spectroscopy by increasing the optical intensity inside an Atomic Layer Deposition (ALD) - coated slot waveguide [21]. The SiN_x waveguide has a non-negligible Raman background of its own, hence other waveguide materials are also being investigated [22]. Recent advances in the development of on-chip coatings with extremely high analyte enrichment factors have led to a boast in the generated Raman signal [23, 24], bringing the technology closer to market.

Optical Coherence Tomography

Another interesting upcoming market for PICs is optical coherence tomography (OCT), with an example circuit shown in Fig.1.3. The applications of OCT range from eye examination to skin lesion analysis or even dental control. An OCT system consists of a broadband light source or a widely tunable laser source to scan over a wide wavelength range. The light is split into a reference path and a sensing path. Afterwards, the light is combined on-chip with a MZI [25]. For a broadband source, on-chip wavelength demultiplexers are being used [26].

1.2 III-V integration techniques

Because silicon is not a direct bandgap material, it is almost impossible to fabricate silicon-based integrated lasers. For this reason, integration techniques that bring III-V opto-electronic components onto a Si circuit are key to enhance the functionality of the circuit. The following section covers the main integration techniques and offers insights into the advantages and disadvantages of each method.

1.2.1 Monolithic InP photonics

Indium Phosphide (InP) photonics circumvents the core problem of integrating III-V onto silicon-based wafers by starting from a III-V wafer and fabricating every component in InP. The main downside is the higher cost associated with III-V materials. The philosophy of leveraging CMOS foundry style processing remains the same as for silicon photonics, however the scale is different [27]. The straightforward integration of lasers, semiconductor optical amplifiers (SOAs), modulators and photodetectors onto the platform has made it the most prevalent platform to date [28]. Most commercial transceiver products thus use InP photonics [7, 29]. Another downside, beside cost, are the higher losses of the passive components and the higher propagation losses of the InP waveguides with respect to Si and SiN$_x$. This impedes the fabrication of certain types of lasers, such as ultra-narrow linewidth lasers [30]. III-V processing is typically done on smaller, 2-4 inch wafers. While InP photonics remains cost-competitive for the current product volumes, it does not provide a competitive solution for higher volumes. At larger volumes, silicon photonics takes the lead in cost-efficiency due to the lower wafer cost and 200 & 300 mm wafer fabrication capabilities. There are various MPW offerings in the InP market, such as the one from SmartPhotonics [31] and the Fraunhofer Heinrich-Hertz Institute [32], both accessible through JePPIX [33].

1.2.2 Epitaxial III-V-on-silicon photonics

Epitaxial III-V on silicon photonics, as the name implies, attempts to grow III-V crystals on the SOI wafer. Integrating the III-V layers onto a silicon substrate is complex due to the large lattice mismatch between the III-V and the silicon, and the differences in thermal expansion coefficient and the polar/non-polar interface. However, several solutions to these problems are being developed. Aspect ratio trapping is one of these approaches [34]. The III-V is grown in trenches defined on the Si wafer using metal-organic vapor phase epitaxy (MOVPE). The seeding layer has a significant defect density, but as the epitaxial growth progresses, the

III-V Processing

Unpatterned InP epitaxial wafer   Patterned InP device wafer
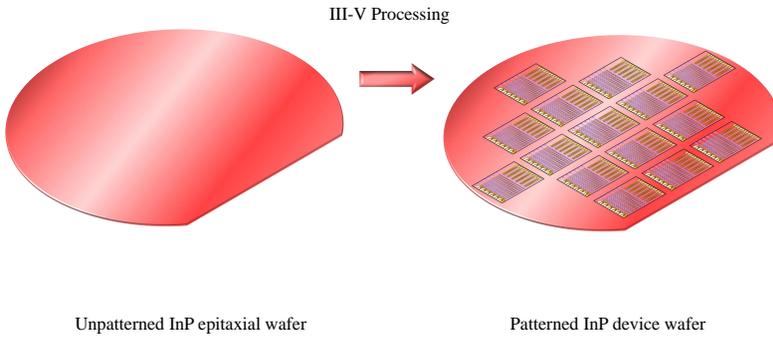
Figure 1.4: Concept image of InP photonics wafer processing, where both active and passive components are made in the III-V (InP) layerstack.

Epitaxial Growth of Nanoridge Lasers

SiPh wafer   Enhanced SiPh wafer
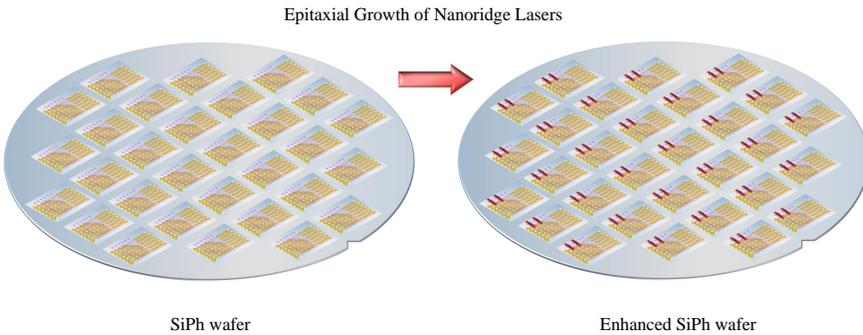
Figure 1.5: Schematic of Hetero-Epitaxial growth, where III-V materials such as GaAs are grown as nanoridges on a silicon target wafer.

dislocation threads move outwards. Consequently, a high quality crystalline III-V material grows on top of the seeding layer. Lasing with optical excitation has been demonstrated [35]. Out of all integration approaches, this has arguably the lowest TRL. Nevertheless, great progress is being made with engineering InP, GaAs and GaSb nanoridges [36], and more recently with demonstrations of high-performance PDs [37].

single-die flip-chip transfer

Gelpack with fully processed III-V devices   target SiPh wafer
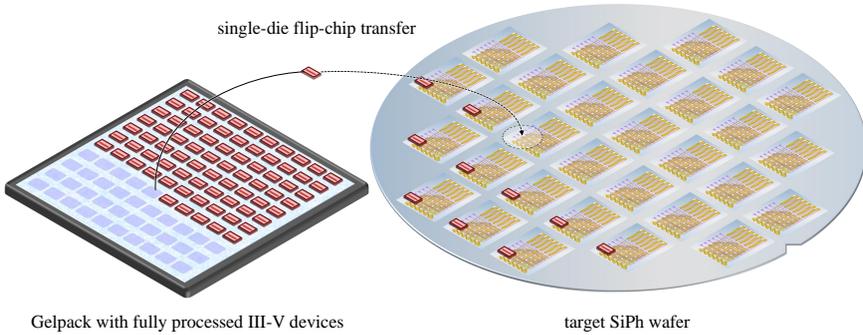
Figure 1.6: Schematic of a pick-and-place transfer of a single device onto a silicon photonics
target wafer. The devices are diced on the native substrate, prior to the transfer process.

1.2.3   Pick-and-place integration

The most common approach of heterogeneous integration is pick-and-placement of
the III-V dies. There are several subcategories: flip-chipping, butt-coupling two
chips, and using a micro-optical-bench (MOB) integration, or a combination of
these methods.

1.2.3.1   Flip-chipping

Borrowed from the electronics industry, flip-chipping creates both a mechanical and
electrical bond between the component and the substrate by soldering the devices
to the substrate. The solder balls are deposited on either the flip-chipped device or
on the target wafer. After the mechanical flipping procedure, the combined system
is heated up to reflow the solder balls and form a solid mechanical, electrical and
thermal connection. Flip-chipped devices are processed on a III-V wafer. They
are then tested and diced before the integration. One of the main advantages is the
possibility of pre-testing the processed III-V dies before the flip-chip procedure. A
downside is the relatively low throughput of the process, with the dies being placed
in a serial, one-by-one, manner. Currently, most application volumes of photonic
integrated circuits can still be managed by flip-chip integration. The technique
has been originally a mainly vertical process, ideally suited for integration of
grating-assisted photodetectors or VCSELs [38]. Recently, efforts are made into
flip-chipping reflecting SOAs or lasers into a locally etched recess with a contacting
pedestal to butt-couple with the waveguide [39], [40], [41].
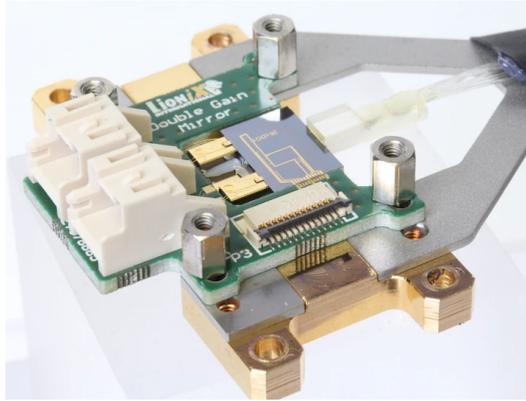
Figure 1.7: Example of a Lionix TriPlex chip with two reflecting SOAs butt-coupled to the facet of the SiN$_x$ PIC. On-chip power levels of over +13 dBm are achieved [43].

1.2.3.2   Butt-coupling

As the last paragraph stated, flip-chipping did not initially offer an approach for facet-coupling. As such, butt-coupling of separate SOAs to PICs offers a viable approach to achieving high efficiency coupling [42]. Lionix is a foundry providing such a solution, achieving over 100 mW of optical power in the waveguide [43]. Also, by combining a reflective SOA (RSOA) with an on-chip mirror, an external cavity laser can be created. These lasers can posses additional functionality such as a wide tuning range and ultra-narrow linewidths [44]. However, butt-coupling remains a die-level process as each RSOA needs to be aligned separately to the facet of the PIC. Current product volumes do not yet require foundries to establish higher throughput processes. Recently made efforts bring facet-coupling forward as a wafer-scale compatible process. On-wafer defined recesses with metal contacting features serve as the landing site for the flip-chip transferred III-V component.

1.2.3.3   Micro-Optical Bench

The integration of different micro-optical components onto a single micro-optical bench (MOB) is practiced by Luxtera, now Cisco. The MOB consists of a substrate with an opening for optical coupling to the PIC. The bond pads allow for wirebond integration, while a ball lens plus reflector are used to focus the light beam towards the grating coupler on the PIC. As both MOB and PIC systems can be optimized and characterized separately before assembly, the compound yield of the final assembled product can be higher. However, the method does not facilitate all needs, e.g. losses associated with the grating-based approach are less suitable with external cavity
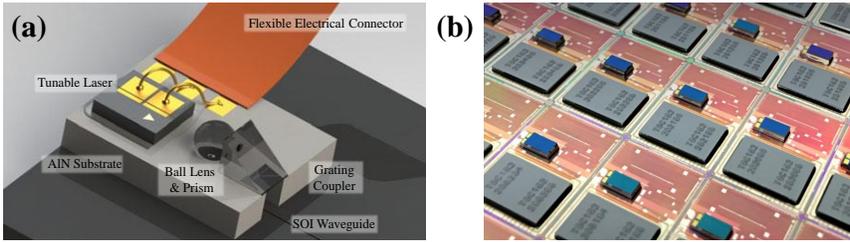
Figure 1.8: (a) Schematic of a Micro-Optical-Bench with laser, substrate, ball lens and prism [45]. (b) MOB-integration on wafer-scale, from Luxtera [5].

laser designs. Typically, a finished laser product (Distributed Feedback (DFB) laser) is packaged in the MOB [45], [46].

1.2.4   Die- and wafer-bonding

Bonding techniques are divided into two categories: direct bonding and adhesive bonding. Direct bonding, as the name implies, does not use an adhesive layer and directly bonds the III-V to the target substrate (Si or SiO_x). The downside is that prior to bonding, both surfaces require thorough cleaning steps to enable a good bond. Also, the surface roughness of the substrates is extremely important. The smallest of defects on either surface can result in a failure. Adhesive bonding uses an adhesive layer, usually DVS-BCB [47], which mitigates the above issues as it planarizes the surface.

Instead of bonding two complete wafers, smaller samples can be bonded in a die-to-wafer scheme. Such an approach mitigates the risk of substrate delamination to a local defect, while also making more efficient use of the costly III-V material. With this process, multiple smaller III-V dies are then bonded to the allocated silicon dies on the target wafer. After bonding, the substrate is again selectively removed and the III-V layers are patterned into functional devices. Most laser-coupling methods rely on adiabatic coupling with waveguide tapers in both the III-V and silicon waveguide. The technique is not suitable for butt-coupling light to a waveguide facet.

The direct bonding technique has been largely developed at the University of California Santa-Barbara (UCSB), while Ghent University pioneered the DVS-BCB adhesive bonding. The first membrane lasers on silicon waveguides were reported in 2006 [48, 49]. For direct bonding, very high-power inside the waveguide (37 mW) and 1 kHz linewidth was demonstrated [50], as well as ultra-wide tunability and 100 Hz linewidth [30]. Other demonstrations from Ghent University include
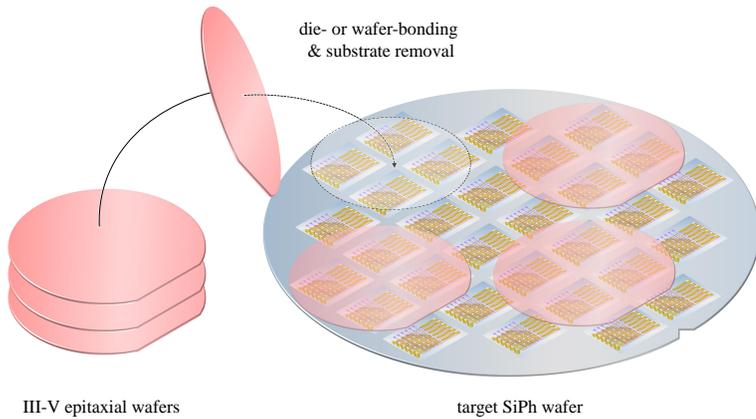
Figure 1.9: Schematic of wafer-to-wafer bonding. After bonding, the III-V substrate is selectively removed and standard III-V processing is performed to pattern the III-V devices.

wide-tunable lasers in the short-wave infrared region [51], GaAs-QD DFB for the O-Band [52], 850 nm half-VCSEL integration with lateral leakage [53], novel electronically tunable InP DFB lasers [54] and high-speed DFB structures [55], [56].

The direct bonding integration method is currently commercialized by Intel in high volumes for telecom transceivers [6]. More recently it was picked up by the UCSB spin-off company NexusPhotonics, who are wafer-bonding GaAs wafers onto SiN_x photonic wafers for near-infrared and visible light applications [57].
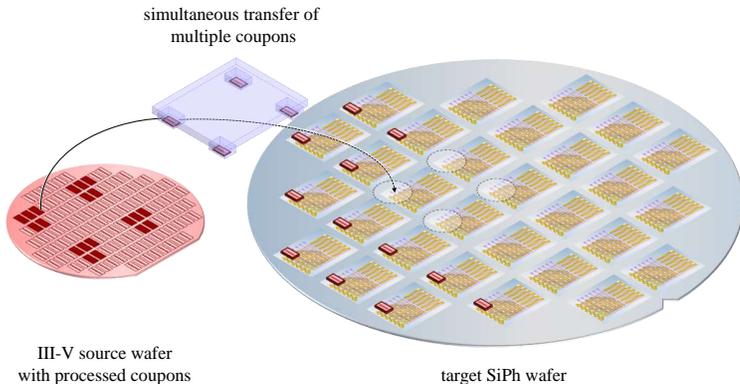
Figure 1.10: Schematic of micro-transfer-printing, where multiple coupons are picked up from a III-V substrate simultaneously, and printed onto a target wafer with a PDMS stamp.

1.2.5   Micro-transfer-printing

Micro-transfer-printing (μTP) or transfer-printing (TP) is an integration technique that aims to bring the best aspects of the previously discussed integration techniques together. Details about the operation principle follow in section 1.3. The core technology was developed by the group of professor John Rogers at the University of Illinois Urbana-Champaign (UIUC) between 2003-2006. The company Semprius was spun-off from UIUC to commercialize the technology for high-performance concentrating photovoltaics. From 2013 onwards, the company X-Celeprint was formed to license and develop the technology further. The technique itself is a pick-and-place method that allows for parallel pick-up and printing of devices with a polydimethylsiloxaan (PDMS) stamp. The printing operation can achieve a high accuracy ($\leq$ 1.0-1.5 μm 3σ) and higher throughput than what is typically obtained by flip-chip or MOB integration. It reduces the risk of printing failure with respect to wafer-bonding due to the localized bonding of only small coupons. Similar to wafer-bonding, transfer-printed devices are in close contact with the optical waveguides. This is ideal for adiabatic coupling of light between the waveguides. Recent work has shown the integration of InP SOAs and DFB lasers on silicon [58–60] and InP SOAs and external cavity lasers on silicon nitride [61] by means of adiabatic coupling. However, TP is more flexible and allows for novel coupling schemes such as butt-coupling [62], [63]. Just as flip-chip integration, it is also compatible with pre-integration testing of devices on the source substrate.

TP is a material independent technique. Coupons from InP, GaAs or GaSb material platforms can be picked up and printed on silicon or silicon nitride waveguide platforms to cover a much broader wavelength range. But the technique can be used just for other purposes as well, such as for integration on flexible substrates [64] or even for the fabrication of micro-LED displays [65].

1.3   Transfer printing of GaAs photonic devices

This section covers the basic considerations of TP in general and TP for GaAs-based components, which are relevant to this work. First, the fundamentals are explained, after which a dummy process flow is detailed for both the source and target substrates. Chapters 2, 3 and 4 will cover their respective application-specific process flow in more depth. The printing and post-processing parts are largely the same for all components in this work, so that part of the discussion is limited to this section.
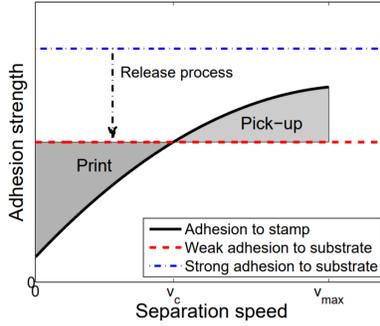
Figure 1.11: Schematic diagram of critical energy release rates, reproduced from [66].

Operation principle

The transfer printing method relies on the velocity-dependent adhesion properties of PDMS [67]. Simply put, when a PDMS stamp is in contact with another material and the PDMS stamp is moved rapidly upwards, the adhesion between the PDMS stamp and the material will be larger than if the PDMS stamp was moving upwards slowly. This property is described by the PDMS separation energy G_{PDMS} in equation 1.1. G_0 is the energy release rate at standstill, v_0 is the velocity where the adhesion energy is double the value at standstill and n is a fitting parameter.

$$G_{PDMS} = G_0 \left[1 + \left(\frac{v}{v_0} \right)^n \right] \tag{1.1}$$

This property is used to delaminate the coupon from the source substrate by moving the PDMS stamp upwards with a sufficiently high speed, with the turnover point indicated by v_c. The speed required to overcome the strength of the molecular bonds between a III-V component and the III-V substrate is too high for a practical system. The speed can be lowered, if the adhesion energy of the substrate is lowered. This can be achieved by performing an undercut or release etch of the devices. Afterwards, the devices are free-standing but kept in place by a set of tethers. The adhesion energy is now much lower than before and the devices can be picked up more easily above a critical velocity:

$$v_c = \left(\frac{G_{substrate} - G_0}{G_0} \right)^{\left(\frac{1}{n} \right)} \tag{1.2}$$

When printing, the stamp laminates the coupon to the target substrate, usually pre-treated with a bonding layer. Figure 1.11 shows that if the PDMS stamp moves sufficiently slowly upwards, the process takes place in the printing zone. The adhesion energy between the target substrate and the coupon is now larger than the adhesion energy between the coupon and the PDMS stamp. The coupon will thus remain on the target substrate and the printing is performed successfully.
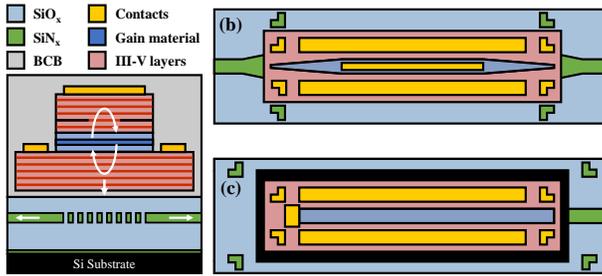
Figure 1.12: (a) Grating-assisted coupling of a VCSEL; (b) Adiabatic coupling of a SOA/laser with tapers in the SiN$_x$ and the III-V; (c) Butt-coupling an edge emitting laser or RSOA to a waveguide inside a recess.

Optical Coupling Schemes

There are three major coupling schemes compatible with transfer-printing: grating-assisted coupling, butt-coupling and adiabatic coupling. Grating-assisted coupling uses a diffraction grating to couple the light into or out of a waveguide. The upside of diffraction gratings are the alignment tolerant characteristics for PD integration and a clear coupling mechanism between vertical and horizontal planes. The downsides are the fairly narrowband and lossy interface to single-mode devices such as VCSELs and other laser types in a MOB configuration.

A edge-coupled and transfer-printed coupon is similar to the technique described in section 1.2.3.2. The III-V waveguide facet interfaces with a dielectric waveguide facet. A typical 1 μm misalignment results in around 3dB coupling loss, although dependent on the configuration and design. The waveguide facet is exposed by locally etching a recess of about 100 μm x 1000 μm. The coupon is then printed into the recess. This technique is not without challenges, as the recess does not allow a uniform coverage of a bonding layer through spincoating, resulting in a lower bonding yield and coupling efficiencies. Both direct bonding and spray-coating a thin bonding layer are good alternatives in this case. Despite the challenges, this approach is a promising candidate for broadband and high-power applications.

The third and most practiced method is adiabatic coupling. The coupling between a III-V waveguide layer and the Si waveguide is achieved by phase-matching both modes through tapering the Si and III-V waveguides. This method allows for straightforward integration of DFB lasers, DBR lasers and SOAs. A DFB laser can be made by defining a grating in the passive waveguides, creating filtered feedback for the transfer printed SOAs. Many instances in both die-or-wafer bonding and transfer-printing use this method. However, for lower index contrast materials, such as SiN$_x$, the width of the III-V taper tips have to be extremely narrow in order to achieve phase-matching. This can be solved by integrating an

intermediate high-index waveguide layer [61]. Typical 1 μm misalignment can be compensated for to -1dB loss with careful design of the adiabatic tapers [68].

1.3.1 Source processing

In this section, a general overview is given on the required process flow in order to prepare GaAs devices for the pick-up procedure of the transfer-printing process. As each specific component has it owns functional and geometrical constraints, the source process flow of these will be covered in more detail in their own chapters.

Device patterning

The contact layers and device layers are in the same stacking order on the source substrate as they will be on the target substrate, in contrast to bonding. In the first step, typically, some sacrificial layers are removed that protect the underlying GaAs epi-stack. Next up is the deposition of a Ti/Au-based P-contact on the top contact layer. The main mesa is usually dry etched with a SiN_x hard mask. This is typically done with $SiCl_4$ or BCl_3 based recipes for $Al_xGa_{1-x}As$ systems. Afterwards, the sidewalls are passivated with a SiN_x layer. Next, the passivation layer is patterned so that the N-contact can be deposited, which is usually a Ni/Ge/Au/Ti/Au alloy.

Release layer

A similar procedure is done for the secondary mesa, in order to access the release layer. This secondary mesa is typically dry-etched for the first part, and finished with a wet etch for the last few 100 nm, to ensure a perfect stop on top of the release layer. With dry-etching, there is a risk of over-etching into the release layer. This might reduce the printing yield as will be discussed later. After the wet etch, another SiN_x passivation is done to protect the sidewalls of the second mesa, as shown in Fig.1.14-(b). Following this, the release layer is patterned and with the same mask, 100 nm is etched into the substrate, as shown in Fig.1.14-(c & d). This ensures the complete removal of the release layer prior to the encapsulation.

Encapsulation

The photoresist encapsulation has two functions in our approach: (1) to protect the devices during the release etch and (2) to form anchor pads and tethering the coupon to these anchors. In other approaches, the anchors and tethers can be made in a different material than the encapsulation, but we limit ourselves to this approach in this work. The anchors are formed on the substrate. Depending on the device geometry, the size and configuration of the anchors vary. The tether forms the
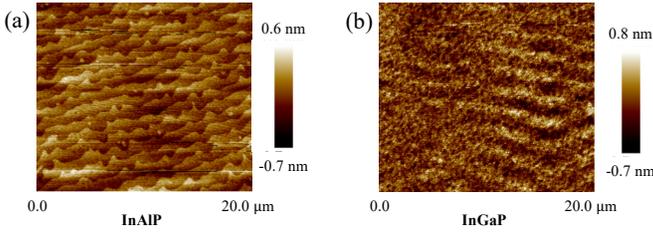
Figure 1.13: AFM measurements of the GaAs source substrate underneath the coupons after pick-up. (a) Shows InAlP-on-GaAs and (b) an InGaP-on-GaAs release layer.

interconnecting part between the anchor and the coupon, and can also be designed to facilitate breaking at a desired location [69]. Several designs are explored in this work due to the varying topologies and sizes of the different devices.

Release etch

In the GaAs material system, there are three likely candidates for a release layer: $Al_{0.95}Ga_{0.05}As$, $In_{0.49}Al_{0.51}P$ and $In_{0.49}Ga_{0.51}P$. The most important property of a release layer is having a good etch selectivity with respect to the substrate and the etch stop layer above the release layer . An atomic force microscopy measurement was performed on available InAlP and InGaP layer systems, as shown in Fig.1.13-(a & b). Both systems have excellent etch selectivity, with reduced risk of oxidation over $Al_{0.95}Ga_{0.05}As$.

HCl can be used as an etchant for each release layer system, as it does not etch GaAs. The release time varies for the different release layers. InAlP etches the fastest, then AlGaAs and then InGaP. The dilution levels also vary: for InGaP, a HCl 2:1 De-ionized water (DI) solution is required to speed things up, while for InAlP a 1:2 dilution is enough. The layer properties are summarized in Table 1.1

After the release, the etchant needs to be removed. As the devices are free-hanging, one needs to take care in rinsing the sample without damaging the fragile coupons. Hence, it is preferred to rinse the sample by dipping it into beakers of de-ionized (DI) water for up to five minutes per cycle and that for 5 cycles. After the rinsing, the sample substrate is left to dry inside a wetbench.

Material	Application	Chapter	Etchant	Etch rate
$Al_{0.90}Ga_{0.10}As$	MSM PD	2	HCl-37% 1:1 DI	~ 1 μm / min.
$In_{0.49}Al_{0.51}P$	PIN PD	3	HCl-37% 1:2 DI	~ 1 μm / min.
$In_{0.49}Ga_{0.51}P$	VCSEL	4	HCl-37%	~ 1 μm / min.

Table 1.1: Release layers used in this work, along with their etchants and etch rates.
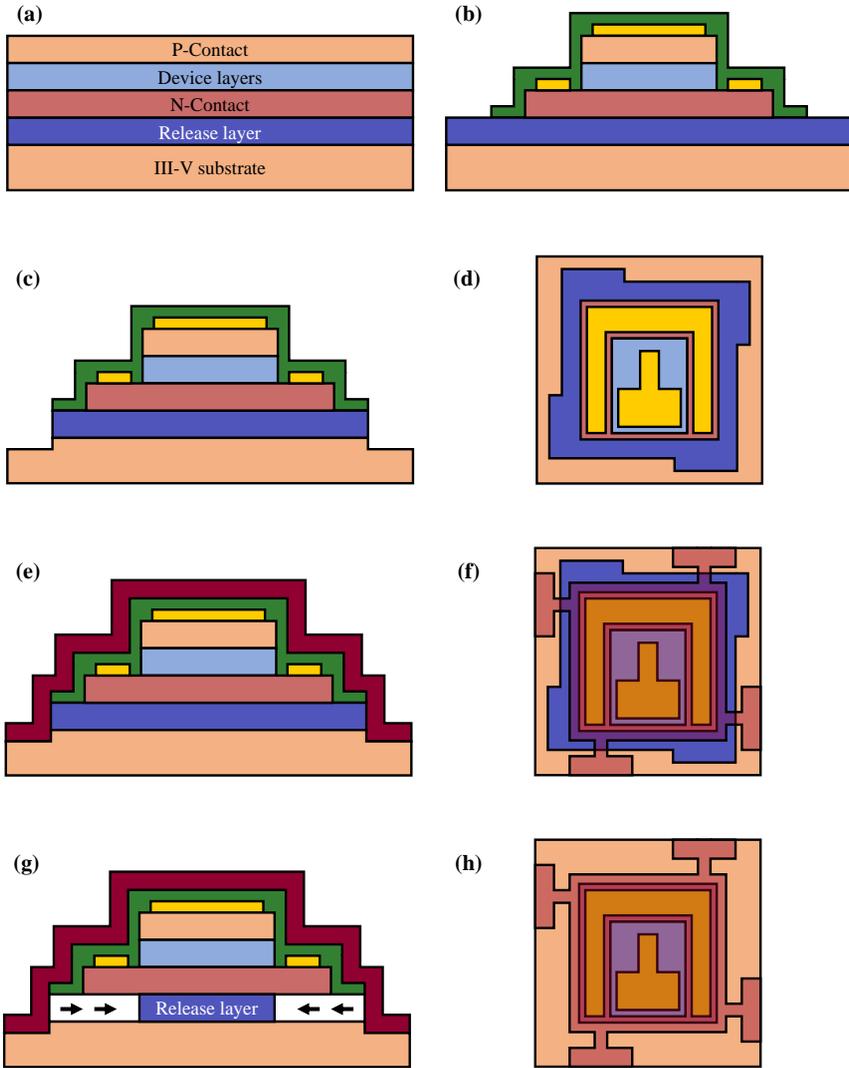
Figure 1.14: Cross-section and top-down schematic overview of the processing steps required on the source substrate prior to transfer-printing: (a) The III-V epitaxial layer stack; (b) the patterned two-mesa device with P- & N-contacts; (c - d) cross-section view and top-down view of the device after patterning the release layer; (e - f) cross-section view and top-down view after encapsulating the devices; (g - h) cross-section and top-down view of the release layer etch.

1.3.2   Micro-Transfer-Printing process

This section tackles the mechanical pick-up and printing process. It is important to note that there are three coordinate systems during printing: the stamp, the source substrate, and the target substrate coordinate system.

Pick-up

The PDMS stamp is lowered until 100 µm above the coupons. There, the alignment is done between the stamp coordinate system and the source substrate coordinate system. After alignment, the stamp is slowly lowered and brought in contact with the coupon. Because of the rate-dependent adhesion properties of PDMS, the tethers break and the coupon sticks to the stamp as it moves rapidly upwards.

Printing

Prior to loading the target substrate in the transfer-printer, a bonding layer is spincoated onto the target substrate. Depending on the applied coupling mechanism, the thickness of the bonding layer can have a large impact on the optical coupling performance. The thickness can be controlled through dilution with mesitylene [70]. For thicker BCB-bonding layers, it is important to do a partial cure at $\sim 135°C$ for ten minutes before printing the devices. Otherwise, the BCB might still introduce a shift of the devices during the full-cure after printing.

The stamp and coupon are lowered to 100 µm above the target substrate. A pattern recognition tool identifies distinct and high-contrast features on the coupons. Examples are the tetris block-shaped P-contact on the device shown in Fig.1.15-(b), and the waveguide layer markers next to the target coupling structure in Fig.1.15-(f). Through the visual pattern recognition system, the target coordinate system can be adjusted to match the stamp coordinate system. After alignment, the stamp laminates the coupon to the target substrate. Once in contact, a shear force is applied on the stamp to move it relative to the coupon. This shear force helps peeling off the stamp from coupon during the upwards movement of the stamp.

Stamp cleaning

After printing, the stage moves to bring the stamp to a scotch tape cleaning substrate. After touch-down, residues on the stamp stick to the cleaning target and a new cycle can start under one minute typically. Important for the cleaning procedure is that the source substrate and the coupons are clean. This implies a cleaning step of the source substrate after the release etch. Once the process flow is optimized for yield and cleanliness, the stamps can last for thousands of cycles (observed at UGent), or up to millions of cycles as verbally advertised by X-Celeprint.
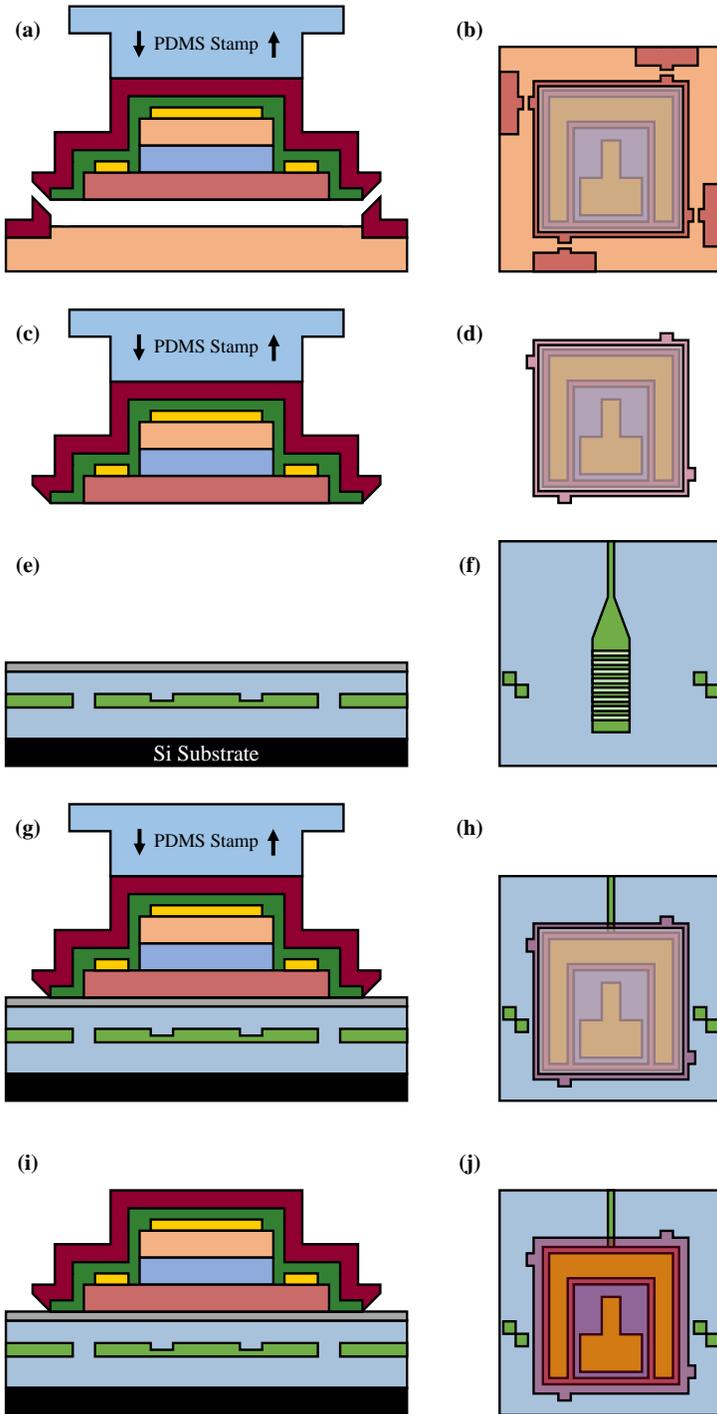
Figure 1.15: Cross-section and top-down schematic overview of the different steps of the micro-transfer-printing process: (a - b) device pick-up after lamination and when the stamp moves rapidly upward, breaking the tethers; (c - d) show the coupon remaining on the stamp; (e - f) has the target substrate with alignment markers and a bonding layer to facilitate printing; (g - h) highlights the device printing where the stamp laminates the coupon to the target substrate and slowly moves upward; (i - j) has the coupon attached to the target substrate.

1.3.3   Post-printing processing

Post-transfer-printing processing is detailed here. After the BCB-planarization of the target substrate, the target substrate is quasi-planar. As such, the following process steps are similar for all devices in this work.

Post-printing treatment

In the first step, the photoresist encapsulation is removed, as it can not withstand the curing temperatures of BCB. A 135°C bake is done to reflow the photoresist and to facilitate the removal in a subsequent RIE etch. Afterwards, the DVS-BCB bonding layer can be fully cured up to 250°C, for a duration of around 2 hours.

Passivation

After full-curing the bonding layer, a planarization of the substrate is done by spincoating a thick DVS-BCB-57 film. The planarization allows for further sample- or wafer-scale processing to be done. In order to remove the topology introduced by the transfer-printed devices, it is best to choose the BCB planarization layer as thick as possible. An additional full-cure of the passivation layer is then performed. Afterwards, the layer is etched back to just above the top-surface of the devices. In this way, the depth of the VIAs to access the bottom contacts is reduced.

Probe Pad Metallization

To access the device contacts, VIAs are etched in the passivation layer. However, the topology of the transfer-printed devices may vary from 2 µm to 9 µm. To facilitate the access of the probe pad metal to the device contacts, the VIAs in the BCB layer are etched with a sloped sidewall. A standard positive lithography step is done with photoresist AZ9260, with a reflow of 2 minutes at 120°C to achieve $\sim$ 45° sidewalls. Ti/Au pads are deposited to probe the devices.

Remarks & Future trends

The process flow described above is the default TP-process. A new trend is coming up to switch to SiN_x based tethers and anchors. This is a more robust solution in terms of shelf-life than the hydration sensitive photoresist polymers. It also opens up the possibility for BCB-passivation and probe pad deposition to be done on the source substrate, thus reducing the processing steps required after printing. A photoresist encapsulation is still used to protect the devices and probe pads during the release etch.
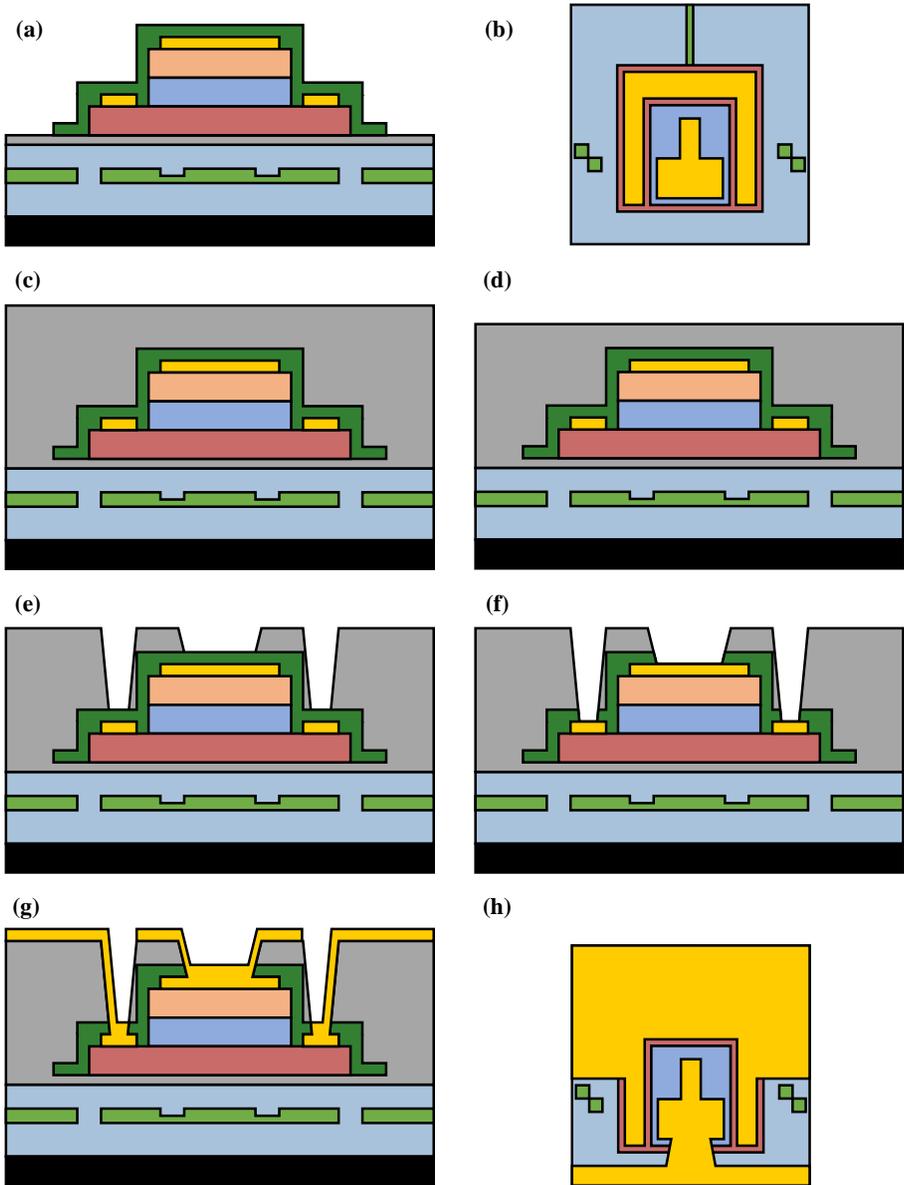
Figure 1.16: Schematic overview of the processing steps on the target substrate: (a-b) after printing, the photoresist encapsulation is removed from the devices; (c) the sample is planarized using a thick DVS-BCB-57 film; (d) this passivation layer is etched back using RIE to just above the top surface of the coupon; (e-f) the device contacts are accessed by opening up VIAs through the BCB-passivation and SiN$_x$ protection layers; (g) the probe pad metal (Au) is deposited and selectively lifted-off from the substrate.
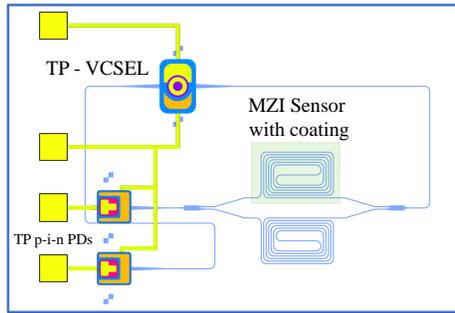
Figure 1.17: Schematic of the PIC layout for a refractive index sensor with a transfer-printed VCSEL as tunable laser and transfer-printed photodiodes.

1.4 Project Architecture

The goal of this work is to demonstrate the integration of near infrared laser sources and photodetectors on a SiN waveguide platform. As the work is carried out partly within the Pix4life project, one of the key architectures of interest has been a refractive index sensor with integrated read-out. However, the integration of such components is not limited to just that application. In this section, more information is provided on the architecture of both the sensor and the possibility of using the technology for a SiN_x photonic interposer.

1.4.1 Refractive index sensor

Within the context of the PIX4life project, one of the project's demonstrators has been a refractive index sensor for wearables. For any wearable sensor, battery life is crucial and therefore the power consumption of the sensor should be reduced to a minimum. With this in mind, vertical-cavity-surface-emitting lasers (VCSELs) become the most prominent candidate for on-chip integration due to their low power consumption and relatively high optical power output. Nowadays, lasing current thresholds below 1 mA are consistently attainable. Their lasing threshold is thus up to 10 or 50 times lower than those from other on-chip laser structures such as DFB lasers. A downside of VCSELs is the narrowband tuning range, which is typically limited from 1 to 3 nm, with a potential extension to 5 nm when using significant self-heating. However, one can design a Mach-Zehnder interferometer for refractive index sensing by matching its free spectral range to the narrowband tuning range of the VCSEL. In this way, the VCSEL can track the MZI resonance shift. Along with the VCSEL, the integration of photodetectors is also studied.
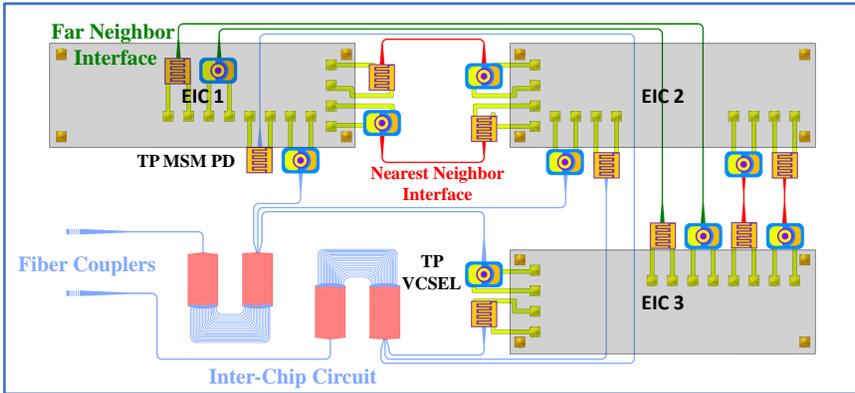
Figure 1.18: Schematic of a possible photonic interposer, with transfer-printed VCSELs and photodetectors to interconnect the different electronic subsystems.

1.4.2 Photonic Interposer

Photonic interposers provide a solution for the bandwidth limitations that electrical interconnects are facing in today's high-speed compute systems [71, 72]. As data processing and data storage needs are ever increasing, so do the bandwidth requirements of these systems. Currently, PIC-based interposers are offering ways for data-aggregation in wavelength-division multiplexing manner on a single channel or fiber [73]. In this way, the amount of fibers required in a data center can be maintained for an increase in data traffic. Figure 2.1 shows a schematic of the proposed SiN_x interposer with GaAs VCSELs and a MSM PD, where three electrical integrated circuits (EICs) are flip-chipped onto the photonic interposer. As the temperature inside such subsystems can exceed 85°C, GaAs VCSELs in combination with a SiN_x PIC is a promising approach. The expertise in 850 nm GaAs VCSELs can be transferred to this platform. Due to their vertical structure, VCSELs also provide a unique opportunity for direct interfacing with optical fibers (e.g. for multi-core fiber solutions).

Recent work in the H2020 PhoxTroT project showcases the advantages of the low-power photonic interposers for Terabit per second data throughput over multiple channels [74, 75]. In the H2020 PASSION project the aim is to flip-chip long-wavelength VCSELs on a silicon fiber-interfacing interposer, bringing aggregated 1 Tbps data rates [76, 77].

1.5 Thesis outline and attribution of work

The goal of this PhD has been to enrich the imec biopix 300 nm nitride platform with additional functionality. The current market offerings of SiN_x waveguide platforms are fairly simple with respect to InP and SOI platforms. Most are limited to passive waveguide structures and phase shifters using the thermo-optic effect. Some companies do offer additional functionality but only on a die-level basis, and for low volumes without a clear path for scaled up production. So our objective has been **to showcase laser integration and photodetection on a SiN chip, and to do so based on transfer printing. This technique offers a clear road for large volume and low-cost production**. By achieving this objective, new application opportunities may arise in low-power sensing or photonic interposers, to name two applications. With this objective in mind, this work is divided into three major sections, covered in the following 4 chapters.

- Can we demonstrate competitive light detection on-chip with the TP-method? Two photodetector configurations are discussed in chapter 2 and 3.

- Can we demonstrate relevant VCSEL-to-PIC light-coupling with the TP-method? This topic is studied in chapter 4.

- Can we demonstrate the feasibility of a VCSEL-PD based sensor in a demonstrator circuit? This question will be answered in the context of gas sensing in chapter 5.

Chapter 1 has introduced the reader to the field of silicon and silicon nitride photonic integrated circuits. It illustrated some of the key applications that have driven the field forward as well as those that look promising and where SiN_x can act as a technology enabler. Different ways of integrating opto-electronic functionality on these platforms were discussed, out of which micro-transfer printing came out as a strong candidate. The process of micro-transfer printing GaAs devices was presented together with the necessary processing steps on both the source and target substrate. Finally, a brief overview was given of the relevant applications that act as the drivers for this work.

Chapter 2 is the first component chapter, that studies the high-speed Metal-Semi-conductor-Metal (MSM) photodetector. The work has been divided between Guanyu Chen for the simulations and measurements and the author for the design and fabrication. The chapter elaborates on the concept of the planar device and the basic theory of the MSM structure. The discussion about the fabrication of the device is mostly limited to the processing on the source substrate. In the next part, the measurement setups and characterization of the devices are discussed. The

chapter ends with a demonstration of a MSM detector transfer-printed directly onto an electronic integrated circuit.

Chapter 3 is the second photodetector chapter, covering p-i-n photodetectors. This type of detector is ideally suited for low-power-consumption bio-sensors. The operation principle, design and layer stack are covered. The discussion about the fabrication is again limited to the source substrate. The final part of the chapter covers the measurement results for single device characterization and for an array of devices printed on a demultiplexing circuit. The design of the PD and PIC, and the measurements were done by the author, while the fabrication responsibilities have been shared with Sulakshna Kumari.

Chapter 4 discusses the integration of a bottom-emitting VCSEL onto the imec SiN_x waveguide platform. A standalone, bottom emitting VCSEL has been co-designed with the SiN_x diffraction grating couplers on the platform. The chapter covers simulations, design, fabrication and characterization of the WG-coupled VCSEL. This work has been a joint effort with Chalmers University of Technology, spearheaded by PhD candidate Alexander Grabowski and overseen by professors Johan Gustavsson and Anders Larsson.

Chapter 5 describes a refractive index sensor made on the imec platform. The concept relies on the functionalization of the waveguides with an analyte-selective coating. In this chapter, the requirements for a VCSEL-based sensor are brought forward, with a custom designed, highly sensitive photonic circuit. The chosen coating for the sensor is a mesoporous silica coating, which is selective to volatile organic compound gasses for environmental safety monitoring. The design and characterization of the passive circuit are done by the author, while Giuseppe Antonacci performed the gas sensing measurements.

The summary and conclusions of this work are found in Chapter 6, along with future prospects for the GaAs-on-SiN_x technology.

1.6   Publications

This dissertation has led to several publications in peer-reviewed journals. Parts of this work have been presented at international conferences, either by Jeroen Goyvaerts or by one of the co-authors. A summary of the research output is given below:

1.6.1 Publications in international journals

1. G. Antonacci **J. Goyvaerts**, H. Zhao, B. Baumgartner, B. Lendl and R. Baets, "Ultra-sensitive refractive index gas sensor with functionalized silicon nitride photonic circuits," *Applied Physics Letters - Photonics*, vol. 5, no. 8, pp.(081301-0)-(081301-5), 2020. https://doi.org/10.1063/5.0013577

2. **J. Goyvaerts**, S. Kumari, S. Uvin, J. Zhang, R. Baets, A. Gocalinska, E. Pelucci and G. Roelkens, "Transfer-print integration of GaAs p-i-n photodiodes onto silicon nitride waveguides for near infrared applications," *Optics Express*, vol. 28, no. 14, pp.21275-21285, 2020. https://doi.org/10.1364/OE.395796

3. E. Haglund, M. Jahed, J. Gustavsson, A. Larsson, **J. Goyvaerts**, R. Baets, G. Roelkens, M. Rensing, P. O'Brien, "High-power single transverse and polarisation mode VCSEL for silicon photonics integration," *Optics Express*, vol. 27, no. 13, pp.18892-18899, 2019. https://doi.org/10.1364/OE.27.018892

4. A. Rahim, **J. Goyvaerts**, B. Szelag, J.M. Fedeli, P. Absil, T. Aalto, M. Harjanne, C. Littlejohns, G. Reed, G. Winzer, S. Lischke, L. Zimmermann, D. Knoll, D. Geuzebroek, A. Leinse, M. Geiselmann, M. Zervas, H. Jans, A. Stassen, C. Dominguez, P. Munoz, D. Domenech, A. L. Giesecke, M.C. Lemme and R. Baets, "Open-Access Silicon Photonics Platforms in Europe," *IEEE Journal on Selected Topics in Quantum Electronics*, vol. 25, no. 5, 2019. https://doi.org/10.1109/JSTQE.2019.2915949

5. M.A.G. Porcel, A. Hinojosa, H. Jans, A. Stassen, **J. Goyvaerts**, D. Geuzebroek, M. Geiselmann, C. Dominguez and I. Artundo, "Silicon nitride photonic integration for visible light applications," *Optic & Laser Technology*, vol. 12, pp.299–306, 2019. https://doi.org/10.1016/j.optlastec.2018.10.059

6. G. Chen, **J. Goyvaerts**, S. Kumari, J. Van Kerrebrouck, M. Muneeb, S. Uvin, Y. Yu and G. Roelkens, "Integration of high-speed GaAs metal-semiconductor-metal photodetectors by means of transfer printing for 850 nm wavelength photonic interposers," *Optics Express*, vol. 26, no. 5, pp.6351–6359, 2018. https://doi.org/10.1364/OE.26.006351

1.6.2   Publications in international conferences

1. J. Zhang, C. Op de Beeck, B. Haq, **J. Goyvaerts**, S. Cuyvers, S. Kumari, G. Muliuk, A. Hermans, A. Gocalinska, E. Pelucci, B. Corbett, A. Jose Trindade, C. Bowers, J. Van CAmpenhout, G. Lepage, P. Verheyen, B. Kuyken, D. Van Thourhout, G. Morthier, R. Baets and G. Roelkens, "Micro-Transfer-Printing for III-V/Si PICs," *Asian Communication and Photonics Conference*, Beijing, China, 2020.

2. **J. Goyvaerts**, S. Kumari, S. Uvin, J. Zhang, R. Baets, A. Gocalinska, E. Pelucci and G. Roelkens, "Transfer-print integration of GaAs p-i-n photodiodes onto silicon nitride photonic integrated circuits," *IEEE Photonics Society- Annual Conference*, Virtual / Vancouver, Canada, 2020. https://doi.org/10.1109/IPC47351.2020.9252495

3. G. Antonacci, **J. Goyvaerts**, H. Zhao, B. Baumgartner, B. Lendl and R. Baets, "Ultra-Sensitivie and compact on-chip gas sensor on a silicon nitride photonic integrated circuit," *SPIE Photonics West Conference*, United States, 2020. https://doi.org/10.1117/12.2557047

4. J. Zhang, G. Muliuk, **J. Goyvaerts**, B. Haq, A. Liles, S. Kumari, J. Juvert, C. Op de Beeck, B. Kuyken, J. Van Campenhout, G. Lepage, P. Verheyen, A. Gocalinkska, E. Pelucchi, B. Corbett, A.J. Trindade, C. Bower and G. Roelkens, "Heterogeneous integration in silicon photonics through micro-transfer-printing," *Micro-Optics Conference (MOC)*, Japan, 2019.

5. J. Gustavsson, E. Haglund, M. Jahed, A. Larsson, **J. Goyvaerts**, R. Baets, G. Roelkens, M. Rensing, P. O'Brien, "5 mW single mode and polarization stable 850-nm VCSEL for silicon photonics integration," *European VCSEL Day*, Brussels, Belgium, 2019.

6. G. Roelkens, J. Zhang, S. Kumari, J. Juvert, A. Liles, G. Muliuk, **J. Goyvaerts**, B. Haq, N. Mahmoud and D. Van Thourhout, "Transfer printing for heterogeneous silicon PICs," *Smart Systems Integrations*, Spain, 2019

7. G. Muliuk, J. Zhang, **J. Goyvaerts**, S. Kumari, B. Corbett, D. Van Thourhout and G. Roelkens, "High-yield parallel transfer print integration of III-V substrate-illuminated C-band photodiodes on silicon photonic integrated circuits," *SPIE Photonics West*, United States, 2019. https://doi.org/10.1117/12.2507373

8. G. Roelkens, J. Zhang, G. Muliuk, **J. Goyvaerts**, B. Haq, C. Op de Beeck, A. Liles, Z. Wang, S. Dhoore, S. Kumari, J. Juvert, J. Van Campenhout, B. Kuyken, D. Van Thourhout, B. Corbett, A.J. Trindade, C. Bower, and

R. Baets, "III-V/Si PICs based on micro-transfer printing," *Optical Fiber Communications Conference and Exhibition (OFC)*, United States, 2019.

9. E. Haglund, S. Kumari, **J. Goyvaerts**, R. Baets, G. Roelkens and A. Larsson, "Vertical-cavity silicon-integrated lasers by bonding and transfer printing," *26th International Semiconductor Laser Conference (ISLC)*, United States, 2018. https://doi.org/10.1109/ISLC.2018.8516256

10. G. Roelkens, J. Zhang, A. De Groote, J. Juvert, N. Ye, S. Kumari, **J. Goyvaerts**, G. Muliuk, S. Uvin, G. Chen, B. Haq, B. Snyder, J. Van Campenhout, D. Van Thourhout and A. Trindade, "Transfer printing for silicon photonics transceivers and interposers," *IEEE Optical Interconnects Conference (OI)*, United States, 2018.

References

[1] Abdul Rahim, Jeroen Goyvaerts, Bertrand Szelag, Jean Marc Fedeli, Philippe Absil, Timo Aalto, Mikko Harjanne, Callum Littlejohns, Graham Reed, Georg Winzer, Stefan Lischke, Lars Zimmermann, Dieter Knoll, Douwe Geuzebroek, Arne Leinse, Michael Geiselmann, Michael Zervas, Hilde Jans, Andim Stassen, Carlos Dominguez, Pascual Munoz, David Domenech, Anna Lena Giesecke, Max C. Lemme, and Roel Baets. *Open-access silicon photonics platforms in Europe*. IEEE Journal of Selected Topics in Quantum Electronics, 25(5):1–18, 2019.

[2] Yole Developpment. *Silicon Photonics and Photonic Integrated Circuits: Technology, Industry and Market Trends*. Technical report, 2019.

[3] Abdul Rahim, Eva Ryckeboer, Ananth Z. Subramanian, Stéphane Clemmen, Bart Kuyken, Ashim Dhakal, Ali Raza, Artur Hermans, Muhammad Muneeb, Sören Dhoore, Yanlu Li, Utsav Dave, Peter Bienstman, Nicolas Le Thomas, Günther Roelkens, Dries Van Thourhout, Philippe Helin, Simone Severi, Xavier Rottenberg, and Roel Baets. *Expanding the Silicon Photonics Portfolio with Silicon Nitride Photonic Integrated Circuits*. Journal of Lightwave Technology, 35(4):639–649, 2017.

[4] Marco A.G. Porcel, Alberto Hinojosa, Hilde Jans, Andim Stassen, Jeroen Goyvaerts, Douwe Geuzebroek, Michael Geiselmann, Carlos Dominguez, and Iñigo Artundo. *Silicon nitride photonic integration for visible light applications*. Optics and Laser Technology, 112(November 2018):299–306, 2019.

[5] Luxtera. *Silicon Photonics Technology*, 2020.

[6] Intel. *Intel Silicon Photonics*, 2020.

[7] Infinera. *Infinera - Solutions*, 2020.

[8] Kasper Van Gasse. *Heterogeneous Silicon Photonic Devices and Subsystems for Microwave Photonics*. PhD thesis, Ghent University, 2019.

[9] Aeva.ai. *Aeva Autonomous Driving*, 2020.

[10] Xenomatix. *Xenomatix Solid-State LIDAR*, 2020.

[11] AMS. *AMS - LIDAR*, 2020.

[12] SensePhotoncis. *Lidar SensePhotonics*, 2020.

[13] D. Martens, P. Ramirez-Priego, M. S. Murib, A. A. Elamin, A. B. Gonzalez-Guerrero, M. Stehr, F. Jonas, B. Anton, N. Hlawatsch, P. Soetaert, R. Vos, A. Stassen, S. Severi, W. Van Roy, R. Bockstaele, H. Becker, M. Singh, L. M. Lechuga, and P. Bienstman. *A low-cost integrated biosensing platform based on SiN nanophotonics for biomarker detection in urine*. Analytical Methods, 10(25):3066–3073, 2018.

[14] Antelope DX. *Diagnostics where you need it*, 2020.

[15] Jiawei Wang, Mariana Medina Sanchez, Yin Yin, Raffael Herzer, Libo Ma, and Oliver G Schmidt. *Silicon-Based Integrated Label-Free Optofluidic Biosensors : Latest Advances and Roadmap*. Advanced Material Technologies, 2020.

[16] Nebiyu A. Yebo, Sreeprasanth Pulinthanathu Sree, Elisabeth Levrau, Christophe Detavernier, Zeger Hens, Johan A. Martens, and Roel Baets. *Selective and reversible ammonia gas detection with nanoporous film functionalized silicon photonic micro-ring resonator*. Optics Express, 20(11):11855, 2012.

[17] V. Rochus, R. Jansen, R. Haouari, B. Figeys, V. Mukund, F. Verhaegen, J. Goyvaerts, P. Neutens, J. O'Callaghan, A. Stassen, S. Lenci, and X. Rottenberg. *Modelling and design of micro-opto-mechanical pressure sensors in the presence of residual stresses*. 2017 18th International Conference on Thermal, Mechanical and Multi-Physics Simulation and Experiments in Microelectronics and Microsystems, EuroSimE 2017, pages 1–5, 2017.

[18] IndigoMed. *Indigomed*, 2020.

[19] Brolis Sensor Technology. *Brolis Blood Sensor*, 2020.

[20] Ashim Dhakal, Frédéric Peyskens, Stéphane Clemmen, Ali Raza, Pieter Wuytens, Haolan Zhao, Nicolas Le Thomas, and Roel Baets. *Single mode waveguide platform for spontaneous and surface-enhanced on-chip Raman spectroscopy*. Interface Focus, 6(4), 2016.

[21] Ali Raza, Stéphane Clemmen, Pieter Wuytens, Muhammad Muneeb, Michiel Van Daele, Jolien Dendooven, Christophe Detavernier, Andre Skirtach, and Roel Baets. *ALD assisted nanoplasmonic slot waveguide for on-chip enhanced Raman spectroscopy*. APL Photonics, 3(11), 2018.

[22] Ali Raza, Stéphane Clemmen, Pieter Wuytens, Michiel de Goede, Amy S. K. Tong, Nicolas Le Thomas, Chengyu Liu, Jin Suntivich, Andre G. Skirtach, Sonia M. Garcia-Blanco, Daniel J. Blumenthal, James S. Wilkinson, and Roel Baets. *High index contrast photonic platforms for on-chip Raman spectroscopy*. Optics Express, 27(16):23067, 2019.

[23] T. H. Stievater, S. A. Holmstrom, D. A. Kozak, R. A. McGill, M. W. Pruessner, N. Tyndall, W. S. Rabinovich, and J. B. Khurgin. *Trace-gas Raman spectroscopy using functionalized waveguides*. 2016 Conference on Lasers and Electro-Optics, CLEO 2016, 3(8), 2016.

[24] Haolan Zhao, Bettina Baumgartner, Ali Raza, Andre Skirtach, Bernhard Lendl, and Roel Baets. *Multiplex volatile organic compound Raman sensing with nanophotonic slot waveguides functionalized with a mesoporous enrichment layer*. Optics Letters, 45(2):447, 2020.

[25] Günay Yurtsever, Boris Považay, Aneesh Alex, Behrooz Zabihian, Wolfgang Drexler, and Roel Baets. *Photonic integrated Mach-Zehnder interferometer with an on-chip reference arm for optical coherence tomography*. Biomedical Optics Express, 5(4):1050, 2014.

[26] Roosje M. Ruis, Arne Leinse, Ronald Dekker, Rene G. Heideman, Ton G. Van Leeuwen, and Dirk J. Faber. *Decreasing the Size of a Spectral Domain Optical Coherence Tomography System with Cascaded Arrayed Waveguide Gratings in a Photonic Integrated Circuit*. IEEE Journal of Selected Topics in Quantum Electronics, 25(1), 2019.

[27] Jos J.G.M. van der Tol, Yuqing Jiao, and Kevin A. Williams. *InP Photonic Integrated Circuits on Silicon*, volume 99. Elsevier Inc., 1 edition, 2018.

[28] Jonathan Klamkin, Hongwei Zhao, Bowen Song, Yuan Liu, Brandon Isaac, Sergio Pinna, Fengqiao Sang, and Larry Coldren. *Indium phosphide photonic integrated circuits*. In 2018 IEEE BiCMOS and Compound Semiconductor Integrated Circuits and Technology Symposium (BCICTS), pages 8–13. IEEE, 2018.

[29] Lumentum. *Lumentum - Optical Communication Products*, 2020.

[30] Minh A. Tran, Duanni Huang, and John E. Bowers. *Tutorial on narrow linewidth tunable semiconductor lasers using Si/III-V heterogeneous integration*. APL Photonics, 4(11), 2019.

[31] SmartPhotonics. *SmartPhotonics*, 2020.

[32] Fraunhofer Heinrich Hertz Institute. *Fraunhofer*.

[33] JePPIX. *JePPIX*, 2020.

[34] Yuting Shi, Zhechao Wang, Joris Van Campenhout, Marianna Pantouvaki, Weiming Guo, Bernadette Kunert, and Dries Van Thourhout. *Optical pumped InGaAs/GaAs nano-ridge laser epitaxially grown on a standard 300-mm Si wafer*. Optica, 4(12):1468, 2017.

[35] Yu Han, Wai Kit Ng, Chao Ma, Qiang Li, Si Zhu, Christopher C. S. Chan, Kar Wei Ng, Stephen Lennon, Robert A. Taylor, Kam Sing Wong, and Kei May Lau. *Room-temperature InP/InGaAs nano-ridge lasers grown on Si and emitting at telecom bands*. Optica, 5(8):918, 2018.

[36] Marina Baryshnikova, Yves Mols, Yoshiyuki Ishii, Reynald Alcotte, Han Han, Thomas Hantschel, Olivier Richard, Marianna Pantouvaki, Joris Van Campenhout, Dries Van Thourhout, Robert Langer, and Bernadette Kunert. *Nano-Ridge Engineering of GaSb for the Integration*. Crystals, 10(4):330–349, 2020.

[37] Cenk Ibrahim Ozdemir, Yannick De Koninck, Didit Yudistira, and Nadezda Kuznetsova. *InGaAs / GaAs Nano-Ridge Waveguide Photodetector Monolithically Integrated on a 300-mm Si Wafer*. 1(1):3–6.

[38] Huihui Lu, Jun Su Lee, Yan Zhao, Carmelo Scarcella, Paolo Cardile, Aidan Daly, Markus Ortsiefer, Lee Carroll, and Peter O'Brien. *Flip-chip integration of tilted VCSELs onto a silicon photonic integrated circuit*. Optics Express, 24(15):16258, 2016.

[39] Shinsuke Tanaka, Seok-Hwan Jeong, Shigeaki Sekiguchi, Teruo Kurahashi, Yu Tanaka, and Ken Morito. *High-output-power, single-wavelength silicon hybrid laser using precise flip-chip bonding technology*. Optics Express, 20(27):28057, 2012.

[40] A. Moscoso-Mártir, F. Merget, J. Mueller, J. Hauck, S. Romero-García, B. Shen, F. Lelarge, R. Brenot, A. Garreau, E. Mentovich, A. Sandomirsky, A. Badihi, D. E. Rasmussen, R. Setter, and J. Witzens. *Hybrid silicon photonics flip-chip laser integration with vertical self-alignment*. Optics InfoBase Conference Papers, Part F122-, 2017.

[41] M. Theurer, M. Moehrle, A. Sigmund, K. O. Velthaus, R. M. Oldenbeuving, L. Wevers, F. M. Postma, R. Mateman, F. Schreuder, D. Geskus, K. Worhoff, R. Dekker, R. G. Heideman, and M. Schell. *Flip-chip integration of InP and SiN*. IEEE Photonics Technology Letters, 31(3):273–276, 2019.

[42] Brian Stern, Xingchen Ji, Avik Dutt, and Michal Lipson. *Compact narrow-linewidth integrated laser based on low-loss silicon nitride ring resonator*. 2018 Conference on Lasers and Electro-Optics, CLEO 2018 - Proceedings, 42(21):21–24, 2018.

[43] Lionix International. *Ultra Narrow Linewidth Laser*, 2020.

[44] R. M. Oldenbeuving, E. J. Klein, H. L. Offerhaus, C. J. Lee, H. Song, and K. J. Boller. *25 kHz narrow spectral bandwidth of a wavelength tunable diode laser with a short waveguide-based external cavity*. Laser Physics Letters, 10(1), 2013.

[45] Bradley Snyder, Brian Corbett, and Peter Obrien. *Hybrid integration of the wavelength-tunable laser with a silicon photonic integrated circuit*. Journal of Lightwave Technology, 31(24):3934–3942, 2013.

[46] Lee Carroll, Jun Su Lee, Carmelo Scarcella, Kamil Gradkowski, Matthieu Duperron, Huihui Lu, Yan Zhao, Cormac Eason, Padraic Morrissey, Marc Rensing, Sean Collins, How Yuan Hwang, and Peter O'Brien. *Photonic packaging: Transforming silicon photonic integrated circuits into photonic devices*. Applied Sciences (Switzerland), 6(12):1–21, 2016.

[47] S. Keyvaninia, M. Muneeb, S. Stanković, P. J. Van Veldhoven, D. Van Thourhout, and G. Roelkens. *Ultra-thin DVS-BCB adhesive bonding of III-V wafers, dies and multiple dies to a patterned silicon-on-insulator substrate*. Optical Materials Express, 3(1):35, 2013.

[48] Alexander W. Fang, Hyundai Park, Oded Cohen, Richard Jones, Mario J. Paniccia, and John E. Bowers. *Electrically pumped hybrid AlGaInAs-silicon evanescent laser*. Optics Express, 14(20):9203, 2006.

[49] G. Roelkens, D. Van Thourhout, R. Baets, R. Nötzel, and M. Smit. *Laser emission and photodetection in an InP/InGaAsP layer integrated on and coupled to a Silicon-on-Insulator waveguide circuit*. Optics Express, 14(18):8154, 2006.

[50] Duanni Huang, Minh A. Tran, Joel Guo, Jonathan Peters, Tin Komljenovic, Aditya Malik, Paul A. Morton, and John E. Bowers. *High-power sub-kHz linewidth lasers fully integrated on silicon*. Optica, 6(6):745, 2019.

[51] Ruijun Wang, Bahawal Haq, Stephan Sprengel, Aditya Malik, Anton Vasiliev, Gerhard Boehm, Ieva Simonyte, Augustinas Vizbaras, Kristijonas Vizbaras, Joris Van Campenhout, Roel Baets, Markus-Christian Amann, and Gunther Roelkens. *Widely Tunable III–V/Silicon Lasers for Spectroscopy in the Short-Wave Infrared*. IEEE Journal of Selected Topics in Quantum Electronics, 25(6):1–12, 2019.

[52] Sarah Uvin, Sulakshna Kumari, Andreas De Groote, Steven Verstuyft, Guy Lepage, Peter Verheyen, Joris Van Campenhout, Geert Morthier, Dries Van Thourhout, and Gunther Roelkens. *13 μm InAs/GaAs quantum dot DFB laser integrated on a Si waveguide circuit by means of adhesive die-to-wafer bonding*. Optics Express, 26(14):18302, 2018.

[53] Sulakshna Kumari, Emanuel P. Haglund, Johan S. Gustavsson, Anders Larsson, Gunther Roelkens, and Roel G. Baets. *Vertical-Cavity Silicon-Integrated Laser with In-Plane Waveguide Emission at 850 nm*. Laser and Photonics Reviews, 12(2), 2018.

[54] Sören Dhoore, Anna Köninger, Ralf Meyer, Gunther Roelkens, and Geert Morthier. *Electronically Tunable Distributed Feedback (DFB) Laser on Silicon*. Laser and Photonics Reviews, 13(3):1–7, 2019.

[55] A. Abbasi, J. Verbist, L. A. Shiramin, M. Verplaetse, T. De Keulenaer, R. Vaernewyck, R. Pierco, A. Vyncke, X. Yin, G. Torfs, G. Morthier, J. Bauwelinck, and G. Roelkens. *100-Gb/s Electro-Absorptive Duobinary Modulation of an InP-on-Si DFB Laser*. IEEE Photonics Technology Letters, 30(12):1095–1098, 2018.

[56] M. Shahin, J. Rahimi Vaskasi, J. Van Kerrebrouck, P. Ossieur, X. Yin, J. Bauwelinck, G. Roelkens, and G. Morthier. *80-Gbps NRZ-OOK Electro-Absorption Modulation of InP-on-Si DFB Laser Diodes*. IEEE Photonics Technology Letters, 31(7):533–536, 2019.

[57] Tin Komljenovic, Hyundai Park, Chong Zhang, and Minh Tran. *Heterogeneous silicon nitride photonics: erratum*. Optica, 7(4):336–337, 2020.

[58] Jing Zhang, Bahawal Haq, James O'Callaghan, Angieska Gocalinska, Emanuele Pelucchi, António José Trindade, Brian Corbett, Geert Morthier, and Gunther Roelkens. *Transfer-printing-based integration of a III-V-on-silicon distributed feedback laser*. Optics Express, 26(7):8821, 2018.

[59] Bahawal Haq, Sulakshna Kumari, Kasper Van Gasse, Jing Zhang, Agnieszka Gocalinska, Emanuele Pelucchi, Brian Corbett, and Gunther Roelkens. *Micro-Transfer-Printed III-V-on-Silicon C-Band Semiconductor Optical Amplifiers*. Laser and Photonics Reviews, 14(7):1–12, 2020.

[60] Bahawal Haq, Javad Rahimi Vaskasi, Jing Zhang, Agnieszka Gocalinska, Emanuele Pelucchi, Corbett Brian, and Gunther Roelkens. *Micro-transfer-printed III-V-on-silicon C-band distributed feedback lasers*. Optics Express, 28(22):32793–32801, 2020.

[61] Camiel Op de Beeck, Bahawal Haq, Lukas Elsinger, Agnieszka Gocalinska, Emanuele Pelucchi, Brian Corbett, Günther Roelkens, and Bart Kuyken. *Heterogeneous III-V on silicon nitride amplifiers and lasers via microtransfer printing*. Optica, 7(5), 2020.

[62] Joan Juvert, Tommaso Cassese, Sarah Uvin, Andreas de Groote, Brad Snyder, Lieve Bogaerts, Geraldine Jamieson, Joris Van Campenhout, Günther Roelkens, and Dries Van Thourhout. *Integration of etched facet, electrically pumped, C-band Fabry-Pérot lasers on a silicon photonic integrated circuit by transfer printing*. Optics Express, 26(17):21443, 2018.

[63] Ruggero Loi, Steven Kelleher, Raja Fazan Gul, Antonio Jose Trindade, David Gomez, Liam O'Faolain, Brian Corbett, Simone Iadanza, Brendan Roycroft, James O'Callaghan, Lei Liu, Kevin Thomas, Agnieszka Gocalinska, Emanuele Pelucchi, and Alexander Farrell. *Edge-Coupling of O-Band InP Etched-Facet Lasers to Polymer Waveguides on SOI by Micro-Transfer-Printing*. IEEE Journal of Quantum Electronics, 56(1), 2020.

[64] Keon Jae Lee, Matthew a. Meitl, Jong-Hyun Ahn, John a. Rogers, Ralph G. Nuzzo, Vipan Kumar, and Ilesanmi Adesida. *1. Bendable GaN high electron mobility transistors on plastic substrates*. Journal of Applied Physics, 100(12):124507, 2006.

[65] X-Display Company. *X-Display*, 2020.

[66] Andreas De Groote. *Heterogeneous integration of multibandgap III-V semiconductor light sources on silicon photonics*. PhD thesis, Ghent University, 2017.

[67] Matthew a. Meitl, Zheng-Tao Zhu, Vipan Kumar, Keon Jae Lee, Xue Feng, Yonggang Y. Huang, Ilesanmi Adesida, Ralph G. Nuzzo, and John a. Rogers. *Transfer printing by kinetic control of adhesion to an elastomeric stamp*. Nature Materials, 5(1):33–38, 2006.

[68] Bahawal Haq and Gunther Roelkens. *Alignment-tolerant taper design for transfer printed III-V-on-Si devices*. 2019 European Conference on Integrated Optics, page T.P02, 2019.

[69] Brian Corbett, Ruggero Loi, James O'Callaghan, and Gunther Roelkens. *Transfer Printing for Silicon Photonics*. In Semiconductors and Semimetals, volume 99, pages 43–70. 2018.

[70] R. Baets G. Roelkens, B. Bataillou, J. Brouckaert, F. Van Laere, D. Van Thourhout. *Using BCB for Photonic Applications*.

[71] Joris Van Campenhout, Peter De Heyn, Guy Lepage, and Wim Bogaerts. *Silicon-Photonics Devices for Low-Power , High-Bandwidth Optical I / O*. pages 2–5. OSA, 2012.

[72] Imec. *Silicon photonic interposers for 400Gb/s and beyond optical interconnects*. 2018.

[73] Jeffrey B Driscoll, Pierre Doussiere, Syed Islam, Raghuram Narayan, Wenhua Lin, Hari Mahalingam, Jung S Park, Yiching Lin, Kimchau Nguyen, Katherine Roelofs, Avsar Dahal, Ranju Venables, Ling Liao, Richard Jones, Daniel Zhu, Sunil Priyadarshi, Bharadwaj Parthasarathy, and Yuliya Akulova. *First 400G 8-Channel CWDM Silicon Photonic Integrated Transmitter*. In 2018 IEEE 15th International Conference on Group IV Photonics (GFP), pages 1–2, 2018.

[74] European Union Seventh Framework Council. *PhoxTroT*, 2020.

[75] Bogdan Sirbu, Yann Eichhammer, Hermann Oppermann, Tolga Tekin, Jochen Kraft, Victor Sidorov, Xin Yin, Johan Bauwelinck, Christian Neumeyr, and Francisco Soares. *3D silicon photonics interposer for Tb/s optical interconnects in data centers with double-side assembled active components and integrated optical and electrical through silicon via on SOI*. Proceedings - Electronic Components and Technology Conference, 2019-May(May):1052–1059, 2019.

[76] Timo Aalto, Mikko Harjanne, Mikko Karppinen, Matteo Cherchi, Aila Sitomaniemi, Jyrki Ollila, Antonio Malacarne, and Christian Neumeyr. *Optical interconnects based on VCSELs and low-loss silicon photonics*. In Henning Schröder and Ray T Chen, editors, Optical Interconnects XVIII, volume 10538, pages 147–159. International Society for Optics and Photonics, SPIE, 2018.

[77] European Union Seventh Framework Council. *H2020 PASSION*, 2020.

2

Micro-transfer-printed GaAs high-speed Metal-Semiconductor-Metal photodetectors

Internet traffic is growing everyday and photonic technology is a key enabler to bring the data to all consumers and network points. Whether the information is sent over a long-haul or a short-haul link over fiber, or through an on-die interconnection, photodetectors will always be required to convert the signal from the optical domain to the electrical domain. In this chapter, we discuss a particular design of a PD, suited for SiN_x photonic interposers. This work has been a collaboration between Guanyu Chen and Jeroen Goyvaerts. The work discussed in this chapter has been published in Optics Express [1].

2.1   Introduction

Optical communication has the upper hand in long-haul communications such as transcontinental and metro fiber networks [2] down to short-reach high-speed links beyond a few meter in data centers [3]. As the data traffic inside and between data centers is expected to grow for the coming decades, the same is true for the infrastructure [4]. In inter-chip communications, facilitated by optical fibers, photonic interposers can play a role in aggregating data sent by transmitters and to facilitate communication between electronic dies on the same interposer. By multiplexing more data streams on a single fiber in a coarse or dense wavelength multiplexing (CWDM/DWDM) scheme, costs can be saved on the fiber network. Current offerings attempt to bridge 100 Tbps [5]. Another approach, more inline with the work presented here, is the interposer architecture based on VCSELs and PDs [6]. Similarly, 2km VCSELs optical links operating at 40 Gbps and 240 fJ per bit power consumption have been demonstrated. [7].

Another possible application of photonic interposers lays in on-chip communication. It has long been expected that photonic interposers will facilitate on-chip communications [8, 9]. Similar to before, DWDM offers here a bandwidth density advantage over electrical links, as well as a range power advantage when using extended multi-chip modules [10]. So far though, non-photonic based solutions have been the norm in the industry: (1) switching to ever larger system-on-chips (SoC) combine CPU power with on-chip High-Bandwidth-Memory for the highest performance [11]; (2) advances in narrow pitch (~ 10 μm) flip-chipping have so far addressed the bandwidth problem by massive parallelization of the busses [12]; (3) novel 3D stacking techniques have addressed the range limitations of electrical links, while using the micro-bump flip-chipping methods [13]. Nevertheless, advances in optical architectures are made to address the future need of ultra-short link optical interposers, with demonstrations reaching 30 Tbps / cm^2 [14], or using re-configurable networks [15] and mode-division-multiplexing [16]. A more recent demonstration has shown a 2.56 Tbps on-chip network in an 8x8x40 Gbps configuration with integrated DFB lasers and a 24 GHz bandwidth for the EAM-PD link [17].

Photodetectors with high bandwidth are an absolute requirement for optical interconnects. There are several different configurations with respect to contact configuration, such as (a) photovoltaic photodetectors, (b) photoconductive photodetectors and (c) avalanche photodetectors [18]. The most common configuration is a p-i-n vertical diode, which is a photovoltaic detector because of its oppo-
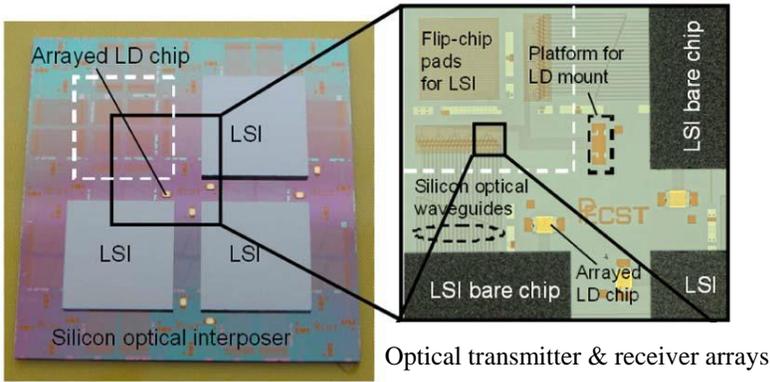
Figure 2.1: A photonic interposer with large-scale-interconnects (LSI) for EIC flip-chip integration. A butt-coupled laser (LD) array provides on-chip CW light. Each EIC-site contains an array of transceivers, interconnected with Si waveguides [14].

sitely doped contact layers. It operates in reverse bias. An MSM photodetector is generally labelled as a photoconductive detector due to it's identical contacts (undoped). Avalanche PDs are characterized by a gain of the signal through carrier-multiplication, leading to the gain-bandwidth product as a figure-of-merit.

Another way to categorize photodetectors is by their geometrical layout. For instance, common packaged p-i-n PDs are vertical diodes, where the absorption length is similar to the thickness of the intrinsic layer. At the same time, a butt-coupled p-i-n diode can have a much larger absorption length than the thickness of the intrinsic layer. Instead of butt-coupling, the optical mode can also be tapered into the III-V absorption layer through adiabatic coupling.

There are also relatively novel, exotic structures to tackle common problems in photodetectors [19]. For instance, uni-traveling carrier photodiodes rely solely on electron mobility to transport charge carriers, as their mobility is higher than the hole mobility. There are instances of InP UTC-PDs with bandwidths of 48 GHz [20], and up to 67 GHz through integrating on an IMOS platform [21]. Another way to improve the load-bandwidth trade-off is by making a distributed photodetector such as traveling wave photodetectors that aim to increase the photocurrent output, while maintaining high bandwidth by sectioning the PD into several compartments.

The MSM photodetectors, as photoconductive devices, have relatively small energy (Schottky) barrier height between the metal contact and the semiconductor [22]. This results in higher leakage currents than p-i-n photodiodes. Due to their configuration and usual interdigitated contacts, MSM PDs have a lower capacitance per unit area than other PD types. This can lead to extremely high bandwidths as
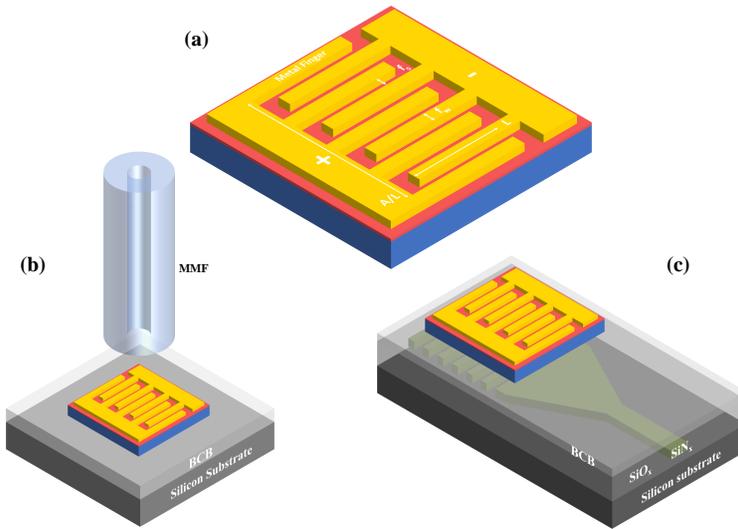
Figure 2.2: 3D concept images of the transfer-print compatible interdigitated MSM photodetector; (a) shows a detailed view of the interdigitated finger parameters; (b) shows the larger PD, which is interfaced from the top-side with a MMF; (c) shows the smaller PD, which is interfaced from the bottom side and forms a grating-assisted waveguide detector.

the devices are typically transit time limited. Early demonstrations already showed 2.0 ps switching time and 150 GHz bandwidth in 1991 [23]. However, due to the interdigitated contact structures, the MSM PDs typically suffer from lower external quantum efficiency associated with the contact blocking parts of the absorption region. This is usually solved by back-side illumination. Other configurations use more lateral contacts in combination with a feeding waveguide underneath the MSM detector [24].

It is for these reasons that MSM photodetectors are interesting candidates for photonic interposers, especially when these interposers are combined with multi-mode fiber links (because of the lower capacitance per unit area of an MSM photodetector compared to a p-i-n structure). Fig. 2.2 shows the MSM photodetector design considered in this work and the two ways in which the optical interface is made: (1) by directly interfacing with a MMF fiber; (2) by using back-side illumination waveguide-grating coupling, suited for intra-interposer communication. Either evanescent coupling or grating-assisted coupling are the natural candidates for PD integration on Si/SiN photonic integrated circuits. Such demonstrations have previously been realized with the integration of InGaAsP p-i-n PDs on SOI [25] or even MSM PDs on SOI for the 1550 nm wavelength range [26]. Recently, transfer-print based approaches for high-speed PDs are showing great potential for wafer-scale integration [27–31].

2.2   Design

The following section and paragraphs cover the basic principles of the operation of a Metal-Semiconductor-Metal photodetector. First, the physics at the contact interfaces is explained. Afterwards the information on the epitaxial layer structure is given and finally the design of the interdigitated finger contacts is discussed.

The concept of the micro-transfer-print compatible MSM detector is detailed in Fig. 2.2. Both the device and the coupling methods for the larger MMF-interfacing and the smaller grating-assisted detectors are detailed. The interdigitated contact comprises of finger with a finger spacing, f_s, and finger width, f_w.

2.2.1   Schottky Contact

The Metal-Semiconductor-Metal (MSM) photodetector is a planar device, meaning that both contacts are in the same plane, and easily accessible in planar processing. A Schottky contact between a metal and a semiconductor occurs when the work function of the metal is larger than the work function of the semiconductor $\phi_m > \phi_{semi}$. The work function is defined as the energy from the Fermi level till the vacuum level, or otherwise the energy needed to extract an electron from the material. As the Fermi levels line up at the junction under zero bias, electrons from the semiconductor flow to the metal side. The negative charge movement leaves a net positive charge on the semiconductor side of the junction, while the charge accumulates at the high-electron density metal interface. Fig. 2.3-(b) shows the resulting band bending at the interface, defined as the built-in potential difference, eV_0, in equation 2.1. This also forms the relevant barrier height from the semiconductor side and can vary under applied external bias. Under forward bias, the height of this energy barrier decreases. Electron current can thus flow more easily from the semiconductor side to the metal. Under reverse bias, the height of this semiconductor energy barrier increases, impeding the flow of current.

$$eV_0 = \phi_m - \phi_{semi} \tag{2.1}$$

From the metal side of the junction, the potential barrier is defined as the Schottky barrier, as defined in equation 2.2. It is defined as the difference between the work function of the metal ϕ_m and the electron affinity of the semiconductor, χ_n. The different energy levels are sketched out in Fig. 2.3.
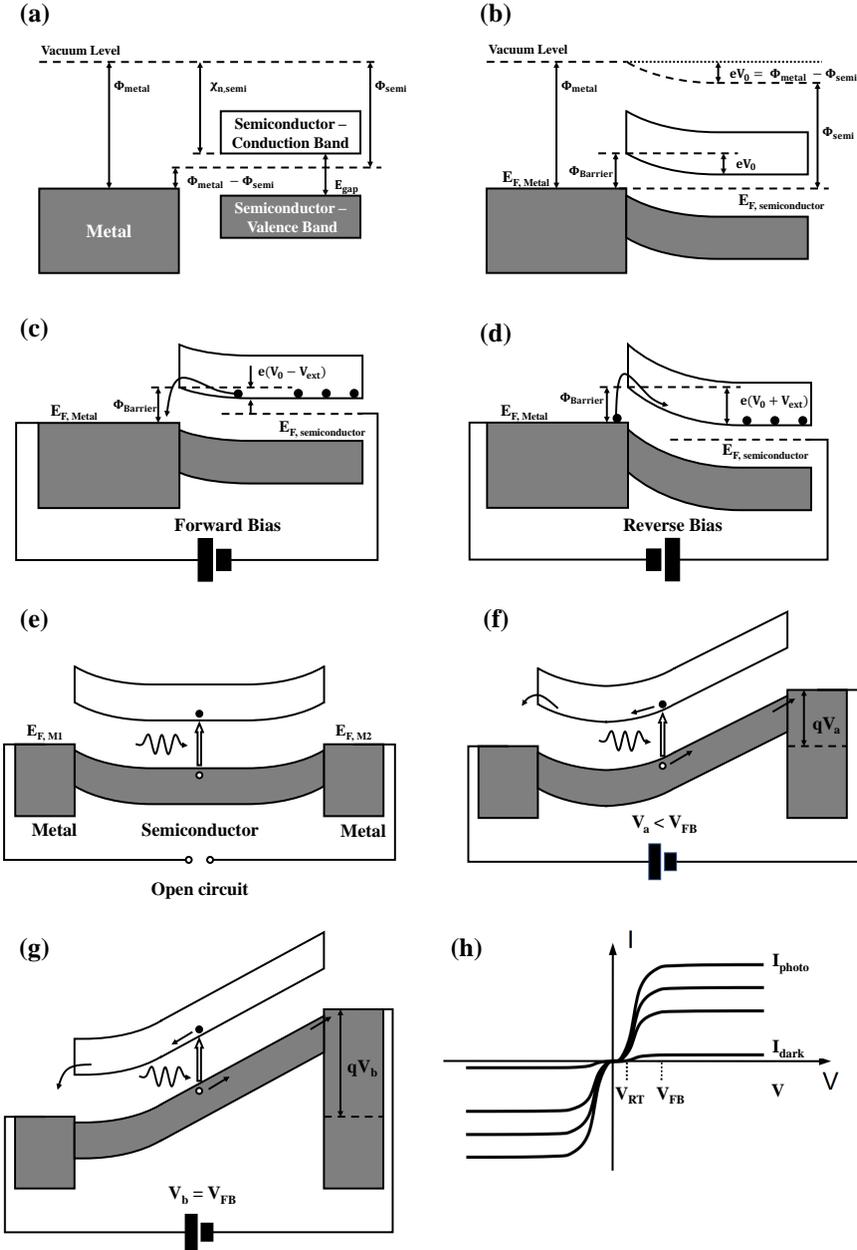
Figure 2.3: (a) Schematic of the relevant parameters of a Schottky junction before contact and (b) after contact, with band bending at the interface and the formation of the Schottky barrier ϕ_B. (c) Schottky contact under forward bias and (d) under reverse bias. (e) Shows the metal-semiconductor-metal junction of the photodetector without external bias. (f) The photocurrent increases for increasing bias voltage. For high bias voltages (g), the barriers disappear and the photocurrent saturates. (h) The IV curve showing the different regimes, under different illumination conditions.

$$\phi_B = eV_0 + \Delta E_{(c,Fn)}$$
$$= \phi_m - \phi_{semi} + (E_{c,semi} - E_{f,semi}) \qquad (2.2)$$
$$= \phi_m - \chi_n$$

Contrary to the semiconductor-barrier, the Schottky barrier does not change significantly under changing bias voltage. However, electrons can hop over this barrier from the metal side to the semiconductor conduction band, and the probability that this happens is exponentially dependent on the Schottky barrier height. The greater the barrier height, the lower the leakage current. Typical Schottky barriers are not very high, leading to larger leakage current compared to other junction based devices.

There are three current regimes for a MSM PD: low current flow below reach-through voltage, injection current flow in between reach-through and flat-band voltage, and current saturation above the flat-band voltage. The reach-through voltage is defined as the voltage for which the sum of the depletion regions of each contact is equal to the electrode gap spacing. Below this voltage, one junction is forward biased (left) and the other junction is reverse biased (right). Below the flat-band voltage, a potential well and barrier remains in the semiconductor, near the forward biased junction. The current flow of electrons is thus limited, and the current flow of the holes is hampered by the built-up charge of the electrons in the potential well.

As soon as reach-through is obtained, the entire semiconductor is depleted and the electric field over the region is continuous and increases linearly. Any additional bias above V_{RT} will reduce the potential barrier at the forward biased junction. As a result of this lowering of the semiconductor-barrier, the photocurrent flow will grow exponentially above reach-through until flat-band is reached. At the flat-band voltage V_{FB}, the potential barrier at the forward biased junction has been reduced to zero, and the electric field will thus become zero at the junction and the energy bands will be flat at that junction (as seen in Fig.2.3-(g)). Above flat-band, the barrier is removed and there is no gain for increasing the bias voltage. The photocurrent thus saturates. Further increasing the bias voltage will slightly increase (1) band bending at the forward biased junction and (2) the current generation at the reverse biased junction. The second one results from the local Schottky barrier lowering effects, in part due to the high electric fields present at the reverse biased junction interface.

Doping the semiconductor allows for tuning the flat-band voltages. This can range from a few volts to several tens of volts. The relation is given in equation 2.3, where q is the elementary charge value, N_D is the doping level in the semiconductor,

L is the electrode spacing and ϵ is the permittivity of the semiconductor. For even higher voltages, breakdown will eventually occur at the reverse biased junction.

$$V_{FB} = \frac{qN_DL^2}{2\epsilon_{semi}} \tag{2.3}$$

2.2.2   Epitaxial Structure

The epitaxial layers can be found in Table 2.1. The layers are grown on a GaAs substrate, with the release layer being a 1 µm thick $Al_{0.90}Ga_{0.10}As$ layer. The choice for a high-Al fraction AlGaAs release layer was made due to limited expertise in InAlP growth of the vendor [32]. Given the etch-rate differences reported in literature [33], it was determined that a 90 % fraction AlGaAs would suffice for the size of the devices targeted in this chapter.

The device layers are an absorption layer of 0.5 µm GaAs and a 50 nm thick $Al_{0.15}Ga_{0.85}As$ contact layer. For choosing the best absorption layer, one needs to balance the trade-off between PD responsivity and bandwidth. If a finger-spacing of 1 µm is targeted, the absorption layer must be more or less half this value, to have a spatially equal distance to the contacts from any point in the absorption layer. Using the absorption factor $\alpha = 1.2 \ 10^4$ $[cm^{-1}]$ at 850 nm [34], the internal absorption, as calculated in equation 2.4, is equal to around 40%. For the application purpose an absorption of around 40% suffices. If a higher efficiency photodetector is targeted, a thicker absorption layer would be advantageous. For the contact layer, the choice was made for a thin 15%-AlGaAs layer. The bandgap energy of AlGaAs scales with the aluminium fraction of the layer. So a 15%-AlGaAs layer has around 13.3% larger band gap than GaAs. This leads to a reduction in the device dark current as it increases the energy barrier between the absorption layer and the metal contact [35].

$$A = (1 - e^{-\alpha \cdot d}) \tag{2.4}$$

The external quantum efficiency, η, takes into account the losses that occur prior to the light entering the absorption layer. Equation 2.5 shows that both the Reflection at the III-V interface and the shadowing effect of the interdigitated contacts are important. The latter factor is particularly relevant for the top-illuminated larger PD, and less relevant for the bottom-illuminated, grating-assisted smaller PD.

$$\eta = (1 - R)\left(\frac{f_s}{f_s + f_w}\right)A \tag{2.5}$$

Given that the contact layer is prone to oxidation, cap layers are required

Layer no.	Type	Material	Thickness [nm]
6	SAC3	GaAs	40
5	SAC2	AlAs	70
4	SAC1	GaAs	4
3	Contact Layer	$Al_{0.15}Ga_{0.85}As$	600
2	Absorption Layer	GaAs	500
1	Release Layer	$Al_{0.90}Ga_{0.10}As$	1000
0	Substrate	GaAs	-

Table 2.1: III-V epitaxial layer stack of the GaAs MSM photodetector.

for wafer storage. The medium Al-fraction makes it difficult to find a suitable passivation layer as the contact layer is attacked by both citric acid etching (GaAs) and also somewhat susceptible to HCl-based etching (AlAs). Thus a more complex system of passivation layers is used. The first layer (SAC1) is a 4 nm GaAs thin layer, which is selectively removed through wet digital etching with great etch depth control of around 1.2 nm of etched material per etch cycle [36]. SAC1 is considered too thin for a thorough passivation, hence a 70 nm AlAs layer (SAC2) was chosen on top of SAC1, which can easily be etched away with high selectivity to SAC1 with a HCl-based etchant. This would leave an AlAs surface of SAC2 exposed on the top, which is also not desirable from an oxidation point of view. The entire structure is therefore sealed off with another 40 nm GaAs passivation layer (SAC3).

2.2.3   Bandwidth

For a MSM photodetector, there are typically two regimes that dictate the bandwidth: transit-time-limited or capacitance-limited (RC) [37]. In a transit-time-limited system, the impulse response of a system is limited by the speed with which the charge carriers move through the semiconductor towards the contacts. The larger the distance between the electrodes, the longer the impulse response time and the lower the bandwidth will be. Vice-versa, if the electrode spacing becomes smaller, the impulse response time dictated by the transit time will shorten. Consequently, the bandwidth increases also.

In a RC limited system, the impulse response is limited by the capacitance of the PD. As the PD size increases, the capacitance increases, resulting in an increase of the impulse response time. For decreasing contact spacing, the capacitance increases as well. As the contact spacing is varied, a transition occurs from transit-time-limited to RC-limited bandwidth regimes, which is discussed next.

2.2.3.1   Transit-time-limited bandwidth

A MSM photodetector is typically biased above V_{RT}. This means that the depletion regions of both junctions extend into each other and a space charge region is formed across the entire semiconductor volume between the contacts. The accompanying electric field is continuous throughout the semiconductor. From the presence of this field, one can assume that the main mechanism of current flow is charge drift due to the electric field, over the slower carrier diffusion process. Given the typical reach-through voltage and the contact spacing, the size of the electric field is in the range of tens of kV/cm. The charge carrier velocity is then within the range of the saturation velocity, v_{sat}, of the charge carriers. So this saturation velocity acts as the limiting factor in the transit time of charge carriers, expressed as [38].

$$\tau = \frac{f_s + 0.5f_w}{2 \cdot v_{sat}} \tag{2.6}$$

For a 2D estimation with only electrons, a 1 μm spacing can be considered between the contacts, with an electron saturation velocity of 1.2 10^7 cm/s [39]. This gives an initial time response of just below 5 ps. The reality is more complex, combining hole and electron velocities and their different barrier heights. Though the 5 ps transit time is a good approximation for the order of magnitude at which the devices operate. Given a constant saturation velocity, this means that larger contact spacing results in a linear increase of the transit time. Vice-versa, smaller contact spacings reduce the transit time and increase the bandwidth in an inversely proportional manner, as shown in Fig.2.4-(b). When taking the 3D picture into account, the thickness of the absorption layer also influences the transit time of the carriers. The absorption layer was therefore chosen to be sufficiently thin at 0.5 μm, in order not to be the dominant contributing factor to the transit time.

2.2.3.2   RC time limited Bandwidth

Any capacitive circuit can be characterized by a load-charging time described with the RC time constant. This time constant defines the time required to charge a capacitor through a load up to 63.8% of the applied DC voltage. The capacitance of a MSM PD is indicated over a unit area. This means that for the multi-mode-fiber application, where the active area is in the range of 70 μm by 70 μm, the total capacitance will be approximately 5 times larger than for the waveguide-coupled application with an active area of 30 μm by 30 μm. In general, the capacitance of a MSM structure on an undoped semiconductor is given by equation 2.7 [40]:

$$C = \frac{K(k)}{K(k')}\varepsilon_0(1+\varepsilon_r)\frac{A}{f_s+f_w}$$
$$= \frac{K(k)}{K(k')}\varepsilon_0(1+\varepsilon_r)(N-1)L \tag{2.7}$$

With ε_0 being the dielectric constant in free space, ε_r the relative dielectric constant of the absorbing material, A the total active area of the PD, L the active region length, N the number of interdigitated fingers, f_s the finger spacing and f_w the finger width. K(k) is the complete elliptical integral, as defined by equation 2.8:

$$K(k) = \int_0^{2\pi} \frac{1}{\sqrt{1-k^2 sin^2\varphi}}d\varphi \tag{2.8}$$

$$k = tan^2\left(\frac{\pi f_w}{4(f_s+f_w)}\right) \tag{2.9}$$

$$k' = \sqrt{1-k^2} \tag{2.10}$$

With these formulas, the capacitance is calculated for both PD sizes, as a function of the finger spacing in Fig.2.4-(a). For the smaller PD, the calculated capacitance is less than 30 fF. Even for the larger PD, the capacitance remains below 90 fF for contact spacings that are above 1 μm. For smaller contact spacings, the corresponding time constant for a 150 fF capacitance and a 50 load is 7.5 ps and is in the same range as the 5 ps estimation for the transit-time limited regime. Fig. 2.4-(b) shows the simulated bandwidth in Lumerical DEVICE. Given the similar time response but different capacitance, it is understandable that the bandwidth of the larger PDs transforms from a transit time limited regime for large contact spacing towards a RC time limited regime for smaller contact spacing [38, 41]. The smaller PDs have a significantly lower capacitance, hence the RC limited regime does not kick in for contact spacings above 0.1 μm. It can be observed that the finger width has little influence on the speed of the device. For our study, nine different parameter sets are investigated. The width and spacing were limited by the lithography process used in defining the interdigitated electrodes.
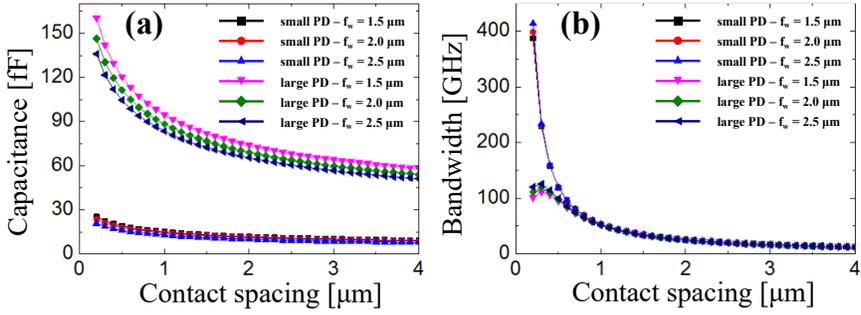
Figure 2.4: Simulated (a) capacitance and (b) bandwidth as a function of contact spacing for both PD sizes. The larger devices become RC limited for smaller contact spacings.

2.2.3.3 Interdigitated finger-contact

Table 2.2 shows the parameter configurations of finger width and finger spacing of the metal contacts of the fabricated devices. The fill factor is limited to 62.5%, in order to reduce the upward reflection of the top-illuminated larger PD. The minimum pitch is set at 3 µm, so that the devices can be fabricated with contact lithography. Lower values of spacing and pitch are desirable, as indicated by Fig. 2.4, and feasible with e-beam lithography, but fall outside the scope of this work. To get a complete analysis, both the smaller and larger PDs are studied with all contact parameters.

Device	Para-1	Para-2	Para-3	Para-4	Para-5	Para-6	Para-7	Para-8	Para-9
f_s [µm]	1.5	1.5	1.5	2.0	2.0	2.0	2.5	2.5	2.5
f_w [µm]	1.5	2.0	2.5	1.5	2.0	2.5	1.5	2.0	2.5
Pitch [µm]	3.0	3.5	4.0	3.5	4.0	4.5	4.0	4.5	5.0
FF [%]	50.00	57.14	62.50	42.85	50.00	55.56	37.50	44.44	50.00

Table 2.2: Overview of the selected parameters for the interdigitated fingers. The configurations shown are compatible with contact lithography.

2.3   Fabrication

The discussion in the following paragraphs on the fabrication of the PDs is limited to the processing steps on the source substrate. An overview of the post-printing steps is given in section 1.3. The devices are made on a sample-scale, fabricated in the cleanroom facilities of Ghent University. Fig.2.5 shows a schematic overview of the process flow in both cross-section and top-down view, while Fig.2.6 shows a detailed overview with microscope images taken during processing.

Sacrificial layer removal

The epitaxial layer design has been discussed in section 2.2.2. A schematic cross-section with labels can be found in Fig.2.5-(a). The SAC-layers are protection layers that protect the oxidation-prone $Al_{0.15}Ga_{0.85}As$ contact layer during storage. SAC1 is a 4 nm GaAs layer, SAC2 is a 70 nm AlAs layer on top of SAC1, and SAC3 is a 40 nm GaAs layer on top of SAC2. First, SAC3 is removed using a citric acid - peroxide (5:1) etchant that selectively stops on top of SAC2. Following, SAC2 is removed using diluted HCl, which also selectively stops on SAC1. Finally, SAC1 is removed by selective digital wet etching [36] in four cycles, at around 1.2 nm removed per etch cycle.

Contact Deposition

After the removal of the sacrificial layers, the metal interdigitated contact fingers are patterned into the photoresist (AZ5214) through contact lithography. The photoresist is spincoated at 5000 RPM to obtain a resist thickness of $\sim 1\mu m$. A thin Ti/Au contact layer, at 4/85 nm, is deposited and lifted-off, shown in Fig.2.5-(b) and Fig.2.6-(a-i & a-ii). The thickness of the metal fingers is limited to less than 100 nm to minimize the mechanical stress of the contact metal onto the III-V devices. Above 100 nm, the stress leads to device failure in over 50% of devices after the release etch. The metal fill factor is chosen to be below 65%, to balance the speed and responsivity of the PD, but it also reduces stress-induced failure of the devices. The lower the fill factor, the less metal present on the III-V and thus the lower the mechanical stress on the coupon.

Mesa Definition

In the next step, shown in Fig.2.5-(c) & Fig.2.6-(b), the coupon mesa is defined by optical lithography and wet etching with citric acid - peroxide (5:1), which has an etch rate of ~ 200 nm per minute. Because the etch is selective, the mesa is over-etched slightly to ensure that the sacrificial layer is reached across the sample.
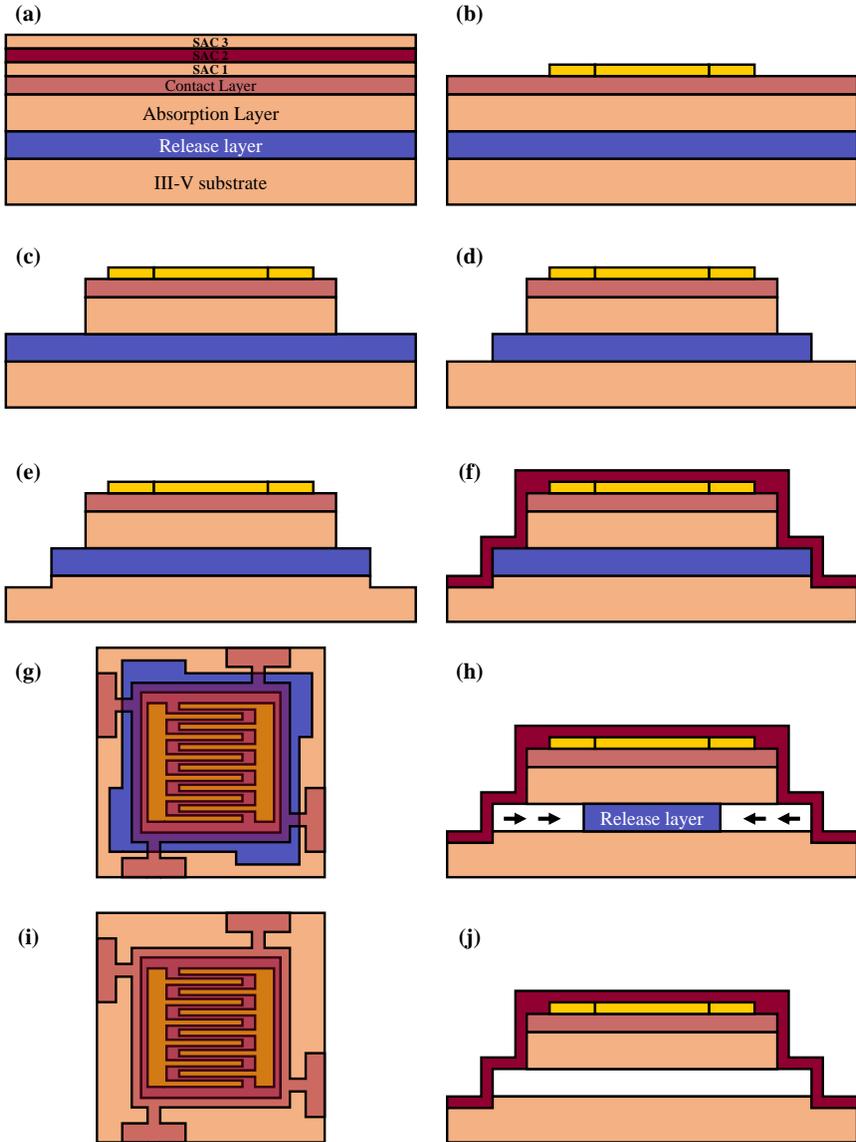
Figure 2.5: Schematic overview of the processing steps on the source substrate of the MSM PD with (a) the removal of the top sacrificial protection layers, (b) Ti/Au contact deposition, (c) mesa formation, (d) patterning of the release layer, (e) etching into the substrate, (f-g) photoresist encapsulation in cross-section and top-down view. The devices are released with a wet underetch (h). The released devices are tethered to the substrate (i-j).

Release layer patterning

The release layer is patterned with HCl-37% - DI (1:1) for 4 minutes to reach the substrate as shown in Fig. 2.5-(e) and Fig.2.6-(c). After the HCl-based etch, three steps of digital etching (DE) are done to clean off any remaining $Al_{0.90}Ga_{0.10}As$ residues from the substrate as in Fig.2.6-(d). The DE-sequence is ended with another HCl:DI (1:1) etch. Typically, the patterning of the sacrificial layer extends slightly ($\sim$ 200 nm) into the substrate in order to better anchor the encapsulation. Fig.2.5-(g) shows that the sacrificial layer is patterned with flaps extending outwards. Those flaps act as easy-access points during the release etch.

Release etch

Fig. 2.5-(f-g) shows how the encapsulation is defined using TI-35 photoresist. The encapsulation resist is hard baked for 5 minutes on a 120°C hotplate. For the final step on the source substrate, the devices are released during a wet etch using HCl-37% for a duration of 1 hour. Afterwards, the devices are freestanding on only the photoresist tethers. Hence, the samples need to be rinsed and dried with care, as described in section 1.3, to avoid delamination of the coupons. The $Al_{0.90}Ga_{0.10}As$ layer leaves a lot of residue on the source substrate and the encapsulation resist. If required, the substrate can still be cleaned by performing additional digital etch steps.

Further steps

The coupons are transfer-printed with a X-Celeprint μ-TP 100 transfer-printing tool. A PDMS stamp with dimensions of 50 μm by 50 μm is used for the transfer-print process of the coupons of size 100 μm by 100 μm and 55 μm by 55 μm for the smaller PD.

For the target wafers, the larger MSM PDs were processed on a high-resistivity silicon wafer (Target substrate 1 or T1), and the smaller PDs were printed on SiN_x waveguides (Target substrate 2 or T2). Fig. 2.6-(g) shows the T1 substrate after printing of the larger PDs. The photoresist encapsulation is still present at this stage and needs to first be removed with a reactive ion etching step. Then, the substrate is planarized with thicker DVS-BCB-57. Sloped VIAs are made into this DVS-BCB to access the contact pads of the device (Fig. 2.6-(i)). The probe pad metal is designed to connect the device to a GSG probe. The deposited metal is a combination of Ti (20 nm) and Au (500 nm), to minimize the capacitance on the connection towards the GSG probe. Fig. 2.6-(k) shows a similar result for the smaller PDs printed on the T2 substrate.
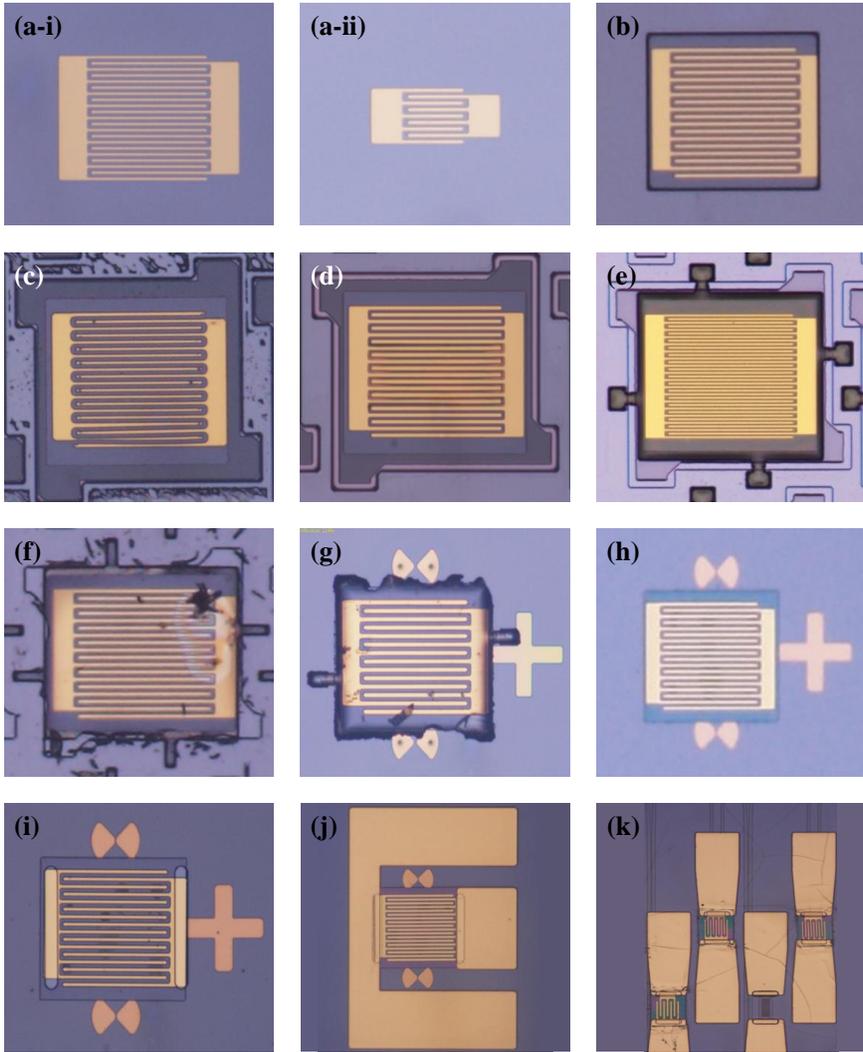
Figure 2.6: Top-down microscope images of the main processing steps prior (source substrate) and post (target substrate) transfer-printing: (a) interdigitated metal finger deposition, (b) mesa formation, (c) sacrificial layer and substrate patterning, (d) sample cleaning with peroxide, (e) photoresist encapsulation, (f) free-standing devices after the release etch, (g) printing the device on T1, (h) encapsulation removal and sample planarization, (i) BCB-VIA etching to access the device and (j-k) probe pad metal deposition on the respective larger and smaller PDs.

2.4   Characterization

This section covers the characterization of the devices. The first part covers the static behavior, while the dynamic behavior is covered afterwards.

2.4.1   Static PD characteristics

The static PD properties, both for the smaller PDs through the waveguide and the larger PDs from the top-side, are measured with a Titanium-Sapphire (TiSapph) tunable laser that is kept fixed at 850 nm. The laser light is split using a 50-50 fiber splitter, with the secondary signal connected to a power meter as a reference signal to calibrate away any laser power fluctuations. The devices are probed with standard DC probes and connected to a Keithley-2400A source-meter unit. Fig.2.7 shows the measurement setup for the PD responsivity measurements. For the larger PDs, a cleaved multi-mode fiber (MMJ-3A3A-IRVIS-62.5/125-3-1) is used to cover the entire active area, to better resemble the application case for inter-chip communication. For the smaller PDs, a single-mode fiber couples the light into the SiN_x waveguide. The PD is illuminated from the bottom side, assisted by a vertical grating coupler. The light coming from the TiSapph laser is redirected through a standard polarization controller to optimize the waveguide coupling. The PIC is designed on the imec-biopix 300 nm platform. The material stack of this platform is suited for the NIR (750 nm - 900 nm) range.

The measurement results are summarized in Fig.2.8. The dark currents are measured with the laser off, and with the PD under different bias voltages. Fig.2.8-(a) and -(b) show these results for the larger and smaller PDs, respectively. The average dark currents measured at -2V bias, for the larger and smaller devices are on average 22 nA and 7.2 nA, respectively. The likely cause of the relatively
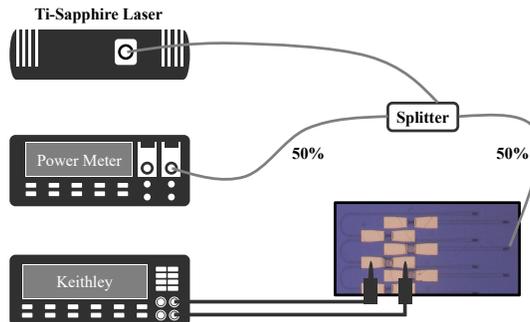
Figure 2.7: Schematic of the optical setup used to measure the static PD characteristics.
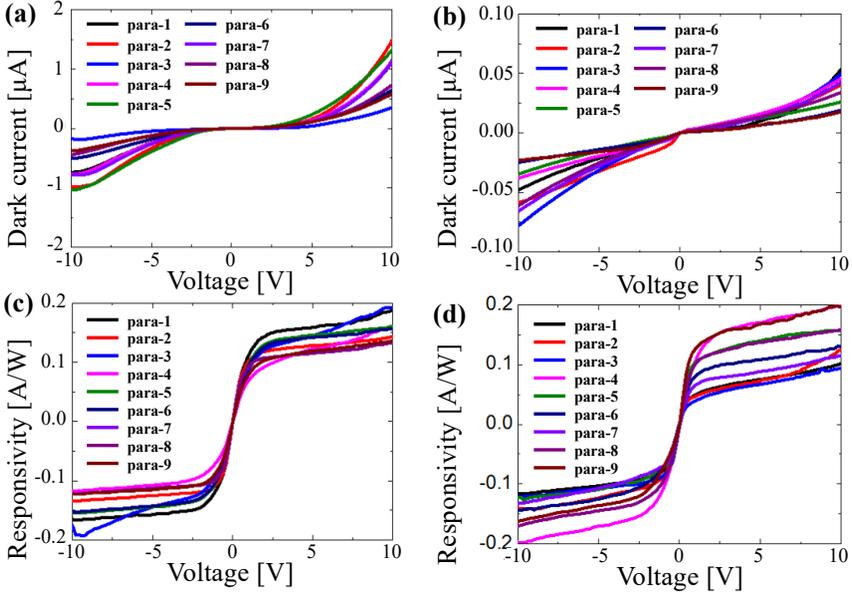
Figure 2.8: Dark current of the (a) larger and (b) smaller PDs for all 9 contact configurations. The corresponding responsivities are shown in (c) and (d).

high dark current can be found in the background p-doping of the MOCVD grown epitaxial layerstack, which effectively lowers the Schottky barrier height.

Fig. 2.8-(c) & -(d) show the responsivity measurements for the larger and smaller PDs, respectively. For the larger PDs, uniform and symmetrical IV curves are obtained for all 9 parameter sets. For the larger PDs, the responsivity is calculated using the optical power in the MMF, measured with a free-space power meter. For the smaller PDs, the optical power inside the waveguide is used, derived from a grating transmission measurement. As such the responsivity includes the GC-to-PD coupling efficiency as well. The small differences after the flat band voltages for the larger PDs are attributed to the different fill-factor configurations, or due to some slight fabrication variations. The average external responsivity of the larger PDs is 0.117 A/W at 2V bias, which corresponds to a quantum efficiency of 17.2%. This value is lower than the 40% internal efficiency, as it includes the shadowing effect of the contacts when illuminated from the top side. Overall, this value is not particularly high, but in line with expectations given the absorption layer thickness of just 0.5 μm. For the smaller PDs, some larger fluctuations are observed. The origin of these variations remains unclear at this moment. The average responsivity is calculated to be 0.1 A/W under 2V bias.
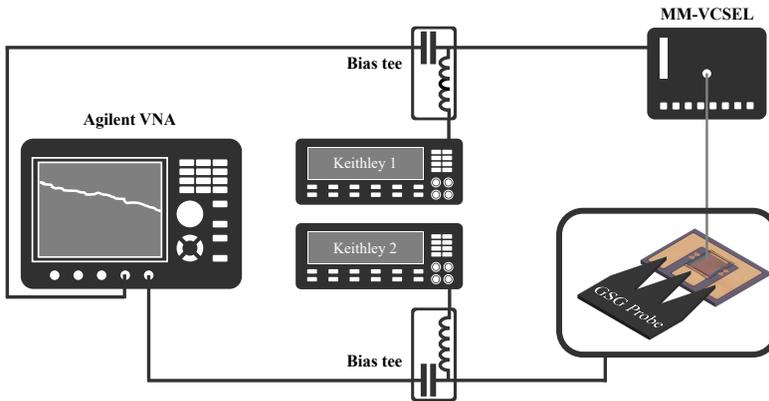
Figure 2.9: The measurement setup used to characterize the small-signal modulation of the larger MSM PDs.

2.4.2 Dynamic PD characteristics

The dynamic measurements characterize the high-speed performance of the PDs. The small-signal bandwidth measurements are measured for both the smaller and larger PDs. The large-signal measurements are only done for the larger PDs. A lack of a high-speed, single-mode-fiber coupled VCSEL has prevented the adequate characterization of the smaller PDs through the SiN$_x$ waveguide. However, it is expected that the device performance is equivalent for both PD sizes at high speeds, as the speed remains limited by the transit time of the carriers for our finger contact configurations.

2.4.2.1 Small-signal characteristics

The setup used to measure the small-signal modulation is shown in Fig. 2.9. The multi-mode VCSEL (VIS V50 - 850M) is biased with a Keithley 2400A source-meter and driven by a Vector Network Analyzer (VNA, Agilent N5247A) via a bias tee. The output modulated light from the VCSEL is vertically coupled to the MSM PD through the MMF. The PD is biased via a bias tee with a secondary Keithley source-meter. The generated photocurrent signal is then coupled back into the VNA. At the start of the measurement, the bandwidth of the VCSEL is determined and calibrated using a high-speed PD (Optilab PD-40-MM-M). A matlab script is used, in conjunction with the Agilent VNA to de-embed the bandwidth deformation of the VCSEL from the overall response of the PD. All the RF cables and high-speed GSG probes (Cascade) are also calibrated and referenced out to find the bandwidth of the PD.
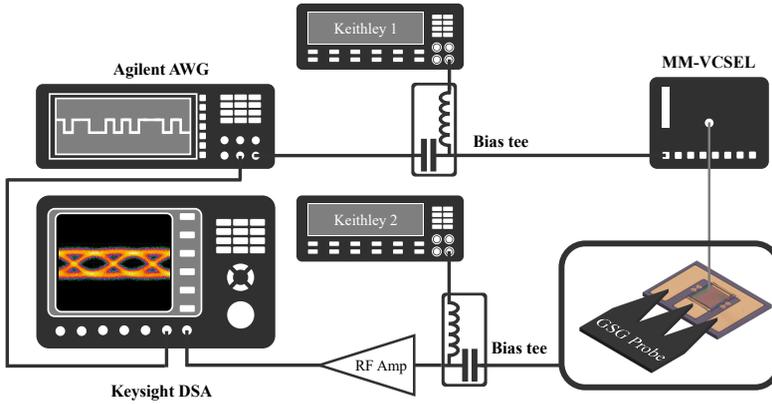
Figure 2.10: The measurement setup used to characterize the large-signal modulation of the larger MSM PDs.

All different contact parameter designs (para-X) perform consistently and the measured S_{21} curves of one of these devices (para-1) is shown in Fig. 2.11-(a). A small roll-off feature is observed at low-frequency, but this can be attributed to an internal gain mechanism inside the PD [42]. This gain can also be observed in the static characterization by the non-flat IV characteristic after the flat band voltage is reached. The bandwidth, neglecting the low frequency roll-off, is just below 20 GHz for a 2V bias of the device.

2.4.2.2 Large-signal characteristics

The setup shown in Fig. 2.10 is used for the large-signal modulation measurements. The multi-mode VCSEL is directly modulated by an arbitrary waveform generator (AWG, Agilent M9502A), which creates a pseudo random bit sequence (PRBS) of length 2^7-1. The modulated light at 850 nm is coupled to the MSM PD through the MMF from the top side of the device. The converted electrical signal from the PD is collected by a GSG probe, amplified with the RF amplifier (SHF S807) and then coupled to the digital signal analyzer (DSA, Keysight DSA-Z 634A). The AWG also sends out a trigger signal to the DSA. Non-Return-to-Zero signals (10, 20, 30 and 40 Gbps) are recorded under 2 V bias for the MSM PD (para-1) and are shown in Fig. 2.11-(c). Clear eye diagrams up to 40 Gbps are observed. There is no significant difference among the studied parameters, indicating that they are all transit-time limited. The difference in open-eye characteristics with the reference PD are present because the reference PD has a 40 GHz bandwidth over the 20 GHz of the studied devices.
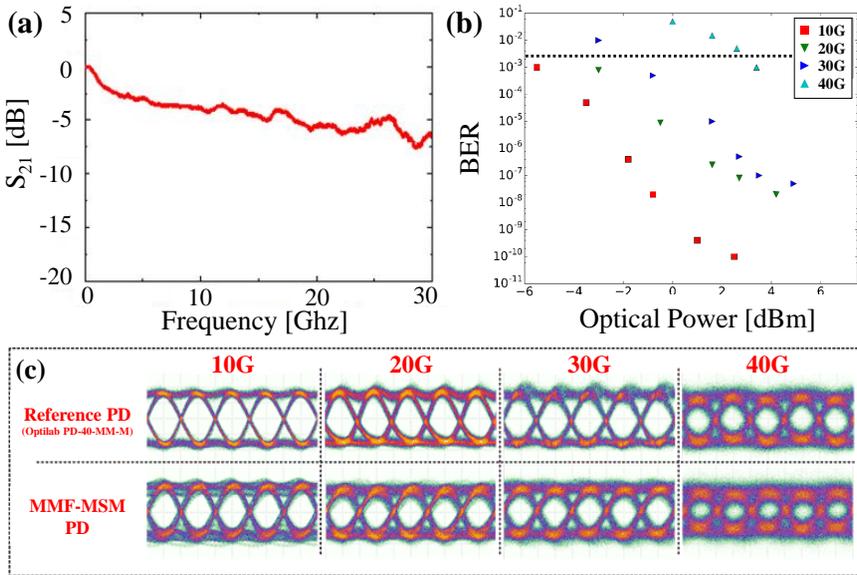
Figure 2.11: A summary of the dynamic measurement results with (a) the small-signal bandwidth measurement, (b) the large-signal bit error rate measurements and (c) the open-eye diagrams at different speeds, for both the larger MSM PD and a reference commercial PD.

The Bit-Error-Rate (BER) measurements, as the name implies, look at the number of errors that are registered with respect to the signal that is sent out. The test was performed based on the same measurement setup, using post-processing in MATLAB to analyze the complete recorded information from the DSA. Fig. 2.11-(b) shows the BER results of the 10, 20, 30 and 40 Gbps signals for the 70 μm by 70 μm MSM PD (parameter-1). The dashed line indicates a bit-error-rate threshold of $3.8 \cdot 10^{-3}$, which enables error free transmission assuming a 7% overhead hard decision forward error correction (HD-FEC) [43]. This can be attained for all transmitted signals. It is worth noting that the MSM PD that is being tested, is not integrated with a trans-impedance amplifier (TIA), which is discussed in the following section.
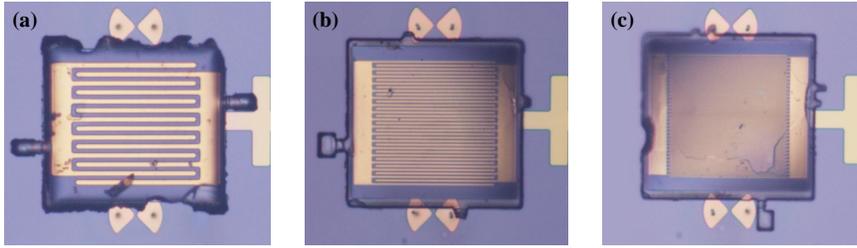
Figure 2.12: Transfer-printed MSM PDs with (a) >3 µm pitch with optical lithography, (b)
∼ µm pitch with e-beam lithography and (c) sub-µm pitch with e-beam lithography.

2.5   Conclusion and future prospects

In this chapter, we discussed the design and fabrication of transfer-print-compatible
Metal-Semiconductor-Metal photodetectors. The larger PDs can be top-surface
illuminated with a MMF for inter-chip communication, while the smaller PDs are
bottom-surface illuminated through a waveguide grating coupler. The responsivies
of the devices are about 0.1 A/W for 2V reverse bias. The bandwidth of the devices
is just under 20 GHz, operating in a transit time limited regime. This limitation
arises from the metal finger pitch restriction of 3 µm due to optical lithography.
The large-signal measurements show error-free transmission up to 40 Gbps for the
standalone larger PDs.

The aim of this project, namely the transfer-print integration of high-speed PDs
at 850 nm, has been achieved. Further improvements in speed could be achieved
for even lower finger-contact pitch, achieved by ebeam lithography. Fig. 2.12
shows the transfer-printing results of e-beam fabricated MSM PDs, with much
smaller pitch compared to contact-lithography-based devices. Ultimately, we were
limited in the bandwidth of the VCSEL (21 GHz) in characterizing these devices
in high-speed measurements. Thus these devices were not pursued further for the
time being. Some slight improvements in the process flow can still be made, mainly
from the lessons learned on VCSEL processing that are discussed in chapter 4.
Most notably, additional SiN_x passivation, the introduction of rounded corners and
the increased usage of the digital etch as a cleaning procedure will improve the
yield of the TP-MSM PD process flow.

References

[1] Guanyu Chen, Jeroen Goyvaerts, Sulakshna Kumari, Joris Van Kerrebrouck, Muhammad Muneeb, Sarah Uvin, Yu Yu, and Gunther Roelkens. *Integration of high-speed GaAs metal-semiconductor-metal photodetectors by means of transfer printing for 850 nm wavelength photonic interposers*. Optics Express, 26(5):6351, 2018.

[2] Geoff Bennett, Kuang Tsan Wu, Anuj Malik, Soumya Roy, and Ahmed Awadalla. *A review of high-speed coherent transmission technologies for long-haul DWDM transmission at 100g and beyond*. IEEE Communications Magazine, 52(10):102–110, 2014.

[3] J A Tatum, D Gazula, L A Graham, J K Guenter, R H Johnson, J King, C Kocot, G D Landry, I Lyubomirsky, A N MacInnes, E M Shaw, K Balemarthy, R Shubochkin, D Vaidya, M Yan, and F Tang. *VCSEL-Based Interconnects for Current and Future Data Centers*. Journal of Lightwave Technology, 33(4):727–732, feb 2015.

[4] Qixiang Cheng, Meisam Bahadori, Madeleine Glick, Sébastien Rumley, and Keren Bergman. *Recent advances in optical technologies for data centers: a review*. Optica, 5(11):1354, 2018.

[5] Roy Meade, Shahab Ardalan, Michael Davenport, John Fini, Chen Sun, Mark Wade, Alexandra Wright-Gladstein, and Chong Zhang. *Teraphy: A high-density electronic-photonic chiplet for optical I/O from a multi-chip module*. Optics InfoBase Conference Papers, Part F160-(Mcm):5–7, 2019.

[6] Bogdan Sirbu, Yann Eichhammer, Hermann Oppermann, Tolga Tekin, Jochen Kraft, Victor Sidorov, Xin Yin, Johan Bauwelinck, Christian Neumeyr, and Francisco Soares. *3D silicon photonics interposer for Tb/s optical interconnects in data centers with double-side assembled active components and integrated optical and electrical through silicon via on SOI*. Proceedings - Electronic Components and Technology Conference, 2019-May(May):1052–1059, 2019.

[7] Ewa Simpanen, Johan S. Gustavsson, Anders Larsson, Magnus Karlsson, Wayne V. Sorin, Sagi Mathai, Michael R. Tan, and Scott R. Bickham. *1060 nm Single-Mode VCSEL and Single-Mode Fiber Links for Long-Reach Optical Interconnects*. Journal of Lightwave Technology, 37(13):2963–2969, 2019.

[8] Andrew Alduino and Mario J. Paniccia. *Interconnects: Wiring electronics with light*. Nature Photonics, 1(3):153–155, 2007.

[9] Günther Roelkens, Liu Liu, Di Liang, Richard Jones, Alexander Fang, Brian Koch, and John Bowers. *III-V/silicon photonics for on-chip and intra-chip optical interconnects*. Laser and Photonics Reviews, 4(6):751–779, 2010.

[10] Joris Van Campenhout, Peter De Heyn, Guy Lepage, and Wim Bogaerts. *Silicon-Photonics Devices for Low-Power , High-Bandwidth Optical I / O*. pages 2–5. OSA, 2012.

[11] Steven Woo. *Breaking Down the AI Memory Wall*, 2019.

[12] Rabindra Das, Vladimir Bolkhovsky, Christopher Galbraith, Daniel Oates, Jason Plant, Renee Lambert, Scott Zarr, Ravi Rastogi, Dmitri Shapiro, Manuel Docanto, Terence Weir, and Leonard Johnson. *Interconnect scheme for die-to-die and die-to-wafer-level heterogeneous integration for high-performance computing*. Proceedings - Electronic Components and Technology Conference, 2019-May(1):1611–1621, 2019.

[13] Kazumasa Tanida, Mitsuo Umemoto, Naotaka Tanaka, Yoshihiro Tomita, and Kenji Takahashi. *Micro Cu bump Interconnection on 3D chip stacking technology*. Japanese Journal of Applied Physics, Part 1: Regular Papers and Short Notes and Review Papers, 43(4 B):2264–2270, 2004.

[14] Yutaka Urino, Tatsuya Usuki, Junichi Fujikata, Masashige Ishizaka, Koji Yamada, Tsuyoshi Horikawa, Takahiro Nakamura, and Yasuhiko Arakawa. *High-density and wide-bandwidth optical interconnects with silicon optical interposers [Invited]*. Photonics Research, 2(3):A1, 2014.

[15] Po Dong, Young Kai Chen, Tingyi Gu, Lawrence L. Buhl, David T. Neilson, and Jeffrey H. Sinsky. *Reconfigurable 100 Gb/s silicon photonic network-on-chip [invited]*. Journal of Optical Communications and Networking, 7(1):A37–A43, 2015.

[16] Guanyu Chen, Yu Yu, and Xinliang Zhang. *Monolithically mode division multiplexing photonic integrated circuit for large-capacity optical interconnection*. Optics Letters, 41(15):3543, 2016.

[17] Chong Zhang, Shangjian Zhang, Jon D. Peters, and John E. Bowers. *8 × 8 × 40 Gbps fully integrated silicon photonic network on chip*. Optica, 3(7):785, 2016.

[18] Michael Bass, Eric W. Van Stryland, David R Williams, Willliam L. Wolfe, J E Bowers, and Y G Wey. *Handbook of Optics: Fundamentals, Techniques and Design*. McGraw-Hill, Inc. New York, NY, USA, page Chapter 17, 1995.

[19] Zeping Zhao, Jianguo Liu, Yu Liu, and Ninghua Zhu. *High-speed photodetectors in optical communication system*. Journal of Semiconductors, 38(12), 2017.

[20] Xiaojun Xie, Naiming Liu, Zhanyu Yang, Anand Ramaswamy, Yang Shen, Matt Jacob-Mitos, Erik Norberg, Jianzhong Zhang, Arthur W. Lichtenberger, Jerrold A. Floro, Greg Fish, Joe C. Campbell, and Andreas Beling. *High-power heterogeneously integrated waveguide-coupled photodiodes on silicon-on-diamond*. 2016 IEEE International Topical Meeting on Microwave Photonics, MWP 2016, 34(1):229–232, 2016.

[21] L Shen, Y Jiao, W Yao, Z Cao, J P Van Engelen, G Roelkens, M K Smit, and J J G M Van Der Tol. *waveguide photodetector on an InP-membrane-on-silicon platform*. 24(8):27213–27220, 2016.

[22] Paul R. Berger. *Metal-semiconductor-metal photodetectors*. Testing, Reliability, and Applications of Optoelectronic Devices, 4285(May 2001):198, 2001.

[23] E. Özbay, K. D. Li, and D. M. Bloom. *2.0 ps, 150 GHz GaAs monolithic photodiode and all-electronic sampler*. IEEE Photonics Technology Letters, 3(6):570–572, 1991.

[24] Joost Brouckaert, Gunther Roelkens, S. K. Selvaraja, Wim Bogaerts, Pieter Dumon, Steven Verstuyft, Dries Van Thourhout, and Roel Baets. *Silicon-on-insulator CWDM power monitor/receiver with integrated thin-film InGaAs photodetectors*. IEEE Photonics Technology Letters, 21(19):1423–1425, 2009.

[25] Gunther Roelkens, Joost Brouckaert, Dirk Taillaert, Pieter Dumon, Wim Bogaerts, Dries Van Thourhout, Roel Baets, Richard Nötzel, and Meint Smit. *Integration of InP/InGaAsP photodetectors onto silicon-on-insulator waveguide circuits*. Optics Express, 13(25):10102, 2005.

[26] Joost Brouckaert, Student Member, Gunther Roelkens, and Student Member. *Compact InAlAs – InGaAs Metal – Semiconductor – Metal Photodetectors Integrated on Silicon-on- Insulator Waveguides*. 19(19):1484–1486, 2007.

[27] Jing Zhang, Andreas De Groote, Amin Abbasi, Ruggero Loi, James O'Callaghan, Brian Corbett, António José Trindade, Christopher A. Bower, and Gunther Roelkens. *Silicon photonics fiber-to-the-home transceiver array based on transfer-printing-based integration of III-V photodetectors*. Optics Express, 25(13):14290, 2017.

[28] Grigorij Muliuk, Nan Ye, Jing Zhang, Amin Abbasi, Antonio Trindade, Chris Bower, Dries Van Thourhout, and Gunther Roelkens. *Transfer Print Integration of 40Gbps Germanium Photodiodes onto Silicon Photonic ICs*. European Conference on Optical Communication, ECOC, 2017-Septe(3):1–3, 2017.

[29] Grigorij Muliuk, Kasper Van Gasse, Joris Van Kerrebrouck, Antonio Jose Trindade, Brian Corbett, Dries Van Thourhout, and Gunther Roelkens. *4 ×25 Gbps polarization diversity silicon photonics receiver with transfer printed III-V photodiodes*. IEEE Photonics Technology Letters, 31(4):287–290, 2019.

[30] EU-H2020 PPP. *Teraboard*, 2015.

[31] EU-H2020 PPP. *Caladan*, 2020.

[32] OEpic Semiconductors. *OEpic*, 2020.

[33] Brian Corbett, Ruggero Loi, Weidong Zhou, Dong Liu, and Zhenqiang Ma. *Transfer print techniques for heterogeneous integration of photonic components*. Progress in Quantum Electronics, 52(February):1–17, 2017.

[34] H.C. Casey Jr., D. D. Sell, and K.W. Wecht. *Concentration dependence of the absorption coefficient for n and ptype GaAs between 1.3 and 1.6 eV*. Journal of Applied Physics, 46(250), 1975.

[35] Batop Optoelectronics. *Energy band gap Eg of Al_{x}Ga_{1-x}As alloys*, 2020.

[36] Gregory C. DeSalvo. *Wet Chemical Digital Etching of GaAs at Room Temperature*. Journal of The Electrochemical Society, 143(11):3652, 1996.

[37] Marc Currie, Fabio Quaranta, Adriano Cola, Eric M. Gallo, and Bahram Nabet. *Low-temperature grown GaAs heterojunction metal-semiconductor-metal photodetectors improve speed and efficiency*. Applied Physics Letters, 99(20):10–13, 2011.

[38] Joost Brouckaert. *Integration of Photodetectors on Silicon Photonic Integrated Circuits (PICs) for Spectroscopic Applications*. PhD thesis, Ghent University, 2011.

[39] A.G.R. Houson, P.A.; Evans. *Saturation velocity of electrons in GaAs*. IEEE Transactions on Electron Devices, 23(6):584–586, 1976.

[40] Yu Chin Lim and Robert Moore. *Properties of Alternately Charged Coplanar Parallel Strips by Conformal Mappings*. IEEE Transactions on Electron Devices, 15(3):173–180, 1968.

[41] Julian B.D. Soole and Hermann Schumacher. *Ingaas Metal-Semiconductor-Metal Photodetectors for Long Wavelength Optical Communications*. IEEE Journal of Quantum Electronics, 27(3):737–752, 1991.

[42] Rong-Heng Yuang, Jia-Lin Shieh, Ray-Ming Lin, and Jen-Inn Chyi. *GaAs metal-semiconductor-metal photodetectors (MSM-PD'S) with AlGaAs cap and buffer layers*. Journal of the Chinese Institute of Engineers, 18(3):445–449, 1995.

[43] Junho Cho, Chongjin Xie, and Peter J. Winzer. *Analysis of soft-decision FEC on non-AWGN channels*. Optics Express, 20(7):7915, 2012.

3

Micro-transfer-printed GaAs p-i-n photodiodes for optical sensing

This chapter describes the development of transfer-print compatible, low dark current p-i-n photodiodes on top of SiN$_x$ grating couplers. The component is especially relevant for co-integration with VCSELs on the same platform, with biosensing as a relevant application field. The work was carried out by Sulakshna Kumari in the context of the MICROPRINCE (H2020) project and by Jeroen Goyvaerts in the context of the PIX4LIFE (H2020) project. The author was responsible for the design of the photodiodes, for a part of the process flow development for the source substrate, for the post-printing processing of the PICs and the measurements. Sulakshna Kumari contributed to the development of the source processing in order to further improve the yield.

3.1   Introduction to SiN_x photonic integrated circuits

The properties of silicon nitride photonic integrated circuits have gained a lot of interest, which has created significant momentum in the academic and commercial market [1–3]. The reason for this is threefold: (1) the broad transparency window of the SiN_x has led to the utilization of the visible spectrum [4], (2) the lower index contrast provides low optical waveguide losses [5, 6] and (3) the lack of two-photon absorption at telecom wavelengths allows for high optical power handling on chip. With the high on-chip power, nonlinear applications like frequency comb generation are more easily attainable [7] or high optical output power LiDAR systems can be built. SiN_x comes in two fabrication flavours: low-temperature, plasma-enhanced chemical vapor deposition (PECVD) or high-temperature, low pressure chemical vapor deposition (LPCVD). The first flavor, due to its lower deposition temperature, is interesting for co-integration with CMOS circuits [4], while the second has a lower propagation loss and a better uniformity over the wafer.

The silicon nitride offerings in Europe are growing rapidly. This section will provide a non-exhaustive list of the offerings and insight into the advantages and disadvantages with respect to applications and the integration of light sources and detectors. For instance, the imec PECVD BioPIX platform consists of 150 nm and 300 nm waveguide thicknesses, for the visible (VIS) range between 400-650 nm and the near-infrared (NIR) between 650-900 nm, respectively. Most other foundries, such as Lionix, Ligentec and CSIC-CNM offer the LPCVD variant with thicknesses ranging from 150 nm to 800 nm or more involved configurations in the TriPlex platform [8]. The most basic forms of each platform are available in multi-project-wafer mode and consist of passive waveguides, passive building blocks, thermo-optic phase shifters, a back-end metal layerstack to drive those phase-shifters and fiber connection modules. Over time, additional functionality is expected. For example, Lionix has demonstrated the co-integration of an InP gain chip for the C-band wavelength range by butt-coupling the individual gain chips [9]. Wafer-bonded, grating-assisted PDs have also been demonstrated on the Ligentec platform at 1550 nm [10]. However, there is a lack of demonstrated integrated components for VIS/NIR wavelengths. This hampers the market breakthrough of shorter wavelength applications such as on-chip OCT, Raman sensing, cell sorting, microscopy, food sorting and others. Several of these applications require many opto-electronic components. For instance, OCT systems with cascaded AWGs can have up to 512 output channels. The demonstration based on the Lionix platform uses a CCD detector array butt-coupled to a single-PIC facet [11].

Another such example is Raman spectroscopy, where a broadband generated spectrum needs to be captured and analyzed with a detector array. Given the restrictions on resolution, neither heterogeneous nor hybrid integration is a good

(a)   **(b)**
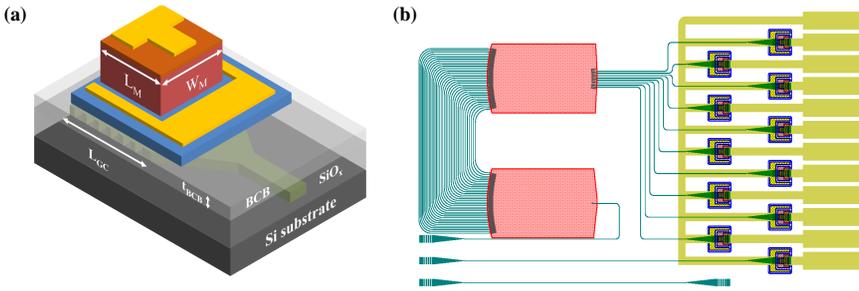
Figure 3.1: (a) 3D model of the PD-on-SiN$_x$ GC system, showing the relevant design parameters for both subcomponenets and (b) a GDS overview of the on-chip spectrometer with p-i-n photodiodes transfer printed onto the output GCs.

solution. Considering these restrictions, the preferred approach in the H2020 project PIX4Life has been a co-integration of BioPIX PECVD SiN$_x$ waveguide circuits on high-resolution CMOS imagers [12].

The application that is most relevant to the work presented in this PhD is refractive index sensing, as discussed in chapter 5. Using analyte-selective coatings, it is possible to detect a range of parameters for both biological and environmental health monitoring. This allows for point-of-care detection of sexually transmitted diseased, tuberculosis, Covid-19 and other diseases, which can fundamentally change the healthcare system [13–15]. Additionally, gas sensors have been demonstrated that can detect ammonia, methane, and other gasses with the same sensing principle [16, 17]. One of the key features of this method is that it allows multiple parameters to be measured simultaneously. This can even be done with different sensitivity levels, spread out over many sensors in parallel. This typically requires more detectors than light sources. It may be required to add even more detectors if the sensor architecture uses a broadband light source with an on-chip interrogator [13]. This showcases the absolute need for the cost-effective, dense and high-throughput integration of PDs for the NIR wavelength range on SiN$_x$ photonic integrated circuits.

It is for the above reasons that we believe that micro-transfer printing brings a real technological and cost advantage over the current standard of flip-chip integration. Therefore, the approach of a SiN$_x$ grating-assisted p-i-n photodetector, shown in Figure 3.1-(a), is investigated in this chapter. The concept has been demonstrated previously [18, 19], although we expand this to a different wavelength range (NIR), a different material system (GaAs) and a different platform (SiN$_x$). The target is to achieve a high responsivity low dark current photodiodes and to demonstrate the transfer-printing capabilities by integrating the devices on an arrayed waveguide grating (AWG) spectrometer as shown in Figure 3.1-(b).
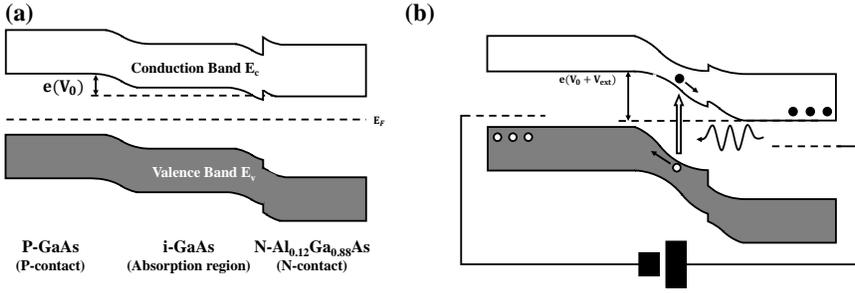
Figure 3.2: Energy band diagrams of the p-i-n junction: (a) unbiased and (b) reverse bias.

3.2 Design of a grating-assisted PD

The following sections cover the basic design principles of the photodetectors and the epitaxial layer stack, followed by the design of the PD - grating coupler structure and the AWG demonstrator circuit.

3.2.1 P-i-N photodetector

The design of the PD-on-GC is shown in Figure 3.1-(a). It is a vertical p-i-n photo-diode, with the light diffracting upwards from the grating, through the transparent n-AlGaAs layer and into the intrinsic GaAs absorption layer. The intrinsic GaAs defines the main PD mesa, which has slightly larger dimensions ($> 10\mu m$) than the grating coupler underneath. As a result, the PD-on-GC is relatively alignment tolerant with over 5 µm of buffer in each direction, well exceeding the $\pm 1\mu m$ accuracy of the transfer-printer.

The p-i-n junction itself is an extension of the pn-junction, where under reverse bias the intrinsic region acts as the absorption region of the junction. A schematic overview of the energy band diagram is given in Figure 3.2-(a). The relevant

Layer no.	Type	Material	Thickness [nm]	Doping [cm^{-3}]	Dopant
6	Protection	In$_{0.49}$Al$_{0.51}$P	500	NID	-
5	P-Contact	GaAs	300	$5 \cdot 10^{19}$	C
4	Absorption	GaAs	2000	NID	-
3	N-Contact	Al$_{0.15}$Ga$_{0.85}$As	600	$3 \cdot 10^{18}$	Si
2	Etch Stop	GaAs	4	NID	-
1	Release	In$_{0.49}$Al$_{0.51}$P	1000	NID	-
0	Substrate	GaAs	-	NID	-

Table 3.1: III-V epitaxial layer stack of the GaAs p-i-n photodetector.

junction layers are highlighted below the schematic. Under reverse bias in Figure 3.2-(b), the depletion region of the junction covers the intrinsic layer. The light passes through the slightly larger bandgap n-AlGaAs layer and is then absorbed. Afterwards, the carriers are swept to the respective contacts.

3.2.2   Epitaxial Layerstack

The epitaxial layer stack of the photodiodes is listed in Table 3.1. The top InAlP layer is a sacrificial protection layer. The device layers (on top) start with a 300 nm p-doped GaAs layer, followed by the intrinsic GaAs absorption layer. The absorption coefficient of GaAs between 750 to 875 nm is 1.7 to 1.2 μm^{-1}. Therefore, the absorption layer is chosen sufficiently thick at 2 μm. The effective absorption length is $\sim 4\mu$m, twice the intrinsic layer thickness because the light passes through the PD once more after reflecting on the P-contact. The amount of light absorbed inside the PD is defined as the internal quantum efficiency (IQE) in equation 3.1. The value is close to unity and ensures a high responsivity for the devices.

$$IQE = \frac{Light\ absorbed\ by\ PD}{Light\ coupled\ into\ PD}$$
$$= 1 - e^{-\alpha \cdot t} \geq 0.95 \tag{3.1}$$

The n-doped contact layer (no.3) is an $Al_{0.15}Ga_{0.85}As$ layer, with a bandgap wavelength of 750 nm. This ensures the transparency over the entire wavelength range of interest. The layer is 600 nm thick, which facilitates processing of the coupons. Underneath the n-contact layer is a thin 4 nm GaAs etch stop layer that ensures optimal etch selectivity and only has a minimal impact on the responsivity.

Three PD sizes are investigated, with main mesa sizes ranging from: (S) 20 μm x 20 μm, (M) 30 μm x 35 μm and (L) 40 μm x 45 μm. With a pitch of 125 μm, more than 2500 PDs and test structures are designed on a 1 cm^2 III-V sample. This high-density configuration is already a 4x improvement over flip-chip products, with a possibility to extend this towards a 6x to 8x improvement in the future.

3.2.3   PIC Design

The wavelength range of interest is 760 to 875 nm, which is too broad for a single grating. Therefore, 2 GCs are designed, one centered around 780 nm and the other around 850 nm. The BioPIX platform consists of a 300 nm thick SiN_x waveguide, with a 150 nm half-etch and a 300 nm full-etch step. This gives rise to three options: a half-etch GC, a full-etch GC and a dual-etch or staircase GC [20]. The half-etch gratings have a lower grating strength, but a higher upward directionality. The full
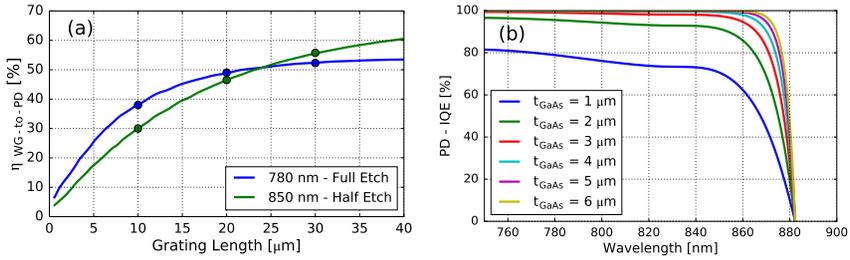
Figure 3.3: Simulation results of the (a) WG-to-PD coupling efficiency η, for varying L_{GC} of the full etch and half etch gratings; (b) internal quantum efficiency of the PD for different intrinsic GaAs thickness values, with the cut-off of the absorption band kicking in at 875 nm.

etch gratings have a higher grating strength but a lower upward directionality due to their symmetry. The staircase grating provides the best of both worlds, but are not used in this work because their feature size is too close to the edge of the technology node. Current fiber reference staircase GCs have too large variation in performance for characterizing the PDs. Figure 3.3 shows the upward diffracted power for the full etch and partial etch grating coupler as a function of grating length.

A secondary consideration to be made is to capture the entire mode field of the light. When using single-mode fibers as a reference measurement for the optical power inside the waveguide, one is constrained by the core size of the fiber. A typical NIR SMF has a core diameter of 4.4 μm (780HP single-mode fiber). A fiber diffraction grating coupler therefore has a typical 5 by 5 μm^2 surface area and uses the full-etch configuration to diffract as much light as possible over the limited 5 μm grating length. However, PDs are not limited to the same mode-size restriction as SMFs, as the mesa can be scaled larger, beyond the core size of the fiber. Therefore, the grating length, L_{GC}, of the GC_{PD} is increased to 10-20-30 μm, while the width was kept at 5 μm. In this way, the same diffraction gratings can be used for both the fiber-based reference measurements and the higher-efficiency PD coupling.

The used 780 nm GC is a uniform, full-etch grating with a 50% fill factor (FF) and a 0.57 μm pitch. The 850 nm GC is a uniform, half-etch grating with a 50% FF and a 0.59 μm pitch. The measured fiber-interfacing reference GCs have an insertion loss of -7.8 and -9 dB per GC, respectively. The coupling efficiency of the 20 μm gratings towards the PD is simulated in Lumerical FDTD, with a 2D model. The WG-to-PD coupling efficiencies, $\eta_{WG-to-PD}$, are 50% for the 780 nm FE grating and 56% for the 850 nm HE grating, with a 30 μm grating length. The overall efficiency of the PD-on-GC system is defined as the external quantum efficiency and relates the light absorbed by the PD to the light inside the waveguide

Property	785nm	850nm
Type	Full-etch	Half-etch
Pitch [µm]	0.57	0.59
FF [%]	50	50
Length [µm]	10-20-30	10-20-30
Width [µm]	5	5
core$_{fiber}$ [µm]	4.4	4.4
IL$_{fiber}$ [dB]	-7.8	-9.0
tol$_x$ PD-GC [µm]	7.5-12.5-17.5	7.5-12.5-17.5
tol$_y$ PD-GC [µm]	5-7.5-7.5	5-7.5-7.5

Table 3.2: Summary of the relevant specifications of the grating couplers, the fibers and the misalignment tolerance of the PD-on-GC system.

as in equation 3.2. Moreover, the PDs are scaled to be slightly larger than the GC dimensions. In this way, a tolerance is built-in into the assembly, which well exceeds the constraints of the micro-transfer-printer itself. A summary of the GC and PD specifications can be found in table 3.2.

$$EQE = \frac{Light\ absorbed\ by\ PD}{Light\ inside\ WG}$$
$$= \eta_{WG-to-PD} \cdot IQE \tag{3.2}$$

In terms of PIC design, reference circuits are designed for the three PD sizes, for each wavelength range. These structures consist of reference gratings and PD transfer-print sites to derive the waveguide-referred responsivity of the devices. The demonstrator circuit is the arrayed waveguide grating spectrometer, designed at 780 nm. The AWG is designed using the Luceda filter toolbox [21], making use of the full etched and half etched waveguides of the BioPIX platform. The half etched rib waveguide reduces phase errors in the delay lines of the AWG. It is a 10 channel spectrometer, with a 1 nm channel width, a 2 nm channel spacing and a FSR of 30 nm. The AWG output channels were distributed to a set of output grating couplers with the same pitch (125 µm) as the PDs on the source substrate. This design thus allows for arrayed PD printing using a multi-post stamp.

3.3 Fabrication

This section describes the fabrication of the photodetector on the InAlP release layer. The InAlP release layer was chosen for its excellent etch selectivity and ease of use in III-V processing. The devices are fabricated with standard III-V processing procedures, which are briefly discussed in the following paragraphs. Figure 3.4 showcases the processing steps in a cross-section or top-down view. Figure 3.5 presents the results and post-processing steps with microscope images.

P-contact
At the start of the process, the InAlP protection layer was removed with a HCl:DI (1:5) solution. The process then starts at Figure 3.4-(a). The Ti/Au p-contact metal stack is first deposited. Just prior to the deposition, the sample is dipped in HCl:DI (1:1) for 5 seconds. This removes all surface oxidation on the P-doped GaAs layer. The p-contact shape is a tetris-like block that facilitates the alignment procedure during transfer printing.

PD mesa
The main mesa of the PD is defined with an ICP-etch, that stops in the N-contact layer. Previously, wet etching was used for the MSM PD in chapter 2, because the absorption layer was relatively thin at 0.5 µ and the release layer was directly below the absorption layer. In the case of the PIN PD, the absorption layer is more than 2 µm thick, and the N-contact layer is sandwiched between the absorption layer and the InAlP release layer. The ICP etch offers improved control and uniformity across the sample over wet etching, for this relatively thick absorption layer etch. The ICP recipe is based on $SiCl_4$ and uses a SiN_x hard mask layer, shown in Figures 3.4-(c) & (d). The etch stops about 100 nm into the $Al_{0.12}Ga_{0.88}As$ N-contact layer in Figure 3.4-(e). Afterwards, a SiN_x passivation layer is deposited to protect the mesa sidewalls.

N-contact
Prior to the contact-deposition, the passivation layer is opened up outside the PD-mesa. Then, a digital etch step is performed, to clean and prepare the n-$Al_{0.12}Ga_{0.88}As$ for further processing. The N-contact is then deposited with a Ni/Ge/Au/Ti/Au metal stack. Similar to the p-contact, the sample is dipped into a HCl:DI (1:1) solution. This happens after the lithography step and prior to the deposition, shown in Figure 3.4-(g). The option to anneal the contacts was preserved for a later stage, in case the performance was below par.
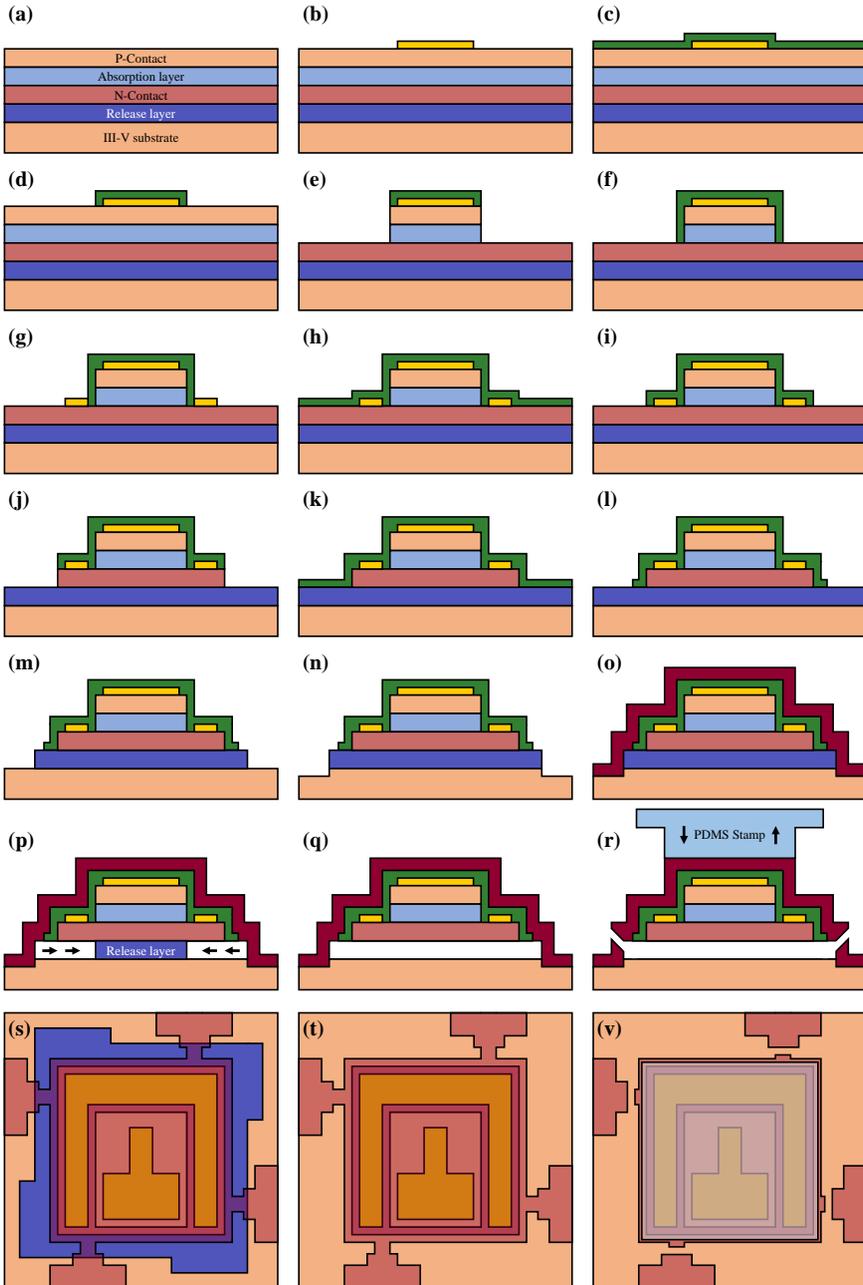
Figure 3.4: Schematic overview of the required processing steps on the source substrate: (a) Shows the blanket epitaxial sample, followed by (b) the P-contact deposition; (c) SiN$_x$ passivation and (d) patterning; (e) the ICP-mesa formation and (f) passivation; (h) N-contact deposition, followed by (h) another passivation and (i) patterning step to then (j) wet etch the second mesa, (k) passivate and (l) pattern the entire device; (m) the patterning of the release layer, (n) with substrate access and (o) PR encapsulation; (p) the wet underetch resulting in (q) quasi-free standing devices and finally (r) pick-up. (s-t-v) illustrate a top-down overview of (p-q-r), showing the devices just prior to the release etch, after the release etch and after pick-up on the PDMS stamp.

N-mesa

The second mesa is defined with a wet etch step. A combination of a SiN_x and photoresist mask was chosen for this etch, illustrated in Figure 3.4-(h to j). The purpose of wet etching is to have a high selectivity with the InAlP release layer. The sample is first dipped into a HCl:DI (1:1) solution, to remove any surface oxidation on the n-$Al_{0.12}Ga_{0.88}$As layer. Following this, the n-AlGaAs and the GaAs etch stop layer are etched simultaneously with a citric acid:peroxide (5:1) etchant until the InAlP release layer is exposed. Afterwards, another SiN_x passivation layer is deposited to protect the sidewalls of the secondary mesa, as in Figure 3.4-(k).

Release layer patterning

The passivation layer of the secondary mesa is opened up first. Subsequently, the release layer is patterned with a HCl:DI (1:5) solution until the substrate is reached. Next, the substrate is etched with a citric acid:peroxide (5:1) solution to etch down $\sim$ 100 nm into the substrate, as shown in Figure 3.4-(m) & -(n).

Encapsulation & release etch

TI-35 is used to protect the devices. They form the tethers that anchor the devices to the substrate, as shown in Figure 3.4-(o). It is important to hardbake the resist after lithography and prior to the release etch. This improves the printing yield.

Figures 3.4-(p,s) show the advancement of the release etch, done with HCl:DI (1:1). After a half hour etch time, the sample is rinsed in DI-beakers instead of under running water. Then, the sample is dried under the wet bench via evaporation. The InAlP layer has excellent etch properties and leaves a clean substrate after etching. As a result, no digital etching is required to remove residues, in contrast to the $Al_{0.90}Ga_{0.10}$As or InGaP systems.

Printing & post-processing

After the release etch, the source sample is ready for transfer printing, as displayed in Figure 3.4-(q,t). In the current design, over 2500 PDs are ready for pick-up. Figure 3.5-(a & b) show the source sample after the release etch is done. The bottom structures in Figure 3.5-(b) are test devices to evaluate the processing quality. One of the key benefits of transfer printing is the option to redistribute the devices, going from a dense array on the source wafer to a sparse configuration on the target wafer. This is showcased with the transfer-printed PDs on the PIC in Figure 3.5-(c). Figures 3.5-(d-i, d-ii) demonstrate PDs printed on the test gratings before and after probe-pad deposition. Figures 3.5-(e-i,e-ii,e-iii) highlights the array printing feature used to achieve a high assembly throughput. These PDs are printed on the output ports of the AWG demonstrator circuit.
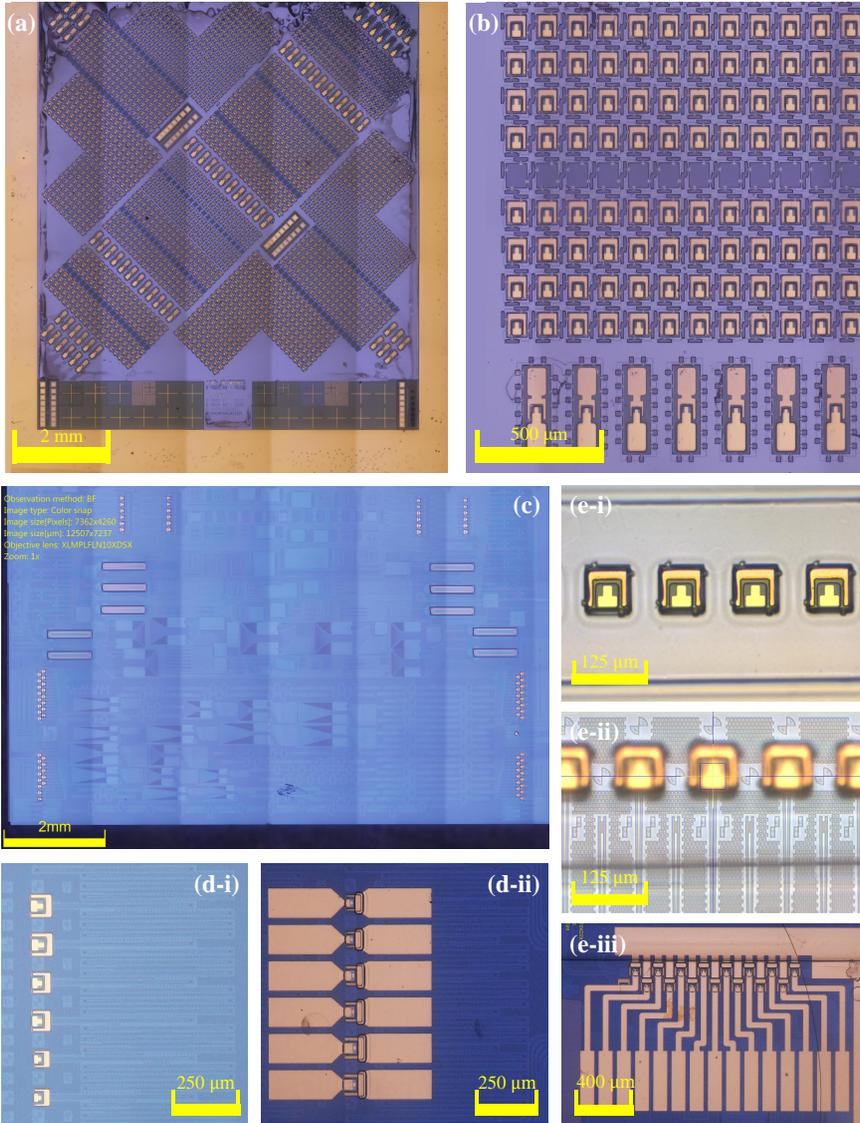
Figure 3.5: Microscope images of (a) the entire source sample, (b) an enhanced local view of the TP-ready PDs and test devices. (c) Shows a PIC with printed PDs across the sample. (d-i & d-ii) displays the PDs on PIC after printing and after probe metal definition on the PD-characterization circuit, while (e-i to e-iii) presents the array printing capability showcased on the spectrometer circuit.

3.4   Measurement results

This section covers the electrical and optical characterization of the standalone PDs, as well as a comparison with the performance of the PDs printed on the AWG demonstrator.

The setup consists of a Titanium-Sapphire (Ti-Sapph) high-power, tunable laser to scan the two wavelength regions of interest: 760 nm to 800 nm and 820 nm to 900 nm. The first region is limited by the range of the Ti-Sapph laser. Below 760 nm the laser can not maintain a lock to a set wavelength, with an unstable output as a result. Between 800 nm and 820 nm ($\sim$ 808 nm), the external cavity switches over to the next FSR. The mirror tuning associated with the FSR change is also unstable in this region. Given that this wavelength range coincides with the edge of the transmission window of each grating, it was excluded from the measurements.

The wavelength is monitored with a high-resolution (High Finesse WS7) wavelength meter. A 50-50 fiber splitter is used to monitor any laser fluctuations. A Keithley 2400 model is used to measure the photocurrent, while a more sensitive 2450 model is used to measure the dark current. There are reference grating coupler transmission test structures on the PIC, to measure the insertion loss of the fiber couplers. The waveguide-coupled power is deduced from the pre-measured insertion loss values of the reference grating couplers and the in situ monitoring of the laser power. The waveguide-coupled power is then used to calculate the responsivity of the PDs.

3.4.1   PD characterization at 780 nm & 850 nm

Given the broad absorption spectrum of GaAs, the PDs were characterized on two different grating couplers, which each cover a part of the spectrum. These are centered around 780 nm and 850 nm, as detailed in section 3.2.2. Two sets of measurements are carried out; the basic electrical measurements that investigate the dark current and resistance, and the electro-optical measurements that look at the wavelength-dependent responsivity of the devices.

The electrical characterization of the PDs is independent from the wavelength range, as the same PDs are printed on each grating. Figure 3.7-(a) plots the IV-curve, given in blue, and the differential resistance, R_{diff}, in black, for a medium-sized PD. For the set of measured devices, the differential resistance is $42 \pm 7\ \Omega$ for the medium sized PD. The resistance values are high in comparison to other GaAs p-i-n PDs, but that is because these devices were not annealed. All results on R_{diff} for the different PD sizes are shown in table 3.3.
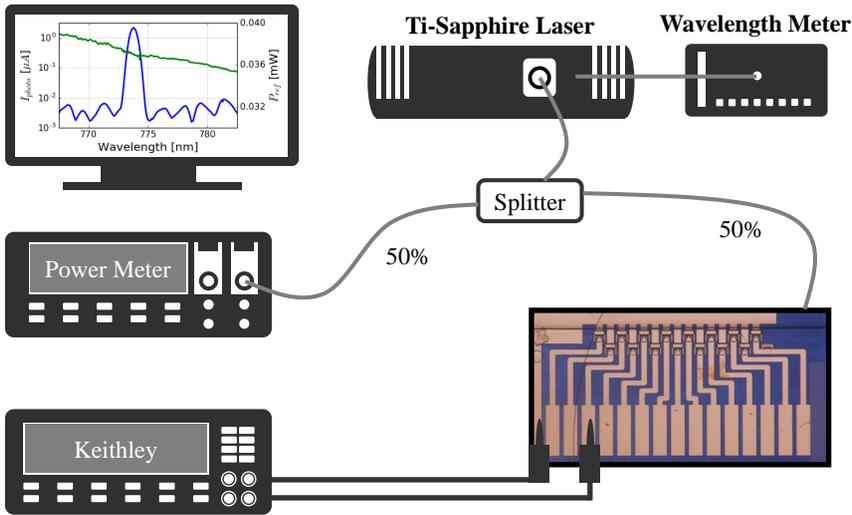
Figure 3.6: Measurement setup with the Titanium-Sapphire tunable laser (760 to 900 nm) used for characterizing the standalone PDs and AWG spectrometer.

Figure 3.7-(b) is a histogram of the measured dark currents of the medium-sized PD. The average dark current of the medium-sized photodetector is 11.48 ± 4.49 pA. This corresponds to a dark current density of 0.76 ± 0.30 μA·cm^{-2}. The values of dark current and dark current density of the other PD sizes are given in table 3.3. This performance equals or exceeds that of commercial PDs, who have dark currents advertised at 0.5 nA. This value translates to < 6.36 μA·cm^{-2} for a 100 μm diameter circular mesa [22].

VI-curves are displayed in Figure 3.7-(c) & -(d) for 780 and 850 nm wavelength, respectively. The graphs show the dark current measured in blue, with the PD-response for varying waveguide-coupled power levels in green and red. From the y-axis log scale, it is clear that having a low dark current opens up the possibility for a large on-chip optical budget. Also, these devices can operate at reverse bias voltages -1 V or lower.

In Figure 3.8-(a) & -(b), the direct photocurrent responses are presented for the small, medium and large PDs, for each wavelength region. The amplitude of the photocurrent depends on the (1) the laser power at a given wavelength and (2) the insertion loss of the grating at that wavelength. The responsivity is thus a better figure-of-merit, as it normalizes the PD photocurrent response to the power inside the waveguide, P_{WG}. This definition of waveguide-referred-responsivity, R_{WG}, is in line with the definition of EQE as shown by the relation in equation 3.3. It is a commonly used definition for waveguide-coupled PDs [19, 23].
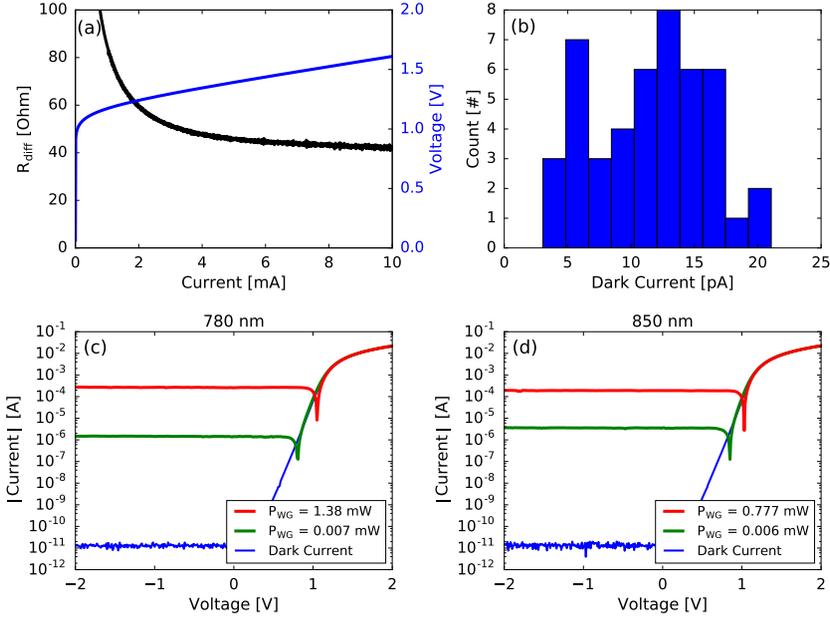
Figure 3.7: The electrical performance of medium-sized PDs with (a) showing the V-I curve and R_{diff} measured up to 10 mA; (b) the distribution of the measured dark current at -1 V reverse bias. The bottom row shows I-V curves for PD-on-GC circuits, illuminated at (c) 780 nm and (d) 850 nm.

$$R_{WG,meas} \leq R_{WG,sim}$$
$$\leq \frac{q}{hf} \cdot \lambda \cdot EQE_{sim} \tag{3.3}$$
$$0.24 - 0.30 \leq 0.38 \quad [A/W]$$

The GC insertion loss for this measurement is base-lined on reference GCs, placed directly above and below the PD measurement circuit. Combining the monitored laser power, and the GC insertion loss, P_{WG} and R_{WG} are derived, with the latter shown in Figure 3.8.-(c) & -(d). From the figure, it is clear that the smaller PDs are under performing. As a reminder, these are printed on the shorter, fiber-based grating couplers and their performance is in line with the simulations. The medium and large PDs are printed on longer gratings. Longer grating lengths scatter more light upwards, leading to the higher responsivities, with our best value of 0.30 A/W for a medium sized PD, published in Optics Express [24]. The difference between the large and the medium PD is not substantial. This indicates that most of the light has already been scattered out for the medium grating length
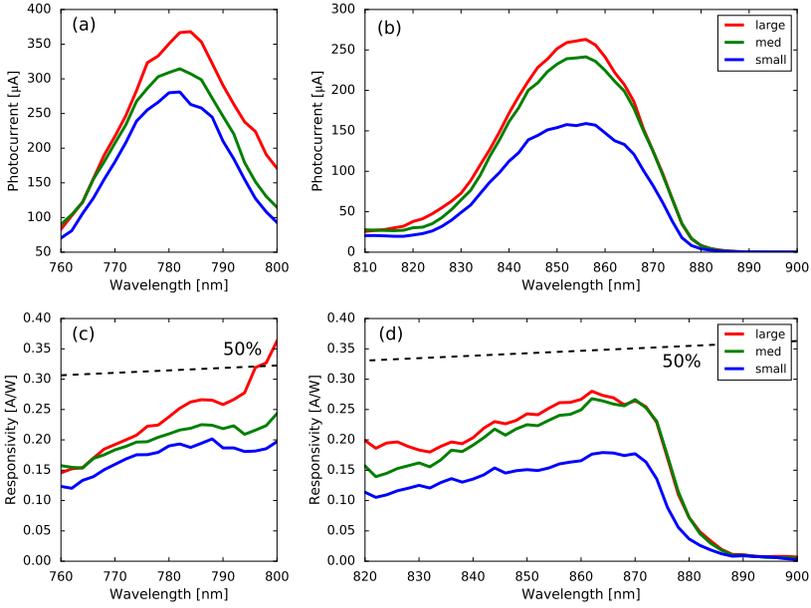
Figure 3.8: Spectral photocurrent (a-b) and corresponding responsivity measurements (c-d) for all PD sizes, for both wavelength ranges.

of 20 μm. The obtained responsivities are around 40% lower than some flip-chip compatible commercial products [25]. It is important to note that the responsivity of the commercial PDs is not a waveguide-referred responsivity. The relatively low $\eta_{WG-to-PD}$ is thought to be the root cause for the lower R_{WG}. It can be improved by (1) increasing the directionality with e.g. a staircase grating [26] or by introducing a bottom reflector underneath the grating [27].

PD Properties	Small	Medium	Large
L_{GC} [μm]	10	20	30
PD size [μm^2]	20 x 20	30 x 35	40 x 45
R_{diff} [Ω]	120 ± 32	42 ± 7	38 ± 11
I_{dark} [pA]	12.06 ± 5.16	11.48 ± 4.49	12.05 ± 3.06
j_{dark} [μA·cm^{-2}]	3.02 ± 1.29	0.94 ± 0.36	0.67 ± 0.17
$R_{WG,780nm}$ [W/A]	0.18	0.21	0.24
$R_{WG,850nm}$ [W/A]	0.14	0.24-0.3	0.26

Table 3.3: Summary of the TP-PD properties.
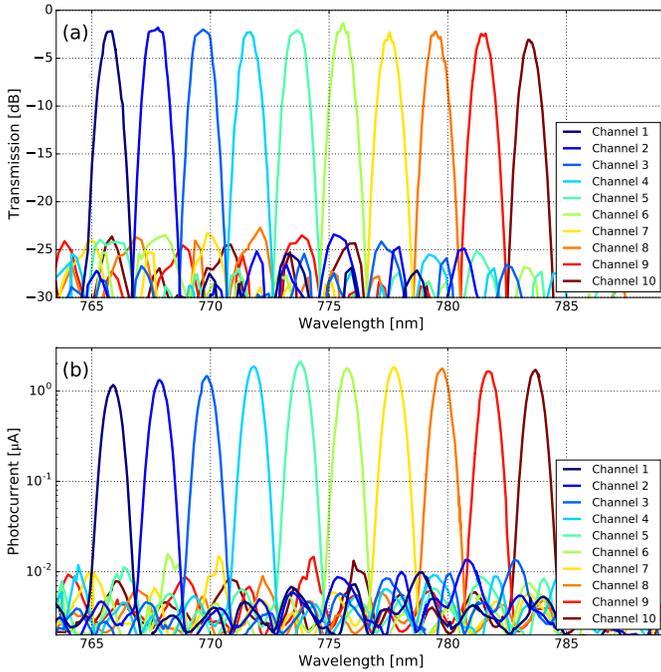
Figure 3.9: Characterization of the AWG-demonstrator circuit, with the measured optical transmission shown in (a) and the measured photocurrent of the transfer-printed PDs on the different output channels in (b). The PDs are transfer-printed on top of the output grating couplers of the AWG-channels, and are measured at a reverse bias of -2V.

3.4.2   Characterization of the AWG-demonstrator

For the AWG characterization, a 10-channel device was designed on the BioPIX 300 nm platform, with a center wavelength at 780 nm. It can be seen in Figure 3.9-(a) that the central wavelength is 6.5 nm off-spec. The measurements were conducted at 11.5° fibre angle to compensate for this offset in the GC transmission spectrum. The photocurrent measurements at -2 V reverse bias are plotted in Figure 3.9-(b).

The spectra in both figures look similar. After printing of the PDs, the cross-talk characteristics of the AWG exceed 20 dB in both the optical and electrical measurements. As the cross-talk keeps on being defined by the AWG, there is no cross-scattered light being collected by neighbouring PDs at a pitch of a 125 µm. Hence, there is no change in performance of the AWG. This circuit also closely resembles the on-chip interrogator circuit of the refractive index sensor in [13]. In that configuration, the light is similarly coupled out with a grating coupler and

collected off-chip in the far-field by a larger CMOS imager sensor. Our proposed solution with integrated PDs allows for further miniaturization and opens up new application opportunities.

3.5   Conclusions

In this chapter the transfer-print integration of low dark current GaAs p-i-n photodetectors is investigated. As the market of silicon nitride photonic integrated circuits is growing, so does the need for a wafer-scale compatible process for the integration of photodetectors.

The section on design covered the PD-on-GC system in more detail. It explained the definitions of waveguide-referred responsivity and studied the opportunities of next generation PIC designs to improve on the presented devices. In short, a road map is presented to improve the responsivity by increasing the upward directionality of the gratings.

In the third part, the process flow transfer-printable GaAs p-i-n PDs is discussed. The process flow covers the basic processing steps. It highlights the capability of µTP for printing single PDs and arrays of PDs.

The results are reviewed in the last section, with a discussion of the electrical and optical characterization of the PDs. Due to the limitations of the involved grating coupler, the waveguide-referred external quantum efficiency remains below 50 %. This translates into a responsivity of up 0.22 A/W for 780 nm and 0.28 A/W at 850 nm. Suggestions are put forward to improve this. The dark current of the GaAs PDs is very low, at just above 10 pA for all PD sizes. Given that the low dark current creates a large on-chip optical budget, this opens up great opportunities for on-chip parallel sensing.

To summarize, the TP-integration method for PDs-on-GCs holds great promise for more complex photonic integrated circuits on a silicon nitride platform. All TP-related benefits have been showcased on a sample-scale basis, while simultaneously presenting promising performance for future applications of SiN_x PICs.

References

[1] Pascual Muñoz, Gloria Micó, Luis A. Bru, Daniel Pastor, Daniel Pérez, José David Doménech, Juan Fernández, Rocío Baños, Bernardo Gargallo, Rubén Alemany, Ana M Sánchez, Josep M Cirera, Roser Mas, and Carlos Domínguez. *Silicon nitride photonic integration platforms for visible, near-infrared and mid-infrared applications*. Sensors (Switzerland), 17(9):1–25, 2017.

[2] Abdul Rahim, Eva Ryckeboer, Ananth Z. Subramanian, Stéphane Clemmen, Bart Kuyken, Ashim Dhakal, Ali Raza, Artur Hermans, Muhammad Muneeb, Sören Dhoore, Yanlu Li, Utsav Dave, Peter Bienstman, Nicolas Le Thomas, Günther Roelkens, Dries Van Thourhout, Philippe Helin, Simone Severi, Xavier Rottenberg, and Roel Baets. *Expanding the Silicon Photonics Portfolio with Silicon Nitride Photonic Integrated Circuits*. Journal of Lightwave Technology, 35(4):639–649, 2017.

[3] Marco A.G. Porcel, Alberto Hinojosa, Hilde Jans, Andim Stassen, Jeroen Goyvaerts, Douwe Geuzebroek, Michael Geiselmann, Carlos Dominguez, and Iñigo Artundo. *Silicon nitride photonic integration for visible light applications*. Optics and Laser Technology, 112(November 2018):299–306, 2019.

[4] Luis Hoffman, Ananth Subramanian, Philippe Helin, Bert Du Bois, Roel Baets, Pol Van Dorpe, Georges Gielen, Robert Puers, and Dries Braeken. *Low loss CMOS-Compatible PECVD silicon nitride waveguides and grating couplers for blue light optogenetic applications*. IEEE Photonics Journal, 8(5), 2016.

[5] Martin H P Pfeiffer, Clemens Herkommer, Junqiu Liu, Tiago Morais, Michael Zervas, Michael Geiselmann, and Tobias J Kippenberg. *Photonic Damascene process for low-loss , high-confinement silicon nitride waveguides*. 6(1), 2007.

[6] Ananth Z. Subramanian, Eva Ryckeboer, Ashim Dhakal, Frédéric Peyskens, Aditya Malik, Bart Kuyken, Haolan Zhao, Shibnath Pathak, Alfonso Ruocco, Andreas De Groote, Pieter Wuytens, Daan Martens, Francois Leo, Weiqiang Xie, Utsav Deepak Dave, Muhammad Muneeb, Pol Van Dorpe, Joris Van Campenhout, Wim Bogaerts, Peter Bienstman, Nicolas Le Thomas, Dries Van Thourhout, Zeger Hens, Gunther Roelkens, and Roel Baets. *Silicon and silicon nitride photonic circuits for spectroscopic sensing on-a-chip [Invited]*. Photonics Research, 3(5):B47, 2015.

[7] Naoya Kuse, Tomohiro Tetsumoto, Gabriele Navickaite, Michael Geiselmann, and Martin E Fermann. *Continuous scanning of a dissipative Kerr-*

microresonator soliton comb for broadband, high-resolution spectroscopy. Opt. Lett., 45(4):927–930, feb 2020.

[8] A Leinse, R G Heideman, M Hoekman, F Schreuder, F Falke, C G H Roeloffzen, L Zhuang, M Burla, D Marpaung, D H Geuzebroek, R Dekker, E J Klein, P W L van Dijk, and R M Oldenbeuving. *TriPleX waveguide platform: low-loss technology over a wide wavelength range*. In Jean-Marc Fédéli, Laurent Vivien, and Meint K Smit, editors, Integrated Photonics: Materials, Devices, and Applications II, volume 8767, pages 86–98. International Society for Optics and Photonics, SPIE, 2013.

[9] Youwen Fan, Jörn P. Epping, Ruud M. Oldenbeuving, Chris G.H. Roeloffzen, Marcel Hoekman, Ronald Dekker, René G. Heideman, Peter J.M. Van Der Slot, and Klaus J. Boller. *Optically Integrated InP-Si3N4 Hybrid Laser*. IEEE Photonics Journal, 8(6), 2016.

[10] Qianhuan Yu, Junyi Gao, Nan Ye, Boheng Chen, Keye Sun, Linli Xie, Kartik Srinivasan, Michael Zervas, Gabriele Navickaite, Michael Geiselmann, and Andreas Beling. *Heterogeneous Photodiodes on Silicon Nitride Waveguides with 20 GHz Bandwidth*. Optics Express, 28(10):W4G.1, 2020.

[11] Roosje M. Ruis, Arne Leinse, Ronald Dekker, Rene G. Heideman, Ton G. Van Leeuwen, and Dirk J. Faber. *Decreasing the Size of a Spectral Domain Optical Coherence Tomography System with Cascaded Arrayed Waveguide Gratings in a Photonic Integrated Circuit*. IEEE Journal of Selected Topics in Quantum Electronics, 25(1), 2019.

[12] Xiaomin Nie, Eva Ryckeboer, Gunther Roelkens, and Roel Baets. *CMOS-compatible broadband co-propagative stationary Fourier transform spectrometer integrated on a silicon nitride photonics platform*. Optics Express, 25(8):A409, 2017.

[13] D. Martens, P. Ramirez-Priego, M. S. Murib, A. A. Elamin, A. B. Gonzalez-Guerrero, M. Stehr, F. Jonas, B. Anton, N. Hlawatsch, P. Soetaert, R. Vos, A. Stassen, S. Severi, W. Van Roy, R. Bockstaele, H. Becker, M. Singh, L. M. Lechuga, and P. Bienstman. *A low-cost integrated biosensing platform based on SiN nanophotonics for biomarker detection in urine*. Analytical Methods, 10(25):3066–3073, 2018.

[14] Patricia Ramirez-Priego, Daan Martens, Ayssar A. Elamin, Pieterjan Soetaert, Wim Van Roy, Rita Vos, Birgit Anton, Ronny Bockstaele, Holger Becker, Mahavir Singh, Peter Bienstman, and Laura M. Lechuga. *Label-Free and Real-Time Detection of Tuberculosis in Human Urine Samples Using a Nanophotonic Point-of-Care Platform*. ACS Sensors, 3(10):2079–2086, 2018.

[15] Mohammed Sharif Murib, Daan Martens, and Peter Bienstman. *Label-free real-time optical monitoring of DNA hybridization using SiN Mach–Zehnder interferometer-based integrated biosensing platform*. Journal of Biomedical Optics, 23(12):1, 2018.

[16] Nebiyu A. Yebo, Sreeprasanth Pulinthanathu Sree, Elisabeth Levrau, Christophe Detavernier, Zeger Hens, Johan A. Martens, and Roel Baets. *Selective and reversible ammonia gas detection with nanoporous film functionalized silicon photonic micro-ring resonator*. Optics Express, 20(11):11855, 2012.

[17] Giuseppe Antonacci, Jeroen Goyvaerts, Haolan Zhao, Bettina Baumgartner, Bernhard Lendl, and Roel Baets. *Ultra-sensitive refractive index gas sensor with functionalized silicon nitride photonic circuits*. APL Photonics, 5(8), 2020.

[18] Jing Zhang, Andreas De Groote, Amin Abbasi, Ruggero Loi, James O'Callaghan, Brian Corbett, António José Trindade, Christopher A. Bower, and Gunther Roelkens. *Silicon photonics fiber-to-the-home transceiver array based on transfer-printing-based integration of III-V photodetectors*. Optics Express, 25(13):14290, 2017.

[19] Grigorij Muliuk, Kasper Van Gasse, Joris Van Kerrebrouck, Antonio Jose Trindade, Brian Corbett, Dries Van Thourhout, and Gunther Roelkens. *4 ×25 Gbps polarization diversity silicon photonics receiver with transfer printed III-V photodiodes*. IEEE Photonics Technology Letters, 31(4):287–290, 2019.

[20] Yang Chen, Robert Halir, Íñigo Molina-Fernández, Pavel Cheben, and Jian-Jun He. *High-efficiency apodized-imaging chip-fiber grating coupler for silicon nitride waveguides*. Optics Letters, 41(21):5059, 2016.

[21] Luceda Photonics. *Filter Toolbox*, 2020.

[22] Inc. Optoway. *Optoway PIN Photodiode*, 2004.

[23] Ruijun Wang, Stephan Sprengel, Muhammad Muneeb, Gerhard Boehm, Roel Baets, Markus-Christian Amann, and Gunther Roelkens. *2 µm wavelength range InP-based type-II quantum well photodiodes heterogeneously integrated on silicon photonic integrated circuits*. Optics Express, 23(20):26834, 2015.

[24] Jeroen Goyvaerts, Sulakshna Kumari, Sarah Uvin, Jing Zhang, Roel Baets, Agnieszka Gocalinska, Emanuele Pelucchi, Brian Corbett, and Gunther Roelkens. *Transfer-print integration of GaAs p-i-n photodiodes onto silicon nitride photonic integrated circuits*. 2020 IEEE Photonics Conference, IPC 2020 - Proceedings, 28(14):21275–21285, 2020.

[25] Inc. VIS. *Vertical Integrated Systems*.

[26] Yang Chen, Robert Halir, Íñigo Molina-Fernández, Pavel Cheben, and Jian-Jun He. *High-efficiency apodized-imaging chip-fiber grating coupler for silicon nitride waveguides*. Opt. Lett., 41(21):5059–5062, nov 2016.

[27] Jianxun Hong, Andrew M. Spring, Feng Qiu, and Shiyoshi Yokoyama. *A high efficiency silicon nitride waveguide grating coupler with a multilayer bottom reflector*. Scientific Reports, 9(1):1–8, 2019.

4

Micro-transfer-printed Vertical-Cavity-SiN$_x$-Integrated-Lasers (VCSILs)

This chapter describes a micro-transfer-printed, bottom-emitting VCSEL that is coupled to a SiN$_x$ waveguide circuit. Like for the work by my predecessor, Sulakshna Kumari, the VCSEL-to-PIC integration efforts stem from a profound collaboration with the VCSEL opto-electronics team of Chalmers University of Technology. The head of the department, Professor Anders Larsson, and professor Johan Gustavsson have overseen the joint Ghent University-Chalmers University work of Emanuel Haglund, Sulakshna Kumari, Erik Haglund, Alexander Grabowski and Mehdi Jahed. I have had the opportunity to work with Erik and Mehdi on the VCSEL flip-chip integration efforts. While the transfer-printing efforts started together with Emanuel, Alexander has carried on this work and has been fundamental in achieving the results discussed in this chapter.
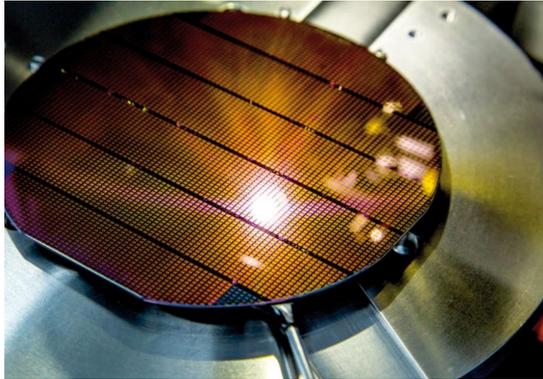
Figure 4.1: Wafer-scale VCSEL manufacturing at Finisar USA (now II-VI Incorporated) [4].

4.1 Introduction

In this section, the reader is introduced to the key properties of vertical-cavity-surface-emitting lasers (VCSELs) and how these properties result in the relevance of VCSEL light sources. An introduction is given to VCSEL - integrated photonics, along with the state-of-the art integration methods demonstrated in literature.

4.1.1 VCSEL properties

VCSELs are surface-emitting lasers, having a set of unique features. Due to the vertical cavity, the footprint of the devices is much smaller than for edge-emitting devices. Moreover, device singulation does not pose major risks for the device performance because the critical, optical facet is on the upper side of the devices. VCSELs also have very low, sub-mA lasing thresholds [1], with conversion efficiencies of up to 63 % for GaAs devices [2], leading to lowest in-class power consumption. Combining the energy efficiency with high bandwidths of up to 35 GHz [3], VCSELs provide low energy consumption per bit of information sent.

VCSELs can also be pre-tested and burned-in on the wafer, prior to the integration in the final product. They can also be easily interfaced with optical fibers. GaAs NIR VCSELs can operate at high temperatures, exceeding 85°C and even up to 125°C, which is relevant automotive optical networking. All these features combined, make VCSELs important laser sources for high-speed optical communication and sensing applications.

4.1.2   VCSEL applications

VCSELs are ideal candidates for short-reach data communication. Up until now, solutions for data communication have been dominated by 850 nm VCSELs. Most of the commercially available VCSELs are oxide-confined. The VCSELs are commonly multi-mode and operating in an On-Off-Keying format (OOK). At the first half of 2010-2020 decade, the standard data rates grew from 10 to 25 Gbps or higher [5]. Improved performance can be found by switching from multi-mode to single-mode VCSELs. This results in higher modulation bandwidth, given the smaller VCSEL apertures [6].

Nowadays, longer-wavelength VCSELs are gaining popularity due to improvements in epitaxial growth, such as the increased gain of the InGaAs quantum wells. At these longer wavelengths, lower fiber chromatic, lower fiber propagation loss and larger temperature stability are to be expected. The higher differential gain of the InGaAs QWs lead to improvements in lasing threshold, modulation bandwidth and conversion efficiency. Demonstrations show 25 Gbps at 85°C [7]. The eye-safety is also better at 980 nm. On the other hand, 850 nm VCSELs have lower free carrier absorption in the DBR mirrors, which in turn leads to lower absorption [8]. Lower absorption enables higher doping concentrations and thus lower electrical resistances, decreasing threshold carrier density and enabling higher modulation bandwidths as well. The use of double-oxide apertures decreases the parasitic capacitance, which further improves the bandwidth [9].
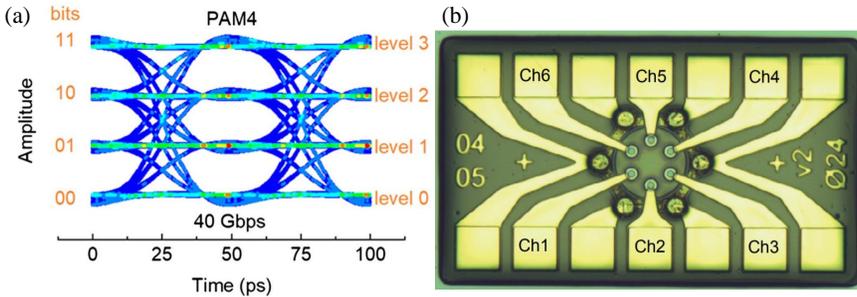
Figure 4.2: (a) Simulated PAM4 eye-diagram at 20 Gbaud [6], and (b) space-division multiplexed VCSEL array for interfacing with multi-core fibers [10].

Further advances in data rates are being investigated on device level (contact quality, epi-growth, etc.) and have been found by using advanced modulation formats (e.g. 94 Gbps data rate for a single VCSEL using multi-level amplitude modulation (PAM4) [11]). This PAM4 modulation has been transferred into data centers with transceiver modules operating at 56 Gbps (28 Gbps PAM4) [12].
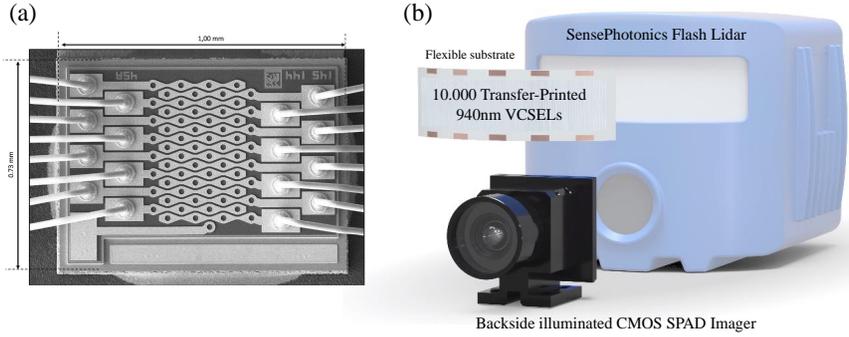
Figure 4.3: (a) VCSEL array used in Apple's FaceID depth sensor [14] and (b) SensePhotonics's 200 meter Flash LiDAR for automotive applications [15].

The current New PIC-based solutions aggregate the total combined bandwidth of multiple long-wavelength VCSELs into a single fiber through a wavelength multiplexing scheme, as pursued in the H2020 PASSION project [13]. Another method to combine several signals into a single fiber strand is through space-division multiplexing, using multi-core fibers to increase the data throughput per fiber, to reduce data center cabling complexity [10].

An entirely different market is 3D sensing with VCSEL arrays. With the release of Face ID in the iPhone X, depth sensing has been introduced to the mass consumer market. The Face ID system uses a VCSEL array from Lumentum, in combination with a diffractive optical element (DOE) to create a +10,000 dot pattern [14], using a structured light approach for face identification. The market has since been extended to a medium-range LiDAR on the backside of the iPhone 12, based on time-of-flight operation.

Another substantial market opportunity for LiDAR is in automotive and warehouse management, where depth sensing and image analysis can enable autonomous driving of vehicles. Depending on the architecture, either a flash-based VCSEL array is used or a scanning-based system. The advantage of using a flash-based lidar system is that the entire system is solid state, without any moving parts. Moreover, they can achieve high resolutions at high frame-rates and by obtaining all data at the same timestamp, the need for post-processing is alleviated. Typical VCSEL-based LiDARs operate at 940nm. One such system is developed by Ibeo Automotive Systems, using VCSELs from AMS [16, 17].

All reported flash-based LiDAR systems use sensitive single-photon avalanche detector (SPAD) CMOS imagers to collect the light. The SPAD imager together with additional light filtering on top of the SPAD improves the signal-to-noise ratio. The narrowband characteristics of VCSELs alleviate the constraints on the optical filters. VCSEL LiDAR arrays can consist of 10k to 50k devices, which means that a single failure has a much smaller impact on the overall system than scanning products (with 1 to 10 devices per system). Transferring these large arrays of VCSELs onto a custom package for a LiDAR product is not straightforward. Hence, SensePhotonics utilizes the same micro-transfer-printing technology studied here for integrating 940nm VCSELs onto flexible substrates [15]. The transfer of VCSELs onto a curved flexible substrate achieves a larger optical field-of-view and helps with power management as the devices are more spread out on the target substrate.
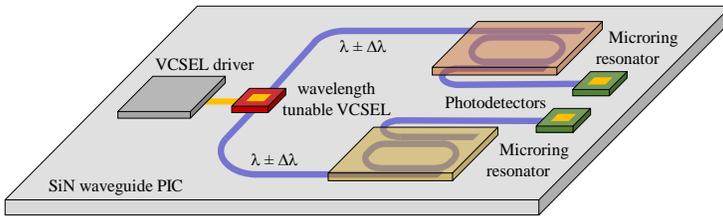
Figure 4.4: PIX4life concept image of a refractive index sensor with an integrated VCSEL.

So far, mainly fiber-based applications (communication) and free-space applications (3D sensing) of VCSELs have been discussed. However, new markets for integrated VCSELs are emerging. There are two prominent candidates discussed in this work: (1) photonic interposers for high bandwidth (density) optical links between electronic ICs and (2) miniaturized (bio-)sensors for wearables.

The rise in required I/O for advanced electronic ICs such as GPUs, have triggered the research on optical I/O to achieve high aggregate bandwidth at low power consumption on a small footprint. While VCSELs can be used to directly interface such GPUs with fiber connections, particular schemes such as interconnecting multiple GPUs through a photonic network layer integrated on a photonic integrated circuit are currently being studied. The use of GaAs near infrared VCSELs in such an application enables at the same time operation at high temperature and the possibility to exploit wavelength division multiplexing, with the promise to result in very low-power high-bandwidth-density optical interconnects .

For PIC-based sensing, VCSELs offer the unique opportunity of having ultra-low power consumption and a compact footprint. They are therefore an ideal light source in wearable sensor devices, of which a circuit concept is shown in Fig.4.4. Recent developments in highly-sensitive refractive index sensors, utilizing custom

developed coating layers, open up several environment and health monitoring applications, such as portable gas sensors that can measure a person's exposure dose towards volatile organic compounds [18], ion analysis in sweat for activity tracking [19], early disease diagnosis of central nervous system components [20], medical point-of-care and point-of-need solutions that can analyzing a patient's urea parameters [21] and self-tests for influenza and coronavirus infections [22].

4.1.3 Low-power waveguide-coupled lasers & VCSELs

There are several demonstrations for waveguide-coupled lasers that compete with the specifications of the bio-sensor put forward in the H2020 PIX4Life project. These specifications are low-power consumption, significant wavelength tuning range and wafer-scale integration on a silicon nitride waveguide platform. Most of the published work however falls outside the NIR (< 1 µm wavelength range).

Some of the earliest work has been on micro-disk laser integration for C-band silicon photonics interposers [23] as shown in Fig.4.5-(a). The III-V material die was bonded onto a silicon PIC, and the III-V processing was done on the SOI after bonding. The micro-disk laser has similar power consumption characteristics as a VCSEL, but the waveguide-coupled power was only up to 20 µW [24]. Another adjacent technology platform is the micro-ring laser implementation [25]. The footprint of this device is already larger, with a ring radius at 50 µm, resulting in a larger power consumption but also larger waveguide-coupled powers. While the power is higher, the latter configuration was not particularly single-mode. Both of these configurations couple the light through evanescent bus waveguide coupling and are therefore very sensitive to misalignment. Another evanescently-coupled laser structure is demonstrated by Crosnier et al. [26] and shown in Fig.4.5-(b). An InP layer structure is bonded onto a Si waveguide and a high-Q laser cavity is formed in an e-beam patterned 1D photonic crystal, with a silicon waveguide structure underneath. The reported lasing threshold is comparable to VCSELs at 0.1 mA and they showcase waveguide-coupled powers of up to 100 µW.

The integration of VCSELs can be divided in two main approaches. The first approach pursues an off-normal coupling angle with respect to the grating coupler used to couple light in the waveguide layer, to avoid optical feedback to the laser cavity and to improve the efficiency of the grating coupler. The second approach uses VCSEL-to-PIC integration through light-coupling at normal incidence with respect to the grating coupler. The latter group can be subdivided into (a) hybrid cavity structures that make use of a III-V half-VCSEL and (b) standalone VCSELs (top or bottom-emitting) that form an extended cavity with the grating coupler. All showcased devices so far are integrated either with a die-bonding approach or
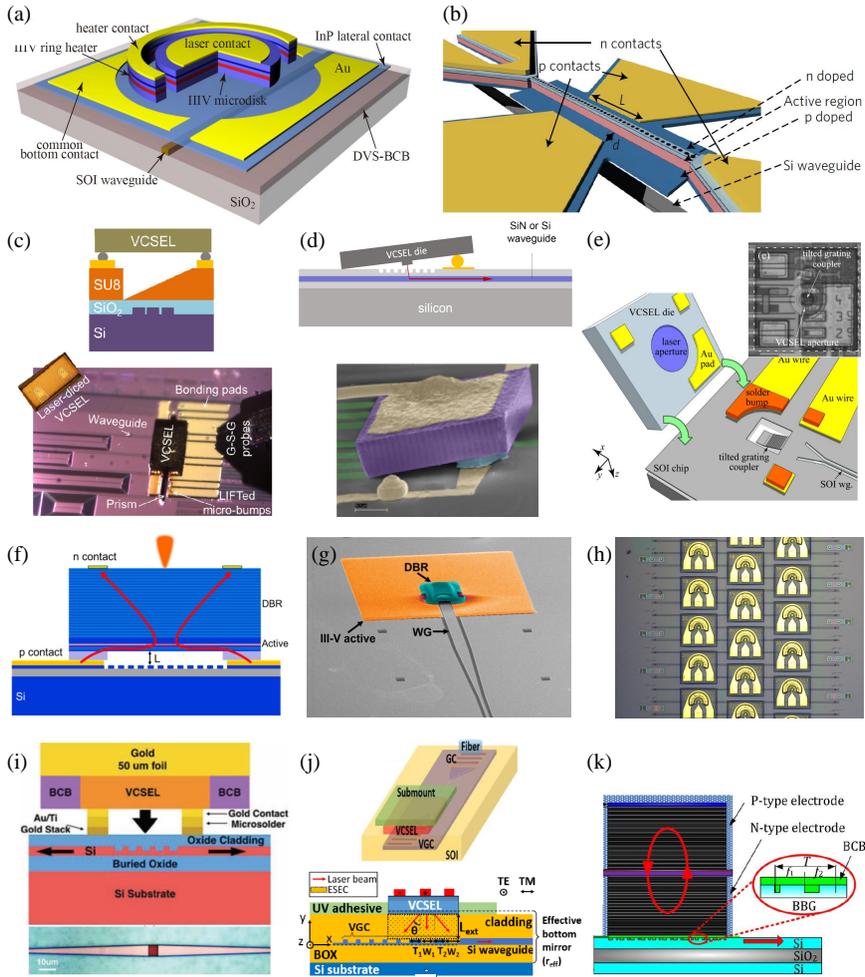
Figure 4.5: Relevant low-power consuming, WG-coupled lasers: with (a-b) non-VCSEL integrated lasers, (c-d-e) VCSELs with off-normal coupling, (f-g-h) III-V half-VCSELs with hybrid cavities and (i-j-k) bottom-emitting VCSELs with normal incidence on the gratings.

through flip-chip integration.

The off-normal coupling allows pre-testing the III-V laser prior to the integration with the PIC. This allows for a straightforward deduction of the coupling efficiency. One of the first demonstrations used a laser-ablated SU8-prism to form a 45°slanted facet for better coupling [27]. This technique allowed for a standard vertical flip-chip of the VCSEL to be combined with the desired off-normal angled coupling with a SiPho grating coupler through refraction as shown in Fig.4.5-(c). The coupling loss of the laser integration was large at -17.7 dB. It appears that there is

no polarization management for matching the VCSEL and the grating polarization. Fig.4.5-(d) shows another way to obtain off-angle coupling, by flip-chipping the VCSEL at an angle [28]. Control over the reflow-temperature and reflow-duration leads to control over the solder-ball height, which in turn controls the desired angle of the device. The authors report a -11.8 dB VCSEL-to-PIC insertion loss for a high-index contrast C-band SiPho platform, resulting in a 138 µW waveguide-coupled power. Similar to the prism-method, there is no VCSEL polarization control in these methods. Hence, the next step has been to create specific high-output-power, single-mode and single-polarization VCSELs for the same flip-chipping based approach [29]. A final off-normal coupling approach is to create a tilted grating coupler by releasing the structure [30]. The buried oxide is removed underneath the grating with an underetch. Through residual stresses, the Si grating coupler structure collapses onto the substrate, thereby creating a tilted interface. The VCSEL is an off-the-shelf, single-mode and single-polarization device, flip-chipped vertically with respect to the substrate. The demonstrated waveguide-coupled power is high at 660 µW for the O-band wavelength range. A schematic and microscope image are shown in Fig.4.5-(e). Lastly, and not shown in Fig.4.5, the H2020 project PASSION has pursued VCSEL integration through a 45°slanted mirror etched at the waveguide facet [31]. It is the only solution without a diffraction grating. The system uses C-band VCSELs in combination with the 3 µm thick VTT SOI platform. The performance is promising, with a coupling efficiency of -5 dB. However there does not appear to be a straightforward way to use this coupling approach on a SiN$_x$ waveguide platform. In short, the off-the-shelf VCSEL integration efforts have an advantage in VCSEL performance and have so far relied on technological innovations on the PIC and assembly side to accommodate coupling into a single-mode waveguide.

The second category of waveguide-coupled VCSELs are composed of hybrid cavities formed with a III-V half-VCSEL and a bottom reflector. The integration is either done with flip-chipping or with die-bonding. For flip-chipping, the most described method makes use of a high index contrast grating structure that acts as both the bottom reflector and the waveguide coupling structure. A flip-chip demonstration in Fig.4.5-(f) shows only top-surface lasing, proving the viability of the HCG [32]. Die-bonding has been used to demonstrate an optically pumped half-VCSEL-on-HCG, shown in Fig.4.5-(g) [33]. The optical pumping through the top-DBR is inefficient, resulting in low waveguide-coupled powers. Another die-bonding demonstration is the hybrid-cavity vertical-cavity-on-SiN$_x$-laser (VCSIL) [34]. In this approach, a III-V half-VCSEL was used together with a bottom dielectric DBR and shallow-etched, weakly-coupled intra-cavity grating, as shown in Fig. 4.5-(h) & Fig.4.6-(a). As a result, the waveguide layer was located inside the cavity. The low-index contrast grating diffracts only a fraction of the vertical oscillating light into the in-plane waveguide, in order to sustain CW lasing. Reported

waveguide-coupled values were 73 µW single-side and a combined 140 µW double-side coupled optical power.

The last category uses either top-emitting or bottom-emitting VCSELs to form an extended cavity with the diffraction grating. Again, either vertical flip-chipping or die-bonding techniques are used to integrate the light source onto the PIC. Wang et al. demonstrated vertical flip-chipping of a standalone laser onto a bidirectional grating coupler that has preferential TE-reflection [35]. The reported waveguide-coupled power was 65 µW, for both outputs combined. This value was lower than expected due to (1) the usage of an off-the-shelf VCSEL without incorporating optical feedback into the design and (2) the lack of polarization control of the VCSEL. Another vertical FC-based integration is demonstrated in [36] and shown in Fig.4.5-(j). The VCSEL was first placed on a submount, prior to bonding with the PIC. By using a carefully designed submount, the optical coupling could be optimized through active alignment. The authors demonstrate reasonable coupling for the O-band wavelength range and achieve polarization control through the grating feedback. Recently, a design study was done on a similar grating coupler [37]. Fig.4.5-(k) shows another demonstration of a bottom-emitting VCSEL die-bonded onto a binary-blazed grating, that diffracts light into a single preferential waveguide direction [38]. The binary blazed grating improves the coupling efficiency for single-side operation.

Other work is not as in-depth as the previously discussed efforts, but they can provide interesting concepts for VCSEL-to-waveguide coupling. One such case is photonic wirebonding, which has been showcased for edge-emitting lasers but appears more suited for vertical cavity lasers [39]. VCSEL-to-polymer waveguide coupling is also demonstrated for multi-mode VCSELs by using 45° slanted waveguide mirrors [40]. Earlier work demonstrated the lateral coupling into III-V waveguides grown on top of the VCSEL layer stack [41].

In this work, we investigate the use of micro-transfer printing to integrate bottom-emitting VCSELs onto SiN_x diffraction gratings. The µTP technique is cost-effective, wafer-scale compatible and can achieve high throughput. It therefore has a competitive advantage over wafer-bonding and flip-chipping used in the previous demonstrations of VCSEL-to-PIC integration. While earlier work from the Photonics Research Group was focused on a half-VCSEL hybrid cavity, in this work, a switch was made to a bottom-emitting full VCSEL configuration. The custom dielectric DBR required in the half-VCSEL approach hinders the broad uptake of the half-VCSEL design. The biopix 300 nm platform also does not provide sufficient index contrast for a SiN_x diffraction grating to replace the dielectric DBR by a HCG-reflector. Therefore, a new VCSEL-to-PIC design is proposed in Fig.4.6-(b). The device is a standalone bottom-emitting VCSEL that
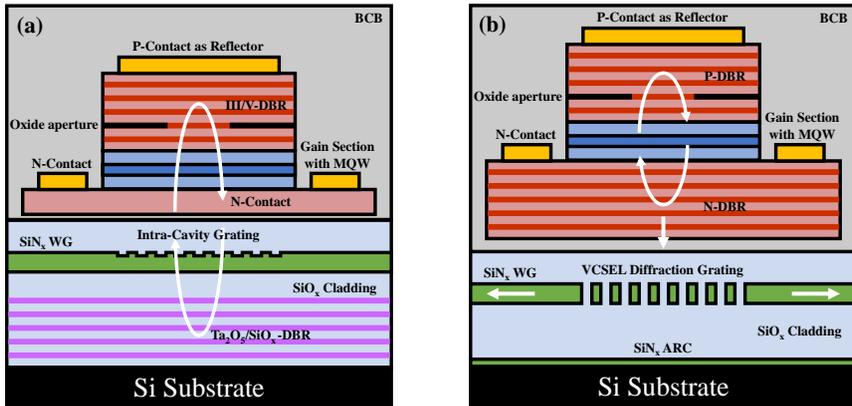
Figure 4.6: 2D cross-section schematics of the VCSEL-to-PIC implementations, investigated by (a) Sulakshna Kumari and (b) Jeroen Goyvaerts within the Photonics Research Group.

can work both standalone, and together with the waveguide diffraction grating structure integrated underneath. The VCSEL is designed to have a partially leaking top DBR mirror. By doing so, the option to characterize test-devices on the source substrate remains. This provides benefits in process monitoring control. The VCSEL diffraction grating is a medium index contrast grating (MCG), that provides optical feedback for pinning the polarization of the VCSEL and that diffracts the light into the waveguides. However, the reflection of the diffraction grating does not have to sustain lasing. The reliance on polarization dependent feedback from the GC is similar in approach as investigated in [35, 36, 38]. The proposed approach also makes use of a bidirectional GC, which is studied in detail in section 4.2. The bidirectional grating coupler allows for both forward and backward propagation modes to be coupled in the waveguide.

A complete overview and comparison between the previously published works and the presented work in this thesis is summarized at the end of the chapter, in table 4.13 in section 4.4.5.

4.2   Design

This section covers the most fundamental aspects in VCSEL design relevant to the coupling into SiN_x waveguides. The first part discusses the basic principles and relies on previously published works that go more in-depth in the underlying physics and operation of vertical cavity surface emitting lasers [8, 42]. Following this, the design of the VCSEL diffraction grating and the extended cavity are studied.

4.2.1   VCSEL fundamentals

A VCSEL is a semiconductor laser which has a vertical cavity, grown by either Molecular Beam Epitaxy (MBE) or Metal-Organic Chemical Vapor Deposition (MOCVD). A typical VCSEL is made of two distributed bragg reflectors (DBR) that form high-reflectivity mirrors. The reflectivity of one DBR is slightly lower, resulting in light passing through that DBR. Between the two mirrors are the active layers that form the gain section of the device. There are one or more high aluminum fraction $Al_xGa_{1-x}As$ layers in close proximity to the gain section. These layer will form the oxide aperture after a wet oxidation step. The confinement by the oxide aperture increases the overlap of the electric current with the optical modes at the location of the gain section. An overview of the current behavior for a back-side contacted device is shown in Fig.4.7. In the schematic, a ring-shaped P-contact is used, which allows the light to couple out upwards.
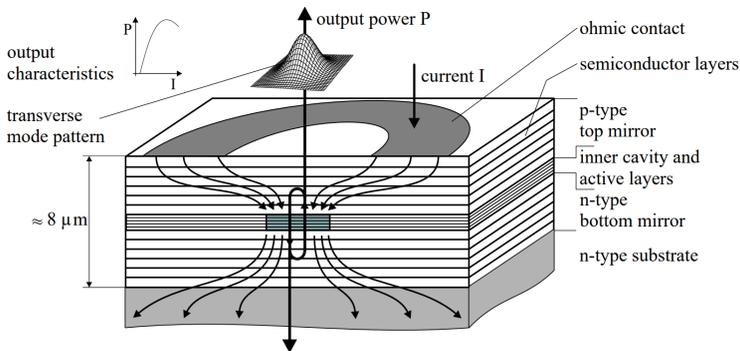
Figure 4.7: Cross-section view of the current flow and light path inside the cavity, along with the device parameters of a back-side contacted VCSEL [42].

In order to achieve lasing, the semiconductor material is electrically pumped until the round trip gain of the cavity equals the round trip losses of the cavity. The round trip loss consists of a loss attributed to light leakage through the mirrors and
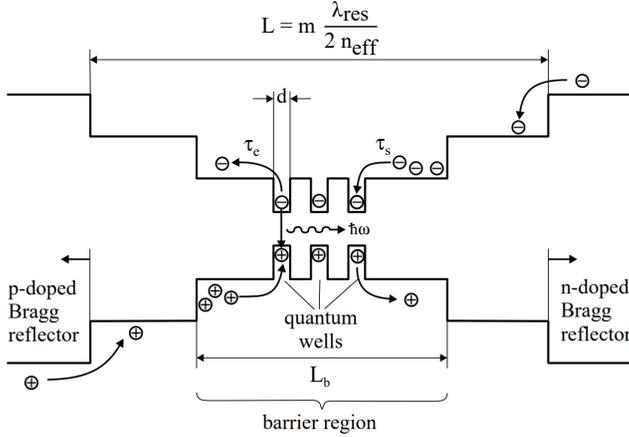
Figure 4.8: Schematic overview of the gain section with MQWs inside the cavity [42].

internal losses inside the cavity, as described by eq. 4.1:

$$g_{th} = \Gamma_l\big[\alpha_i + \alpha_m\big]$$
$$= \Gamma_l\Big[\alpha_i + \frac{1}{2L}ln\Big(\frac{1}{R_tR_b}\Big)\Big] \tag{4.1}$$

In this equation Γ_l is the longitudinal confinement factor, α_i is the internal cavity loss and α_m the mirror losses. L is the cavity length assuming perfect mirrors and R_t and R_b are the reflectivities of the top and bottom mirror, respectively.

The electrical pumping induces a population inversion between the energy levels in the quantum wells to induce stimulated emission. Below threshold, there is already some spontaneous emission. Above threshold, all pumped carriers will contribute to the stimulated emission process. Therefore, the carrier concentrations will not change substantially above the threshold value. As a result the gain is clamped at the threshold value and the output power will rise drastically for higher pumping power. The quantum well materials of a GaAs VCSEL can be based on AlGaAs [43], or (strained) InGaAs [44], InAlGaAs [45] or InGaAsP [46].

The photon lifetime inside the cavity is described by equation 4.2. ν_g is the group velocity of the lasing mode inside the cavity. The photon lifetime, dependent on mirror losses, is an important parameter that influences the threshold and the damping rate of high-speed VCSELs and can be tuned for improving the bandwidth [47].

$$\frac{1}{\tau_p} = \nu_g\big[\alpha_i + \alpha_m\big] \tag{4.2}$$

4.2.1.1 DBR mirrors

VCSELs use either DBR or HCG mirrors, which can provide reflectivities above 99.5 %. They require extremely high-reflectivity mirrors due to the relatively short gain section of a VCSEL. DBR mirrors consist of multiple quarter wavelength thick layers (eq. 4.3), designed around the Bragg wavelength λ_B. The refractive index difference between a single pair is obtained by using high and low aluminum containing $Al_xGa_{1-x}As$ layers.

$$d_{high} = \frac{\lambda_B}{4\,n_{high}} \quad \text{and} \quad d_{low} = \frac{\lambda_B}{4\,n_{low}} \tag{4.3}$$

DBR-mirrors have a quasi-perfect reflection over a certain wavelength range. This wavelength range is called the DBR stop-band, and is centered around the Bragg wavelength (here 845 nm). For a GaAs VCSEL, the stop-band is approximately 100 nm wide and is defined by equation 4.4, with $n_{g,eff}$ being the spatially averaged group index inside the cavity and Δn the index contrast between the materials of the DBR layer pair [42]:

$$\Delta\lambda_{stop} = \frac{2}{\pi}\frac{\lambda_B\Delta n}{n_{g,eff}} \tag{4.4}$$

The reflectivity of the DBR mirror is described by equation 4.5, with n_0, n_1, n_2 and n_t being the refractive indices of the originating medium, the DBR layer pairs and the terminating medium. By increasing the number of layer pairs N, the reflectivity tends towards 100%. For the bottom-emitting VCSEL in this work, it is implied that the bottom DBR has a lower reflectivity than the top DBR, as the light is escaping the cavity downwards.The bottom DBR thus has 24 pairs, while the top DBR has 29 DBR pairs. The 29-pair top mirror is not a perfect reflector, still allowing a fraction of the light to escape from the top-side. In this manner, it is possible to characterize the devices on the GaAs substrate as well.

$$R_{DBR} = \left[\frac{\left(\frac{n_1}{n_2}\right)^{2N} - \left(\frac{n_1^2}{n_0 n_t}\right)}{\left(\frac{n_2}{n_1}\right)^{2N} + \left(\frac{n_1^2}{n_0 n_t}\right)}\right]^2 \tag{4.5}$$

4.2.1.2 Longitudinal mode control

In contrast to edge-emitting lasers, VCSELs have very short cavities. The former have a much longer cavity length compared to the resonant wavelength, leading to several different longitudinal modes that can achieve lasing. Longitudinal mode selection in a Fabry-Perot laser arises from overlap with the gain spectrum: whichever

mode reaches gain threshold first, will lase first. VCSELs, on the other hand, have a cavity length of approximately the same size as the resonant wavelength of the device. The resonance condition to achieve lasing, assuming perfect and abrupt DBR mirrors, relates the fact that the optical field after a single round trip has to match the original field as described in equation 4.6:

$$exp\left(-j\frac{2\pi}{\lambda_{res}/n_{eff}}2L\right) = 1 \tag{4.6}$$

Where L is the inner cavity length as defined in Fig. 4.8 and n$_{eff}$ is the effective index of the inner cavity. The length of the inner cavity can be extracted as follows:

$$L = \frac{m\lambda_{res}}{2n_{eff}} \quad \text{or} \quad \lambda_{res} = \frac{2Ln_{eff}}{m} \tag{4.7}$$

This implies that the shortest cavity can be half the resonant wavelength of the laser. Typical inner cavity lengths range from one half to one and a half times the resonance wavelength. The length can be tuned to increase the overlap of the standing wave pattern with the quantum wells inside the gain section. In reality, the cavity length is larger than just the spacing between the DBRs as the light penetrates into the DBR as well. Hence, an effective length of the DBRs have to be incorporated as well into the effective cavity length, as done in equation 4.8.

$$L_{eff} = L + L_{eff,DBR_t} + L_{eff,DBR_b} \tag{4.8}$$

With the effective cavity length, the resonance condition of equation 4.7 simply changes into the condition of equation .

$$exp\left(-j\frac{2\pi}{\lambda_{res}/n_{eff}}2L_{eff}\right) = 1 \tag{4.9}$$

Using the effective VCSEL length, the longitudinal mode spacing is approximated by equation 4.10 [42].

$$\Delta\lambda_m \approx \frac{\lambda^2}{2L_{eff}n_g} \tag{4.10}$$

Assuming an effective VCSEL length of approximately 1.3 µm, the resulting longitudinal mode spacing is then around 110 nm. Therefore, the next longitudinal mode falls outside of the gain spectrum and outside of the stop-band of the DBR. This confirms the longitudinal single-mode behavior of a VCSEL cavity.
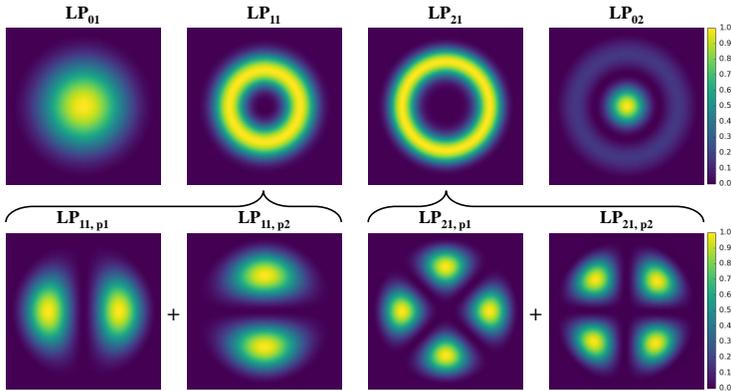
Figure 4.9: Most relevant transverse modes inside a circular VCSEL.

4.2.1.3   Transverse mode control

The multi-mode behavior of VCSELs is thus dictated by the transverse modes inside the cavity. Transverse modes are described by Bessel-functions, with Fig.4.9 giving an overview of the first four competing modes with the lowest threshold gain for radial symmetric confined VCSELs. At low current densities, the overlap with the carriers in the quantum wells is the greatest for the fundamental LP_{01} mode. As the current increases, the carrier density becomes more concentrated at the edges of the oxide aperture (because of spatial hole burning), where the overlap with the higher order radial LP_{11} and LP_{21} is larger. These 'doughnut' transverse-modes, LP_{11} & LP_{21}, are a superposition of two orthogonal polarization states, as shown on the bottom row of Fig.4.9. For radial-symmetric structures, both are equally present. With the introduction of a VCSEL-diffraction grating, it is expected that one of the orthogonal states will be more suppressed than the other [34].

The transverse mode shapes are described by Bessel functions and encompassed within the transverse confinement factor Γ_t [48]. For decreasing aperture diameter D_{ap}, there is a decrease of LP_{01} modal power, resulting in lower output powers of the fundamental mode for small apertures. At the same time, the effective difference in threshold gain with the higher-order transversal modes increases drastically and forces the device into single-mode operation.

The higher-order transverse modes lase at shorter wavelengths, and their wavelength spacing is inversely quadratic dependent on the aperture diameter. This implies that the transverse mode spacing between the different modes also increases for smaller apertures:
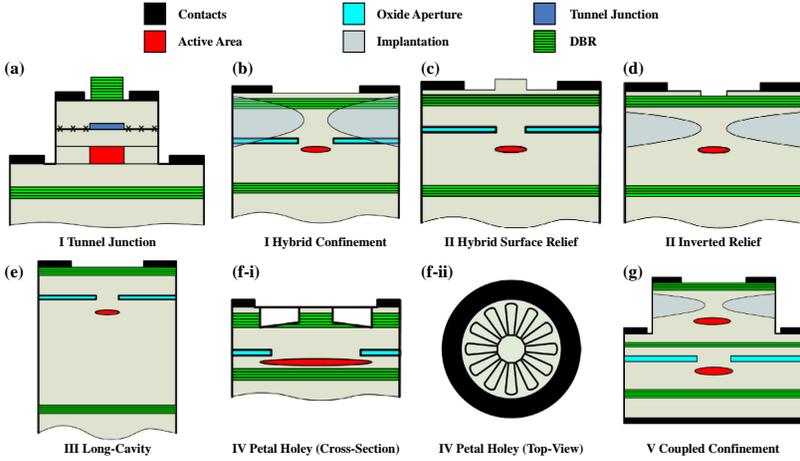
Figure 4.10: Schematic overview of the most relevant transverse polarization confinement methods: (a) tunnel junction, (b) oxide and implant confinement, (c) oxide and surface relief, (d) implant and inverted surface relief, (e) long-cavity VCSEL, (f) Petal-Holey structure on top DBR and (g) coupled-cavity VCSELs [50]

$$\Delta\lambda_{lp,l'p'} = \lambda_{lp} - \lambda_{l'p'}$$
$$\propto \frac{1}{D_{ap}^2} \quad (4.11)$$

There are several ways to suppress the higher order transverse modes and improve the modal gain of the fundamental mode. The five main categories, each with multiple implementations, are: (1) increase modal gain of the fundamental LP$_{01}$ mode, (2) increase mirror losses away from the optical axis of the VCSEL by removing DBR pairs in a surface relief or inverted relief manner [49], (3) increase diffraction losses by having longer cavities, (4) increase scattering losses by etching a holey structure on the top surface and (5) inject multiple currents in coupled-cavity VCSELs, leading to complex dynamic behavior that suppresses higher-order transverse modes. A few methods are shown in Fig.4.10, reproduced from [50].

4.2.1.4 Thermal characteristics

The resonance wavelength is determined by the cavity length, as illustrated in equation 4.7. As a consequence, the temperature-dependent behavior of the resonance wavelength is dictated by the temperature dependent behavior of the effective cavity index. This dependence is about 0.065 nm wavelength shift per Kelvin temperature change for GaAs lasers [51], which is five times less than the temperature-dependent
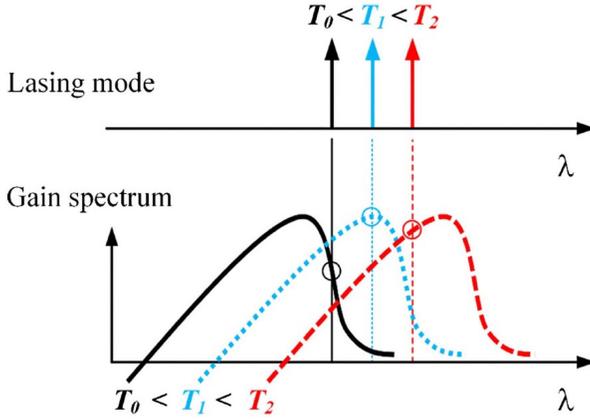
Figure 4.11: Detuning of λ_{res} and the gain spectrum [6].

shift of the gain spectrum. Consequently, the resonance wavelength will detune with respect to the gain spectrum under changing temperature conditions, as illustrated in Fig.4.11.

The actual temperature inside the cavity is dictated by the differential equation 4.12. Here, T_0 is the environmental temperature and the dissipated power ,P_{diss}, is defined by the input electrical power minus the optical power generated by the laser. The cavity temperature is time-dependent, with the dynamics determined by the thermal time constant τ_{th} in equation 4.12. The thermal time constant consist of the thermal resistance R_{th} and the thermal capacitance C_{th} of the cavity.

$$T = T_0 + P_{diss}R_{th} - \tau_{th}\frac{dT}{dt} \tag{4.12}$$

$$\text{with} \quad P_{diss} = P_{elec} - P_{opt} \quad \text{and} \quad \tau_{th} = R_{th}C_{th} \tag{4.13}$$

The definition of the thermal resistance is shown in equation 4.14 and derived from the steady-state of equation 4.12. The previously described temperature dependent behavior of the effective cavity index is here referred to as C_2, while C_1 can be deduced from tracking the LP_{01} wavelength shift for different injected bias currents. The thermal resistance is used to compare the thermal performance of the laser prior and after printing onto different substrates, with different thermal resistances.

$$R_{th} = \frac{\Delta T}{\Delta P_{diss}} = \frac{\Delta\lambda/\Delta P_{diss}}{\Delta\lambda/\Delta T} = \frac{C_1}{C_2} \qquad [K/mW] \tag{4.14}$$

4.2.2   VCSEL diffraction grating

The VCSEL diffraction grating used in this work couples the light from the vertical VCSEL cavity into the in-plane SiN$_x$ waveguides. The proposed approach uses a vertical-to-horizontal symmetric diffraction. The incoming light has no x-component of the k-vector, meaning that the coupling has to be symmetric for conservation of momentum. This is described in the k-vector diagram in Fig.4.12-(a), and visually by the FDTD cross-section simulation of Fig.4.12-(b). For the described case, the grating diffraction vector K of equation 4.15 matches the propagation constant of the waveguide guided mode β of equation 4.16.

$$K = \frac{2\pi}{\Lambda} \tag{4.15}$$

$$\beta = \frac{2\pi}{\lambda} n_{eff} \tag{4.16}$$

As a consequence of this condition, the grating period Λ, is described by equation 4.17. With the wavelength close to 850 nm, the effective index of the guided close to 1.60 RIU, the grating period is suspected to be close to 530 nm. A full FDTD sweep is done of the grating parameters, to find the most optimal configuration for maximum waveguide coupling. The results are described in the next paragraphs.

$$\Lambda \sim \frac{\lambda}{n_{eff}} \tag{4.17}$$
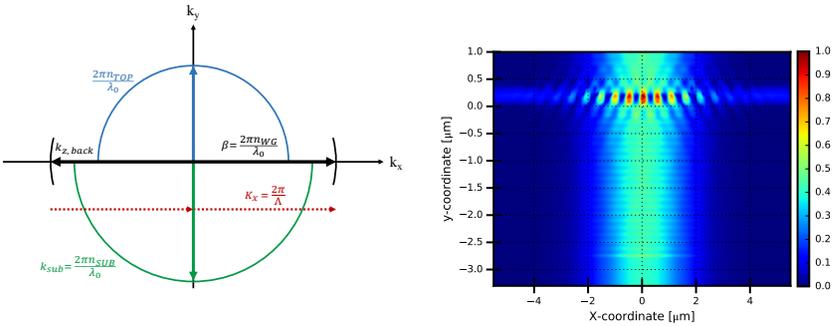
Figure 4.12: (a) Vector diagram of a vertical-coupling diffraction grating and (b) FDTD simulations of the field intensity at the diffraction grating.
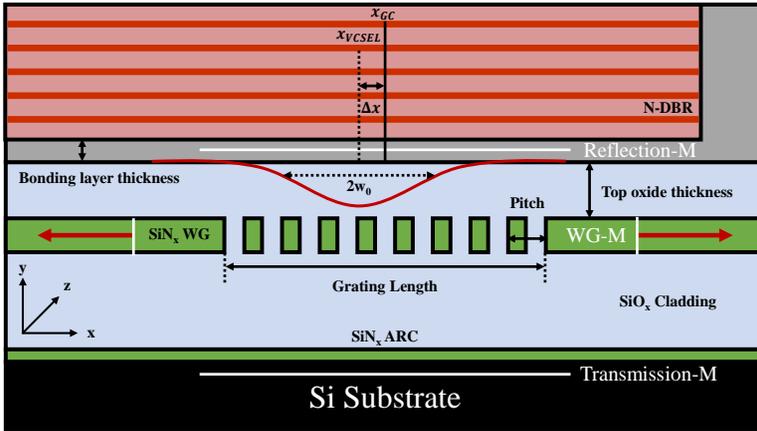
Figure 4.13: FDTD model of the diffraction grating, with the relevant parameters used in the simulations, such as beam width w_0, grating length L_{GC}, the TOX thickness, grating pitch & FF and the VCSEL-to-grating misalignment Δx.

Fig.4.12-(b) shows the FDTD-based simulation of a downward emitting gaussian-beam onto the diffraction grating. The field intensity is highest at the center teeth of the diffraction grating. Due to the medium-index contrast grating, a large fraction of the light passes through the grating into the substrate. The biopix 300 nm platform has an anti-reflective coating between the buried oxide and the silicon substrate. This means that most of the light is not reflected back towards the diffraction grating. As a consequence, the resonant characteristics between the substrate and the waveguide layer are greatly diminished.

Fig.4.13 shows a model schematic used in Lumerical FDTD Solutions. In first instance, only the diffraction grating parameters are analyzed to find the polarization-pitch-fill factor combination that has both a high reflection a large coupling efficiency. The light is emitted from the bottom side of the VCSEL. The bottom DBR mirror is omitted to speed up the simulations. FDTD-monitors placed at the backside of the source, inside the substrate and at the SiN_x waveguides. These collect the reflection of the grating, the 'lost' transmission into the substrate and deduce the waveguide-coupling efficiency, respectively.

Other important parameters are the grating width, grating length L_{GC}, and the misalignment between the VCSEL and the center of the grating Δx_{VCSEL}. The transfer-printing process may introduce a misalignment. This misalignment can lead to an imbalance between the waveguide-coupled output powers of the left and right waveguide.
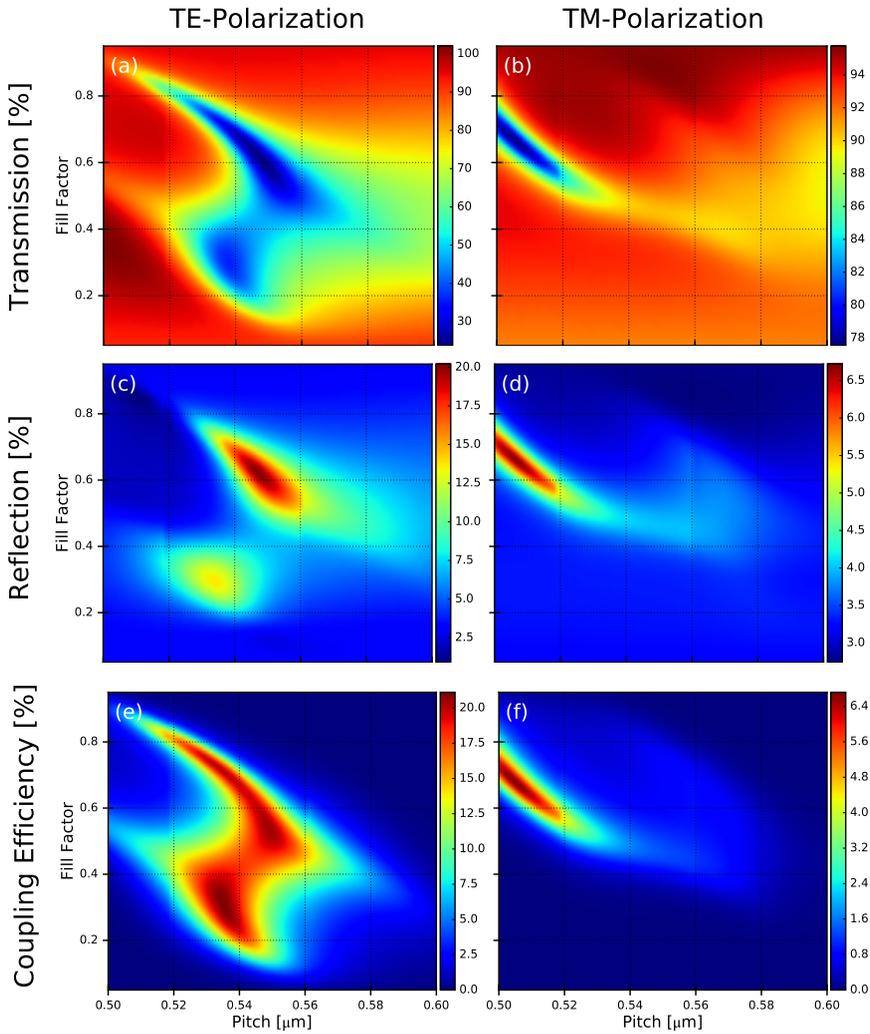
Figure 4.14: FDTD simulations on pitch-FF combinations for TE and TM polarized Gaussian sources: (a & b) transmission into the Si substrate, (c & d) upward grating reflection and (e & f) single-side waveguide coupling efficiency. The simulations were performed for a 1/e^2 power diameter of 5 µm.

The results of a 2D sweep for pitch and fill-factor of the grating are shown in Fig.4.14, for both TE and TM polarized light sources. The top row illustrates the transmission of the gaussian beam through the grating, and collected in the substrate monitor. The regions in red have the highest transmission and are of least interest for waveguide-coupling. The middle row show the reflection of the grating towards the VCSEL. Comparing figures (c) and (d), it is clear that the regions of high reflection differ between TE and TM polarized light incident on the grating. This is an important feature, as with the right grating design, allows for an increased feedback of the TE-polarization in the VCSEL III-V cavity. This will in turn lead to a feedback induced polarization pinning of the laser. Lastly, the bottom row shows the single-side coupling efficiency to the waveguide. As the grating is designed for coupling TE-polarized light into the waveguide, it is clear that the values in (e) are substantially larger than in (f). To summarize, with a grating design around 550 nm pitch and 60 % fill factor, the reflection of the TE-polarization is larger than for the TM-polarization at a difference of about 15 %. This helps to stabilize the VCSEL output polarization and match it to the TE-designed diffraction grating. The values of the transmission, reflection and coupling shown in the figure, are the averaged integrated values between 840 nm to 850 nm, and are defined as follows:

$$R_{avg} = \frac{\int_{840nm}^{850nm} R(\lambda)\, d\lambda}{\int_{840nm}^{850nm} d\lambda}$$

$$T_{avg} = \frac{\int_{840nm}^{850nm} T(\lambda)\, d\lambda}{\int_{840nm}^{850nm} d\lambda} \tag{4.18}$$

$$CE_{ss,avg} = \frac{\int_{840nm}^{850nm} CE_{ss}(\lambda)\, d\lambda}{\int_{840nm}^{850nm} d\lambda}$$

The second FDTD simulation studies the resonance effect inside the top oxide between the grating and the bottom DBR of the VCSEL. The beam is launched inside the VCSEL cavity and the substrate transmission and waveguide-coupling efficiencies are normalized to T_{PIC}, defined in equation 4.19. R_{DBR}, the reflection of the DBR, is also measured with the reflection-monitor placed inside the cavity, above the source.

$$T_{PIC} = 1 - R_{DBR} \tag{4.19}$$

The results of the second set of simulations are shown in Fig.4.15 for a pitch of 549 nm, a fill factor of 65% and $1/e^2$ power diameter of 5 μm. The difference in reflection of the two polarization states was $\sim 15\%$ in favor of the TE mode,

collected just above the grating. This difference diminishes throughout the DBR grating, and depends on the thickness of the top oxide. The difference varies from 0.25% higher reflection for the TM mode to 0.50% higher reflection for the TE mode, as can be seen in Fig.4.15-(a). The range of the top oxide thickness simulation is limited by evanescent losses. For t$_{TOP}$ under 600 nm, the waveguide-coupled power will be absorbed again by the III-V layers of the laser. The coupling efficiency shown in Fig.4.15-(b) follows the same periodic trend of about 300 nm. The maximum single-side coupling efficiencies at 845 nm varies by a factor two, from just below 15% at 600 or 900 nm thickness to 7.5% at around 750 nm.

Fig.4.16 analyses the influence that the transfer-printing associated misalignment, Δx in Fig.4.13, has on the waveguide coupling efficiency. Fig.4.16-(a & b) show the normalized single-side coupling for the left and right waveguide. Highlighted in red is the parameter space for which the coupling loss is less than -3 dB. The figures show that if the grating is too long, it requires that the VCSEL is offset with respect to the grating, in order to achieve the best coupling performance. Both waveguide results are combined in Fig.4.16-(d-e-f), for a 1/e^2 power diameter of 3-5-7 μm. The combined efficiency is normalized versus twice the maximum coupling efficiency for the single-side coupling efficiency of Fig.4.16-(a or b), as shown in equation 4.20:

$$CE_{comb} = \frac{CE_{left} + CE_{right}}{2 \cdot CE_{single}} \tag{4.20}$$

The simulations show that the combined waveguide-coupled power reaches a maximum at a grating length of 6-7-8 μm, for aperture sizes 3-5-7 μm. The larger apertures show a larger misalignment tolerance, expressed as the parameter space (red) for which at least 50 % of the light is coupled into the waveguide. At the same time, the larger apertures also achieve higher combined (left & right) efficiencies of 88% for the 7 μm aperture versus the 75% for the 3 μm aperture.

Fig.4.16-(c) shows the imbalance (IMB) between the left and right waveguide ports, defined in equation 4.21.

$$IMB = \big|P_{left} - P_{right}\big|[dB] \tag{4.21}$$

A diffraction grating is inherently alignment sensitive, enhanced by the relatively small mode sizes at 850 nm. Highlighted in red is the boundary condition for which the imbalance between the waveguides remains smaller than a 3 dB difference. It can be seen that the zone described by this boundary condition extends from the central axis, and allows for more than 1 μm of misalignment of the VCSEL from the center of the diffraction grating.
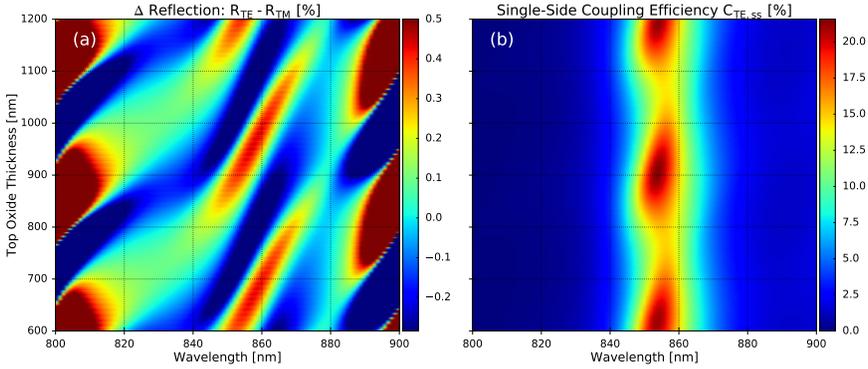
Figure 4.15: FDTD simulation results on the influence of the top oxide thickness on the (a) the reflection difference between both polarization states inside the VCSEL cavity and (b) the influence on the single-side TE-coupling efficiency into the waveguide.
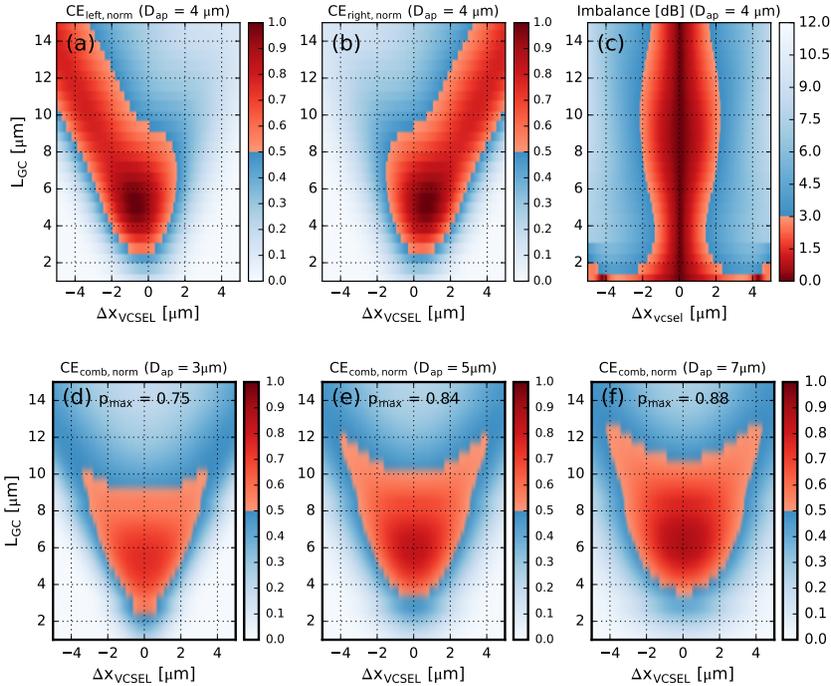
Figure 4.16: FDTD simulations of the µTP-misalignment sensitivity. (a & b) show the single-side misalignment sensitivity; (c) the left-vs.-right WG imbalance as a function of VCSEL misalignment. (d, e & f) show misalignment sensitivity of the combined left-right double-side waveguide coupling, normalized to $2 \cdot p_{single}$. The blue color illustrates L_{GC}-misalignment configurations leading to a coupling loss larger than -3 dB in (a/b/d/e/f) and to an imbalance larger than 3 dB in (c).
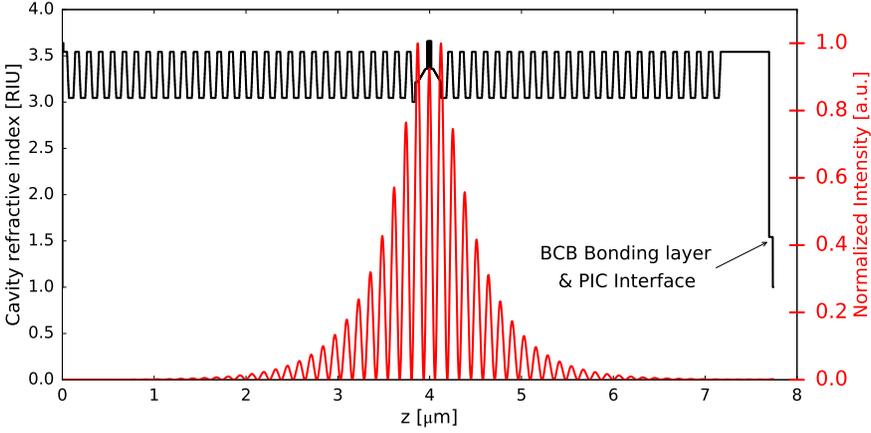
Figure 4.17: 1D TMM Model of the refractive index alongside the propagation axis in black and the optical field amplitude distribution in red.

4.2.3 Transfer matrix model of the extended cavity

The design of a VCSEL is done with a custom 1D transfer-matrix model (TMM) [42], developed by Johan Gustavsson at Chalmers University of Technology. Like other transfer-matrix models, plane wave propagation determines the intensity and phase of the waves transmitted and reflected through the layers and interfaces. A generalized, 2 layer model is given in equation 4.22. The transition is described between medium 1 and 2, for both forward (f) and backward (b) propagating waves, with the interaction summarized in the transfer matrix T.

$$\begin{pmatrix} E_{1,f} \\ E_{1,b} \end{pmatrix} = \begin{pmatrix} T_{1,1} & T_{1,2} \\ T_{2,1} & T_{2,2} \end{pmatrix} \begin{pmatrix} E_{2,f} \\ E_{2,b} \end{pmatrix} = T \begin{pmatrix} E_{2,f} \\ E_{2,b} \end{pmatrix} \tag{4.22}$$

The TMM is particularly suited for multi-layer stacks. In that case, the transfer matrix T represent the entire layerstack, as described by equation 4.23.

$$T_{stack} = T_1 \cdot T_2 ... T_i ... T_{N-1} \cdot T_N \tag{4.23}$$

The multi-layer interaction is described as the multiplication of the transfer-matrix for each interface and medium. The definitions of the interface and medium matrices are given in equations 4.24 and 4.25, where L is the layer thickness, β the propagation constant of the light in that medium. $r_{x,y}$ and $t_{x,y}$ are the respective reflection and transmission coefficients at the interface

$$T_{interface} = \frac{1}{t_{1,2}} \begin{pmatrix} 1 & r_{1,2} \\ r_{1,2} & 1 \end{pmatrix} \quad \text{and} \quad T_{medium} = \begin{pmatrix} e^{-j\beta L} & 0 \\ 0 & e^{j\beta L} \end{pmatrix} \quad (4.24)$$

$$r_{1,2} = \frac{n_1 - n_2}{n_1 + n_2} \quad \text{and} \quad t_{1,2} = \frac{2n_1}{n_1 + n_2} \quad (4.25)$$

The final layer of the multilayer TMM model is an equivalent grating layer, which encaptures the phase and reflection of the system described in Fig.4.13. The reflection of the grating layer is calculated based on the overlap integrals of coupled-mode theory [52–54]. Equations 4.26 and 4.27 describe the reflection values for TE and TM polarized light with respect to the grating orientation for a 2D FDTD simulation environment. The numerator details the overlap between the reflected, or diffracted, beam with the originally Gaussian shaped beam launched from the III-V cavity. The denominator normalizes the power with respect to the incident light beam in order to retrieve the reflection coefficient of the light coupling back into the III-V cavity.

$$R_{TE} = \frac{\left| \int \left(E_{diffr,z}(x) e^{j\phi_{diffr,z}(x)} \right) \cdot e^{-\frac{x^2}{\pi w_0^2}} dx \right|^2}{\int |E_{VCSEL}|^2 dx} \quad (4.26)$$

$$R_{TM} = \frac{\left| \int \left(E_{diffr,x}(x) e^{j\phi_{diffr,x}(x)} \right) \cdot e^{-\frac{x^2}{\pi w_0^2}} dx \right|^2}{\int |E_{VCSEL}|^2 dx} \quad (4.27)$$

Here, w_0 is the beam width of the Gaussian beam launched from the VCSEL, corresponding to a specific VCSEL aperture. Both the beam width and the associated divergence angle are calculated based on a cold-cavity vectorial eigenmodes model of a VCSEL. The respective values can be found in table **??**. The majority of the FDTD simulations are performed for the 5 μm aperture VCSEL.

The phase $\phi_{diffr}(x)$ and field amplitude are registered with the reflection monitor, placed just above the launched beam. The net phase Φ_{diffr} is a function of x and plugged into the mode overlap integral equations 4.26, 4.27. However, as the transfer matrix model of the VCSEL cavity is one dimensinsal, the phase as function of x has to be summarized into a single value. Hence, a parabolic fit is made of the local phasefront, $\phi_{diffr}(x)$, between the beam waist radius

oxide aperture [µm]	Spot size at oxide aperture [µm]	Divergence Angle [°]
3	3.35	12.7
4	4.70	9.0
5	6.14	6.9

Table 4.1: Beam properties of the bottom emitting VCSEL incident onto the diffraction grating. The estimated divergence angle is the full beam angle.

from $-0.5w_0$ to $+0.5w_0$. The 0D value of the phasefront is then the value of the parabolic fit at the center of the beam ($x == 0$):

$$\Phi_{TMM} = \phi_{parabolic-fit}(0) \tag{4.28}$$

The net phase of the diffracted wave, Φ_{diffr}, is used as input in the TMM model and is sensitive to the type of grating. For the low index contrast grating, there is only a minimal refractive index variation along the principal axis of the grating. Therefore, the reflected part of the diffracted wave approximates a plane wave, with a rather uniform response in phase across the x-axis [34]. In contrast, a high index contrast grating has strong variation in the refractive index along the principal axis of the grating. This translates into a strongly diffracted wave close to the grating teeth. With the local field fluctuations, there is an associated variation of the phase along the x-direction. The averaged phase can be obtained from fitting a parabolic function between the $\pm w_0$ of the phase of the diffracted field. For a medium-index-contrast diffraction grating, this approach is required for small values of the TOX. For values exceeding 750 nm, the phase of the diffracted field is settling, as is expected in the far field response.
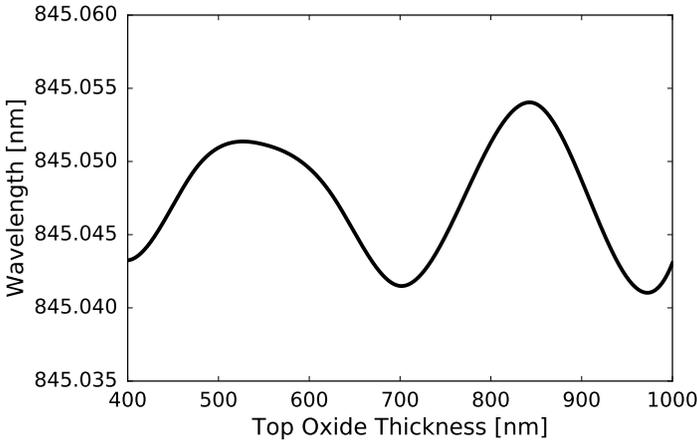
Figure 4.18: VCSEL wavelength stability for varying top oxide thickness.

These values of the reflectivity and phase are simulated for different values of the TOX, between 400 nm and 1000 nm, and for VCSEL-to-grating misalignment of up to ±1.5µm. For this R&D project, the top oxide thickness was determined with an etch back from the standard top oxide thickness value of 2.2 µm. Higher control can be implemented using CMP processing after the development is complete. Table 4.2 shows a few key VCSEL properties of the devices on the GaAs source substrate, on a Sapphire target substrate and on a PIC target substrate. For the latter, the simulated configuration has a TOX thickness of 750 nm, and without any misalignment. The swept parameters are studied further in the next paragraphs. Figure 4.18 shows that with the chosen approach, the VCSEL emission wavelength remains largely constant, with a difference less than 0.02 nm across the entire parameter range.

The feedback of the VCSEL diffraction grating is polarization sensitive, as described by equations 4.26 & 4.27. Figure 4.19 shows the material gain threshold values of both the TE and TM polarization of the VCSEL cavity. It is clear that the medium index contrast grating has a significant influence on the threshold gain of the cavity as intended by our design. This effect can be advantageous, with the capability of the diffraction grating to pin the polarization of the VCSEL cavity to the preferred orientation matching the diffraction grating. It is clear that the threshold gain difference between both polarizations is largest in between 750 nm and 800 nm of top oxide thickness above the grating coupler. The measurement range is therefore focused on these ranges. For TOX-values lower than 600 nm, the light that is coupled into the waveguide starts leaking back into the III-V layer, thus reducing the net coupled power into the waveguide.
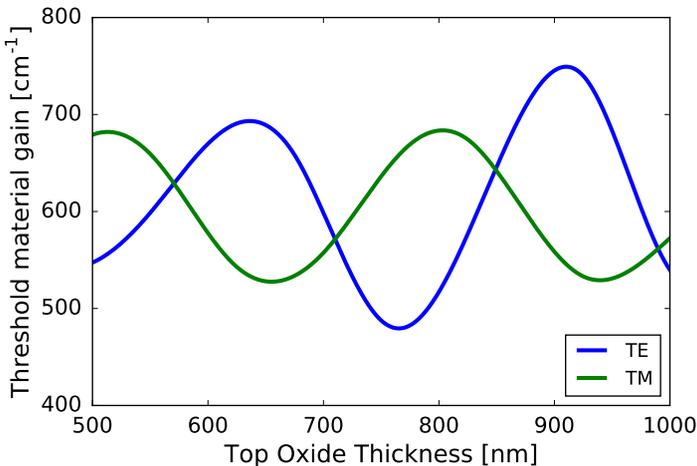
Figure 4.19: Material threshold material gain difference between the TE and TM polarization states of the fundamental mode.
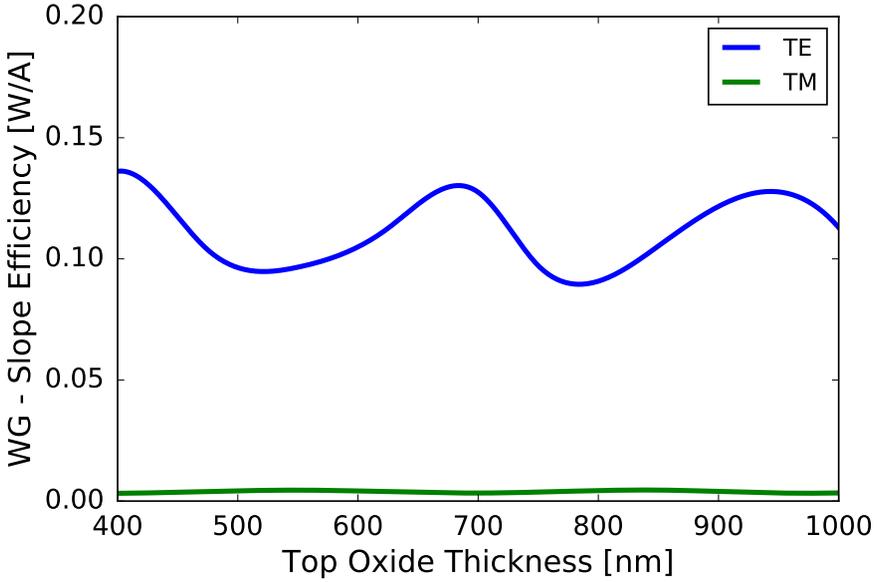
Figure 4.20: The WG-coupled slope efficiency is plotted against the TOX variation, for both the TE and the TM polarization. The notable difference originates from the preferential coupling efficiency of the diffraction grating for the TE-polarization.

Properties	Source-GaAs	Target-Sapphire	Target-PIC (TE)	Target-PIC (TM)
λ_{res} [nm]	845.061	845.060	845.045	845.051
Q_{cavity} [-]	8311.54	12901.06	15762.85	12320.24
g_{th} [1/cm]	934.33	600.96	491.89	629.43
Photon lifetime [ps]	3.729	5.79	7.071	5.527
SE - TOP [W/A]	0.039	-	0.071	0.055
SE - BOT [W/A]	-	0.450	-	-
SE - WG [W/A]	-	-	0.094	0.004

Table 4.2: Simulated VCSEL properties for different terminating substrates, with a top oxide thickness of 750 nm for the PIC target substrate.

Figure 4.20 shows the simulated waveguide-coupled slope efficiency of the VCSELs that are transfer-printed onto the waveguide diffraction grating. The WG-coupled SE comprises of the bottom slope efficiency of the VCSEL with the coupling efficiency of the diffraction grating. As the diffraction grating is designed for preferential coupling of the TE polarization, the TM waveguide-coupled TM SE is low in comparison.

The misalignment introduced by the transfer-printing process is investigated in Figure 4.21 and Figure 4.22, for a diffraction grating of 7 μm length. The typical misalignment associated to the micro-transfer-printing process is ± 1 μm, 3σ. The threshold material gain of the TM mode is independent of the misalignment, as the
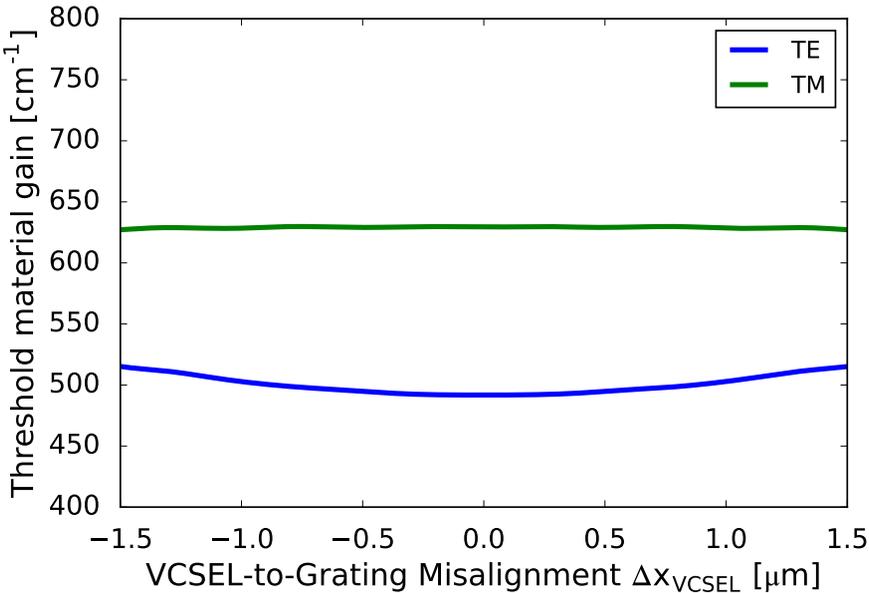
Figure 4.21: Material threshold gain of the TE and TM polarizations versus the possible VCSEL-to-Grating misalignment associated with the transfer-printing process. The simulated values are for a case of a top oxide thickness of 750 nm.

TM mode is not exciting a waveguide mode. In contrast, the TE mode is exciting a waveguide mode and is thus sensitive to the waveguide-coupled misalignment, similar as described in Fig.4.16. However, Figure 4.21 shows that the threshold material gain of the TE polarization is always lower than the threshold material gain of the TM polarization over the relevant misalignment range. The TE polarization thus remains the preferred lasing state of the VCSEL. The simulated values shown in Figure 4.21 are for a top oxide thickness value of 750 nm. It is thus a requirement that the TOX value is engineered appropriately to have a stable laser configuration.

As mentioned previously, the WG-coupled slope efficiency comprises both the III-V design as the coupling efficiency of the diffraction grating. As a result, the sensitivity to misalignment is also dependent on these two contributions. As the threshold material gain is fairly stable, the dominant contribution arises from the misalignment sensitivity of the coupling efficiency of the diffraction grating. The single-side waveguide-coupled slope efficiencies follow the trend set by the previously discussed FDTD simulations given in Figure 4.16-(a) & (b). Combining both channels of the bi-directional grating coupler results in a double-side slope efficiency, which can go up to 0.18 W/A. Both the single-sided and double-sided WG-coupled SE are plotted with respect to the misalignment in Figure 4.22.
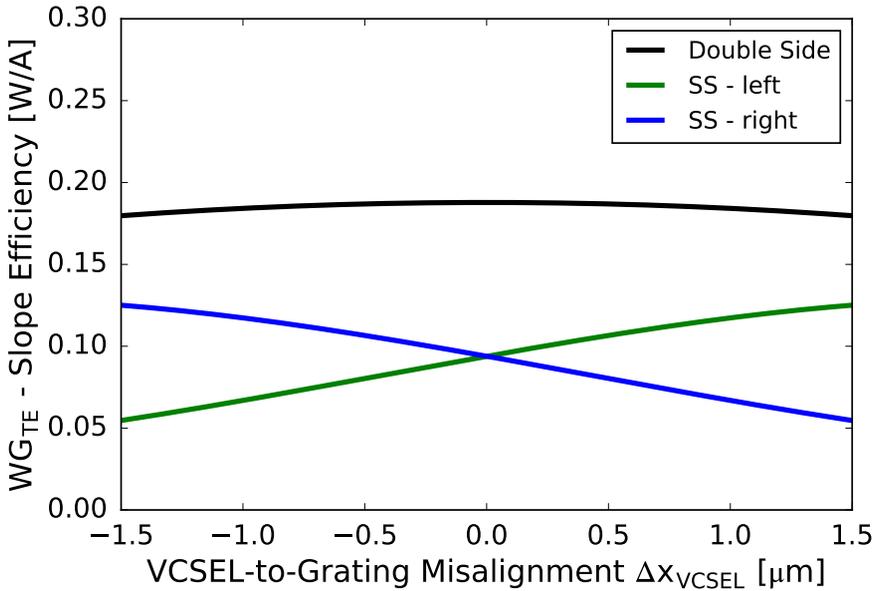
Figure 4.22: Waveguide-coupled slope efficiency versus the possible VCSEL-to-Grating misalignment associated with the transfer-printing process.

In conclusion, an extended cavity VCSEL has been designed through the use of FDTD and TMM simulation software. The FDTD simulation software allows to design a diffraction grating coupler that preferentially couples in the TE polarized light into the waveguide, while also having a larger reflection for of the TE polarization. The phase and reflection of the incident Gaussian-like beam onto the diffraction grating is captured in the FDTD model and fed into the TMM model. By doing so, we optimize the top oxide thickness for maximum performance, meaning maximum waveguide-coupled slope efficiency of up to 0.18 W/A and threshold gain difference of more than 100 $cm-1$. Lastly, the misalignment sensitivity of the VCSEL-on-Grating configuration is analyzed and found to be stable within the typical transfer-printing range of ±1µm.

4.3 Fabrication

In this section all fabrication related topics are discussed. First, a brief summary is given on the main considerations in the design of the epitaxial layer structure. Afterwards, the device design and the process flow of the devices on the source substrate are laid out. A demonstration is shown of the transfer-printing process of the VCSELs and of the final results of VCSELs on photonic integrated target substrates. The last part covers the main hurdles encountered in optimizing the overall yield of the entire fabrication and transfer-printing process.

4.3.1 Epitaxial layerstack

The epitaxial layer design for the bottom-emitting VCSEL can be found in table 4.3. The wafers were ordered from Jenoptik, in Jena, Germany [55]. The main features and design follow from the simulations described in the previous section. Due to set out specifications (transfer-printing & bottom-emitting devices), additional criteria were taken into consideration for the epitaxial layer design.

Firstly, the goal was to maintain top-emitting characterization capabilities of standard VCSELs. In this case the top-mirror DBR was limited to 29 DBR pairs to allow for a small fraction of the light to leak out when utilizing a p-ring top contact. With these test structures, the laser properties (lasing threshold, differential resistance, slope efficiency, thermal resistance, tuning range, SMSR) can already be characterized on the GaAs wafer before the transfer-printing process.

Secondly, the required transfer-printing layers (no. 1-4) are included. The buffer layer (no. 4) acts as an intermediary between the standard ICP-dry etch processing and the next wet-etch step to underetch the devices. At a thickness of 528 nm, there is sufficient height to stop the dry etch on target and allow for surface preparation and subsequent wet etching of the buffer layer. Following the advice of the foundry, InGaP was chosen as a release layer over InAlP due easier and better growth quality of InGaP over InAlP. In between the buffer layer and the release layer, there is another thin GaAs etch stop layer (no. 3). The layer is placed outside the VCSEL III-V cavity, and absorbs only a fraction of the light with a thickness of 4 nm. The etch stop layer provide a near 100 % etch selectivity over InGaP when using a HCl-based etchant.

The N-type dopant levels are lower than the P-type dopant levels. Silicon (Si) is used as the default dopant for n-type GaAs. At dopant levels exceeding 5E+18, Si-pairs and Si-clusters are formed that lower the crystal quality [56]. In order to obtain Ohmic contacts, an annealing step of the n-metal is required.

No.	Type	Material	Repeat	Mole F-start(x)	Mole F-Finish(x)	PL[nm]	Thickness [nm]	Doping
30	P-Contact	GaAs					10.0	1E+20 - C (P)
29	P-Contact	$Al_xGa_{1-x}As$		0.12			39.8	5E+19 - C (P)
28	P-Contact	$Al_xGa_{1-x}As$		0.90	0.12		20.0	6E+18 - C (P)
27	DBR	$Al_xGa_{1-x}As$	27	0.90			48.6	3E+18 - C (P)
26	DBR	$Al_xGa_{1-x}As$	27	0.12	0.90		20.0	4E+18 - C (P)
25	DBR	$Al_xGa_{1-x}As$	27	0.12			40.4	3E+18 - C (P)
24	DBR	$Al_xGa_{1-x}As$	27	0.90	0.12		20.0	6E+18 - C (P)
23	DBR	$Al_xGa_{1-x}As$	2	0.90			48.6	2E+18 - C (P)
22	DBR	$Al_xGa_{1-x}As$	2	0.12	0.90		20.0	2E+18 - C (P)
21	DBR	$Al_xGa_{1-x}As$	2	0.12			40.4	2E+18 - C (P)
20	DBR	$Al_xGa_{1-x}As$	2	0.90	0.12		20.0	2E+18 - C (P)
19	Aperture	$Al_xGa_{1-x}As$		0.98			30.0	2E+18 - C (P)
18	GRINSCH	$Al_xGa_{1-x}As$		0.60			26.4	2E+18 - C (P)
17	GRINSCH	$Al_xGa_{1-x}As$		0.37	0.60		85.0	
16	MQW	$Al_xGa_{1-x}As$		0.37			20.0	
15	Gain	$In_xGa_{1-x}As$	4	0.10		835	4.0	
14	MQW	$Al_xGa_{1-x}As$	4	0.37			6.0	
13	Gain	$In_xGa_{1-x}As$		0.10		835	4.0	
12	MQW	$Al_xGa_{1-x}As$		0.37			20.0	
11	GRINSCH	$Al_xGa_{1-x}As$		0.60	0.37		85	
10	DBR	$Al_xGa_{1-x}As$		0.90			58.9	3E+18 - Si (N)
9	DBR	$Al_xGa_{1-x}As$		0.12	0.90		20.0	3E+18 - Si (N)
8	DBR	$Al_xGa_{1-x}As$	23	0.12			40.4	3E+18 - Si (N)
7	DBR	$Al_xGa_{1-x}As$	23	0.90	0.12		20.0	3E+18 - Si (N)
6	DBR	$Al_xGa_{1-x}As$	23	0.90			48.6	3E+18 - Si (N)
5	DBR	$Al_xGa_{1-x}As$	23	0.12	0.90		20	3E+18 - Si (N)
4	Buffer	$Al_xGa_{1-x}As$		0.12			526.8	3E+18 - Si (N)
3	Etch Stop	GaAs					4	
2	Release	$In_xGa_{1-x}P$		0.49			500	
1	Buffer	GaAs					500	
0	Substrate	GaAs						

Table 4.3: III-V epitaxial layerstack of a GaAs bottom-emitting VCSEL.

4.3.2   Mask Design

One of the advantages of transfer-printing, besides the high-throughput wafer-scale compatibility, is the ability to handle components at a smaller scale than what is achievable with flip-chipping tools. As a result, the transfer-printing method makes more efficient use of the costly III-V epitaxial materials. There are two major contact mask designs for the TP-VCSEL in this work. Gen1 designs have an equal x- & y- pitch of 150 μm. For the Gen2 design the y-pitch can be reduced to 100 μm, shown in Fig.4.23-(Top). Future modifications can be made to reduce the footprint to 100 μm by 85 μm. Looking at commercially available VCSELs for flip-chipping, typical dimensions of single-packaged and arrayed devices are 250 μm by 250 μm pitch [57]. In comparison to these values, transfer-printing offers a 7.3x reduction in footprint per device over flip-chipping.

Wafer-bonded devices have an additional footprint cost. The usable x- & y-pitch are namely determined by the pitch of the photonic circuit. The VCSEL diffraction grating requires a taper length of 250 μm, which translates into an approximate 600 μm x-pitch for two adjacent structures. The y-pitch can be lower at 250 μm. A different architecture of the photonic circuit can gain some of the lost area. However, the total footprint will always remain larger than the dense configuration on the GaAs source substrate. With these numbers, the transfer-printing method has a 17.5x size reduction compared to the wafer-bonding technique.
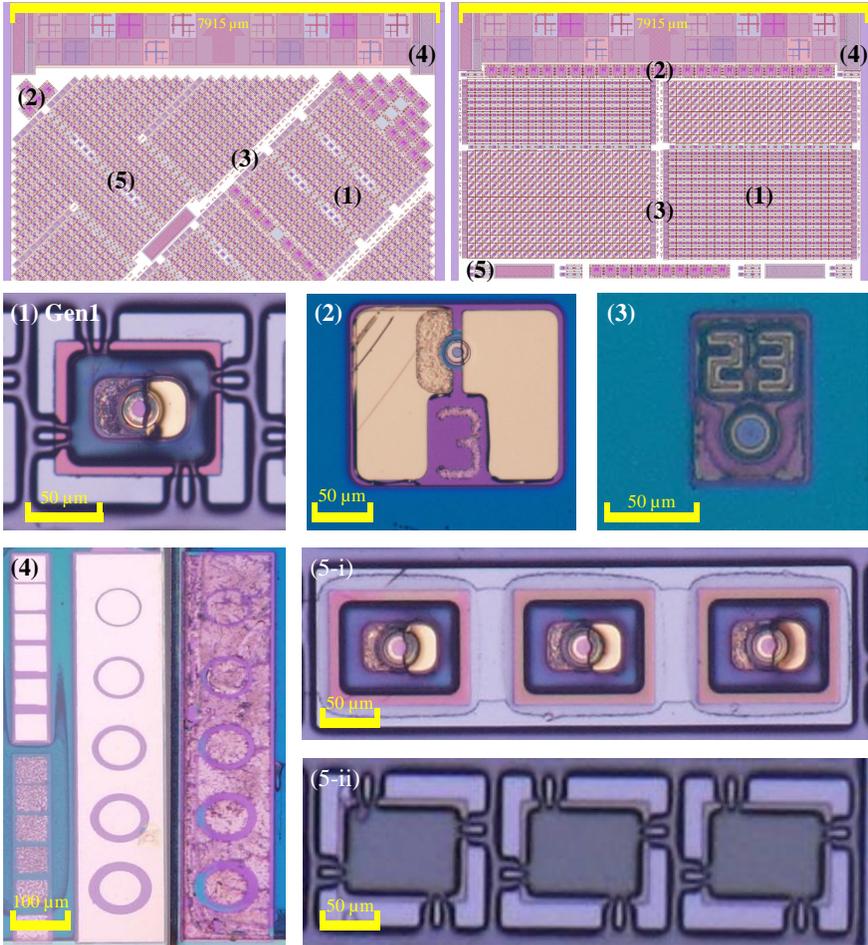
Figure 4.23: The top row illustrates the device distribution between Gen1 and Gen2 devices on the source substrate. The middle row shows microscope images of the TP-VCSEL coupon, the larger on-source test structure and the oxide aperture reference structure. The bottom rows shows microscope images of additional test structures used, such as P- & N-contact TLM test structures, un-tethered devices and dummy encapsulations.

4.3.3　Source

The main processing steps of the fabrication of the TP-VCSEL on the source substrate are illustrated in Fig 4.24. Steps (a) to (i) are done at Chalmers University of Technology, and the latter ones at Ghent University-imec. After transfer-printing, the process is similar to that described in section 1.3.2. The discussion is restricted mostly to the configuration of the Gen2 devices.

P-type Contact Metallization
The surface is cleaned and a lithography step is used to define the p-contact. Ti/Pt/Au (20nm/50nm/100nm) is deposited with electron beam evaporation (Fig. 4.24-(b)). The sample is annealed after the n-contact deposition, to make the contacts Ohmic. For the test devices on the source-substrate, a ring-type contact is used through which the laser can still emit from the top. For the TP-devices, a circular disk is chosen that acts as a mirror on top of the P-DBR in Gen2 devices.

P-DBR Mesa Definition
First, a SiN$_x$ hard mask is sputtered. A positive lithography step is used to define the circular mesa with respect to the P-contact markers. Five aperture sizes (3,4,5,6,7 μm) are defined, using mesa diameters of 23,24,25,26,27 μm. The P-type DBR is etched with a ICP-RIE, based on a mixture of SiCl$_4$ and Ar. A top-down laser interferometer controls the etch depth in order to stop inside the n-type DBR layer (no. 8), as illustrated in Fig. 4.24-(c).

Aperture Formation
Another SiN$_x$ passivation layer of $\sim$ 100 nm is deposited to protect the exposed AlGaAs from oxidation. A positive lithography step is used to open up the passivation layer on the sidewalls of the p-DBR mesa with an NF$_3$ plasma etch, exposing the high-aluminum fraction layers. The oxide aperture is then formed by selective wet oxidation of the Al$_{0.98}$Ga$_{0.02}$As-layer in water vapour at elevated temperature [58]. An oxidation rate of $\sim$ 0.20 μm/min at 420°C is expected for Al$_{0.98}$Ga$_{0.02}$As [59].

N-type Contact Metallization
The SiN$_x$ passivation layer is removed with RIE to expose the n-contact AlGaAs layer (Fig.4.24-(e)). A positive photolithography step patterns the n-contact. Prior to the deposition, the sample is briefly dipped into an HCl:H$_2$O 1:1 solution to remove any native oxide that might have formed on the contact layer. A combination of Ni/Ge/Au (20nm/50nm/100nm) is deposited; where the Ni improves the adhesion and the Ge is a dopant for the n-AlGaAs. After deposition, the n-contact is annealed.
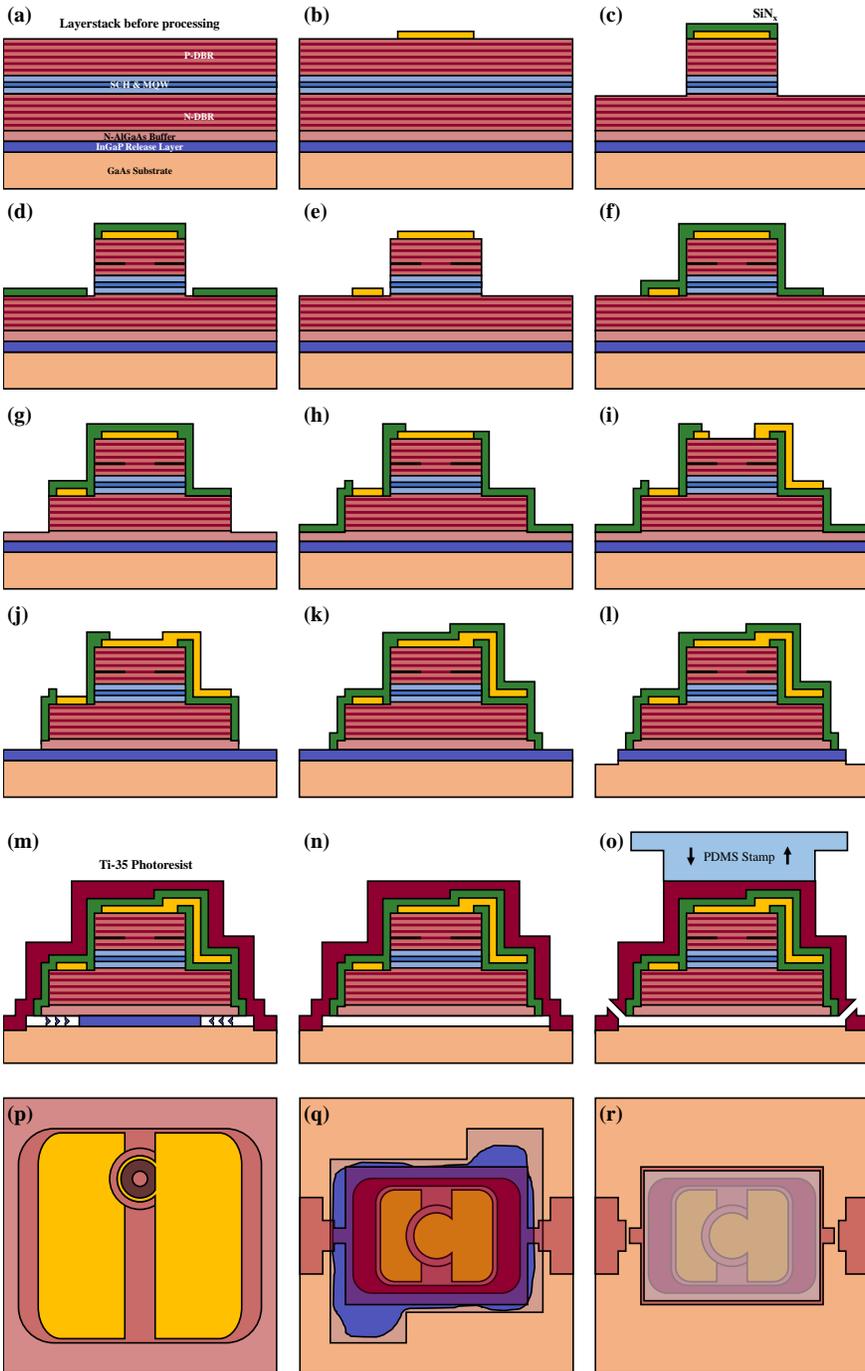
Figure 4.24: Schematic overview of the process steps on the source substrate for fabricating transfer-print compatible VCSELs: (a) the epitaxial layerstack; (b) the P-contact deposition; (c) the main mesa ICP etching; (d) the oxide aperture formation; (e) N-contact deposition; (f) SiN$_x$ passivation and patterning; (j) secondary mesa ICP etching; (h) contact opening; (i) contact pad deposition; (j) buffer layer wet etch; (k) buffer layer sidewall passivation; (l) release layer and substrate patterning; (m) wet underetch; (n) substrate cleaning and quasi-free standing coupons with lastly (o) pick-up of the devices. A selection of steps also show top-down schematics, with (i & p) the on-source test structure, (m & q) the device

N-DBR Mesa Definition

A combination of a ~ 100 nm SiN$_x$ hard mask and photoresist are used to pattern the n-DBR with an ICP etch (Fig.4.24-(f)). A positive lithography step defines rounded mesas down to the buffer layer (Fig.4.24-(g)). Afterwards, the sample is passivated with an additional ~ 250 nm SiN$_x$ to avoid oxidation of the buffer layer.

Pad Metallization

The SiN$_x$ layer is first opened up at the respective p-& n-contact locations (Fig.4.24-(h)). Large probe pads are deposited on the on-source test structures with top-surface emission (Fig.4.24-(j & p)), which can be characterized at this stage in the process flow. A smaller p-pad is deposited for the smaller VCSELs (Fig.4.24-(i)), to facilitate the VIA access of both contacts after printing (Fig.4.24-(q/r)).

Buffer Mesa Definition

Another lithography opens the SiN$_x$ on the buffer layer. Wet etching is preferred as it provides high selectivity with the SAC layer, improving TP-yield. Moreover, an oxidation layer is still formed on the InGaP if the GaAs buffer layer is dry-etched. A digital etch procedure cleans the sample in HCl (10 sec) - H$_2$O$_2$ (30 sec). It is repeated 3 times and finishes with another HCl-step [60]. The n-AlGaAs buffer layer is then etched in citric acid C$_6$H$_8$O$_7$:H$_2$O$_2$ peroxide (5:1) for approximately 2 minutes. Another SiN$_x$ layer (275 nm) is deposited to protect the sidewalls.

Substrate Access

An additional lithography step opens the sidewall passivation of the buffer mesa. The following lithography step patterns the InGaP release layer. A HCl:H$_2$O (2:1) solution is used to etch through the 500 nm InGaP release layer. The etch rate varied from wafer to wafer, resulting in etch rates of 400 nm/min down to 100 nm/min. Using the same photoresist pattern, 200 nm of the substrate was etched in 1 min with a citric acid:peroxide etch (5:1).

Encapsulation & Release Etch

The final lithography step defines the encapsulation of the devices. Prior to spincoating the photoresist, the sample is dipped into HCl:H$_2$O (1:1) to remove any oxide. After development, the resist is hardbaked to avoid sticking to the PDMS stamp. The devices are typically released in HCl-37%, for a duration of 100 minutes and on top of a rotator (50 RPM). The sample is then rinsed within a DI beaker to remove the HCl and to avoid coupon delamination. Residues from the outer InGaP remain. An additional digital etch procedure is done to clean the substrate. The devices are now ready for pick-up.

4.3.4 Transfer-Printing

The devices are transfer-printed using a μ-TP-100 transfer-printer of X-Celeprint. Prior to printing, the target substrates are prepared with a thin bonding layer that acts as an adhesive. A BCB-35:mesitylene (1:6) dilution is spincoated at 3000 RPM. After printing the devices, the bonding layer thickness is approximately 40 nm.
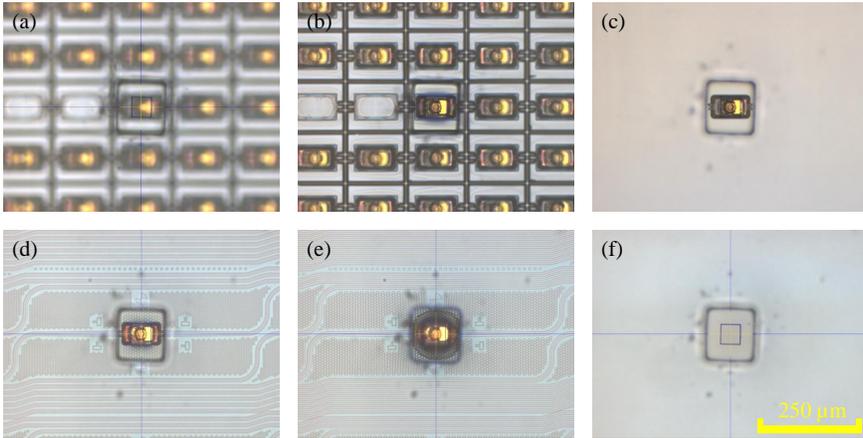
Figure 4.25: An overview of the Micro-Transfer-Printing steps performed for picking up a single Gen2 VCSEL (a-b-c) and printing onto a diffraction grating (d-e-f).

Fig.4.25 shows microscope images of the individual steps of a single-coupon micro-transfer-printing process. Fig.4.25-(a) shows the printer with the optics focused on the stamp (devices out-of-focus). Fig.4.25-(b) shows the stamp moving down, coming into contact with the VCSEL-coupon and thus brining the devices into focus. Fig.4.25-(c) shows the stamp and VCSEL coupon after the stamp rapidly pulls upward from the source substrate. Fig.4.25-(d) shows the alignment procedure between done between the VCSEL coupon and the pattern recognition markers on the PIC target substrate. Fig.4.25-(e) shows the stamp pushing the VCSEL down onto the PIC substrate. A slight overdrive is noticed, deforming the shape of the stamp surrounding the coupon. Fig.4.25-(f) shows the stamp after it has been slowly peeled-off from the printed VCSEL. The VCSEL remains on the PIC substrate and the stamp is ready for the cleaning procedure. The stamp then moves back to a scotch-tape pad to clean any remaining photoresist residues after which the next cycle can start. A single print takes less than 1 minute.

Fig. 4.26 shows microscope images of just the printing process, but this time for an array of VCSEL coupons printed at the same time using a multi-post stamp (125 µm vertical pitch). Here, prior to Fig. 4.26-(a), the array of devices are picked up. Then the multiple VCSELs are transferred to the PIC substrate. Fig. 4.26-(a) shows the alignment procedure of the printer on the array of VCSELs. Fig. 4.26-(b) shows the array of VCSELs being printed and the shear force being applied to the array, to facilitate the detachment. Fig. 4.26-(c) shows the moment on which the PDMS stamp delaminates from the individual coupons and Fig. 4.26-(d) shows again the stamp brought upward. This demonstrates the overall achieved yield of the process flow.
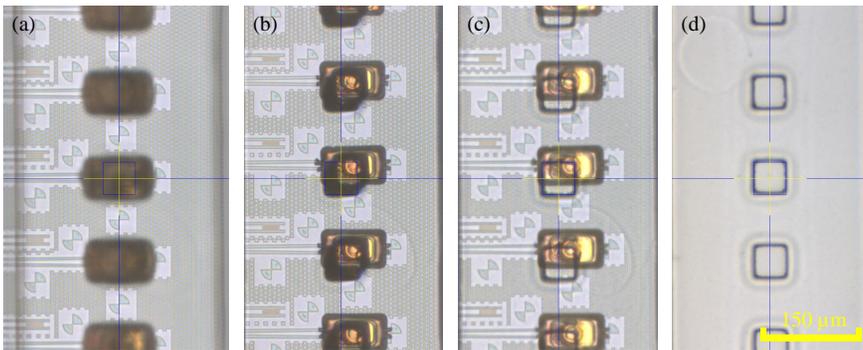
Figure 4.26: An overview of the Micro-Transfer-Printing steps for printing an array of multiple VCSELs (Gen2) onto waveguide diffraction gratings.

4.3.5 Target chips

In this work, VCSELs were transfer-printed on two types of target substrates. The first one is the photonic integrated circuit, based on the imec biopix-300nm platform, where the bottom-emitted light is coupled into the waveguide via a diffraction grating. The key figures of merit are the waveguide coupled power and the coupling efficiency of the diffraction grating. In order to evaluate the coupling efficiency, it is required to know the total downward output power. The second target substrate is therefore made from sapphire, which is transparent and allows us to characterize the downward output power of the VCSELs.

The processing steps after printing are similar for both the photonic integrated circuits and the sapphire substrate. They include the removal of the photoresist encapsulation, curing of the BCB bonding layer, sample planarization with another BCB layer, curing of that BCB layer, etching VIAs into the planarization layer, accessing the device contact pads and depositing the device probe pads. All these
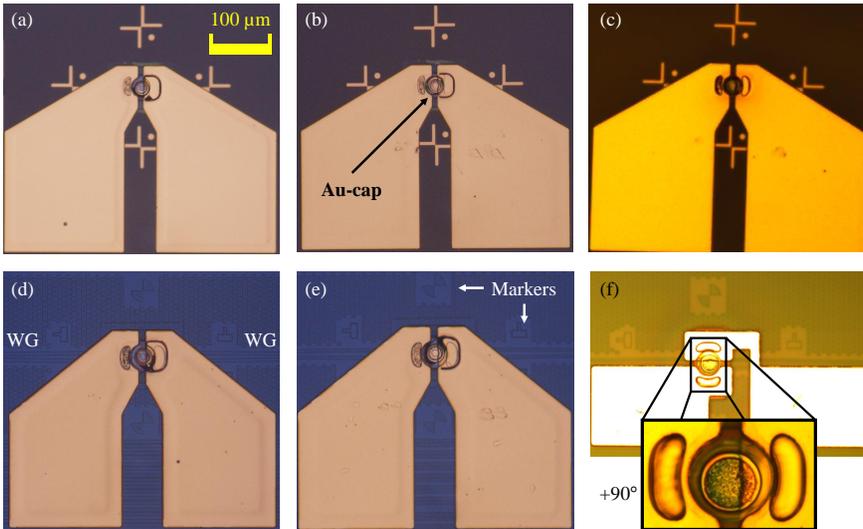
Figure 4.27: The top row shows VCSELs printed on the transparent sapphire substrate for (a) Gen1 coupon, (b) Gen1.5 coupon and (c) Gen2 coupon. The bottom row shows VCSELs printed on a PIC for (d) Gen1 coupon, (e) Gen1.5 coupon and (f) Gen2 coupon.

steps have been highlighted and discussed previously in chapter 1, section 1.3.2. Fig.4.27 lays out the different VCSEL-target combinations investigated in this work. Shown from left to right are the Gen1 (without top Au-cap), Gen1.5 (post-printing deposited Au-cap) and Gen2 devices (on-source deposited Au-cap). An important difference between the target substrates is the top oxide thickness of the PIC. It is a key performance parameter for coupling light into the waveguide efficiently and providing polarization sensitive feedback. These criteria are not relevant to the sapphire substrate. Important to note is that the top oxide thickness of the PIC, at 0.8 μm, deviates from the standard MPW-offering of 2.0 μm.

4.3.6 Process Optimizations
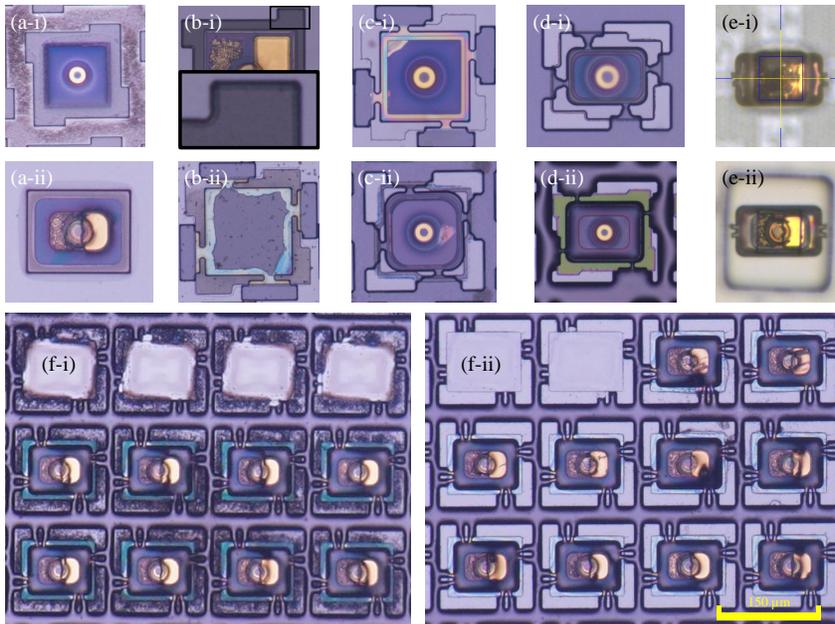
Figure 4.28: Most common and important processing obstacles encountered in this work: (a) release layer oxidation, (b) InGaP isotropic etch rate variations, (c), release etch induced coupon damage, (d) PR encapsulation conformal thickness variation, (e) coupon shadowing during printing and (f) substrate cleaning.

Release Layer Oxidation

The purpose of the buffer layer is to separate the N-DBR Mesa ICP-etch from the final wet etching steps. The preference for wet etching stems from the sensitivity to oxidation of AlGaAs. For the first wafer delivery, the buffer layer was omitted. This resulted in severe surface damage of the InGaP layer after the ICP etching. Attempts at cleaning the surface were mostly unsuccessful, due to the change in surface chemistry after oxidation. The original process flow was feasible with the inclusion of the buffer layer in the second wafer batch. The difference in sample surface quality can be seen between Fig.4.28-(a-i) & (a-ii).

InGaP Isotropic Etching

Etching InGaP is mainly performed in concentrated HCl [61] and is found to etch quasi-isotropic in this work, in contrast to InAlP [62]. Fig.4.28-(b-i) shows a similarly sized coupon on an InAlP release layer. In that case, the etch front

follows the crystalline axis of the InAlP material closely, and etches fastest under a 45°angle, as is typical for III-V wet etching. Based on this, the coupons in the Gen1 mask were oriented at 45°as well. Fig.4.28-(b-ii) shows a dummy encapsulation through which the release etch is monitored. The anisotropic nature of the InGaP etch is apparent and gives flexibility to match the rotation of the coupons on the source to the target. This also helps to better align the polarization of the grating.

Release Layer Etch & Coupon Damage

The InGaP release layer is etched in 37% concentrated HCl. At this concentration, the time of the release etch is too long for the standard SiN_x protection. Over the duration of the release etch, the etchant penetrates the passivation layer at the corners of the coupon, as can be seen in Fig. 4.28(c-i). There are two options to mitigate the issue; (1) increase the passivation layer thickness or (2) mitigate the pinhole formation in the corners by rounding the mesas. The corner-rounding was attempted first, since the amount of SiN_x passivation on the coupons is already substantial. This approach resolved the issue as can be seen in Fig.4.28-(c-ii).

Photoresist Encapsulation Thickness

The transfer-printed VCSEL has a relatively large thickness of $\sim 10.5\mu m$, which is 3 times taller than typical edge emitting devices. The encapsulation needs to protect the coupon across the entire surface. The standard thickness of TI-35 photoresist after spincoating is about 3.5 μm. Therefore, to encapsulate thicker coupons, it is advisable to switch to thicker photoresists (AZ9260) [63]. However, even for large topography structures, photoresist tends to behave as a conformal coating. To achieve a high pick-up yield, the tethers need to be made sufficiently narrow and thin. However, if the width of the encapsulation is only slightly wider than the width of the N-DBR mesa, as in Fig.4.28-(d-i), the tether will be vastly thicker than intended. By placing the tether too close to the mesa, it falls underneath the quasi-conformal photoresist-sidewall, which is much larger than the specified spincoated value. For example, the narrow point of the resist can be designed in the 1 - 4 μm range, but it went up to 15 μm in the described case, preventing the pick-up of the coupons. The solution here is to switch back to the thinner TI-35 and to increase the encapsulation width over the width of the N-DBR mesa. As a result, the photoresist 'settles' to the desired thickness and the coupons can be picked up with high yield. Fig.4.28-(d-ii) shows this extended encapsulation design.

Coupon Shadowing

Fig. 4.28-(e-i) & (e-ii) show two Gen2 devices picked up with a PDMS stamp. The first image has low-contrast and the contact features are not very clear with respect
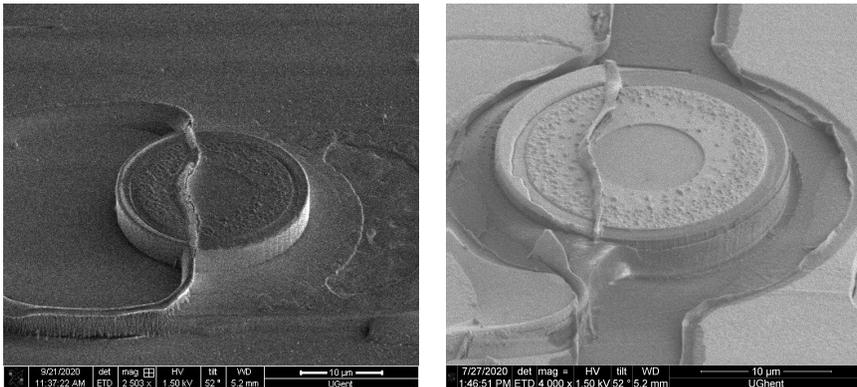
Figure 4.29: SEM images, showcasing the edge of the P-pad sticking out, creating a sharp quasi-vertical topographic feature on the top-side of the coupon.

to the second image. For the first image, the coupon becomes partially delaminated from the stamp. As a result, pattern recognition did not work and a manual print had to be performed. At the time of writing, the solution to this issue has been identified, although not yet implemented.

The 'Pad Metallization' step provides easier access to the p-contact. This was a requirement for Gen1 devices, because it can be difficult to accurately access the ring-shaped p-contact without also covering the entire P-DBR mesa. It appears, however, that the P-DBR step height is too large, causing the edges of the P-pad to curl upwards. Even with the photoresist encapsulation, this rather sharp transition can delaminate the coupon partially from the stamp. The subfigures (a-d) of Fig.4.28 reveal that most of the process development has been done on simplified samples, where the 'Pad Metallization' was not included. As a result, the issue was not prevalent for most of the development efforts and was only identified towards the end of development. By replacing the p-contact rings with p-contact disks in Gen2 devices, the restrictions on accessing the contact are alleviated as well.

Substrate Cleaning

During the development work, it became apparent that the outer parts of the release layer are only partially dissolved during the release etch. Therefore it leaves residue particles behind, which are shown in Fig.4.28-(f-i). From experience, InGaP is more susceptible to these residues than InAlP. Hence, an additional digital etch cleaning is performed after the release. This step consists of a 30 second peroxide dip, followed by a 10 second dip in a HCl:H$_2$O (1:2) dilution. Afterwards, the devices are clean and the printing yield improves.
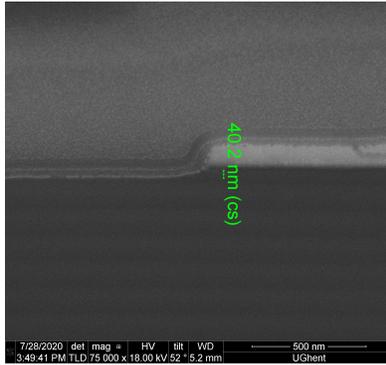
Figure 4.30: FIB cross-section of the damaged P-DBR top layer, after all fabrication steps.

Top Surface Light Leakage - Gen1.5 & Gen2 VCSELs

Gen1 devices are designed to operate with a III-V/air interface. This means that after the BCB planarization (post-printing), the BCB layer has to be etched back to expose the P-DBR mesa to air. The SiN$_x$ layer on top of the DBR is then removed as well. The RIE step to remove the BCB and SiN$_x$ layers is executed slightly longer to compensate for layer variations across the die. This etch, while selective, still damages the top III-V DBR-layer as shown in Fig.4.30. The standing wave pattern in the VCSEL is sensitive to this top-surface interface. For a thickness change of 40 nm, the reflection changes from in-phase to anti-phase. A gold metal cap is deposited to mitigate this issue. The yield of the gold-cap deposition after printing was insufficient. It was therefore decided to deposit the metal-cap on the source, as a p-contact disk, for the Gen2 devices.

4.3.7   Conclusion

Within this section, the fabrication details and issues have been highlighted. A summary of the considerations for the epitaxial layer structure was reviewed first. The design of the devices was studied, highlighting the epitaxial cost benefit that transfer-printing offers over flip-chipped devices. Afterwards, the process flow of the source sample was studied. Following this, a brief demonstration was shown of the transfer-printing process of the VCSELs in both single-device printing and array printing, showcasing the high-throughput capability. The VCSELs have been printed on two substrates types: transparent sapphire for characterizing the bottom output power of the VCSELs and PICs for waveguide-based coupling of the light. The section finished with an overview of the changes made to improve the yield of the source processing, the transfer-printing process and the overall device performance. Recommendations are also made for further improvements.

4.4 Measurement results

This section reviews the measurement results of the fabricated and transfer-printed VCSELs. There are three main categories of devices that were evaluated: (1) the on-source test devices, measured on the GaAs substrate, with the light collected from the top-surface, (2) the VCSELs, printed on the transparent sapphire substrates, to characterize the total amount of downward emitted power and (3) the waveguide-coupled VCSELs after printing on the PIX4life PICs.

Both LIV and spectral measurements are carried out, from which a range of parameters can be extracted. The findings are discussed in the next paragraphs. For the on-source test devices, both LIV and spectral measurements were performed through the partially leaking top DBR. These measurements act as a reference on whether transfer printing has a performance penalty associated with it. The sapphire plate measurements were bottom-emitting measurements, with the light transmitted through the transparent substrate. The bottom-emitted light does not allow for easy fiber access, and thus the light is collected with a large area detector. This limits the analysis to LIV and corresponding parameters deduced from the LIV measurements.

There are two source-fabrication runs in this work, each with their a specific VCSEL design. The design of the first run, Gen1, does not have a top-Au reflector, while the design of the second one, Gen2, has a top-Au reflector integrated in the source process flow. Gen1.5 devices have a Au-cap deposited after the initial processing. These changes in the process flow are substantial in terms of device performance. Over the course of the section, the different Gen-designs are compared on their performance. Table 4.4 displays the types of measurements, performed on each type of device, for the fabrication runs made in this work.

Type	On-Source (TOP)	Sapphire substrate (BOT)	biopix-PIC (WG)
Fabrication	Gen1 & Gen2	Gen1 & Gen1.5 & Gen2	Gen1 & Gen1.5 & Gen2
LIV	I$_{th}$, SE, P$_{opt}$, R$_{diff}$	I$_{th}$, SE, P$_{opt}$, R$_{diff}$	SE, P$_{wg}$, P$_{wg}$(T), R$_{diff}$
Spectral	$\Delta\lambda$, R$_{th}$, SMSR	X	$\Delta\lambda$, R$_{th}$, SMSR

Table 4.4: Measurement categorisation of the different substrates.

4.4.1 Vertical emission (top & bottom surface)

The following subsections cover the main laser properties derived from the LIV measurements. A comparison is made between the on-source test devices with top-surface emission and the on-sapphire-printed devices with bottom-surface emission. Device properties of both fabrication rounds, Gen1 & Gen2, are highlighted.

4.4.1.1   Lasing Threshold

One of the key advantages of transfer-printing a complete VCSEL, is the ability to characterize the laser on the source substrate with top-surface emission. Fig.4.31-(a) plots the lasing threshold values for the different lasers measured on the source substrate. The results are in line with expectations in terms of variation between the different aperture sizes [64]. It is clear that the Gen2 devices have lower lasing threshold values than Gen1 devices. This is likely due to an off-target oxide aperture wet oxidation step. For some of the devices of the Gen2 fabrication, the apertures are slightly smaller (0.5-1.0 μm) than the designed values.
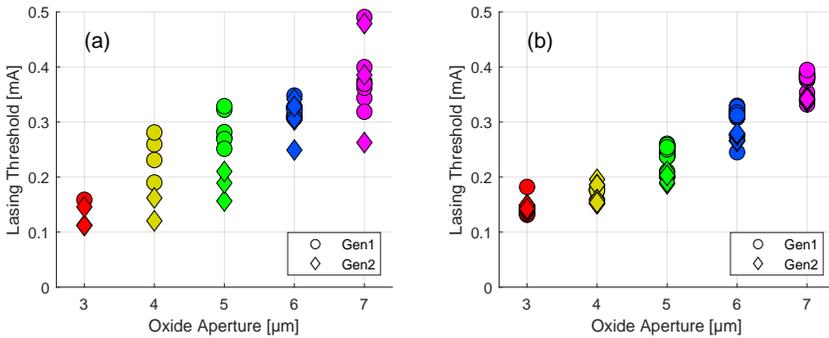
Figure 4.31: Lasing thresholds for Gen1 & Gen2 VCSELs as measured on (a) the source substrate (top-emission) and (b) the transparent sapphire substrate (bottom-emission).

Fig.4.31-(b) maps the same lasing threshold value as measured on the bottom-emitting VCSELs printed on the sapphire substrate. More devices are assessed than the on-source top-surface emitting VCSELs (limited number). The deviation between the values is also lower, indicating that the on-source test structures were disproportionately impacted by the deviation in the wet oxidation step to form the aperture. A summary of the average and deviation values can be found in table 4.5. The lasing thresholds presented here are significantly lower compared to the half-VCSEL on SiN_x [34] and other VCSEL-to-PIC efforts in table 4.13.

Lasing Threshold [mA]	3μm	4μm	5μm	6μm	7μm
Gen1 - Source	0.09 ± 0.10	0.24 ± 0.04	0.29 ± 0.03	0.32 ± 0.01	0.38 ± 0.05
Gen1 - Target	0.14 ± 0.02	0.17 ± 0.01	0.24 ± 0.02	0.31 ± 0.02	0.38 ± 0.02
Gen2 - Source	0.12 ± 0.02	0.14 ± 0.03	0.19 ± 0.03	0.31 ± 0.03	0.38 ± 0.11
Gen2 - Target	0.14 ± 0.00	0.16 ± 0.02	0.20 ± 0.01	0.27 ± 0.01	0.34 ± 0.00

Table 4.5: Lasing Threshold of the VCSELs.

4.4.1.2 Slope efficiency

The slope efficiencies for the on-source VCSELs are presented in Fig.4.32-(a), while those for the sapphire substrate transfer-printed VCSELs are shown in Fig.4.32-(b). A similar conclusion holds, namely, the spread on the on-source VCSELs is more prominent and not entirely representative for the transfer-printed devices. For the apertures above 3 µm, the slope efficiency falls between 0.4 and 0.5 W/A. The smallest aperture size shows a reduced slope efficiency, which can be intuitively understood due to higher optical scattering around the smaller oxide aperture.
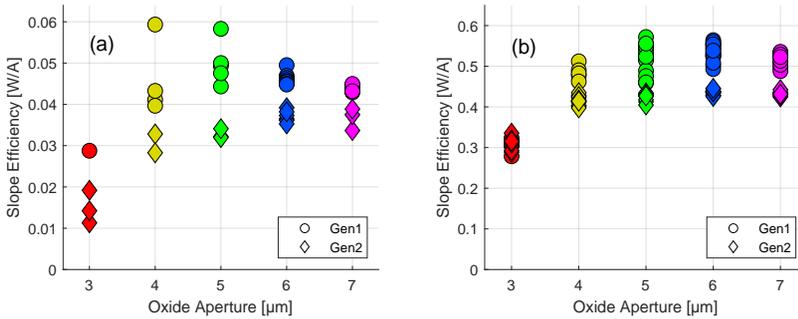
Figure 4.32: Slope efficiencies of Gen1 & Gen2 VCSELs as measured on (a) the source substrate (top-emission) and on (b) the transparent sapphire substrate (bottom-emission).

A comparison can also be found in table 4.6. The measurements are in agreement with the simulated values described in section 4.2.3. The slope efficiencies of these VCSELs are limited due to the combination of a the relative lossy top-mirror that lowers the internal quantum efficiency [65].

4.4.1.3 Differential resistance

The differential resistance values, measured at the current of maximum optical output, are summarized in Fig. 4.33 and table 4.7. In comparison to other VCSELs, the differential resistance for the larger aperture values is quite low. This indicates

Slope Efficiency [W/A]	3 µm	4 µm	5 µm	6 µm	7 µm
Gen1 - Source	0.02 ± 0.01	0.05 ± 0.01	0.05 ± 0.00	0.05 ± 0.00	0.04 ± 0.00
Gen1 - Target	0.31 ± 0.02	0.48 ± 0.02	0.52 ± 0.04	0.53 ± 0.02	0.52 ± 0.01
Gen2 - Source	0.01 ± 0.00	0.03 ± 0.00	0.03 ± 0.00	0.04 ± 0.00	0.04 ± 0.00
Gen2 - Target	0.31 ± 0.01	0.42 ± 0.01	0.42 ± 0.01	0.44 ± 0.01	0.43 ± 0.00

Table 4.6: Slope efficiencies of the VCSELs.

good contact formation with the rapid thermal annealing step after the n-contact deposition, and highly conducting DBRs. The variation in differential resistance is larger for the smaller aperture sizes. This can be attributed to the larger influence on diameter variations for the smaller aperture sizes. The inverse relationship to the aperture is pronounced.
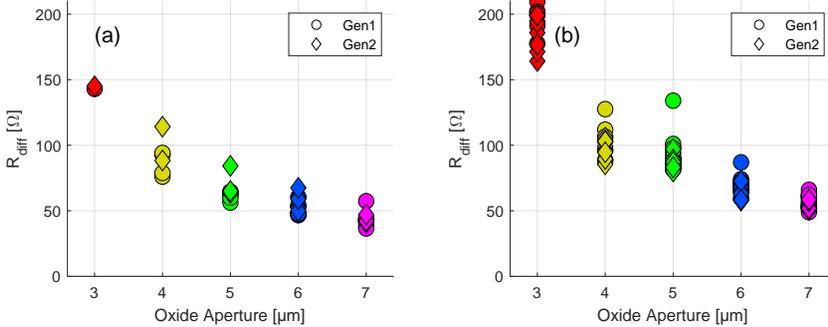
Figure 4.33: Differential resistance values of Gen1 & Gen2 VCSELs as measured on (a) the source substrate (top-emission) and on (b) the sapphire substrate (bottom-emission).

The relatively high differential resistance values for the smaller apertures, is an indication for strong self-heating effects at low bias currents. The smaller apertures will therefore thermally tune their wavelength with a lower power consumption, albeit at a lower total optical power as well. A remark, both subfigures in Fig. 4.33 are plotted on the same scale, which is most representative for all devices. As suggested by the values in table 4.7, some data points fall outside the figure scale. This further validates a slight mismatch in the intended aperture diameter design.

4.4.1.4 Output power

Fig.4.34 showcases the light-current curves of the Gen1 devices. Gen2 devices are not included in the figure, but are present in table 4.8. In this table, the maximum output power is given at thermal roll-over. The on-source VCSELs operate as

R_{diff} [Ω]	3μm	4μm	5μm	6μm	7μm
Gen1 - Source	140.86 ± 2.96	85.45 ± 9.30	61.68 ± 3.16	50.70 ± 4.91	43.37 ± 6.21
Gen1 - Target	196.26 ± 12.31	106.18 ± 14.93	91.39 ± 12.05	70.01 ± 5.86	57.08 ± 5.01
Gen2 - Source	248.33 ± 97.50	101.24 ± 18.24	70.94 ± 11.56	57.14 ± 6.55	43.44 ± 3.21
Gen2 - Target	189.39 ± 14.30	96.47 ± 7.31	86.97 ± 5.49	66.63 ± 5.52	53.90 ± 2.49

Table 4.7: Differential resistance of the VCSELs.
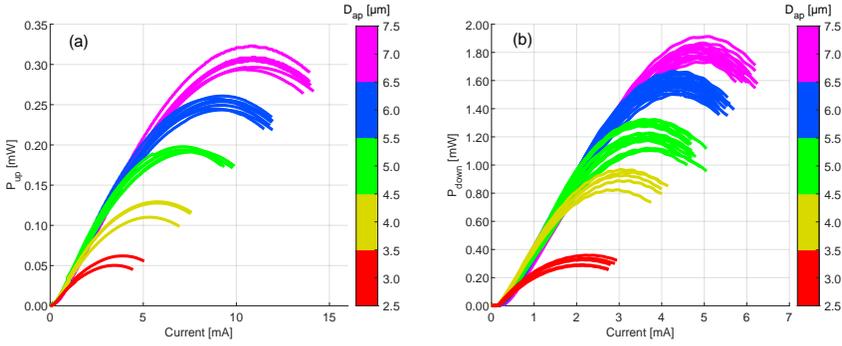
Figure 4.34: LI curves of (a) Gen1 VCSELs measured on the source substrate (top-emission) and of (b) Gen1.5 VCSELs measured the transparent sapphire substrate (bottom-emission).

designed, only emitting a fraction of the power from the top-side. The bulk of the optical output power is emitted downwards.

The ratio of downward to upward emitted output power (P_{DOWN}/P_{UP}), obtained from the measurements of the transfer-printed devices on the target and the test devices on the source substrate respectively, is shown in table 4.8. From that ratio, the increase in performance of Gen1.5 devices over Gen1.0 devices is clear, due to the deposition of the gold-cap on Gen1.5 devices. Although the effect is pronounced, the 3 µm aperture device seems the least sensitive to this change with only a 6.6% increase versus 25% or higher for the other devices. The maximum output power of the Gen2 devices is lower than for the Gen1 devices. Part of this can be attributed to the off-spec aperture diameter. Also the P_{DOWN}/P_{UP} ratio seems to have increased. This is attributed to a variation in the oxide aperture formation on the source substrate, which affected the test structures disproportional over the transfer-print coupons.

Output Power [mW]	3 µm	4 µm	5 µm	6 µm	7 µm
Gen1 - Source P_{UP}	0.06 ± 0.01	0.13 ± 0.02	0.20 ± 0.01	0.25 ± 0.01	0.31 ± 0.01
Gen1 - Target P_{DOWN}	0.30 ± 0.01	0.71 ± 0.04	0.98 ± 0.04	1.27 ± 0.02	1.45 ± 0.01
Gen1 - P_{DOWN}/P_{UP}	5.00	5.46	4.90	5.08	4.68
Gen1 - Source P_{UP}	0.06 ± 0.01	0.13 ± 0.02	0.20 ± 0.01	0.25 ± 0.01	0.31 ± 0.01
Gen1.5 - Target P_{DOWN}	0.32 ± 0.03	0.91 ± 0.06	1.23 ± 0.08	1.59 ± 0.05	1.81 ± 0.05
Gen1.5 - P_{DOWN}/P_{UP}	5.33	7.00	6.15	6.36	5.84
Gen1 → Gen1.5	+ 6.6 %	+ 28.2 %	+ 25.5 %	+ 25.2 %	+ 24.8 %
Gen2 - Source P_{UP}	0.02 ± 0.01	0.07 ± 0.01	0.12 ± 0.01	0.16 ± 0.01	0.21 ± 0.01
Gen2 - Target P_{DOWN}	0.26 ± 0.02	0.62 ± 0.02	0.87 ± 0.03	1.09 ± 0.01	1.27 ± 0.02
Gen2 - P_{DOWN}/P_{UP}	13.0	8.86	7.25	6.81	6.05

Table 4.8: Maximum optical output power of the fabricated VCSELs at thermal roll-over.

4.4.2   Waveguide-coupled emission

The following section covers the main properties of the waveguide-coupled VCSELs (VCSILs), such as the waveguide-coupled power and coupling efficiency, the device polarization, the top oxide layer thickness, the coupling imbalance and thermal tuning range limitations.

As an introduction to the section, Fig. 4.35 presents an overview of the performance parameters of the VCSIL with the highest waveguide-coupled power in this work. This device has a top oxide thickness above the grating coupler of 930 nm ± 15 nm. The grating has a pitch of 0.544 μm and a fill factor of 72.5%. Clear single-mode behavior is obtained, with a suppression ratio of 39.5 dB or higher over a 3.5 nm tuning range. The ripple on the LI-curve is identified as external cavity feedback related to the waveguide circuit design of the PIC and is further described in section 4.4.2.5. The asymmetry in the roll-over current is not understood at this time, with this being observed in less than 1% of the measured devices.
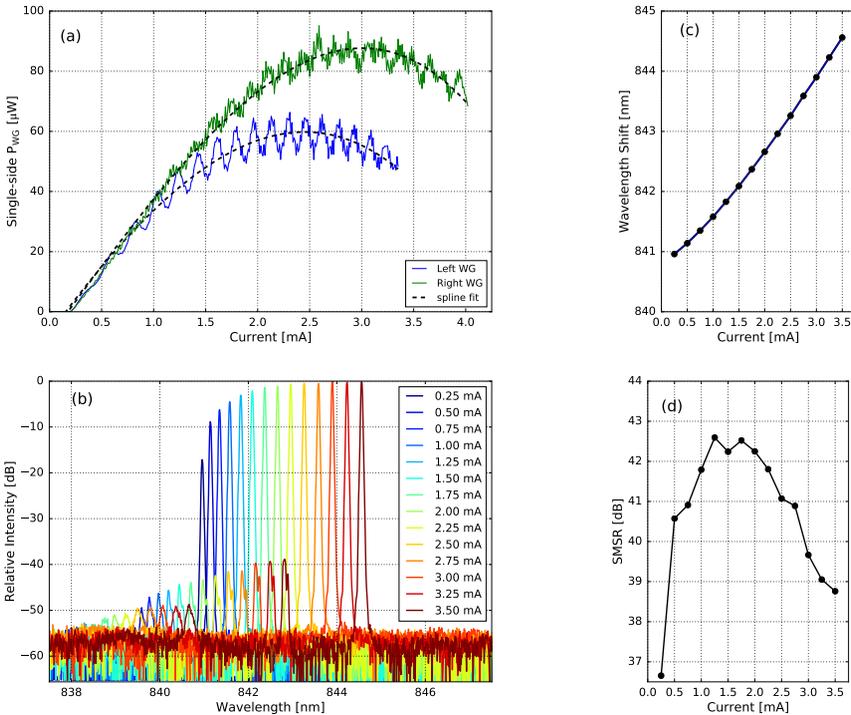
Figure 4.35: (a) Waveguide-coupled LI measurements for both output waveguides. (b) Superimposed spectral measurements at different bias currents. The wavelength tuning range in (c) and the SMSR (d) are derived from the measurements in (b).

GC$_{OUT, Left}$ Reference GC test   GC$_{OUT, Right}$

Figure 4.36: PIC Design of different TP-sites of the VCSILs. Reference fiber couplers are on the left and right side of the output. Those test structures allowed to track variations on the die and between the different dies. The observed GC efficiency is between -8 to -10 dB/GC.

4.4.2.1   Diffraction grating & coupling efficiency

Based on the simulations described in section 4.2.2, a selection of grating parameters are chosen to optimize the coupling performance. Fig.4.36 illustrates the PIC design of the different test-sites. They consist of six different pitch values, each with a five element sweep of the fill-factor, as highlighted in table 4.9.

A good comparison between the various grating couplers requires a large data set. Therefore, VCSILs were printed and post-processed on several different PICs. A one-to-one comparison can not be made, due to the parameter sweeps from PIC to PIC (top oxide thickness, oxide aperture diameter, polarization angles between VCSIL and GC differed for Gen1 and Gen2 devices). The transfer-printing step also introduces a misalignment, which in part influences the coupling performance. This misalignment is, in part, larger due to the coupon shadowing effect described in section 4.3.6. Therefore, the waveguide-coupled powers of the different VCSILs on the same PIC, were normalized to the highest waveguide-coupled value on the same PIC. Those normalized results are then averaged over all the different PICs. In this manner, the influence of variations on a single case are reduced. The results of this relative comparison are shown in Fig.4.38. Looking at the relative performance differences, it is clear that low-pitch and low-FF combinations are not ideal. The larger fill-factors and larger grating pitches are providing the best results. Based on this, fill-factors of 70 % or higher are best, permitted the design rules allow for these features.

Pitch	XS	S	M	L	XL
0.544 [µm]	0.525	0.575	0.625	0.675	0.725
0.547 [µm]	0.525	0.575	0.625	0.675	0.725
0.549 [µm]	0.500	0.550	0.600	0.650	0.700
0.552 [µm]	0.450	0.500	0.550	0.600	0.650
0.554 [µm]	0.450	0.500	0.550	0.600	0.650
0.558 [µm]	0.425	0.475	0.525	0.575	0.625

Table 4.9: Pitch-FF configurations of the bidirectional gratings used in the PIC design.
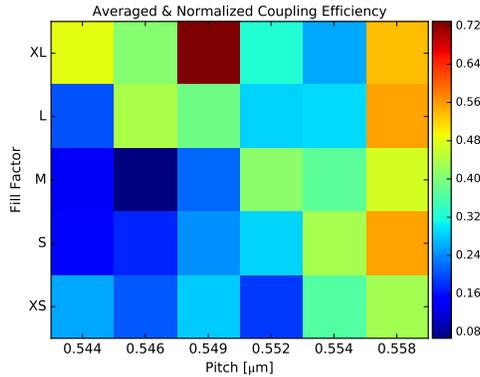
Figure 4.37: Relative coupling efficiency for different diffraction grating parameters.

The absolute coupling efficiency depends on the total downward emitted power. For other integration schemes, a top-surface emitting VCSEL is often used, which can be characterized for total optical output prior to integration. This approach is not possible for transfer-printed bottom-emitting devices. The best approximation is to compare the waveguide-coupled power with the downward emitted power measured through the sapphire substrate. The obtained LIV-curves from Fig.4.34 show a thermal roll-over that occurs at quasi-similar bias currents of around 3 mA for the 4 μm aperture devices.

The highest performing VCSILs are Gen2, 4μm aperture devices. Looking at the test structures to monitor the oxide aperture diameter, there is some uncertainty in the obtained diameter. The power level of 0.62 mW of the 4μm VCSELs is used as the upper limit, while the 0.87 mW of the 5 μm VCSELs is used as the lower limit, from table 4.8. Building on these assumptions, the best-performing device of Fig.4.35 has a single-side coupling efficiency, CE_{ss}, between 8.62% and 12.10%. The double-side coupling efficiency, CE_{ds}, lays between 16.09% and 22.58%. Fig.4.38 plots the waveguide-coupled powers of three other VCSILs. Based on the same bottom-emitting power levels as before, the coupling efficiencies of those devices are:

(left) CE_{ss} is between [5.40-7.58]% and the CE_{ds} is between [10.00-14.00]%; (middle) CE_{ss} is between [6.67-9.35]% and the CE_{ds} is between [10.92-15.32]%; (right) CE_{ss} is between [7.13-10.00]% and the CE_{ds} is between [11.95-16.77]%.

The top oxide thickness values for each device are 850 nm, 670nm and 610nm, respectively. The values for the coupling efficiencies are a bit lower than the simulated values in Figure 4.15-(b). The difference is in part explained by the the difference of a 5 μm aperture, single-mode device used in the simulations.
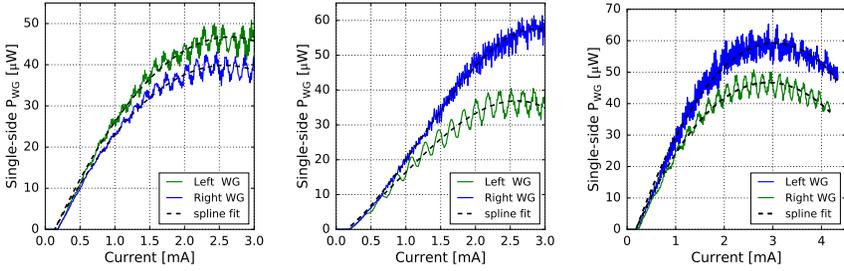
Figure 4.38: Single-side waveguide coupled powers, for (left) 0.549 µm pitch and 70% fill factor, (middle & right) 0.544 µm pitch and 72.5% fill factor.

4.4.2.2   Polarization

The fabricated VCSELs have a circular mesa and a circular shaped aperture. The circular symmetry has no preferential polarization orientation. Only above threshold current, under the influence of the electro-optic effect, the polarization tends to follow the [011] or the [0$\bar{1}$1] crystal axis [66]. For the case of the TP-VCSIL, the diffraction grating introduces a polarization sensitive component into the extended cavity of the VCSIL. Section 4.2.2 clarifies how the phase and reflection of the grating lead to a lower threshold gain in the preferred orientation of the GC. This sensitivity to the direction of the grating coupler is measured in two ways: (1) using a free-space polarizer to characterize the top-surface emission and (2) with a dedicated designed on-chip circuit, shown in Fig.4.39-(a). The on-source devices are characterized with a free-space polarizer. The measurements, highlighted in green in Fig.4.40-(a), confirm the preferred polarization state along the main axis (0° and 90°) of the VCSELs on the source substrate. Θ_{pol} is defined as the angle between the main crystal axis and the orientation of the polarization of the grating, as shown in Fig.4.39-(b).
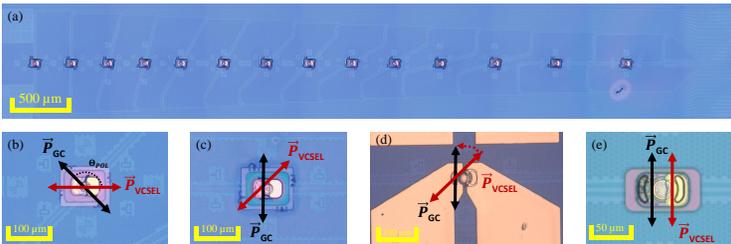
Figure 4.39: (a) The PIC polarization test structure with varying tilt angle of the diffraction grating. A generalized description of polarization mismatch is shown in (b). The standing hypothesis of Gen1, Gen1.5 and Gen2 VCSELs are described in (c)-(d)-(e) respectively.
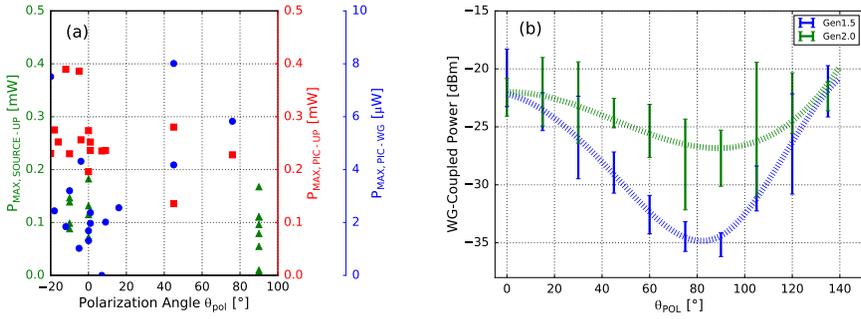
Figure 4.40: (a) Top-surface polarization measurements of on-source VCSELs along the crystal axis are marked in green. On-PIC, top-surface emitting VCSILs are shown in red and are mostly still aligned along the crystal axis. Waveguide-coupled powers of on-PIC VCSILs are in blue and indicate a higher waveguide-coupled power for those VCSILs that locked their polarization with the GC at a 45° offset from the crystal axis in Gen1. (b) Polarization-sensitive measurements are plotted for varying GC tilt angles shown in Fig.4.39-(a), for both Gen1 and Gen2 devices. Changes to the Gen2-mirror boost the polarization-locking and the VCSILs becomes more independent from the GC tilt angle.

The Gen1 devices had no Au-cap, and thus could also be characterized in top-emission, shown in red in Fig.4.40-(a). The figure illustrates that most red devices can not switch their polarization angle from the on-source state (0° or 90°) to the GC-direction (45° from main crystal axis). The waveguide-coupled measurements in blue confirm that the devices that switched their polarization state to match the polarization of the GC, outperformed those that did not. Top-emission measurements on Gen1-PIC devices showed increased output power from the top mirror. This indicated a sustained damage to the top-DBR interface during the BCB etchback, as described in 4.3.6. As a result, both the downward emitted power and the grating-induced feedback are reduced, which leads to a weakened capability of the diffraction grating to lock the polarization of the VCSEL.

By including a gold cap on top of the mesa, the phase of the reflection was corrected in Gen1.5 devices. This leads to more downward output power and more power into the waveguide. A description of the change is shown in Fig.4.39-(c) to (d). The Gen2 devices are re-oriented on the source substrate to align the main crystal axis with the grating axis, as displayed in Fig.4.39-(e). The inclusion of the top gold mirror protects the devices from damaging the top-DBR.

The on-chip polarization test structure is measured for six PICs for both Gen1 and Gen2 devices. The polarization of the grating changes across the array and with respect to the inherent polarization of the VCSEL. The results for the changing polarization angle Θ_{pol}, between the VCSEL and the GC, demonstrate the improved

polarization-pinning capability of the Gen2 devices compared to the Gen1 devices.

Overall, the analysis of the polarization of the devices indicates that there are inherent polarization-locking capabilities in the current system. Further improvements can be found by optimizing the metal stack and process flow of the top gold cap. It is also expected that by changing the grating parameters to a > 70 % fill factor, the pinning-capability will be improved.

4.4.2.3   Oxide aperture diameter

The oxide aperture confines the path of the carriers in the quantum wells, and the VCSEL output beam. This, in turn, has an impact on the amximum output power and the spectral characteristics. Fig.4.41 shows the influence of the aperture diameter on the waveguide-coupled power of the VCSILs. To simplify the LI-curves, only the spline-fits are shown of the single-side waveguide-coupled measurements.

For Gen1.5 devices, the focus lies on 3 μm devices and 4μm VCSILs. Both apertures provide a stable output, and are confirmed to be single-mode. The sweep is thus extended to 5 μm devices in the Gen2 fabrication round. The 5 μm devices are relatively single-mode, with SMSR above 20 dB. For 6 μm devices or higher, the devices are no longer single-mode, and become susceptible to polarization- and mode-hopping. The WG power of the multimode devices is equal or less than that for the single-mode devices, which couple more efficiently into the waveguide.

The difference in aperture size carries over in the waveguide-coupled output powers. One can also notice the difference in waveguide-coupled power for each aperture between Gen1.5 & Gen2. This can likely be attributed to a slight off-spec oxide aperture formation. Fig. 4.41 showcases only a selection of the best devices, as misalignment due to manual printing would skew the balance of performance.
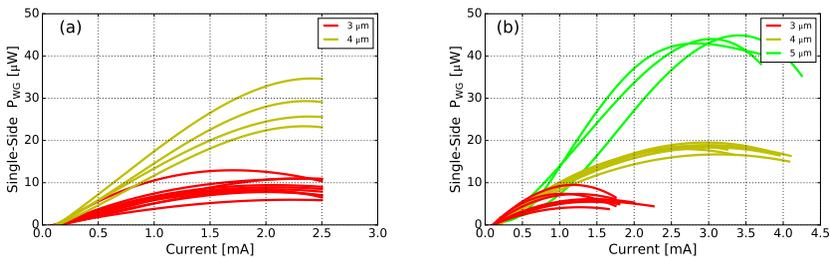
Figure 4.41: Single-side WG power of (a) 3-4 μm Gen1 & (b) 3-4-5 μm Gen2 VCSILs.
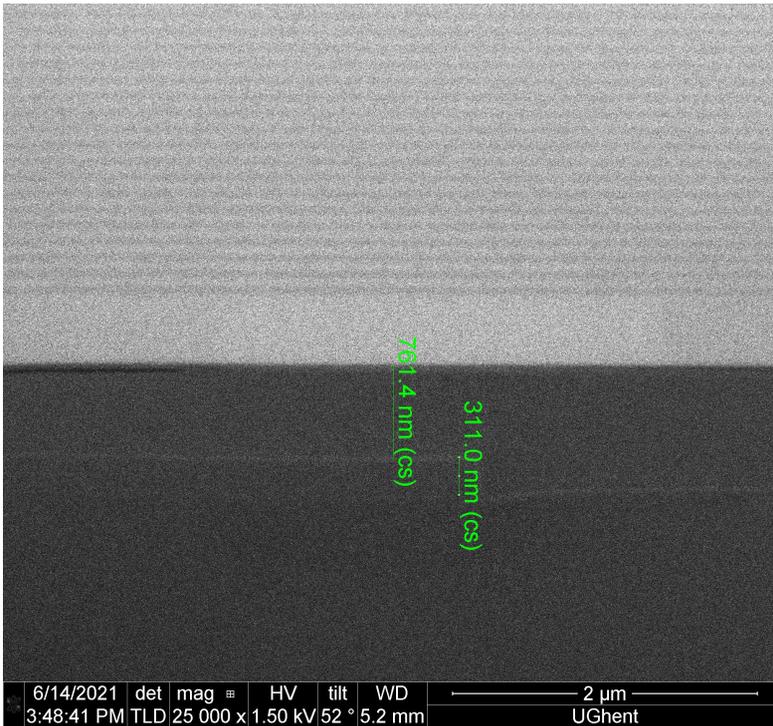
Figure 4.42: FIB cross-section of a VCSIL from the Gen2 fabrication run. The extended cavity thickness is approximately 760 nm.

4.4.2.4 Top oxide thickness

The top oxide thickness on top of the grating coupler is an important parameter of the extended vertical cavity of the VCSIL. An external cavity between the bottom-DBR and the grating. If the VCSIL output is in resonance with the extended cavity, the WG-coupled power can vary by a factor of two. The thickness of the top oxide will determine the resonance, which varies with a period of approximately 300 nm, as discussed in section 4.2.2.

For both Gen1 and Gen2 devices, respectively 3 and 4 PICs are chosen to vary the top oxide thickness and study the influence on the waveguide-coupling efficiency, as shown in Fig.4.43. The target thickness of the chips coming from imec was 750 nm. The top oxide thickness of the PICs is measured with a profilometer with respect to openclad waveguide structures. Variations in top oxide thickness are introduced by either etching part of the layer or by depositing additional SiO_x on top.
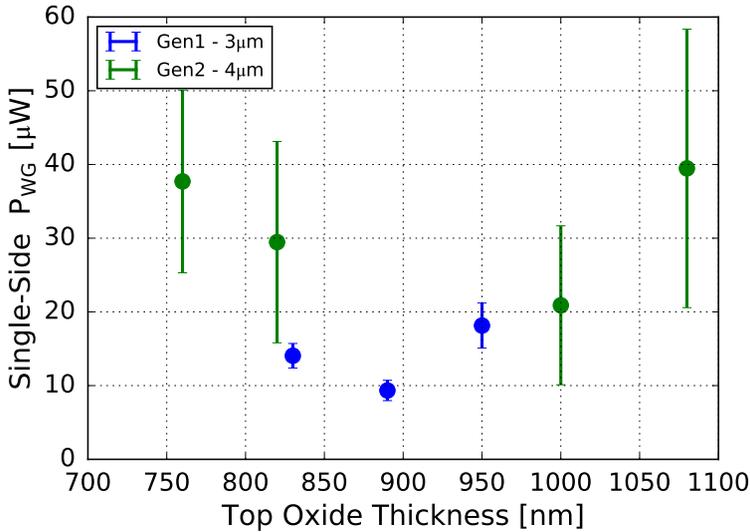
Figure 4.43: Influence of the top oxide thickness on the single-side waveguide coupled power, with a sweep of 3μm Gen1 VCSILs and 4 μm Gen2 VCSILs.

The Gen1 sweep is made with 3 μm oxide aperture devices, with a top oxide centered around 750 nm. With $\pm$ 60nm variations, the initial sweep was too narrow. For the next iteration on Gen2 devices (4 μm) the sweep range is extended. The top oxide thickness is limited to 600 nm, as the WG-coupled light would leak back into the III-V material of the VCSEL for lower values. The larger variations on the Gen2 data are attributed to (1) worse misalignment due to shadowing, which is discussed in section 4.3.6 and (2) variation on the oxide aperture diameter during the Gen2 fabrication. As a result, D_{ap} can vary from 3-4.5 μm. From Fig. 4.43, it appears that the periodic maxima in waveguide-coupled power are around 750 nm and 1050 nm. Looking back at Fig. 4.19, it can be seen that $g_{th,TE}$ also has a local minimum at approximately the same top oxide thickness the ones measured in Fig. 4.43. This means that for those values $g_{th,TE} < g_{th,TM}$ and the device is in the most stable TE-lasing condition, leading to the larger values of single-side waveguide power observed here.
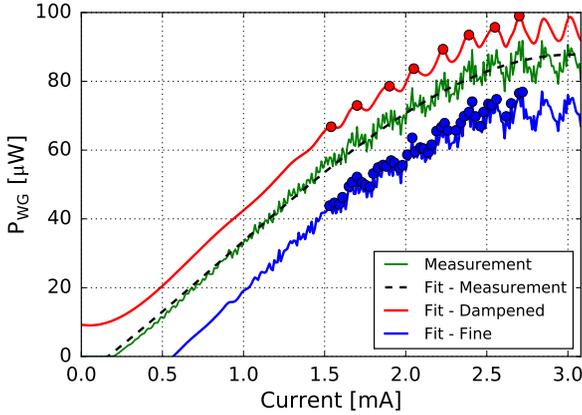
Figure 4.44: Extended cavity Fabry-Pérot feedback, induced by fiber grating couplers on the left and right output sections of the test circuit.

4.4.2.5   External cavity feedback

The LI-measurements show a ripple imposed on the output. This is attributed to a Fabry-Pérot cavity formed between the VCSEL grating and the fiber coupling grating. The fiber couplers reflect part of the light back towards VCSEL diffraction grating, forming a weak extended cavity mirror. The interference of the forward and backward propagating light leads to the ripples seen in the measurements.

The extended cavity length can be deduced from the Fabry-Pérot equation 4.29. The FSR is related to the current-spacing of the local extrema of the ripple, indicated by dots in Fig.4.44. The current-spacing can be converted to a wavelength spacing (FSR) if one knows the current-to-wavelength conversion. This conversion factor can be deduced from spectral measurements that relate the thermal wavelength shift to the applied bias current of the VCSELs. For a 4μm VCSIL, this value is ~ 1.25 nm per mA.

$$L_{cavity} = \frac{\lambda^2}{2n_{g,WG}FSR} \tag{4.29}$$

The output fiber couplers are grouped together for multiple VCSILs, as can be seen in Fig.4.36. As a consequence, in most cases, the left and right cavity lengths are different. This results in Fabry-Pérot induced ripples with different periodicity on the left and right waveguides, and a superposition of both present on a single-side measurement. In Fig.4.44, the signal is decomposed with spline fits of different damping factors to isolate the long- and short-cavity influences. This confirms that the designed length of the extended grating cavity matches the

cavity length associated with the measured ripple. The error is less than 5% and is attributed to the approximate value used to describe the non-linear relation of the wavelength-to-current conversion over the entire bias range.

While the Fabry-Pérot ripple is present in the current waveguide design, there are ways to suppress the feedback, namely by (1) avoiding reflection through the use of tilted grating couplers [67] or (2) increasing the extended cavity length: by incorporating the VCSILs in a larger photonic circuit, the ripples will dampen out.

4.4.2.6   Mode size & coupling imbalance

A test structure is used to analyze the grating length, L$_{GC}$, shown in Fig.4.45-(a). The simulations in section 4.2.2 indicate an optimized grating length of $\sim$ 5,6 µm for the aperture diameters of 3,4 µm, which are confirmed by the results. The standard grating of 8 µm length, designed to accommodate all apertures, was over designed with respect to the main single-mode apertures of 3 and 4 µm. Improved mode matching will lead to higher coupling efficiencies.

Fig.4.45-(b) reveals the imbalance in output power between both output waveguides, for different PICs. This can be attributed to manual misalignment and the shadowing effect hindering the alignment accuracy, as discussed previously in section (4.3.6). PIC numbers 5 to 8 are associated to the top oxide parameter sweep of section 4.4.2.4 and the imbalance shown here is attributed to the variation in Fig.4.43. The grating-based coupling is sensitive to misalignment, with simulations indicating 3 dB imbalance per 1.2 µm misalignment. With a $\pm$ 1.0 µm accuracy, an imbalance lower than 3 dB is attainable with modifications to the process flow.
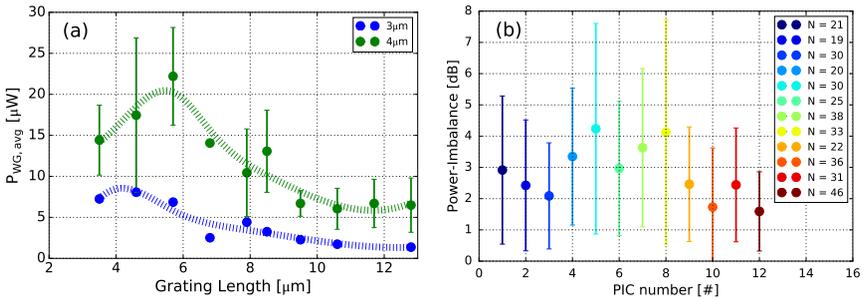
Figure 4.45: (a) WG power versus L$_{GC}$, (b) the power imbalance between the WG outputs.

4.4.3   Spectral properties

In the following part, the spectral properties of the VCSEL are discussed. The spectral measurements are dependent on the VCSEL diffraction grating, but the gathered spectral measurements are just a subset of the LIV measurements discussed in section 4.4.2. Hence, a thorough investigation into the dependency of the grating parameters of the diffraction grating is not given in this work. The measurements do include data from both the on-source and waveguide-coupled VCSELs. VCSELs transfer-printed on sapphire substrates, are excluded because they were characterized with a large-area detector instead of a fiber-coupled setup.

4.4.3.1   Wavelength tuning range $\Delta\lambda_{VCSEL}$

The wavelength tuning range of Gen1.5 VCSELs is shown in Fig.4.46-(a). The entire data set is plotted in Fig.4.46-(b). All other properties are influenced by aperture size, except for the wavelength tuning range, as this is just dictated by the internal temperature inside the cavity at roll-over. This internal temperature, while independent on the aperture size, is reached at lower electrical dissipated power for the smaller apertures than for the larger aperture diameters.
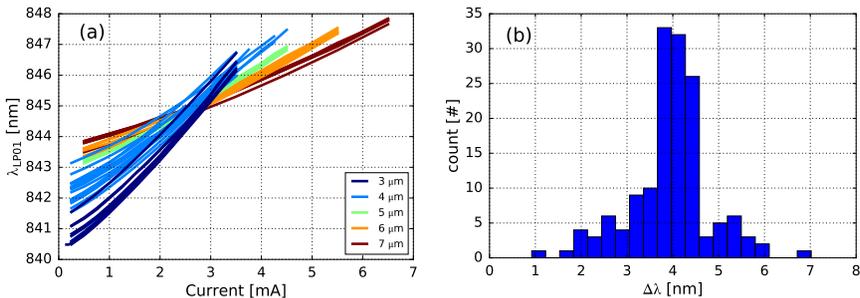
Figure 4.46: (a) Wavelength tuning range of Gen1 VCSELs and (b) Histogram of the wavelength tuning range of all devices.

Figure 4.46 translates the difference in aperture to the wavelength at the onset of lasing. The difference between the smaller and larger devices can reach more than 3 nm for devices fabricated in the same run. Between runs, with samples from various wafers, the difference can be even larger. Table 4.10 illustrates the wavelength shift normalized over the current density. The larger aperture devices show the largest wavelength shift for a specific current density. The same values for the transfer-printed waveguide-coupled VCSELs can also be found in Fig. 4.48.

$\Delta\lambda/j\ [nm/(kA.cm^2)]$	3µm	4µm	5µm	6µm	7µm
Source - Gen1	0.41	0.43	0.51	0.60	0.67
Source - Gen2	0.69	0.64	0.71	0.81	0.88
Target - Gen1	0.47 ±0.03	0.64 ±0.09	0.72 ±0.00	0.88 ±0.02	1.03 ±0.02
Target - Gen2	0.59 ±0.04	0.58 ±0.08	0.86 ±0.07	1.02 ±0.01	-

Table 4.10: The wavelength shift normalized over the applied current density for each aperture of the fabricated devices.

4.4.3.2 Thermal Performance

The devices are thermally limited in performance, due to the low thermal conductivity of the silicon oxide cladding and the surrounding BCB layer. This is translated into the early roll-over feature of the devices, at comparably low bias currents versus the bias current levels for the on-source test structures. The thermal resistance R_{th} describes the relation between the average temperature inside the VCSEL cavity and the amount of electrical power dissipated by the device. The impact of the transfer-printing on this parameter will be assessed. The method to extract the value is discussed in section 4.2.1.4 [51].

For the on-source devices, the dissipated power was derived as in equation 4.13. The top-surface emitted light was multiplied by $\left(1 + \frac{P_{DOWN}}{P_{UP}}\right)$. For the waveguide-coupled VCSELs, the variation due to misalignment and the performance of the diffraction grating made it less clear how much power was originally emitted from the VCSEL. In first order approximation, the dissipated power is equal to the input electrical power of the device. The C_1 constant in equation 4.14 consists of the relative wavelength shift for a certain power dissipation. C_1 is derived from different spectral measurements of the same device, at different bias currents as those in Fig.4.48. A summary can be found in table 4.11 and in Fig.4.49-row 6. An increase in the thermal resistance is noted after transfer-printing. This can be attributed to the lower thermal conductivity of BCB and silicon oxide, with respect to the GaAs source substrate at 0.29 (BCB) and 1.2 (SiO$_x$) vs. ~ 55 (GaAs) W m^{-1}°C^{-1} [68], [69], [70]. The higher the thermal resistance, the less power is required to scan a certain wavelength range. Associated to this, thermal roll-over is likely to occur sooner. Therefore, there is a trade-off between peak output power and power consumption to scan the wavelength range.

R_{th} [K/mW]	3µm	4µm	5µm	6µm	7µm
Source - Gen1	7.26	4.72	3.70	3.14	2.67
Source - Gen2	11.76	6.55	4.96	4.01	3.32
Target - Gen1	8.85 ±0.38	7.46 ±0.86	5.71 ±0.02	5.05 ±0.12	4.45 ±0.07
Target - Gen2	10.51 ±0.41	6.96 ±0.67	6.94 ±0.44	6.01 ±0.03	-

Table 4.11: Thermal resistance R_{th} of the fabricated and transfer-printed VCSELs.
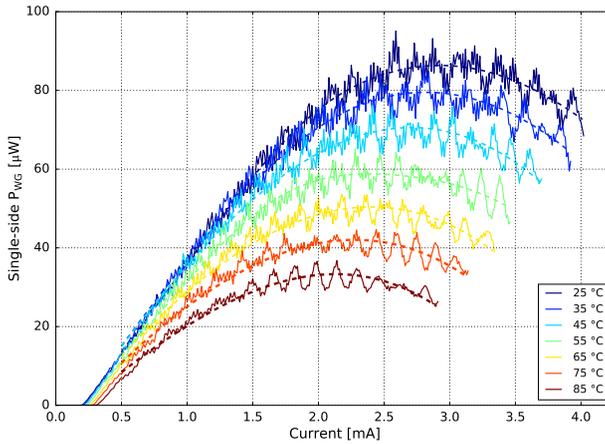
Figure 4.47: WG coupled power under different ambient (chuck) temperatures.

Even with the higher thermal resistance, the devices have similar behavior to other VCSELs at elevated temperatures. Figure 4.47 shows the LI-curves for different ambient temperatures, controlled by a heated chuck. The light is captured with a MMF. The variations in temperature between the PIC and the ambient air impede accurate alignment with a single-mode fiber. Decent WG-coupled power is achieved for the entire investigated temperature range. The net power coupled into the waveguide is more than sufficient for a multiplex refractive index sensor, is within the same order of magnitude for plasmonic-assisted Raman Spectroscopy [71], and can be used for a short-range optical link with an appropriated high-sensitivity receiver [72].

4.4.3.3   Transverse Side Mode Suppression

The origin of higher order transverse modes of VCSELs are studied in section 4.2.1.3. The side-mode-suppression-ratio (SMSR) is deduced from spectral measurements by comparing the output power of the main LP_{01} mode to the most prominent higher order mode. The waveguide-coupled power is collected in a SMF through a fiber coupler and measured with the optical spectrum analyzer. A summary of the SMSR values of the measured devices is given in table 4.12 and displayed in Fig.4.49-row 7. It is important to note that the measured values of the SMSR provide a lower limit to the device performance. The waveguide-coupled power of the VCSILs is constrained below 100 µW for a single-side coupling. For most cases, the signal lies in between -20 to -10 dBm. The measured spectral power is located around -30 to -35 dBm, by taking into account a fiber coupler insertion loss of -8 to -9 dB and a setup associated insertion loss of -1.0 to -3 dB. For SMSR

values exceeding 50 dB, the observed spectrum is close to the noise floor of the OSA. In some cases, the SMSR could not be measured and is defined as the range until the OSA noise floor. For 3 µm VCSILs, the average observed SMSR is 39.57 dB. The actual SMSR of the devices is likely closer to 50 dB.

Looking at the spectra in Fig.4.48-(a), the device with the best SMSR performance is displayed, which has a 4µm aperture, a pitch of 549 nm, a fill factor of 70% and a top oxide thickness of 850 nm. Above 1 mA, the SMSR is consistently higher than 47 dB. Similarly, Fig.4.48-(b) is a demonstration of the suppression capabilities of the diffraction grating. This device has a 4 µm aperture, a grating of 554 nm, a fill factor of 50% and a top oxide thickness of 780 nm. The side-mode suppression is dictated by the second higher order transverse mode at 845 nm. Fig.4.48-(c-i) & (c-ii) are the output spectra of both waveguides of the same device, which has a 5 µm aperture, a grating of 549 nm, a fill factor of 70% and a top oxide thickness of 780 nm. Given the discrepancy between both sides, the transfer-printing process is likely to have introduced a certain misalignment. This figure demonstrates that it is possible to design diffraction gratings that suppress the higher order modes. In order to simulate this interaction, one needs higher order bessel-beams as light sources in a 3D FDTD environment. This is challenging from a numerical point of view and is still under development [73].

To conclude, the SMSR of the transfer-print compatible VCSELs are boosted by the integration on top of the VCSEL diffraction grating. A common definition of single-mode lasing is kept at an SMSR of 20 dB. This is, on average, achieved for devices of up to 5 µm. There are clear demonstrations where the first higher order mode is actively suppressed and there are strong indications of the influence of printing misalignment on the suppression. When 3D FDTD-solutions allow to accurately model the higher order bessel-beams along with the diffraction grating, new considerations can be made to further improve the single-mode aspects of the device. Given the partial top-side emission, there is a possibility to integrate a mode-selection filter on the surface of the top-DBR, prior to the gold-cap deposition. This way, one can expect a SMSR of 30 dB for standalone devices with aperture of up to 7 µm [29]. The integration with a diffraction grating is a promising way to boost this SMSR-value even further from a joint top & bottom mode filtering.

SMSR [dB]	3µm	4µm	5µm	6µm	7µm
Source - Gen1	34.20	14.24	2.11	0.75	0.55
Source - Gen2	33.25	35.75	10.94	1.51	0.49
Target - Gen1	40.25 ±5.28	41.38 ±3.58	17.76 ±2.94	9.05 ±2.81	6.51 ±1.89
Target - Gen2	39.01 ±2.55	34.51 ±9.03	21.31 ±5.78	14.03 ±3.22	-

Table 4.12: Side Mode Suppression Ratio (SMSR) for the fabricated VCSELs.
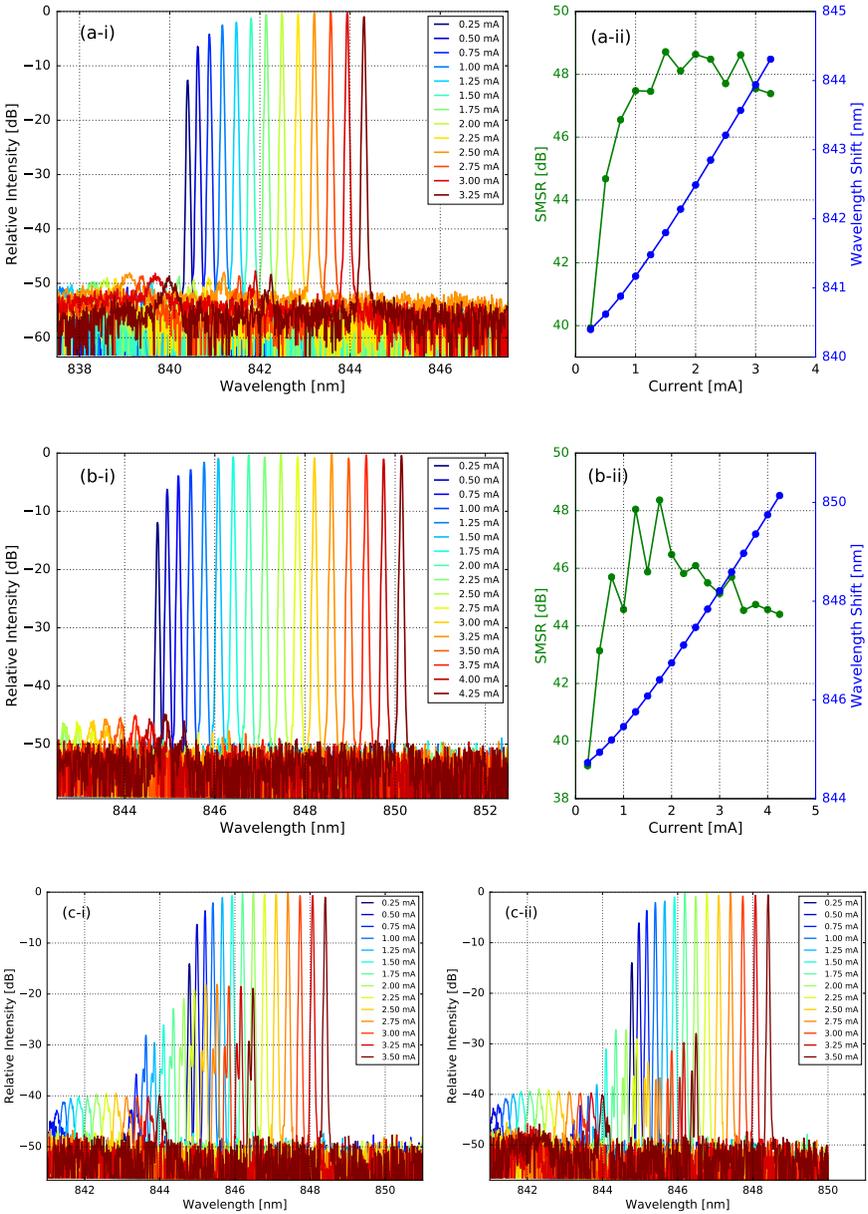
Figure 4.48: Optical spectra at different VCSEL bias currents (i), with the corresponding SMSR and wavelength tuning range in (ii) for (a) a waveguide-coupled VCSEL with the highest reported SMSR and (b) the best example of first higher order mode suppression. (c-i) and (c-ii) show the optical spectra with different behavior of the higher order transverse modes for the same VCSEL for the left and right output waveguide respectively.
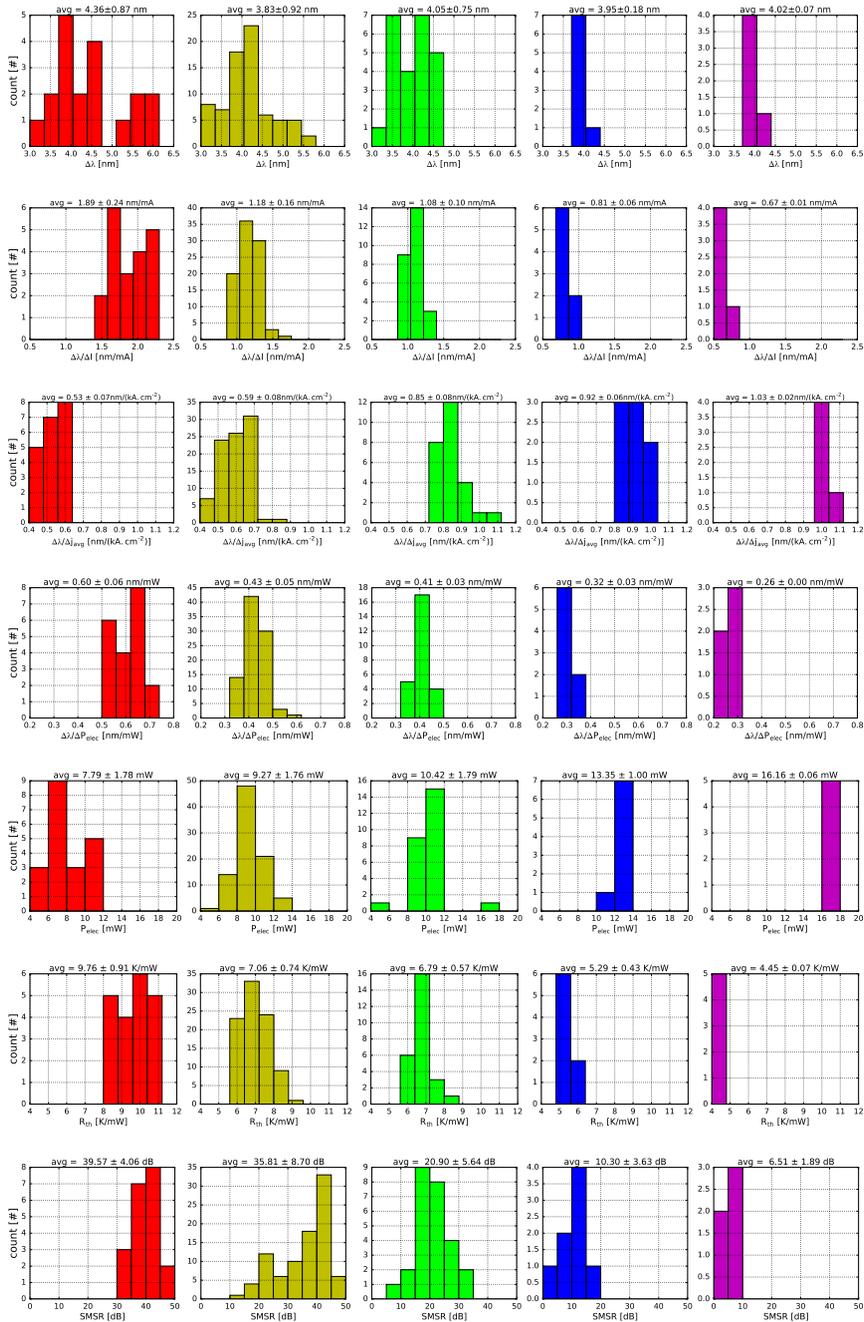
Figure 4.49: *Spectral properties separated by aperture size, starting with the 3µm devices on the left side (red), to the 7 µm devices on the right side (magenta): the total wavelength shift $\Delta\lambda$ in row 1, $\Delta\lambda$ normalized to the applied current in row 2, $\Delta\lambda$ normalized to the applied current density in row 3, $\Delta\lambda$ normalized to the applied power in row 4, the total power consumption in row 5, the thermal resistance values in row 6 and the SMSR values in row 7.*

4.4.4   VCSILs for wearable sensors

The following section highlights a few relevant parameters for using TP-VCSILs in sensors with the requirement of low power consumption. These sensors are typically found in wearable applications.

4.4.4.1   High-Speed Thermal Wavelength Tuning

So far, only DC power consumption and quasi-static wavelength scanning have been discussed. Switching to a higher speed wavelength scanning brings benefits for specific sensor architectures. First, accurate tracking of the sensor signal can be achieved by sampling more data points within a certain time frame. Secondly, for a specified number of data points, the overall on-time of the device can be reduced, leading to lower energy consumption. This is done by sampling the sensor in short time frames, similar to a pulsed operation mode.

The tuning capabilities of the VCSEL are dictated by the thermal characteristics of the VCSEL. The lasing wavelength is set by the average cavity refractive index. The temperature dynamics inside the cavity are defined by the thermal time constant, as mentioned in section 4.2.1.4. From the perspective of a sensor, it is important to understand how much the tuning range is influenced by the frequency of the driving signal. The tunable laser needs to maintain a certain tuning range to interrogate the sensor. The setup used in the experiment is shown in Fig.4.50.

The VCSEL in the setup is DC-biased with a current-voltage source. An arbitrary waveform generator (AWG) and a bias tee are used to apply a sinusoidal signal with 1V peak-to-peak on top of the DC bias. The light is collected from the output fiber coupler with a single-mode fiber and the optical spectrum analyzer
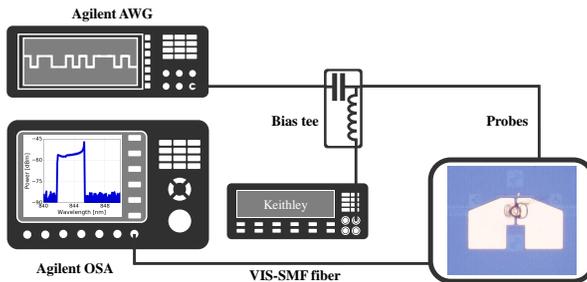
Figure 4.50: Measurement setup used to characterize the thermal tuning range of the VCSELs at high frequency driving voltages.
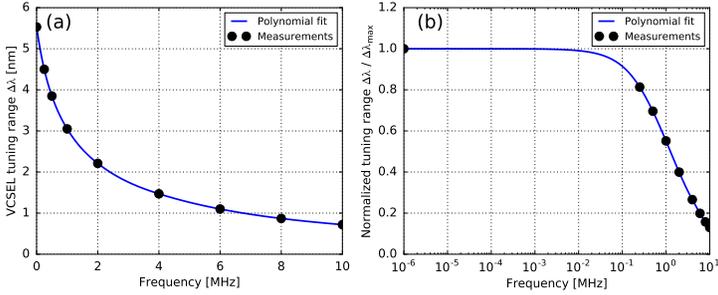
Figure 4.51: (a) Shows a reduction of the tuning range Δλ for increasing driving frequency, (b) with the same results in a normalized log-plot, showing the -3dB point at 1 MHz.

(Agilent OSA) reads out the broadband spectrum, as illustrated in the inset of Fig.4.50. The sinusoidal driving voltage translates into a tilted bathtub curve due to the V-I and I-L relationships of the VCSEL. From the edge peaks, the tuning range of the VCSIL can be determined at different driving frequencies.

Fig.4.51 shows the extent to which the tuning range decreases for increasing driving frequencies. Typical VCSEL thermal constants are on the order of 1 μs [74]. Correspondingly, the normalized -3 dB tuning range is approximately 1 MHz.

4.4.5 Comparison to the literature

The key performance indicators of the TP-VCSEL and all previously published works are summarized in table 4.13. A first remark that can be made is that all non-VCSEL and low-power lasers have planar light output, evanescently coupled in a bus waveguides. Those devices are particularly sensitive to misalignment, even for the optical lithography used with die-bonding. This architecture does not lend itself easily towards transfer-printing. Most transfer-printed electro-optic components either use diffraction gratings or alignment tolerant adiabatic tapers to reduce the impact of misalignment on performance.

There is one approach, of the H2020 PASSION project, that couples a VCSEL into a waveguide using total internal reflection with a 45° mirror. The mirror is fabricated using a crystallographic undercut of the 3μ thick silicon waveguide on the VTT platform. The performance is remarkable, although this approach of an undercut etch is not transferable to a silicon nitride platform. Therefore, a different coupling scheme is required for short wavelength VCSEL sources.

All other VCSEL-based approaches couple light through a diffraction based grating into the waveguide. The performance of the grating depends significantly

on the mode size and the grating strength. Knowing this, one should expect lower coupling efficiencies for the 850 nm SiN_x grating couplers in comparison to silicon gratings. The most direct competitor of this work is thus the die-bonded VCSIL with intra-cavity grating [34]. While the reported waveguide powers are similar, the TP-VCSEL has better performance in terms of lasing threshold, power consumption and side-mode suppression, due to being a standalone VCSEL. All of these are of great importance in biosensing applications. Moreover, the TP-VCSEL is easier to fabricate, costs less and is more scalable.

Looking at the reported waveguide-coupled powers and coupling efficiencies, it becomes clear that High-Contrast-Gratings in combination with half-VCSELs, do not live up to their simulated coupling results. This is likely due to larger misalignment sensitivity of HCGs. Regarding this, the most promising implementation is the aforementioned SiN_x-VCSIL which in fact does not use a HCG. The functionality of the HCG is rather split into two separate components with a bottom dielectric DBR for reflection and an intra-cavity grating (LCG) for coupling [34].

Finally, angled flip-chipped technology does not appear mature enough yet to be scaled towards larger volumes. The passive alignment technique in combination with the changing shape of the solder bump during reflow to introduces too much variation and misalignment to achieve high yield. Standard or vertical flip-chipping methods are therefore preferred. Still, most of these implementations do not sufficiently take polarization management into account, leading to lower coupling efficiencies. The notable exception is the tilted silicon vertical grating coupler demonstration [30]. New MEMS-based photonic platforms appear to be a suitable candidate for developing this VCSEL-based interface. The question if this strategy can be applied towards a SiN_x platform at a reasonable price, remains open. It requires additional investigation into stress management of the SiN_x layer to implement a controlled collapse of the grating coupler. The processing approach for the SiN_x wafers is more straightforward in the proposed approach of TP-VCSILs.

Reference	Laser Type & Integration	PIC-technology	λ [nm]	I_{th} [mA]	Slope efficiency [W/A]	R_{ap} [μm]	Max. P$_{WG}$ [μW]	Coupling Efficiency [dB]	SMSR [dB]
This work	μTP BE VCSEL-on-bidirectional GC	biopix 300 nm (imec)	845	0.16-0.20	0.42 (vert.) & 0.04 (SS-WG)	4±1	85 (SS) & 140 (DS) at 3.0 mA	-10.64 to -9.17 (SS) -7.93 to -6.46 (DS)	>40
Ruan et al. [30]	Vertical FC VCSEL-on-Si-VGC	O-Band SiPho, released and tilted VGC	1310	1.0	0.073	~ 4	660 at 10mA	-5.4	50
Haglund et al. [29]	Angled FC VCSEL-on-SiN with mode field P-filter	biopix 300 nm *not published (imec)	850	0.4	1.2	5 (ox. aperture) 3 (mode aperture)	104* at 3mA	-13.82*	>30
Aalto et al. [31]	Flip-chipped VCSEL on 45° etched Si-WG	3μm C-Band-SOI (VTT)	1550	<2.5	~ 0.3	N.A.	~ 1000 at 14.2 mA	-4.4	>35
Kumari et al. [34]	Die-Bonded Half-VCSEL-on-bidirectional GC	custom biopix 300 nm, substrate dielectric DBR	855	1.13	0.45 (vert.) & 0.08 (SS-WG)	5	73 (SS) & 140 (DS) at 2.6 mA	-12.52 (SS) -9.68 (DS)	29
Crosnier et al. [26]	Die-Bonded InP 1D PhC with evanescent coupling	C-Band SiPho	1550	0.1	NA	15 (L_{cav})	100 at 0.5 mA	-0.32	>60
Yang et al. [36]	FC-VCSEL-on-transparent submount, die-bonded to PIC	O-Band SiPho (Leti)	1330	0.7	0.064 (WG)	<6	126 at 3.7mA	-7.92	49
Li et al. [38]	Die-Bonded BE VCSEL on binary blazed GC	C-Band SiPho (220nm)	1550	NA	NA	5	126 at 7mA	-4.87	~ 45
Lu et al. [28]	Angled FC VCSEL-on-Si (no Polarization control)	C-Band SiPho	1547	1.25	0.012	NA	138 at 13.5mA	-11.8	35
Park et al. [33]	Optically-pumped & Die-Bonded Half-VCSEL	C-Band SiPho, with SS-coupling via HCG	1486	1.1	NA	~ 5	0.013, at P$_{pump}$=110 μW	-39.2*	27.5
Wang et al. [35]	Vertical FC VCSEL on bidirectional GC	Custom SiPho 300nm Si & 800nm BOX	NA	~ 1.1	~ 0.01	NA	65 at 10.0mA	-13.5 (SS)	NA
Kaur et al. [27]	Vertical FC VCSEL through-prism-VGC	C-Band SiPho (220nm), off-nominal VGC	1550	1	NA	NA (<3)	6.76 at 5.0mA	-17.7	>40
Ferrara et al. [32]	Vert. FC Half-VCSEL on Si-HCG	Custom SOI, without in-plane WG-coupling	1578	7	0.3 (vert.)	8	NA	NA	>40
Zhang et al. [25]	Microring Laser with evanescent bus WG	O-Band SiPho (imec)	1340	12.3	0.077	50 (R$_{ring}$)	1000 at 42 mA	NA	15
Liu et al. [24]	Microdisk Laser with evanescent bus WG	C-band SiPho (220nm) (imec)	1550	0.3	0.014	3.5 (R$_{disk}$)	20 at 2.5mA	NA	25
Van Campenhout et al. [23]	Microdisk Laser with evanescent bus WG	C-band SiPho (220nm) (imec)	1550	0.5	0.03	3.75 (R$_{disk}$)	10 at 1.6mA	-3.37 (simulated)	25

Table 4.13: A comparison between key performance indicators of different low-power

4.5   Conclusions and outlook

Within this chapter, we have introduced and demonstrated the concept of a transfer-print-compatible, bottom-emitting VCSEL on a SiN_x waveguide platform. At the start, the state-of-the-art of low-power integrated lasers was summarized. Next, the reader was briefly introduced to some of the fundamental concepts in VCSEL design and the most relevant performance parameters for this work.

The simulations of the VCSEL diffraction grating discussed in section 4.2.2, illustrated the viability of the waveguide-coupled concept. With careful design, the diffraction grating can demonstrate higher reflection of the TE-mode over the TM-mode. This difference can raise up to 16% for certain pitch and fill factors combinations. The resulting single-mode gain thresholds are 400 cm^{-1} and 550 cm^{-1} for the TE and TM polarization, respectively.

A detailed list of all practical aspects, such as epitaxial layer design, the chosen process flow and possible pitfalls and improvements for that process flow are given in section 4.3.

For the final major section of this chapter, the results of the transfer-printed VCSELs are presented. We have demonstrated competitive results in terms of standalone laser performance. This indicates that the transfer-printing method does not negatively impact the device performance. Moreover, we have achieved highly competitive waveguide power levels and coupling efficiencies for a silicon nitride waveguide platform at 850 nm. By doing so, a key target of the PIX4life project is demonstrated by integrating a narrowband and low-power-consumption tunable laser on the biopix platform.

When looking at previously published work on low-power consuming waveguide-coupled lasers, it is clear that the presented work is better in terms of compatibility with wafer-scale manufacturing, coupling efficiency and single-mode behavior. Next to this, lasing occurs at lower thresholds compared to other 850 nm alternatives and the reported waveguide-coupled powers are comparable. Also, most of the aforementioned points remain valid for the comparison to proposed C-band solutions. Some reported cases achieve higher waveguide powers and coupling efficiency, either due to active alignment or with a SiPho-based MEMS solution. However, these are not necessarily transferable to SiN_x.

Over the course of the chapter, key areas of improvement have been identified and recommendations have been made. A summary of those recommendations on the three main areas of work are as follows:

- VCSEL design: It is valuable to investigate methods to increase single-mode

characteristics for larger aperture diameters. One possible way is through the introduction of a mode selection grating filter. This is defined on the surface of the top-DBR and prior to the gold cap deposition. Besides transverse mode suppression, it can also offer additional polarization control [29]. Though, it remains to be studied whether the feedback effect is strong enough to constrain the mode effectively.

- Process Flow:

  (a) Changes have to be made to address yield for automated printing. By not depositing dedicated p-pads on the coupon, the issue of coupon delamination to the stamp is likely mitigated.

  (b) It remains unclear whether annealing the contacts after the deposition of the gold cap influences the properties of the gold cap as a mirror.

  (c) Improve the high-speed characteristics by introducing a low-k dielectric such as BCB to isolate the P-probe pad from the n-contact.

  (d) Lastly, improvements can still be made that offer larger flexibility in measure-ready-devices that have a larger footprint by (1) increasing nitride passivation further to avoid pin-holes to withstand the longer etch time (2) switching to the AlAs release layer system that reduces the etch time for the current process flow.

- PIC design:

  (a) From this first iteration work, a selection of diffraction gratings in terms of pitch, fill factor and grating length showcased better performance and can act as baseline for next iterations.

  (b) A follow-up investigation on the suppression characteristics of the diffraction grating can be exploited for future designs. The use of Bessel beam FDTD sources can deliver a better understanding of the complex coupling behavior. The Fabry-Pérot induced ripple on the LI measurement can also be addressed by including tilted grating couplers and increasing the unit test length to better match application circuits.

To conclude, the work discussed in this chapter demonstrated a promising integration method of low-power-consumption narrowband tunable lasers onto a silicon nitride waveguide platform. The devices are ideally suited for interrogating small FSR Mach-Zehnder based biosensors. The current performance levels facilitate complex architectures. Nevertheless, there is still room for improved performance in next iterations of the TP-VCSILs.

References

[1] D L Huffaker, L A Graham, H Deng, and D G Deppe. *Sub-40 μA continuous-wave lasing in an oxidized vertical-cavity surface-emitting laser with dielectric mirrors*. IEEE Photonics Technology Letters, 8(8):974–976, aug 1996.

[2] Delai Zhou, Jean-Francois Seurin, Guoyang Xu, Alexander Miglo, Daizong Li, Qing Wang, Mukta Sundaresh, Sam Wilton, Joe Matheussen, and Chuni Ghosh. *Progress on vertical-cavity surface-emitting laser arrays for infrared illumination applications*. In James K Guenter and Chun Lei, editors, Vertical-Cavity Surface-Emitting Lasers XVIII, volume 9001, pages 93–103. International Society for Optics and Photonics, SPIE, 2014.

[3] Nasibeh Haghighi, Gunter Larisch, Ricardo Rosales, Martin Zorn, and James A. Lott. *35 GHz Bandwidth with Directly Current Modulated 980 nm Oxide Aperture Single Cavity VCSELs*. Conference Digest - IEEE International Semiconductor Laser Conference, 2018-Septe:245–246, 2018.

[4] Optics.org. *Finisar readies Sherman plant for VCSEL production*, 2018.

[5] Jose Pozo and Elena Beletkaia. *VCSEL Technology in the Data Communication Industry*. PhotonicsViews, 16(6):21–23, 2019.

[6] Anjin Liu, Philip Wolf, James A. Lott, and Dieter Bimberg. *Vertical-cavity surface-emitting lasers for data communication and sensing*. Photonics Research, 7(2):121, 2019.

[7] A. Larsson, E. Simpanen, J. S. Gustavsson, E. Haglund, E. P. Haglund, T. Lengyel, P. A. Andrekson, W. V. Sorin, S. Mathai, M. Tan, and S. R. Bickham. *1060nm VCSELs for long-reach optical interconnects*. Optical Fiber Technology, 44(May 2017):36–42, 2018.

[8] Anders Larsson and Johan S Gustavsson. *Single-Mode VCSELs*, pages 119–144. Springer Berlin Heidelberg, Berlin, Heidelberg, 2013.

[9] A Larsson. *Large aperture 850 nm VCSELs operating at bit rates up to 25 Gbit/s*. Electronics Letters, 44(15):907–908(1), 2008.

[10] Anders Larsson, Petter Westbergh, Johan S. Gustavsson, Erik Haglund, and Emanuel P. Haglund. *High-speed VCSELs and VCSEL arrays for single- and multi-core fiber interconnects*. Vertical-Cavity Surface-Emitting Lasers XIX, 9381:93810D, 2015.

[11] K Szczerba, T Lengyel, M Karlsson, P A Andrekson, and A Larsson. *94-Gb/s 4-PAM Using an 850-nm VCSEL, Pre-Emphasis, and Receiver Equalization*. IEEE Photonics Technology Letters, 28(22):2519–2521, nov 2016.

[12] II-VI Incorporated. *II-VI Incorporated Introduces 56 Gbps PAM4 VCSEL Arrays for 400 Gigabit Ethernet Transmission*, 2019.

[13] European Union Seventh Framework Council. *H2020 PASSION*, 2020.

[14] Junko Yoshida. *EE Times*, 2019.

[15] SensePhotonics. *940nm Global Shutter Flash LiDAR with 200-Meter Range for Mass-Market Automotive Applications*, 2021.

[16] Optics.org. *VCSELs to feature in production vehicle lidar systems from 2022*, 2020.

[17] AMS. *AMS as leading VCSEL Supplier*, 2020.

[18] Giuseppe Antonacci, Jeroen Goyvaerts, Haolan Zhao, Bettina Baumgartner, Bernhard Lendl, and Roel Baets. *Ultra-sensitive refractive index gas sensor with functionalized silicon nitride photonic circuits*. APL Photonics, 5(8), 2020.

[19] Dhruv R. Seshadri, Ryan T. Li, James E. Voos, James R. Rowbottom, Celeste M. Alfes, Christian A. Zorman, and Colin K. Drummond. *Wearable sensors for monitoring the physiological and biochemical profile of the athlete*. npj Digital Medicine, 2(1), 2019.

[20] Krzysztof Kobielak, Eve Kandyba, and Yvonne Leung. *Skin and Skin Appendage Regeneration*. Elsevier Inc., 2015.

[21] D. Martens, P. Ramirez-Priego, M. S. Murib, A. A. Elamin, A. B. Gonzalez-Guerrero, M. Stehr, F. Jonas, B. Anton, N. Hlawatsch, P. Soetaert, R. Vos, A. Stassen, S. Severi, W. Van Roy, R. Bockstaele, H. Becker, M. Singh, L. M. Lechuga, and P. Bienstman. *A low-cost integrated biosensing platform based on SiN nanophotonics for biomarker detection in urine*. Analytical Methods, 10(25):3066–3073, 2018.

[22] Bakr Ahmed Taha, Yousif Al Mashhadany, Mohd Hadri Hafiz Mokhtar, Mohd Saiful Dzulkefly Bin Zan, and Norhana Arsad. *An analysis review of detection coronavirus disease 2019 (Covid-19) based on biosensor application*. Sensors (Switzerland), 20(23):1–29, 2020.

[23] J Van Campenhout, P Rojo Romeo, P Regreny, C Seassal, D Van Thourhout, S Verstuyft, L Di Cioccio, J-M Fedeli, C Lagahe, and R Baets. *Electrically Pumped InP-Based Microdisk Lasers Integrated with a Nanophotonic Silicon-On-Insulator Waveguide Circuit*. Opt. Express, 15(11):6744–6749, 2007.

[24] Liu Liu, Thijs Spuesens, Günther Roelkens, D. Van Thourhout, P. Regreny, and P. Rojo-Romeo. *A thermally tunable microdisk laser built on a IIIV/Silicon-on-insulator heterogeneous integration platform*. IEEE Photon. Technol. Lett, 22(17):1270–1272, 2010.

[25] Chong Zhang, Di Liang, Geza Kurczveil, John E. Bowers, and Raymond G. Beausoleil. *High temperature hybrid silicon micro-ring lasers with thermal shunts*. Conference on Lasers and Electro-Optics Europe - Technical Digest, 2015-Augus, 2015.

[26] Guillaume Crosnier, Dorian Sanchez, Sophie Bouchoule, Paul Monnier, Gregoire Beaudoin, Isabelle Sagnes, Rama Raj, and Fabrice Raineri. *Hybrid indium phosphide-on-silicon nanolaser diode*. Nature Photonics, 11(5):297–300, 2017.

[27] K.S. Kaur, A.Z. Subramanian, P. Cardile, R. Verplancke, J. Van Kerrebrouck, S. Spiga, R. Meyer, J. Bauwelinck, R. Baets, and G. Van Steenberge. *Flip-chip assembly of VCSELs to silicon grating couplers via laser fabricated SU8 prisms*. Optics Express, 23(22):28264, 2015.

[28] Huihui Lu, Jun Su Lee, Yan Zhao, Carmelo Scarcella, Paolo Cardile, Aidan Daly, Markus Ortsiefer, Lee Carroll, and Peter O'Brien. *Flip-chip integration of tilted VCSELs onto a silicon photonic integrated circuit*. Optics Express, 24(15):16258, 2016.

[29] Erik Haglund, Mehdi Jahed, Johan S. Gustavsson, Anders Larsson, Jeroen Goyvaerts, Roel Baets, Gunther Roelkens, Marc Rensing, and Peter O'Brien. *High-power single transverse and polarization mode VCSEL for silicon photonics integration*. Optics Express, 27(13):18892, 2019.

[30] Ziliang Ruan, Yuntao Zhu, Pengxin Chen, Yaocheng Shi, Sailing He, Xinlun Cai, and Liu Liu. *Efficient Hybrid Integration of Long-Wavelength VCSELs on Silicon Photonic Circuits*. Journal of Lightwave Technology, 38(18):5100–5106, 2020.

[31] Timo Aalto, Mikko Harjanne, Mikko Karppinen, Matteo Cherchi, Aila Sitomaniemi, Jyrki Ollila, Antonio Malacarne, and Christian Neumeyr. *Optical interconnects based on VCSELs and low-loss silicon photonics*. In Henning Schröder and Ray T Chen, editors, Optical Interconnects XVIII, volume 10538, pages 147–159. International Society for Optics and Photonics, SPIE, 2018.

[32] James Ferrara, Weijian Yang, Li Zhu, Pengfei Qiao, and Connie J. Chang-Hasnain. *Heterogeneously integrated long-wavelength VCSEL using silicon high contrast grating on an SOI substrate*. Optics Express, 23(3):2512, 2015.

[33] Gyeong Cheol Park, Weiqi Xue, Alireza Taghizadeh, Elizaveta Semenova, Kresten Yvind, Jesper Mørk, and Il Sug Chung. *Hybrid vertical-cavity laser with lateral emission into a silicon waveguide*. Laser and Photonics Reviews, 9(3):L11–L15, 2015.

[34] Sulakshna Kumari, Emanuel P. Haglund, Johan S. Gustavsson, Anders Larsson, Gunther Roelkens, and Roel G. Baets. *Vertical-Cavity Silicon-Integrated Laser with In-Plane Waveguide Emission at 850 nm*. Laser and Photonics Reviews, 12(2):1–7, 2018.

[35] Yun Wang, Stevan S. Djordjecvic, Jin Yao, John E. Cunningham, Xuezhe Zheng, Ashok V. Krishnamoorthy, Michael Muller, Markus Christian Amann, Richard Bojko, Nicolas A.F. Jaeger, and Lukas Chrostowski. *Vertical-cavity surface-emitting laser flip-chip bonding to silicon photonics chip*. 2015 IEEE Optical Interconnects Conference, OI 2015, 6:122–123, 2015.

[36] Yisu Yang, Gligor Djogo, Moez Haque, Peter R. Herman, and Joyce K. S. Poon. *Integration of an O-band VCSEL on silicon photonics with polarization maintenance and waveguide coupling*. Optics Express, 25(5):5758, 2017.

[37] Xiyu Zhang, Yisu Yang, Kai Liu, Yongqing Huang, Xiaofeng Duan, and Xiaomin Ren. *The design of bi-layer vertical grating coupler for the hybrid integration of VCSEL with stable polarization on silicon photonics*. In Asia Communications and Photonics Conference (ACPC) 2019, page M4A.273. Optical Society of America, 2019.

[38] Hongqiang Li, Xiangdong Ma, Danyang Yuan, Zanyun Zhang, Enbang Li, and Chunxiao Tang. *Heterogeneous integration of a III-V VCSEL light source for optical fiber sensing*. Optics Letters, 41(18):4158, 2016.

[39] Muhammad Rodlin Billah, Matthias Blaicher, Tobias Hoose, Philipp Immanuel Dietrich, Pablo Marin-Palomo, Nicole Lindenmann, Aleksandar Nesic, Andreas Hofmann, Ute Troppenz, Martin Moehrle, Sebastian Randel, Wolfgang Freude, and Christian Koos. *Hybrid integration of silicon photonics circuits and InP lasers by photonic wire bonding*. arXiv, 5(7), 2018.

[40] Yi Wei Xu, Aron Michael, and Chee Yee Kwok. *Fabrication of smooth 45° micromirror using TMAH low concentration solution with NCW-601A surfactant on silicon*. In Hark Hoe Tan, Jung-Chih Chiao, Lorenzo Faraone, Chennupati Jagadish, Jim Williams, and Alan R Wilson, editors, Device and Process Technologies for Microelectronics, MEMS, Photonics, and Nanotechnology IV, volume 6800, pages 400–408. International Society for Optics and Photonics, SPIE, 2008.

[41] D. A. Louderback, G. W. Pickrell, H. C. Lin, M. A. Fish, J. J. Hindi, and P. S. Guilfoyle. *VCSELs with monolithic coupling to internal horizontal waveguides using integrated diffraction gratings*. Electronics Letters, 40(17):1064–1065, 2004.

[42] R. Michalzik and K. J. Ebeling. *Operating Principles of VCSELs*. pages 53–98. 2003.

[43] S. A. Blokhin, M. A. Bobrov, A. A. Blokhin, A. G. Kuzmenkov, A. P. Vasil'ev, Yu M. Zadiranov, E. A. Evropeytsev, A. V. Sakharov, N. N. Ledentsov, L. Ya Karachinsky, A. M. Ospennikov, N. A. Maleev, and V. M. Ustinov. *Emission-Line Width and α-Factor of 850-nm Single-Mode Vertical-Cavity Surface-Emitting Lasers Based on InGaAs/AlGaAs Quantum Wells*. Semiconductors, 52(1):93–99, 2018.

[44] Sorcha B. Healy, Eoin P. O'Reilly, Johan S. Gustavsson, Petter Westbergh, Åsa Haglund, Anders Larsson, and Andrew Joel. *Active region design for high-speed 850-nm VCSELs*. IEEE Journal of Quantum Electronics, 46(4):506–512, 2010.

[45] Yi An Chang, Jun Rong Chen, Hao Chung Kuo, Yen Kuang Kuo, and Shing Chung Wang. *Theoretical and experimental analysis on InAlGaAs/AlGaAs active region of 850-nm vertical-cavity surface-emitting lasers*. Journal of Lightwave Technology, 24(1):536–542, 2006.

[46] E G Turitsyna and S Webb. *Simple design of FBG-based VSB filters for ultra-dense WDM transmission ELECTRONICS LETTERS 20th January 2005*. Electronics letters, 41(2):40–41, 2005.

[47] Petter Westbergh, Johan S. Gustavsson, Benjamin Kögel, Åsa Haglund, and Anders Larsson. *Impact of photon lifetime on high-speed VCSEL performance*. IEEE Journal on Selected Topics in Quantum Electronics, 17(6):1603–1613, 2011.

[48] Rainer Michalzik and Karl Joachim Ebeling. *Generalized BV Diagrams for Higher Order Transverse Modes in Planar Vertical-Cavity Laser Diodes*. IEEE Journal of Quantum Electronics, 31(8):1371–1379, 1995.

[49] Å Haglund, J. S. Gustavsson, J. Vukušić, P. Modh, and A. Larsson. *Single Fundamental-Mode Output Power Exceeding 6 mW From VCSELs With a Shallow Surface Relief*. IEEE Photonics Technology Letters, 16(2):368–370, 2004.

[50] W. Nakwaski. *VCSEL structures used to suppress higher-order transverse modes*. Opto-electronics Review, 19(1):119–129, 2011.

[51] Markus Daubenschüz and Rainer Michalzik. *Parameter extraction from temperature-dependent light-current-voltage data of vertical-cavity surface-emitting lasers*. Semiconductor Lasers and Laser Dynamics VII, 9892(April 2016):98920R, 2016.

[52] Wei-Ping Huang and Jianwei Mu. *Complex coupled-mode theory for optical waveguides*. Optics Express, 17(21):19134, 2009.

[53] Dirk Taillaert, Peter Bienstman, and Roel Baets. *Compact efficient broadband grating coupler for silicon-on-insulator waveguides*. Optics Letters, 29(23):2749, 2004.

[54] Ernst-Georg Neumann. *Single-Mode Fibers*. Springer-Verlag Berlin Heidelberg, Berlin, 1 edition, 1988.

[55] Jenoptik. *Jenoptik Wafer Epitaxy*, 2021.

[56] Si-doped Gaas. *Vacancy formation in n-type silicon-doped GaAs*. (Hurle 1999):29–50, 1995.

[57] Vertical Integrated Systems (VIS). *VCSEL, PD, LED – Optical Chips*, 2021.

[58] Kent M. Geib, Kent D. Choquette, Hong Q. Hou, and B. E. Hammons. *<title>Fabrication issues of oxide-confined VCSELs</title>*. Vertical-Cavity Surface-Emitting Lasers, 3003:69–74, 1997.

[59] Kent D. Choquette, Kent M. Geib, Carol I.H. Ashby, Ray D. Twesten, Olga Blum, Hong Q. Hou, David M. Follstaedt, B. Eugene Hammons, Dave Mathes, and Robert Hull. *Advances in selective wet oxidation of AlGaAs alloys*. IEEE Journal on Selected Topics in Quantum Electronics, 3(3):916–925, 1997.

[60] Gregory C. DeSalvo. *Wet Chemical Digital Etching of GaAs at Room Temperature*. Journal of The Electrochemical Society, 143(11):3652, 1996.

[61] J. W. Lee, S. J. Pearton, C. R. Abernathy, W. S. Hobson, F. Ren, and C. S. Wu. *Investigation of wet etching solutions for In0.5Ga0.5P*. Solid State Electronics, 38(11):1871–1874, 1995.

[62] Thor Ansbæk, Elizaveta S. Semenova, Kresten Yvind, and Ole Hansen. *Crystallographic dependence of the lateral undercut wet etch rate of Al 0.5 In 0.5 P in diluted HCl for III–V sacrificial release*. Journal of Vacuum Science & Technology B, Nanotechnology and Microelectronics: Materials, Processing, Measurement, and Phenomena, 31(1):011209, 2013.

[63] Joan Juvert, Tommaso Cassese, Sarah Uvin, Andreas de Groote, Brad Snyder, Lieve Bogaerts, Geraldine Jamieson, Joris Van Campenhout, Günther

Roelkens, and Dries Van Thourhout. *Integration of etched facet, electrically pumped, C-band Fabry-Pérot lasers on a silicon photonic integrated circuit by transfer printing*. Optics Express, 26(17):21443, 2018.

[64] Marc Jungo, Fabrice Monti Di Sopra, Daniel Erni, and Werner Baechtold. *Scaling effects on vertical-cavity surface-emitting lasers static and dynamic behavior*. Journal of Applied Physics, 91(9):5550–5557, 2002.

[65] Gye Mo Yang, Michael H. MacDougal, Vasily Pudikov, and P. Daniel Dapkus. *Influence of Mirror Reflectivity on Laser Performance of Very-Low-Threshold Vertical-Cavity Surface-Emitting Lasers*. IEEE Photonics Technology Letters, 7(11):1228–1230, 1995.

[66] M P van Exter, A K van Doorn, and J P Woerdman. *Electro-optic effect and birefringence in semiconductor vertical-cavity lasers*. Phys. Rev. A, 56(1):845–853, jul 1997.

[67] Yanlu Li, Diedrik Vermeulen, Yannick De Koninck, Gunay Yurtsever, Günther Roelkens, and Roel Baets. *Compact grating couplers on silicon-on-insulator with reduced backreflection*. Optics Letters, 37(21):4356, 2012.

[68] Dow Inc. *Dow CYCLOTENE™ 3022-35 Bisbenzocyclobutene (BCB) Electronic Resin*.

[69] Technical University Wien. *Silicon Dioxide Properties*.

[70] S.m. Sze and K. Ng Kwok. *Properties of Si and GaAs*. Physics of Semiconductor Devices, pages 790–790, 2006.

[71] Ali Raza, Stéphane Clemmen, Pieter Wuytens, Muhammad Muneeb, Michiel Van Daele, Jolien Dendooven, Christophe Detavernier, Andre Skirtach, and Roel Baets. *ALD assisted nanoplasmonic slot waveguide for on-chip enhanced Raman spectroscopy*. APL Photonics, 3(11), 2018.

[72] Takashi Takemoto, Hiroki Yamashita, Toru Yazaki, Norio Chujo, Yong Lee, and Yasunobu Matsuoka. *A 25-to-28 Gb/s High-Sensitivity (-9.7 dBm) 65 nm CMOS Optical Receiver for Board-to-Board Interconnects*. IEEE Journal of Solid-State Circuits, 49(10):2259–2276, 2014.

[73] Zhefeng Wu, Yiping Han, Jiajie Wang, and Zhiwei Cui. *Generation of Bessel beam sources in FDTD*. Optics Express, 26(22):28727, 2018.

[74] Klein Johnson, Mary Hibbs-Brenner, William Hogan, and Matthew Dummer. *Advances in red VCSEL technology*. Advances in Optical Technologies, 2012, 2012.

5

Ultra-sensitive refractive index sensors for wearable applications

This chapter focuses on a refractive index sensor as a demonstrator application for the opto-electronic components discussed in chapters 3 & 4. Due to delays in the development of the TP-VCSEL, the results in this chapter are limited to the characterization of Mach-Zehnder Interferometers (MZIs) as transducers of refractive index sensors. Two application cases are studied, ion-based sweat sensing for activity tracking and volatile organic compound (VOC) sensing for environmental health tracking. The ion-coating is developed by Bosch GmbH and the VOC-coating is developed by TU Vienna. The design work in this chapter is carried out by Jeroen. External partners have done the development and deposition of the coatings onto the PICs. The characterization of the transducer is executed by Michael Stumber (Bosch) for the ion-sensor and by Giuseppe Antonacci for the VOC-sensor.

5.1   Introduction to refractive index sensors.

On-chip optical waveguides can sense the surrounding environment through the evanescent tail of the guided mode inside the waveguide. Typically, the surrounding material, or cladding, is SiO_x. For biosensors, the SiO_x is removed, after which the waveguide becomes exposed to air, or to any desired coating or functionalization layer applied on top of the waveguide. This principle of waveguide-based optical sensing allows for several forms of light-matter interaction and analysis. Among others, the forms of interaction include absorption spectroscopy, Raman spectroscopy and interferometric sensing, for which refractive index changes in one optical path leads to phase changes inside the waveguides, and hence an intensity change at the output of the interferometer.

Each of those principles have advantages and disadvantages. For instance, absorption spectroscopy requires a broadband light source to interrogate the spectral regions of interest, as is also the case in glucose sensing [1]. This can either be with SLEDs or widely tunable lasers, with the latter being more difficult to integrate. Selectivity to the analyte is determined by choosing the wavelength regions where there is no cross-sensitivity with other molecules.

In contrast to that, Raman spectroscopy generates a broadband signal from a single laser pump beam. Specificity can be obtained through identification of the fingerprint spectra of the analytes in the Raman signal. The drawbacks are the low-intensity of the Raman signal, the Raman background introduced by the waveguide structure, both leading to relatively low limits of detection and tough requirements on the spectrum analyzer.

Lastly, refractive index sensors rely on an interferometric circuit. The interferometric circuit acts as a transducer of the analyte change to a phase or intensity change of the optical signal. Several different transducers, such as ring resonators, Vernier resonators, Mach-Zehnder Interferometers, Young Interferometers and others have been demonstrated previously. The drawback for refractive index sensing is that it requires a coating or functionalization layer to achieve specificity for the target analyte. The key components of a refractive index based system are fairly simple, resulting in lower cost systems compared to other techniques. It is therefore the method of choice for a low-cost wearable sensor such as an ion-sweat sensor for activity tracking or a portable gas sensor for environmental monitoring. The following sections provide a brief description of the different transducer architectures used in refractive index sensing, the state of the art on refractive index based gas sensing and the proposed approach for this work.
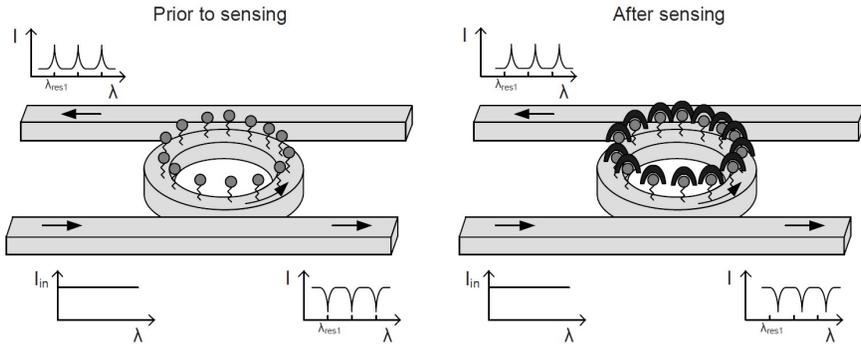
Figure 5.1: Concept of a microring refractive index sensor for which a specific analyte binding leads to a change in the resonance wavelength, expressed as $\Delta\lambda_{res}$.

Microring resonators

Single microring sensors are the most simple on-chip implementation of a refractive index transducer. Examples cover a wide range of applications such as acetylene detection [2], trinitrotoluene (TNT) [3], ammonia [4–7], acetone and dimethyl methylphosphonate [8], as well as a range of biosensors. The system has a 2π periodicity, although the phase is not the typical parameter used to describe the system. Rather, the resonance wavelength λ_{res}, or more specific, the shift in resonance wavelength $\Delta\lambda_{res}$ is used to analyze the state and/or the evolution of the system. The resonance wavelengths of these rings are described by equation 5.1, the free-spectral range (FSR) by equation 5.2 and the sensitivity (S) by equation 5.3:

$$\lambda_{res} = \frac{n_{eff}L}{m}, \quad m = 1, 2, 3, ... \tag{5.1}$$

$$FSR = \frac{\lambda^2}{n_g L} \tag{5.2}$$

$$S_{MRR} = \frac{\Delta\lambda}{\Delta n_{eff}} \propto L \tag{5.3}$$

With L the circumference of the ring, n_{eff} the effective index of the mode inside the ring, n_g the group index of the mode inside the ring and m denoting the amount of times the the wavelength of light fits inside the ring. From the above equations, it becomes clear that the circumference of the ring is the single major design parameter for basic ring resonators such as all-pass filters (APF) and add-drop filters (ADD). As a result, either the sensor sensitivity can be optimized for a given application target, or the FSR can be optimized to fall within the measurable range of the measurement setup, but not both at once. A Vernier ring filter, with a sensing and reference ring cascaded after each other, offers more flexibility. The spectral envelope (FSR$_{Vernier}$) and sensitivity (S) are defined as follows [9]:
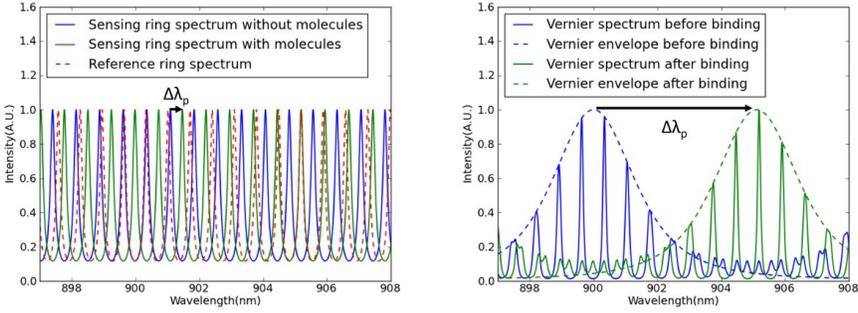
Figure 5.2: (left) Spectra of an add-drop ring resonator prior to analyte bonding (blue) and after analyte bonding (green), with a wavelength shift of the peak $\Delta\lambda_p$ occurring due to the analyte binding event. (right) Similar analyte binding spectra for a Vernier cascade ring filter with $\Delta\lambda_p$ defined between the envelope of the filter peaks, reproduced from [9].

$$p_{env} = FSR_{vernier} = \frac{FSR_s \cdot FSR_r}{|FSR_s - FSR_r|} \tag{5.4}$$

$$S = \frac{\Delta\lambda_p}{\Delta n_{eff}} \propto \pm p_{env} \cdot \frac{L_s}{\lambda_{peak}} \tag{5.5}$$

With FSR_s and FSR_r the free spectral range of the sensing ring and the cascaded reference ring, respectively, and L_s the circumference of the sensing ring. Rather than tracking a single resonance, the envelope of all resonances of the Vernier spectrum is used. $\Delta\lambda_{peak}$ is defined as the shift of the envelope spectrum, as shown in Figure 5.2. The Vernier architecture allows for more flexibility in the design, leading to a more than 10-fold improvement in sensitivity over a comparable microring resonator [10]. A brief overview of published sensitivity levels and limits of detection are shown in table 5.1.

While ring resonator based sensors have proven to be sensitive transducers, they are not perfect. The extraction of phase shift $\Delta\Phi$ is not trivial. The phase delay spectrum is asymmetric, with sharp changes at resonance and a fairly flat response in between. As such, the phase of the system can not readily be extracted at any given point along a 2π spectral period, with a consistent sensitivity. As mentioned previously, tracking $\Delta\lambda_{res}$ is a better alternative. However, this requires the measurement of a large part of the ring spectrum, ideally with a significantly high resolution at the resonance peak/dip. Afterwards, a Lorentzian function can be fitted to the measured data and the wavelength shift is defined as the shift between the 2 fitted functions of any two concentration levels. In order to obtain a good fit, one must interrogate the Lorentzian resonance with adequately high resolution. Usually a high-resolution tunable laser is used for the wavelength scanning, although this
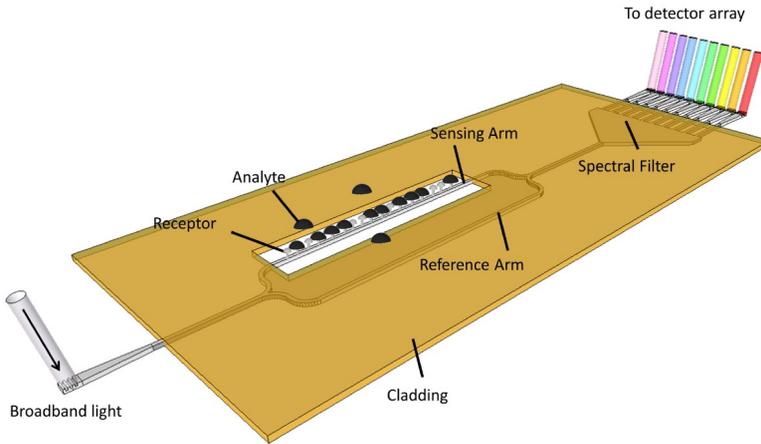
Figure 5.3: Concept illustration of a MZI based refractive index sensor, with an external broadband light source and an on-chip AWG interrogator, reproduced from [9].

is not a strict requirement for Vernier filters. A proof-of-concept demonstration of a Vernier-filter-based sensor with an on-chip AWG as interrogator was shown in [11]. This makes it a direct competitor for broadband interrogated MZI sensors. However, in a head-to-head comparison, it has been shown that the performance of the MZI sensor is better in most cases [12]. It is therefore that silicon based microring resonators, such as All-Pass filters, Add-drop filters and even Vernier filters, are not further considered in this work.

Mach-Zehnder interferometer

The on-chip Mach-Zehnder Interferometer (MZI) consists of a beam splitter, two waveguides (sensing waveguide and reference waveguide) and a waveguide combiner. An example is shown in Figure 5.3. Previous demonstrations of MZI-based refractive index sensors consist, among others, of a perchloroethylene gas sensor [13], a CO_2 and N_2 gas sensor [14], a methane gas sensor [15], an ethanol gas sensor [16], an optical pressure sensor [17], a urine based Tuberculosis sensor [18], a blood based sensor for protein detection [18, 19] and a DNA hybridization monitor [20]. The key figures of merit can be found in table 5.1. The shape of a MZI signal is described by equation 5.6, with the intensity at a MMI-combiner defined as I_{MZI}, comprising of the contributions of the sensing arm light input I_s and the reference arm I_r and the interference contribution due to the phase difference between the coated sensing arm L_s and the oxide-cladded reference arm L_r.

$$I_{MZI} = I_s + I_r + 2\sqrt{I_s I_r} \cdot cos\left(\frac{2\pi}{\lambda}(n_{eff,s}L_s - n_{eff,r}L_r)\right) \qquad (5.6)$$

The sinusoidal output of the MZI is better suited for signal processing than the Lorentzian shape of the microring filters. Various read-out and signal processing methods have been demonstrated in literature and are also highlighted in table 5.1. Some of these are discussed in more detail in section 5.2. A broad classification of the applied methods is as follows:

1. λ_{fixed} & intensity tracking

2. λ_{fixed} & coherent phase tracking - used in this work

3. λ_{broad} (Laser or SLED) & λ_{res} tracking - used in this work

4. λ_{broad} (Laser or SLED) & phase tracking

Using a fixed wavelength laser with a single MZI is not ideal. The sensitivity of the standard configuration is also phase dependent with $dI/d\Phi \propto sin(\Phi)$. This results in a dip in sensitivity near the intensity extrema of the sinusoidal signal.

Similarly, in the second method, the accuracy of the deduced phase shift varies when using a single read-out output. The minimum detectable phase shift increases rapidly near the extrema of the signal. It is therefore better to implement a 90° or 120° hybrid coupler [21, 22].

A broadband light source, such as a tunable laser or a SLED, allows to capture the entire 2π spectrum, if the sensor is designed well. Given that the 2π spectrum is captured, the varying sensitivity issue is not a concern in this approach. As the measurement captures the wavelength response of the MZI, the easiest parameter extraction is the wavelength shift, which is most commonly done. However, it is trivial to switch back to an expression of phase change, as the entire phase spectrum over wavelength is captured.

Thus far, there have been demonstrations in literature of MZI readout using a broadband light source in combination with on-chip spectrometers. Such a configuration can be used for low-cost, point-of-care sensors where the PIC is used as an expendable cartridge. An external SLED and an external imager are used for light generation and light capture [18]. Another option has been to also integrate both the SLED and the detector array on chip. This targets dedicated and longer lasting sensors [19].
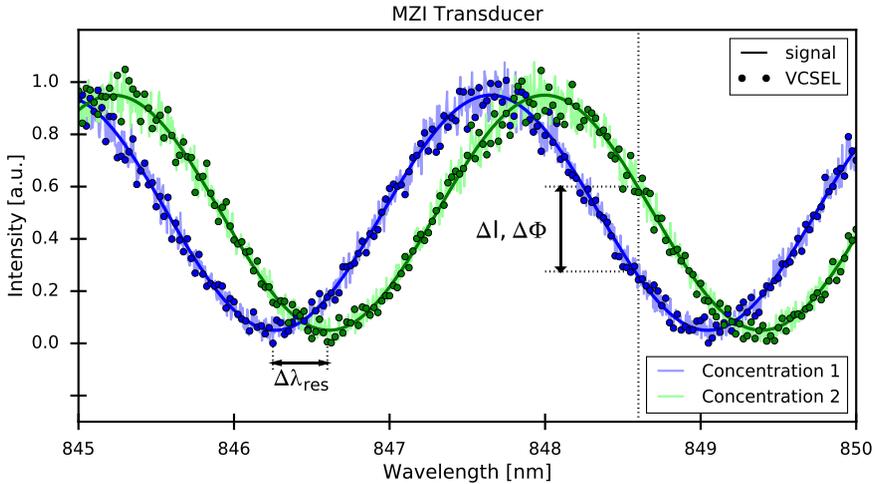
Figure 5.4: Read-out of a MZI as a bio-sensing transducer. Upon a concentration change, the phase difference between both arms changes, resulting in a shifted spectrum. With a fixed laser (dashed vertical line), phase and intensity variations are monitored. With spectral analysis, changes in phase or in resonant wavelength are typically tracked. Signal reconstruction is based on the speed and averaging of the sampling procedure and/or scanning resolution as when sweeping the wavelength..

Currently there have been no demonstrations with on-chip integrated lasers, only external benchtop laser systems are used for interrogation. In contrast to the SLED + AWG systems, lasers have superior spectral power density, leading to higher SNR and therefore to improvements in the accuracy of the captured signal for each data point. The resolution of a tunable laser is limited by the linewidth of the laser. As a results, more data points can be captured than with an AWG, where a large number of output channels results in a large on-chip footprint. This improvement in SNR and resolution can in turn lead to improvements in curve-fitting accuracy, resulting in lower minimum detectable wavelength shifts for the same MZI transducer, assuming similar noise contributions in both cases.

An illustration of the studied laser interrogated MZI transducer can be seen in Figure 5.4, where two MZI spectra for varying concentrations of the analyte are illustrated. Artificial noise is added to closely mimic a measurement result. The underlying signal is also shown in the full line. The dot markers are the sampled measurement data of the noisy signal. Fitting the sampled data shows that a good fit can be achieved for a laser interrogated sensor in a wavelength scanning measurement. For a fixed wavelength interrogation, either intensity or phase changes can be extracted to reconstruct the underlying signal. This will be studied more in depth in section 5.2.

Reference	Analyte	System (Meas. Method)	Transducer	Sensitivity	LOD
This work Antonacci, Goyvaerts et al. [23]	acetone isopropyl alc. ethanol	BB Source & OSA (3)	MZI	0.22 nm/ppm 0.06 nm/ppm 9.12 nm/ppm	65 ppb 247 ppb 1.6 ppb
Martens et al. [18]	TBC-IgG	SLED λ_{broad} & on-chip AWG (3)	MZI	2340 nm/RIU	$6\cdot10^{-6}$
Murib et al. [20]	cDNA	SLED λ_{broad} & on-chip AWG (3)	MZI	NA	100-fM
Ghosh et al. [16]	Ethanol	Laser λ_{fixed} (1)	MZI	0.7/RIU [norm. Power]	17 ppm
Dullo et al. [15]	methane	Laser λ_{fixed} (2)	MZI	$2.67\cdot10^{-4}$ rad/ppm	17 ppm
Misaikos et al. [24]	propanol	on-chip SLED & AWG + PDs (4)	MZI	581 rad/RIU	$1.09\cdot10^{-5}$ RIU
Halir et al. [22]	Demo	Laser λ_{fixed} (2)	MZI (1x3)	1/2 (cte)	$5\ 10^{-1}$ degree
Yebo et al. [7]	Ammonia	Laser λ_{broad} (3)	APF	NA	5 ppm
Reddy et al. [25]	Toluene	Laser λ_{fixed} (2)	FP + APF	NA	28 ppb
Claes et al. [11]	Demo	SLED λ_{broad} & on-chip AWG (3)	Vernier	1070 nm/RIU	$1.6\cdot10^{-5}$ RIU
Bruck et al. [26]	Streptavidin	Laser λ_{fixed} (2)	MZI	NA	1.66 nM
Claes et al. [10]	Demo	Laser λ_{broad} (3)	Vernier	2169 nm/RIU	$8.3\cdot10^{-6}$ RIU
Orghici et al. [3]	TNT	Laser λ_{broad} (3)	APF	7.4 ppm/ppb	0.5 ppb
Iqbal et al. [27]	Streptavidin	Laser λ_{broad} (3)	APF	163 nm/RIU	60fM
Claes et al. [28]	Demo	Laser λ_{broad} (3)	APF	298nm/RIU	$4.2\cdot10^{-5}$ RIU
Densmore et al. [21]	IgG AB	Laser λ_{fixed} (2)	MZI (1x3)	NA (cte)	$4\cdot10^{-4}$ rad
Robinson et al. [2]	acetylene	Laser λ_{broad} (3)	APF	490 nm/RIU	10^{-4} RIU
Zinoviev et al. [29]	DNA	Laser λ_{fixed} (1)	MZI	NA	10 pM
De Vos et al. [30]	Streptavidin	Laser λ_{broad} (3)	ADD	NA	10ng/l 10^{-5} RIU
Passaro et al. [4]	Ammonia	Laser λ_{broad} (3)	APF	125 nm/RIU	4 ppm

Table 5.1: Select overview of transducer performance of PIC-based refractive index sensors.

Optical Gas Sensors

The main application of this work is focused on VOC-sensing. A brief overview is given of the main techniques of optical gas sensing, mainly on-chip. While several approaches use refractive index based sensors, the preferred technique can vary and is typically tailored to the target gas.

There is a lot of interest in ammonia detection for industrial and environmental monitoring. And, since breath ammonia is considered to be a bio-marker for several conditions, it is also valuable in the medical sector. The gas can be detected with split-waveguide absorbance measurements, showcasing a LOD of 50 ppm [31]. But, ammonia has a strong preferential adsorption in a ZnO nanoporous coating. Therefore, refractive index based solutions using ring resonators and MZIs have showcased LODs of $\pm$ 1 to 5 ppm [4, 7, 31], while 20 ppm can be achieved with absorption spectroscopy [32].

Another method for on-chip gas sensing is non-dispersive infrared (NDIR) sensing. Recently, a demonstration of a low-cost CO_2 sensor reached a limit of detection of 100 ppm [33], suitable for automotive application. The operation principle uses a 2D integrated cylinder, which is coated in gold. The light enters the cavities and reflects multiple times, enhancing the on-chip optical path length for the light-gas interaction. The system is designed to operate with flip-chipped IR LEDs and PDs.

Methane sensing is especially relevant for leak detection in the oil and gas market. A commonly used level is 0.1 % of the lower explosion limit (LEL), which translates to 100 ppm. One of the earlier demonstrators was built using micro-optical components, achieving a limit of detection of about 100 ppm [34]. Using absorption spectroscopy, a whole range of gasses, including methane have been detected with limits of detection ranging from 100 ppm to 20 ppm [32].

VOCs in general have adverse health effects [35]. Hence, a push for low-cost portable sensors is made for environmental and health monitoring applications. Given the wide range of VOCs, Raman sensing has been a promising candidate for multiplex sensing. As mentioned previously, the Raman signal is quite weak. To have a relevant limit of detection, the Raman solutions require similar coatings, as used in this work. The same mesoporous silica coating has a 594 ppm, 157 ppm and 53 ppm limit of detection for acetone, ethanol and isopropyl alcohol using Raman spectroscopy. Another demonstration uses HCSFA2, a superabsorbent polymer for detection of acetate, methyl salicylate and dimethyl sulfoxide with 600 ppm, 360 ppb and 7.6 ppb limits of detection, respectively [8].

Reference	Gas	Technique (Meas. Method)	Transducer	Sensitivity	LOD
This work Antonacci, Goyvaerts et al. [23]	acetone isopropyl alc. ethanol	Δn-(3)	MZI	0.22 nm/ppm 0.06 nm/ppm 9.12 nm/ppm	65 ppb 247 ppb 1.6 ppb
Zhao et al. [36]	acetone isopropyl alc. ethanol	Raman	NA	NA	594 ppm 53 ppm 157 ppm
Xia et al. [33]	CO_2	Absorption	2D Cylinder	NA	100 ppm
Tombez et al. [32]	methane	Absorption	NA	772 ppmv $Hz^{-1/2}$	20 ppm
Ghosh et al. [16]	Ethanol	Δn-(1)	MZI	0.7/RIU [norm. Power]	17 ppm
Holmstrom et al. [8]	acetate methyl salicylate dimethyl sulfoxide	Raman	NA	NA	600 ppm 360 ppb 7.6 ppb
Dullo et al. [15]	methane	Δn-(2)	MZI	$2.67 \cdot 10^{-4}$ rad/ppm	17 ppm
Stievater et al. [37]	DMMP acetone NB	Absorption	NA	NA	2 ppb 140 ppm 1.5 ppm
Yebo et al. [7]	Ammonia	Δn-(3)	APF	NA	5 ppm
Reddy et al. [25]	Toluene	Δn-(3)	FP + APF	NA	28 ppb
Orghici et al. [3]	TNT	Δn-(3)	APF	7.4 pm/ppb	0.5 ppb
Robinson et al. [2]	acetylene	Δn-(3)	APF	490 nm/RIU	10^{-4} RIU
Passaro et al. [4]	Ammonia	Δn-(3)	APF	125 nm/RIU	4 ppm
Brandenburg et al. [31]	Ammonia	Absorption	Split-WG	NA	1 ppm

Table 5.2: Select overview of demonstrations of PIC-based optical gas sensing.
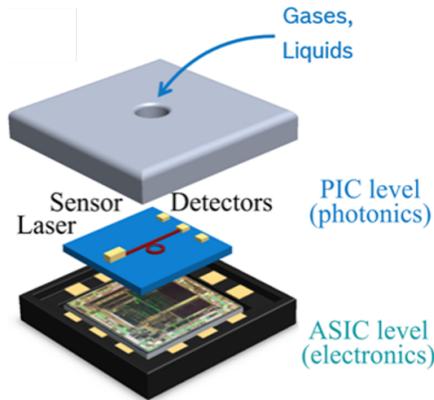
Figure 5.5: Concept illustration of a PIC-based sensor for liquid and/or gas detection. The top cover illustrates the micro-fluidic interface that guides the analyte to the coated waveguide section of the refractive index sensor.

Proposed Approach

The broader goal of this work has been to heterogeneously integrate a narrowband tunable laser (VCSEL) and photodetector by means of transfer-printing, to obtain a high performance refractive index sensor. The footprint of the sensor is reduced due to (1) using small footprint opto-electronic components, such as a VCSEL and p-i-n PD, and (2) by removing the large on-chip spectrometer/interrogator. With the transfer-print technique, fabrication complexity can be separated as much as possible, with III-V processing on the III-V substrate and utilizing the most basic passive silicon nitride waveguide platform to implement the interferometer.

By including a narrowband tunable laser, the interrogation resolution can be increased many-fold. Typically 5 to 10 sample points are used in a SLED + interrogator system, but this can increased easily to over 500 by using a 0.01 mA current resolution, as described in chapter 4. Multiplying the number of samples by 50 leads to improvements in fitting, which in turn leads to lower limits of detection than for the SLED + AWG alternative.

Within the pix4life project, the target has been to use these MZI-based transducers for ion-based sweat sensing and volatile organic compound gas detection for environmental monitoring. A concept image is shown in Figure 5.5.

Due to delays in the development of the transfer-printed VCSEL and a mid-project switch in sensing analyte, only a demonstration of the individual building blocks is achieved in this work. While the considerations for the narrowband tunable laser are still discussed in section 5.2, the discussion of the results is focused around the characterization of the transducers.

5.2   Design of a laser interrogated MZI $\triangle$n-sensor

The transducer architecture is only a part of the story of a photonic integrated sensor. The entire system consists of (1) a suitable analyte sensitive coating layer and (2) a waveguide cross-section design with an evanescent tail expanding into the surrounding medium, (3) the transducer architecture and (4) the method of reading out. The extent of the evanescent tail determines the conversion efficiency of refractive index changes of the coating to changes of the effective index of the guided mode. The response of the sensor is described by equation 5.7, which showcases the inter-dependencies starting from the concentration of the analyte, $c_{analyte}$, to the change in the refractive index of the coating, $n_{coating}$, to the change in the effective index of the guided mode, n_{WG}, to the phase argument of the MZI, Φ, to the specific signal that is being extracted of the MZI.

The sensitivity of the sensor can be broken down into these different contributions, as shown in equation 5.8 and equation 5.9, where $S_{coating}$ relates to the sensitivity of the analyte-sensitive coating; how significant the refractive index of the coating changes to varying concentrations of the analyte. Similarly, S_{WG} describes how much the effective index of the guided mode changes due to a change in the index of the coating. S_{Φ} in turn relates the change in effective index of the guided mode to the change of the phase argument of the MZI circuit. Lastly, S_{SIG}, describes how effectively the change in phase argument is translated into the signal being measured. The type of signal being measured is dependent on the type of source and read-out mechanism and is discussed in more detail in the next subsections.

$$SIG_{sensor} = SIG_{MZI}(\Phi_{MZI}(n_{WG}(n_{coat}(c_{analyte})))) \tag{5.7}$$

$$\frac{\Delta SIG_{sensor}}{\Delta c_{analyte}} \left[\frac{\text{dBm / rad / nm}}{c_{analyte}} \right] = \frac{\Delta SIG_{MZI}}{\Delta \Phi_{MZI}} \cdot \frac{\Delta \Phi_{MZI}}{\Delta n_{WG}} \cdot \frac{\Delta n_{WG}}{\Delta n_{coat}} \cdot \frac{\Delta n_{coat}}{\Delta c_{analyte}} \tag{5.8}$$

$$S_{sensor} = S_{SIG}(\Phi_{MZI}) \cdot S_{\Phi}(n_{WG}) \cdot S_{WG}(n_{coat}) \cdot S_{coating}(c_{analyte}) \tag{5.9}$$

The different contributions in equation 5.9 are discussed in the following paragraphs and subsections, starting from the coating contribution working backwards to the signal extraction from the phase change of the MZI sensor.
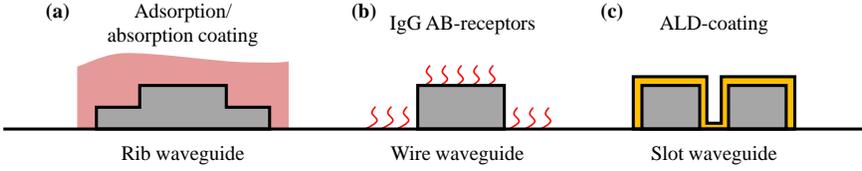
Figure 5.6: Overview of different waveguide configurations and types of coatings that can be used for waveguide-based sensing. Different combinations of each are possible. This work uses a coating similar as in (a), with a TE-wire waveguide shown in (b).

Coating

Equation 5.8 in its entirety describes the relation between the changes in the sensor signal response to the change in analyte concentration, $\Delta c_{analyte}$. The interaction of the coating with a specific analyte is highly dependent on the chemistry of the coating and the bonding interaction between the desired analyte and the coating. In this work, ion-sensitive coatings in liquids and VOC sensitive coatings are studied. The relation for $S_{coating}$ can be extracted from studying the coating response with i.e. absorption ellipsometry [38]. Depending on the signal extraction (covered in the following subsections), the general trend can be deduced from the measurements of the MZI system. The relevant analyte dependent behavior in this work is described by equations 5.10 and 5.11:

$$\Delta n_{coat,ion} = \alpha \cdot \Delta c_{analyte,ion} \tag{5.10}$$

$$\Delta n_{coat,VOC} = \alpha \cdot \Delta c_{analyte,VOC}^{1/\gamma} \tag{5.11}$$

α, β and γ are fitting parameters and are extracted from a reference or calibration measurement. The behavior is analyzed in section 5.4. A nonlinear response, such as that in equation 5.11 can have a profound effect on the sensor response. In order to characterize the transducer as a standalone component, the response is typically studied with well defined RIU liquids (salt-based) in the absence of a coating layer [10, 12, 28].

Waveguide cross-section

The second factor in equation 5.9, S_{WG}, describes the influence of the waveguide cross-section design on the change in index of the waveguide mode. Figure 5.6 shows three different combinations of waveguides with three coating layer options. From left to right, the rib, the wire and the slot waveguides are ranked in increasing

sensitivity. The high confinement in the slot makes it ideal for sensing. However, associated to the high confinement are the higher modal losses, making it more difficult to work with. Moreover, the gap between the waveguides can be too small for a uniform coverage of the coating along the entire waveguide length. So, while slot waveguides are a viable option for ALD-coating in Raman sensing and IgG coating in antibody sensing, they are less suited for thicker coatings such as ion-sensitive polymer coatings and VOC-sensitive mesoporous silica coatings. Therefore, the wire-waveguide is used in this work as the waveguide cross-section of choice.

Imbalanced MZI circuit

The next contribution in equation 5.9 is the phase sensitivity S_Φ of the imbalanced MZI. The phase argument, Φ, of the MZI function is given in equation 5.12:

$$\Phi = \frac{2\pi}{\lambda}(L_s n_s - L_r n_r) \tag{5.12}$$

Here, the effective index of the guided mode is defined as n_s and n_r for the sensing arm and the reference arm, respectively. As mentioned previously, L_s and L_r are the arm/spiral lengths of the sensing arm and reference arm of the MZI. Intuitively, one can easily expect that the sensitivity of the MZI is dependent on the arm length of the sensing arm. The definition of the MZI-phase sensitivity is shown in equation 5.13, and in equation 5.14, where the phase response in normalized between 0 and 1 instead of 0 and 2π:

$$S_\Phi = \frac{\Delta\Phi(n_s)}{\Delta n_s} = \frac{2\pi}{\lambda_0}L_s \tag{5.13}$$

$$S_{\Phi,norm} = \frac{\Delta\Phi(n_{sens})/2\pi}{\Delta n_{sens}} = \frac{L_s}{\lambda_0} \tag{5.14}$$

An important constraint on periodic transducers is the ambiguity in the phase argument for values exceeding 2π. One way around this ambiguity is to sample the signal at sufficiently high frequency, ensuring that the correct order of the periodic signal is tracked over time. The sampling frequency is highly dependent on the application; ranging from few Hz for bio-applications to kHz range ultrasound detection. Combining several MZI sensors with different sensitivities can be a simpler solution. Using the definition of a normalized phase responsivity of equation 5.14, the unambiguous sensor has $S_{\Phi,norm} = 1$ over the relevant analyte concentration range, while more sensitive sensors can have values larger than 1 (i.e. 10,100,1000). By combining their phase responses, a highly sensitive and
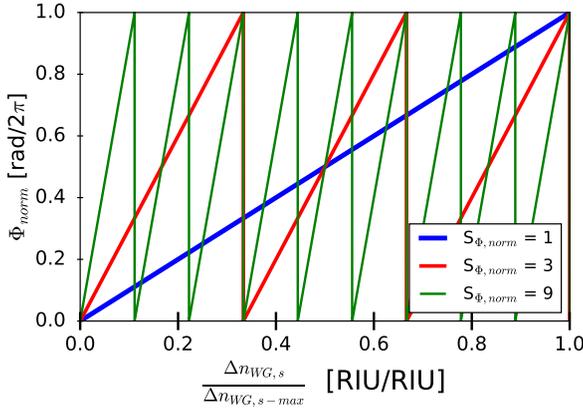
Figure 5.7: Normalized phase response for the predetermined, normalized analyte concentration range. By combining different MZI sensors, the entire concentration range is covered with high sensitivity and without ambiguity in the phase response.

non-ambiguous sensor can be designed. Figure 5.7 shows such a normalized phase response of a sensor with mixed sensitivities.

Similarly to the phase sensitivity, the free spectral range (FSR) can be intuitively understood as dependent on the difference of the arm lengths between the reference arm and the sensing arm. From the phase argument of the sinusoidal MZI response in equation 5.12, the periodicity in frequency can be derived as in equation 5.15, with $n_{g,s}$ and $n_{g,r}$ the group index of the guided mode in the reference and sensing arms:

$$p_f = FSR_f = \frac{c}{\mid L_s n_{g,s} - L_r n_{g,r} \mid} \tag{5.15}$$

After transformation, the free spectral range on a wavelength scale can be obtained as in equation 5.16 [9]. The spectral period forms a constraint on the design of the MZI, given a certain bandwidth of the narrowband tunable laser. In order to adequately sample the cosine, the spectral period must be smaller than the tuning range of the tunable laser. A good rule of thumb is half of the tuning range $\Delta\lambda$ of the laser.

$$p_\lambda = FSR_\lambda = \frac{\lambda^2}{\mid L_s n_{g,s} - L_r n_{g,r} \mid} \tag{5.16}$$

In this work, the spectral period (FSR$_\lambda$) is targeted to be between 0.5 and 2 nm, given a tuning range of approximately 5 nm for a narrowband tunable laser
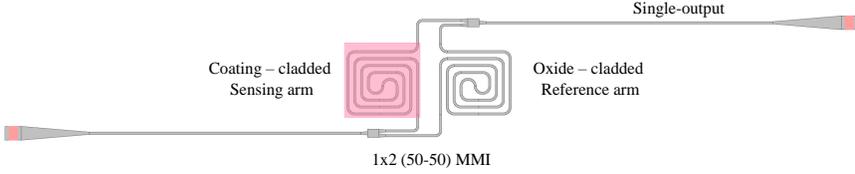
Figure 5.8: Commonly used MZI design as a Δn-sensor, using a 50/50 splitter with a single output. The left spiral sensing arm has the top SiO_x cladding removed, exposing the waveguide to the environment or coating.

like a VCSEL. If the phase-sensitivity of the MZI is chosen based on the analyte concentration range & coating sensitivity, and the spectral period of the MZI is chosen as $p_\lambda < 0.5 \cdot \Delta\lambda_{laser}$, the MZI arm lengths can be extracted. L_s is shown in equation 5.17, obtained directly from equation 5.14. L_r, on the other hand, is shown in equation 5.18 and derived from the definition of the spectral period of equation 5.16, after plugging the values of the spectral period, the sensitivity and L_s into the equation [9].

$$L_s = \mid S_{\Phi,norm} \mid \lambda_0 \tag{5.17}$$

$$L_r = \frac{1}{n_{g,r}}\Big(L_s n_{g,s} - sign(S_\Phi)\frac{\lambda^2}{p_\lambda}\Big) \tag{5.18}$$

Here, sign(S_Φ) is the signum function, which gives the sign of the sensitiviy of the phase-argument. Defining the values of the sensitivity and spectral period, the MZI design parameters, L_s and L_r can be extracted and a Mach-Zehnder interferometer circuit shown in Figure 5.8 can be designed. There, a 50/50 MMI or Y-splitter is used to split the light into two arms, the reference arm and the sensing arm. The sensing arm, as explained previously, is exposed to the surrounding environment after the top oxide cladding is removed. Afterwards, the sensor can be functionalized by applying a coating on top. At the end of the path, both reference arm and sensing arm are combined in another 2-to-1 combiner. The obtained interference pattern is recorded with a single-output channel. Equation 5.6 has previously detailed the intensity response of the MZI as a function of the phase.

Limit of Detection

Besides sensitivity, the limit of detection (LOD) is another key figure-of-merit of any sensor as it describes the lowest possible change in analyte concentration that can be detected by the sensor. Typically, the response of the registered signal is

measured over time to analyze the stability or noise floor of the sensor response. LOD_{SIG} is thus defined as the signal change equal to the standard deviation σ or 3σ of the sensor response as in equation 5.19.

$$LOD_{SIG}(c_{analyte}) = (3) \cdot \sigma_{SIG}(c_{analyte}) \tag{5.19}$$

In most reported cases, the description of the LOD is limited to that of a zero-concentration response. For this value, the LOD describes the smallest net concentration value that can be detected. However, the LOD is not necessarily constant over the entire concentration range. Equation 5.19 therefore takes a more general approach and defines an LOD for each concentration value of the analyte, $c_{analyte}$, over the relevant concentration range.

Equation 5.20 relates the minimum detectable change of the signal response to the concentration of the analyte by dividing it by the global sensor sensitivity. Similar to the description of LOD_{SIG}, the $LOD_{analyte}$ is not necessarily constant over the entire concentration range, due to a possible non-constant sensitivity S_{sensor}. It is therefore better to define the $LOD_{analyte}$ over the entire relevant concentration range.

$$LOD_{analyte}(c_{analyte}) = \frac{LOD_{SIG}(c_{analyte})}{S_{sensor}(c_{analyte})} \tag{5.20}$$

Note that, for highly sensitive MZI sensors, the LOD of the analyte does not necessarily scale down for increasing sensitivity [9]. If the dominant noise factor is not equal between both arms, and thus has a more pronounced effect on the sensing arm, the LOD will not scale down. This can be dependent on light-matter interaction at the coating layer. It thus needs to be studied independently for each application case.

Some of the most relevant sensor parameters have been introduced so far, except for S_{SIG}. This factor depends on the read-out method for the desired signal. A subdivision can be made between the fixed wavelength operation of a laser and the broadband interrogation due to wavelength tuning of the laser.

5.2.1 Fixed wavelength read-out

For the fixed wavelength read-out, there are three different subcategories that have previously been demonstrated: intensity tracking, phase tracking and coherent phase tracking. For each of those read-out methods, the $n_{WG,s}$ dependent phase argument of equation 5.12 is the underlying parameter that is being extracted.

Intensity tracking

With intensity tracking the signal analysis is limited to the recording of the change in output power for a change in analyte concentration. This is the least accurate method for analyzing the MZI response, as the sensitivity of the signal read-out is not a constant, but rather sinusoidal dependent on the phase argument. Starting from equation 5.6, the contributions can be simplified as a bias intensity I_{bias} and a varying, contribution I_{var}.

$$S_{SIG} = \frac{\Delta I}{\Delta \Phi_{MZI}}, \qquad I = I_{bias} + I_{var} \cdot cos(\Phi_{MZI})$$

$$(5.21)$$

$$= -I_{var} \cdot sin(\Phi_{MZI})$$

This dependence can be re-written in terms of the extinction ratio (ER) of the signal. As the intensity is the to-be-measured parameter, S_{SIG} benefits heavily from having large on-chip powers I_{max} and having a large ER, as evident from equation 5.23. Moreover, the sensitivity is not constant, which is not ideal. Hence this method is not ideal for extracting the phase-argument from the MZI.

$$I_{var} = \frac{I_{max} - I_{min}}{2}$$

$$(5.22)$$

$$= \frac{I_{max}}{2} \cdot \left(1 - \frac{1}{ER}\right), \qquad ER = \frac{I_{max}}{I_{min}}$$

$$|S_{SIG}| = \frac{I_{max}}{2} \cdot \left(1 - \frac{1}{ER}\right) \cdot |sin(\Phi)|$$

$$(5.23)$$

$$|S_{SIG,norm}| = |sin(\Phi)|$$

Figure 5.9 shows an example of this read-out scheme. Random, Gaussian distributed noise is added on top of the signal. The magnitude of the noise is chosen so that the ratio of the power of the signal to the standard deviation of the noise is equal to Signal-to-Sigma (StS). Depending on the exact source configuration, detector parameters and analyte behavior, the individual contributions to the noise can vary. This approach only gives a holistic overview of the net noise contribution to the amplitude of the signal, to study how the extraction of the phase-argument is dependent on the chosen signal to-be-measured.

Figure 5.9-(a) & displays the case for 10^1 StS. As mentioned, the sensitivity is non-constant, thus requiring calibration around a desired bias point (here Φ=0 in (b)). In (c), the sinusoidal sensitivity is presented, over a normalized phase range. When the sensitivity drops to zero at $k\pi$, the LOD_{SIG} increases, as is shown in

Figure 5.9: Example of an intensity-tracking read-out of an MZI sensor with noise introduced by MC based deviations on top of the signal, with (a) an uncalibrated and calibrated response around a targetted bias point. (b) Shows the calibrated and normalized response over a 2π normalized phase range, with $S_{read-out}$ in (c) and the obtained LOD_{FOM} in (d). The cosine signal has zero-sensitivity near $k\pi$, resulting in spikes in the LOD range.

figure 5.9-(d). The LOD_{SIG} is defined in equation 5.24 as the standard deviation of the difference between the measured signal and the known fitted function following the cosine response, divided by the signal sensitivity, S_{SIG}, which is a sinusoidal signal. The simulated noise of the Monte-Carlo simulations are proportional to the local signal amplitude. For different StS values profiles, the results change, as shown in (d).

$$LOD_{SIG} = \frac{3 \cdot \sigma(I_{sim} - I_{fit})}{S_{SIG}} \tag{5.24}$$

Given that the sensitivity is extremely dependent on the phase-argument, the previous reports biased the sensor at the $\pi/2$ phase point in the near-linear operating regime. In order to identify the $\pi/2$ phase point, a calibration step is necessary. This can be done with a tunable laser, but defeats the point of operating at a fixed wavelength. Another method could be to introduce a phase shifter to tune the MZI response. Moreover, phase ambiguity remains in this scheme for values where $\Phi > \pi$. Therefore we conclude that the intensity tracking method is not a viable approach to interrogate the MZI transducer.
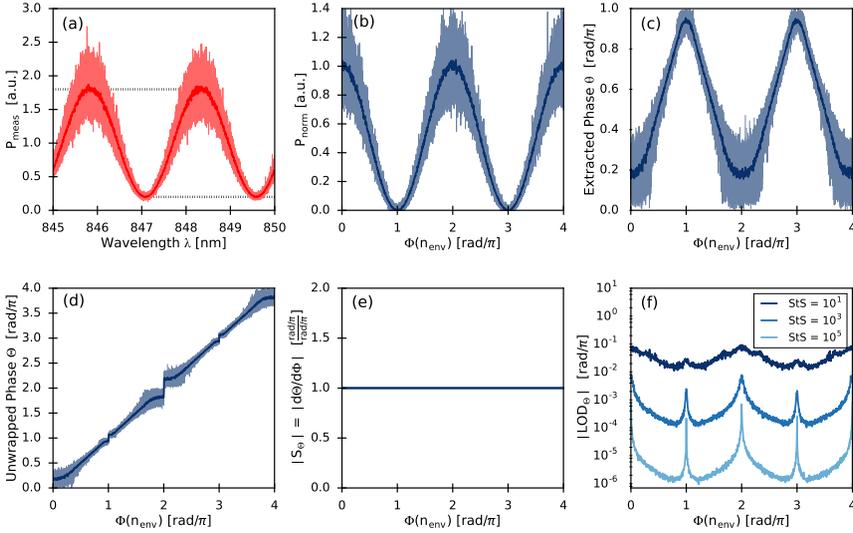
Figure 5.10: Example of a single-output phase tracking of the MZI sensor. (a) Shows a calibration step to determine I_{bias} and I_{var}. From the MC simulations in (b), the ambiguous phase is extracted in (c) and unwrapped in (d). The sensitivity of the phase response is constant, but the LOD_{SIG} in (e) has a phase-dependent variation near the $k\pi$ points.

Single output phase tracking

With the phase-tracking method, the aim is to extract the linear phase-relation from the sinusoidal intensity. To do so, the intensity has to be normalized between 0 and 1, in order to apply the inverse cosine operation of equation 5.25. To perform the normalization, a reference or calibration measurement is required to obtain I_{bias} and I_{var}. This can be done with a test measurement or with a wavelength sweep as shown in Figure 5.10-(a). The inverse cosine function aims to undo the variable sensitivity dependence of the cosine function in order to obtain a 1-to-1 linear relation between the original phase argument and the extracted phase argument.

$$\Theta_{SIG} = cos^{-1}\left(\frac{I_{meas} - I_{bias}}{I_{var}}\right) \tag{5.25}$$

The extracted phase is plotted over a 4π range in Figure 5.10-(c). The phase ambiguity between $[0\text{-}\pi]$ and $[\pi - 2\pi]$ remains. Again, if the signal is sampled at high frequency (above the frequency of any change in the environmental refractive index), the phase can be unwrapped as displayed in (d). However, due to the single output and inverse cosine function, the unwrapping method is unstable near the $k\pi$ points. For values outside the $[+1, -1]$ range, the extraction breaks down,
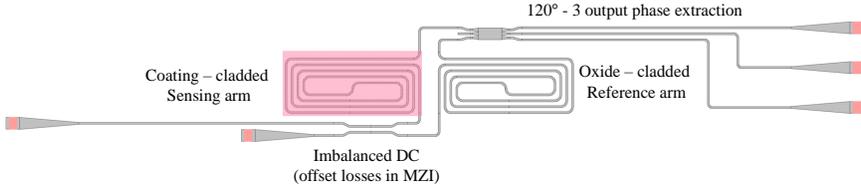
Figure 5.11: The MZI Δn-sensor used in this work, which combines a long spiral, a highly sensitive phase argument, a full phase extraction and a loss-compensating directional coupler as input splitters.

resulting in a skewed function with reduced sensitivity at the $k\pi$ points. As a result, the LOD_Θ, defined in a similar manner as in equation 5.24, in the phase space shown in (f) exhibits peaks of suboptimal LOD performance. While the method is an improvement over intensity tracking, the single-output phase tracking is not performing uniformly across the entire response range of the sensor.

Coherent, multiple output phase tracking
 The final fixed wavelength method is to do a full, non-ambiguous reconstruction of the 2π phase signal. In order to do that, a $120°$ or $90°$ hybrid coupler is required from which the different output powers p_i can be measured. An example of a modified design of the refractive index sensor used in this work is shown in Figure 5.11. In this design, an imbalanced DC is used to offset losses in the sensing arm if the propagation losses of the sensing coating are significantly larger than those for the reference arm. From the three different output powers, a complex signal, described by equation 5.26, can be obtained with transformations shown in 5.27.

$$s = x + jy \tag{5.26}$$

$$x = p_2 - 0.5p_1 - 0.5p_3$$
$$y = \frac{\sqrt{3}}{2}(p_3 - p_1) \tag{5.27}$$

Figure 5.12-(b) plots the s-signal in red onto an ellipse for an uncalibrated response. For the ideal case, the s-signal maps onto a circle. However, due to imperfections in fabrication and deviations in the splitting ratio, the mapped response can be twisted and is best described by an ellipse. Using a least-square fitting method, the function of the ellipse can be obtained from the reference measurements of the uncalibrated response in red [39]. The origin of the ellipse, and the width and length of the primary axis can be obtained from the fitting
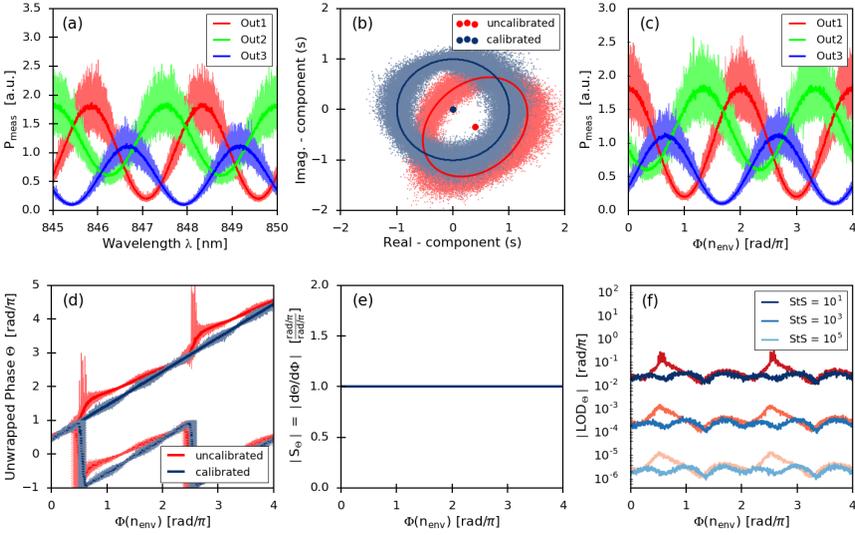
Figure 5.12: An example of the steps required for an unambiguous phase extraction measurement, with the reference calibration measurements in (a), the ellipse-to-unit circle mapping in (b) and the actual measurement in (c). The wrapped and unwrapped phase signal (over 4π range) are shown in (d) with the linear sensitivity and LOD_{SIG} in (e). With calibration, the LOD has a flat response over the entire phase range.

function. With these values, and after normalization, the transformation towards a unit circle can be defined as in equation 5.28.

$$\begin{pmatrix} c_x \\ c_y \end{pmatrix} = \begin{pmatrix} w \cdot cos(\phi) & -h \cdot sin(\phi) \\ w \cdot sin(\phi) & h \cdot cos(\phi) \end{pmatrix}^{-1} \cdot \begin{pmatrix} s_x - e_{x,o} \\ s_y - e_{y,o} \end{pmatrix} \qquad (5.28)$$

The measured data points can be mapped onto the unitary circle by using the transformation matrix. From the calibrated values, the phase can be extracted in accordance to equation 5.29. Figure 5.12-(d) shows the extracted phase values for both the uncalibrated (red) and calibrated (blue) signals. Within a 2π phase range, the signal can be unambiguously extracted. The unwrapping over an extended range can also be performed if the expected phase jumps are smaller than 2π over the measurement time.

$$\Theta_{SIG} = \arctan(y, x) \qquad (5.29)$$

The downsides of this approach is the larger footprint, the additional signal processing efforts, and the accuracy of the least-squares fitting procedure for finding the coefficients of the transformation matrix and the non-uniform sensitivity and LOD_Θ for an uncalibrated sensor. For smaller StS ratios, the accuracy of the fit reduces. Another disadvantage are the increased losses, going from a -3 dB 2-port MMI to a -5 dB 3-port MMI for combining the signal. Overall, the downsides are outweighed by the unambiguous extraction, the constant response and the independent behavior of the LOD over the phase-range after calibration. Therefore, this method is best suited for fixed wavelength measurements.

5.2.2   Wavelength interrogation

In chapter 4, the thermal wavelength tuning capability of the transfer-printed VCSEL is discussed. A 4 nm tuning range $\Delta\lambda_{laser}$ can be achieved at the peak of the LI curve, with a quasi-linear response between the VCSEL bias current and the wavelength shift. Biasing beyond the LI-peak, at 90% roll-over, the response becomes more nonlinear, while a tuning range close to 5 nm can be attained.

With the thermal tuning of the laser, a 'broadband interrogation' of the MZI can be performed. A comparison is made between laser-based and LED-based tracking of the resonance wavelength shift in the next paragraph. Following this, comments are made on the reconstruction of phase-change when using a broadband interrogation method.

Tracking of the resonance wavelength shift $\Delta\lambda_{res}$
The tracking of the resonant wavelength shift for a laser-based and a LED-based interrogation is demonstrated in Figure 5.13. The MZI response is sampled in the wavelength space. From this set of discrete measurement points, the cosine-signal can be reconstructed from a fitting procedure. The change of the resonance wavelength $\Delta\lambda_{res}$ can be readily obtained from the reconstructed optical spectrum of the MZI.

The tracking of the resonance wavelength shift entails that the phase-state $\Phi = 2k\pi$ remains constant and that a modified wavelength is found that satisfies this condition. A derivation of this condition starts in equation 5.30, where the phase arguments are compared between resonance states 0 and 1, where the wavelength difference between these two states is given by $\Delta\lambda_{res} = \Delta\lambda$.

$$\Phi(n_{s0}, \lambda_0) = \Phi(n_{s1}, \lambda_1)$$

(5.30)

$$\frac{2\pi}{\lambda_0}(L_s n_{s0}(\lambda_0) - L_r n_r(\lambda_0)) = \frac{2\pi}{\lambda_1}(L_s n_{s1}(\lambda_1) - L_r n_r(\lambda_1))$$

To bridge the change in resonance wavelength, the wavelength dependent behavior of the refractive indices have to be taken into account. This is expressed in equation 5.31, for both the sensing arm and the reference arm respectively.

$$n_{s1}(\lambda_1) = n_{s0}(\lambda_0 + \Delta\lambda)$$

$$= n_{s0}(\lambda_0) + \left.\frac{dn_{s0}}{d\lambda}\right|_{\lambda_0} \Delta\lambda$$

$$\cong n_{s0}(\lambda_0) + \Delta n_{eff,s} + \left.\frac{dn_{s0}}{d\lambda}\right|_{\lambda_0} \Delta\lambda$$

$$n_{r1}(\lambda_1) = n_{r0}(\lambda_0 + \Delta\lambda)$$

(5.31)

$$= n_{r0}(\lambda_0) + \left.\frac{dn_{r0}}{d\lambda}\right|_{\lambda_0} \Delta\lambda$$

$$\cong n_{r0}(\lambda_0) + \left.\frac{dn_{r0}}{d\lambda}\right|_{\lambda_0} \Delta\lambda$$

The change of the wavelength-factor of the phase argument of state 1 can be expressed as in equation 5.32, as the change in the wavelength range (less than a few nm) is small in comparison to the original wavelength (≈ 850 nm).

$$\frac{2\pi}{\lambda_0 + \Delta\lambda} \cong \frac{2\pi}{\lambda_0 + \Delta\lambda} \cdot \left(\frac{\lambda_0 + \Delta\lambda}{\lambda_0}\right) \cdot \left(\frac{\lambda_0 - \Delta\lambda}{\lambda_0}\right)$$

$$\cong \frac{2\pi}{\lambda_0} \cdot \left(\frac{\lambda_0 - \Delta\lambda}{\lambda_0}\right)$$

(5.32)

$$\cong \frac{2\pi}{\lambda_0} \cdot \left(1 - \frac{\Delta\lambda}{\lambda_0}\right)$$

It is now possible to plug in the relations of equations 5.31 and equation 5.32 into the phase relation of equation 5.30. After some manipulation, the relation in equation 5.33 can be obtained.

$$L_s \Delta n_{eff,s} = -\frac{\Delta\lambda}{\lambda_0}\left(L_s\left\{\left.\frac{dn_{s0}}{d\lambda}\right|_{\lambda_0} - n_{s0}\right\} - L_r\left\{\left.\frac{dn_{r0}}{d\lambda}\right|_{\lambda_0} - n_{r0}\right\}\right)$$

(5.33)

The group index, defined as in equation 5.34, is identified and substituted in equation 5.33 to obtain the final relation of equation 5.35, which relates the change in refractive index of the sensing arm, $\Delta n_{eff,s}$, to the change in the resonance wavelength $\Delta\lambda$, as function of the group index values of both the reference arm and the sensing arm.

$$n_g = n_{eff} - \lambda_0 \frac{dn_{eff}}{d\lambda_0} \tag{5.34}$$

$$\frac{\Delta\lambda}{\lambda_0} = \frac{L_s \Delta n_{s,eff}}{L_s n_{g,s} - L_r n_{g,r}} \tag{5.35}$$

From the final part, the new definition of the MZI-sensitivity for resonance wavelength tracking be readily obtained as in equation 5.36, and as a normalized sensitivity in equation 5.37. The latter normalizes the wavelength shift addressed by the targeted analyte concentration range $\Delta n_{eff,s}$, to a single FSR of the MZI.

$$\begin{aligned} S_{SIG,\Delta\lambda} &= \frac{\Delta\lambda}{\Delta n_{eff,s}} \\ &= \frac{L_s}{L_s n_{g,s} - L_r n_{g,r}}\lambda_o \\ &= \frac{L_s}{\lambda_0}p_\lambda \end{aligned} \tag{5.36}$$

$$S_{SIG,norm} = \frac{\Delta\lambda/p_\lambda}{\Delta n_{eff,s}} = \frac{L_s}{\lambda_0} \tag{5.37}$$

The definition of S_{SIG} and $S_{SIG,norm}$ for resonant wavelength tracking are identical to those obtained for the phase-change S_Φ and $S_{\Phi,norm}$. This proofs that the phase argument is unambiguously extracted over the 2π phase range, but remains confined to the range defined by the spectral period. Similar to what is described in Figure 5.7, multiple MZI-sensors can operate in parallel, with varying sensitivity levels.

Figure 5.13 shows the measurement procedure to track the resonant wavelength with a tunable laser configuration. The entire figure is presented for StS values of 10^1 and 10^2. The advantage of λ-interrogation is that the entire underlying 2π phase space can be captured with a single channel, further simplifying the PIC layout. The downside is the reduction in the sampling frequency, as 2 parameters are now scanned: wavelength over time. Previously, for a λ_{fixed} read-out, the sampling rate was defined by the bandwidth of the detector. In the case of the wavelength scanning method, the scan speed is limited by the thermal time constant of the VCSEL. However the MHz sampling frequency of the VCSEL is well above the relevant sampling speed for the most common PIC-based biosensing applications.
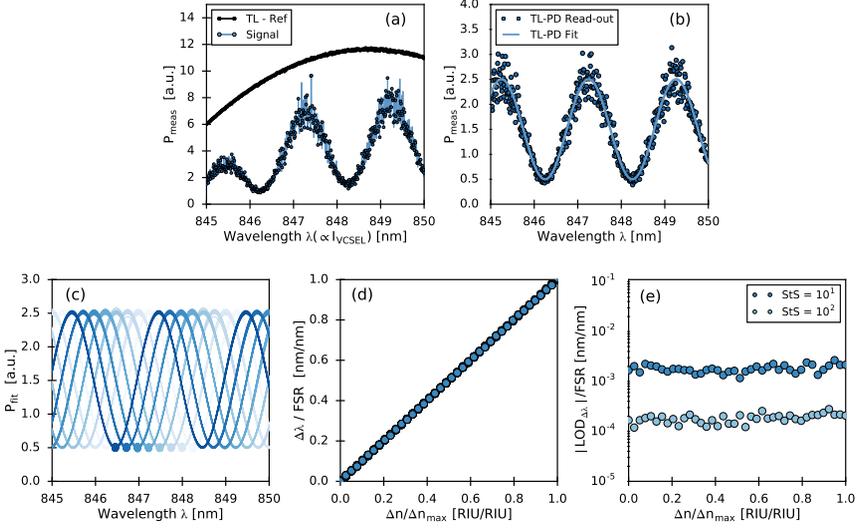
Figure 5.13: Example of the λ-interrogation by a tunable laser in blue. The reference, signal and sampling points are shown in (a). The sampled points and fits, after normalization, are plotted in (b). (c) shows the 50 MC fitted curves for 7 different concentration values. (d) Shows $\Delta\lambda_{res}/p_\lambda$ over the relevant refractive index range (no offset). (e) Shows the obtained LOD_{SIG} for the different StS values.

Tracking the phase of the λ-interrogated signal

As previously described, the wavelength interrogation captures the entire 2π phase space. From this, the phase $\Delta\Phi$ can be extracted for any given wavelength. This approach is a combination of the previous wavelength interrogation and the phase-extraction methods that are described for the fixed wavelength operation. There is no clear benefit compared to the previous method. The downside is a additional signal processing. Tracking $\Delta\lambda_{res}$ is linear in response and can be more readily obtained from a reconstructed λ-spectrum, and is therefore the preferred method.

5.2.3 PIC design

From the read-out methods described in the previous section, three-output phase tracking and resonant wavelength tracking are chosen for the final design. With the thermal tuning range of a VCSEL, the ellipse-to-circle calibration measurements can be performed in-situ.
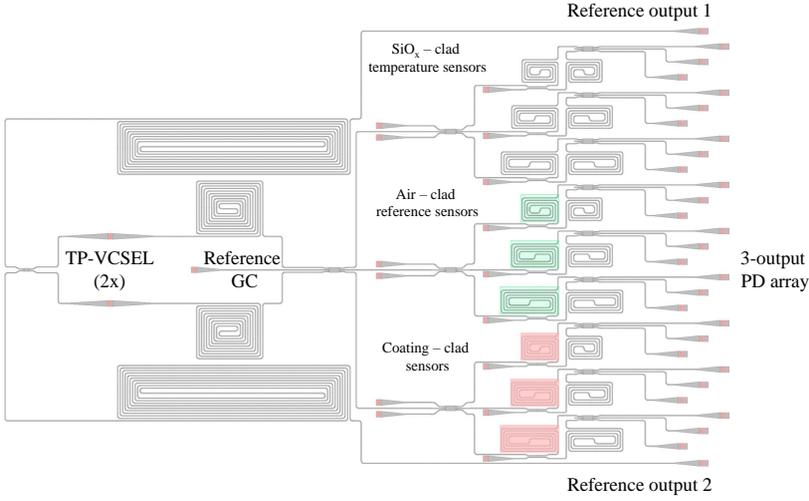
Figure 5.14: Proposed architecture of a next-generation Δn-sensor, using transfer-printed VCSELs and photodetectors for on-chip light generation and detection. There are three sets of sensors: temperature, environmental reference and analyte sensor. Each consist of 3 different sensitivities (S1 S2 S3) and three output channels for full phase-extraction.

Also, as shown in Figure 5.11, a directional coupler with an imbalanced output is used as the input splitter of the MZI. Through the power offset, the comparably high propagation losses of the polymer coating are compensated. The purpose with this offset is to obtain an equal power ratio at the input of the 50/50 combiner, as given by equation 5.38. These intensity values at the combiner can be related back to the intensities at the unbalanced splitter through their respective propagation losses, as shown in equation 5.39. In order to determine $\alpha_{coating}$, additional waveguide propagation loss test structures are required. If a suitable splitting ratio is reached, the ER increases, which aids in the accuracy of the fitting algorithms.

$$I_{s,comb} = I_{r,comb}$$

$$(5.38)$$

$$I_{s,splitter} \cdot e^{-\alpha_{WG,s} \cdot L_s} = I_{r,splitter} \cdot e^{-\alpha_{WG,r} \cdot L_r}$$

$$\frac{I_{s,splitter}}{I_{r,splitter}} = e^{-\alpha_{WG,r} \cdot L_r + \alpha_{WG,s} \cdot L_s} \qquad (5.39)$$

The required steps for designing an MZI refractive index sensor for bio and gas sensing applications are the following: (1) identifying coating response (linear vs. non-linear), (2) defining the required analyte concentration range for the application, (3) determining the coating propagation losses, (4) include an arm length / sensitivity sweep of the MZIs in Gen1 design, in order to find the appropriate arm length that
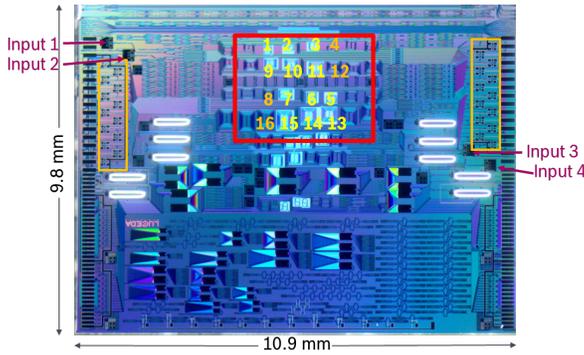
Figure 5.15: Pix4life MPW PIC with 16 MZI sensors used in this work. A single VCSEL GC drives 4 sensors, leading to 12 outputs gratings that interface with p-i-n PD arrays.

covers the desired analyte concentration range and (5) calculate L_s and L_r based on the chosen sensitivities to accommodate to the tuning range $\Delta\lambda_{laser}$ of the laser.

If information is present on the coating behavior, the change in the effective index of the guided mode can be simulated for a chosen waveguide cross-section. If it is not available, a broader range of target sensitivities has to be included for during the first design, to calibrate the waveguide cross-section overlap and the coating response. After a first iteration, the sensitivity of the photonic circuit is to be fine tuned on the desired analyte concentration range in Gen2 design.

Thus far, the change in response, ΔI, $\Delta\lambda$ or $\Delta\Phi$, have been defined with respect to the zeroth-order or environmentally stable response of the same sensor, as is commonly done in analyzing the standalone performance of a sensor. However, exposed and un-coated MZI sensors are a more suitable candidate for a final product. With these reference sensors, fluctuations in the environment (i.e. liquid), including the temperature, can be referenced out. The difficulty herein lays in selectively spotting the desired sensors during the fabrication process.

Finally, oxide-clad temperature sensors are required to measure any changes in output due to a change in the environmental temperature. These can be calibrated with respect to athermal temperature sensors if required [40]. All of the aforementioned sensors are highlighted in the proposed architecture of Figure 5.14. The figure highlights a redundant MZI sensor design, with mixed sensitivities for both the temperature and exposed reference sensors. There are two VCSEL input-coupling sites, as a form of redundancy, along with spiral based delay lines to offset the Fabry-Pérot fringes described in chapter 4. The sensor architecture serves as a design guideline for following work, while the design shown in Figure 5.15 is used for the ion-based sweat sensor in the PIX4life project.
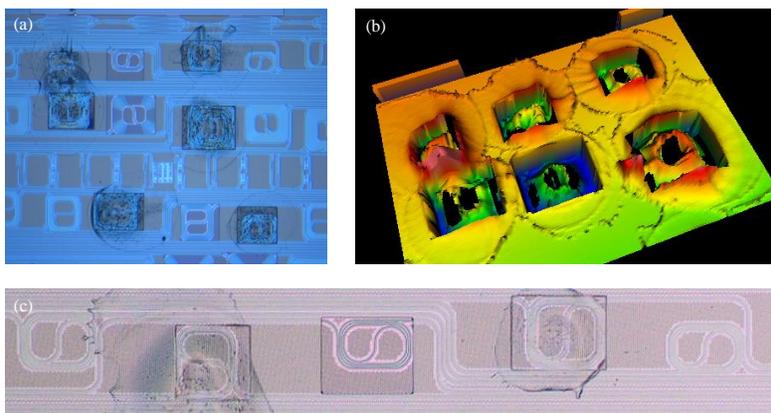
Figure 5.16: (a) PIC with Femtojet printed polymer coatings. (b) A 3D representation of a microscope image, showing the roughness and non-uniformity of the coating. (c) PIC with both sodium and potassium sensitive coatings, for a multi-parameter sensor.

5.3   Development of the analyte-sensitive coatings

In this section, the technical details of the utilized coatings are highlighted, for both the ion-sensing polymer coating and the VOC-sensing mesoporous silica coating.

5.3.1   Ion-sensitive polymer coatings

The ion selective coating is based on an organic polymer matrix, which incorporates molecules with selective ion binding sites. The individual matrix materials, known as Selectophores, are bought from Sigma-Aldrich.

The coatings are deposited with a Femtojet Express from Eppendorf International, suited for depositing small volumes of polymer matrices. The polymer coating is diluted with cyclohexanone (1:1) and then deposited under a pressure pulse.Afterwards, the coating is dried in ambient atmosphere.The results of the deposition process are shown in Figure 5.16. The coatings were not uniform, with severe topography across the spiral sensing arm of the MZI sensor. Other techniques were investigated, such as inkjet printing and array spotting. But, both of these methods suffered from cartridge blockage due to the relatively viscous PVC matrix. Attempts were made to mitigate this issue by adding surfactants into the matrix. However, due to the soap-like nature of the surfactants, the coatings delaminated upon wetting during the sensing experiments. Therefore, the Femtojet printer was used instead.
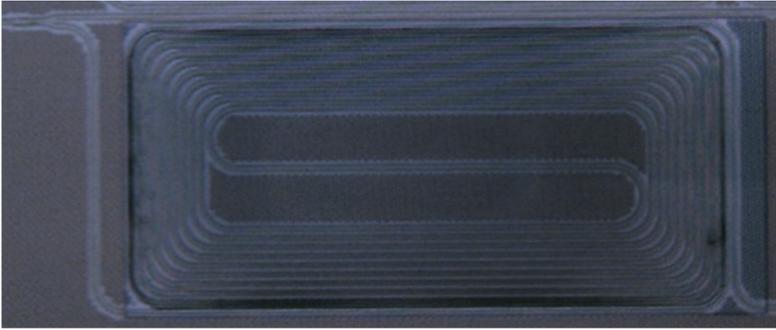
Figure 5.17: Microscope image of a mesoporous silica sensing layer, spincoated on top of the spiral sensing arm of the MZI.

5.3.2 VOC-sensitive mesoporous silica coating

The VOC coating has been developed by Bettina Baumgartner at the Research Division of Environmental Analytics of the Technical University of Vienna. The fabrication and performance of the coatings were reported [38, 41, 42]. The coatings are fabricated using acidic hydrolysis, the condensation of tetraethoxysilane in ethanol and a bromide based surfactant. The polymer gel is then spincoated on top of the PIC to create a 3D hexagonal lattice and heated up to 400 ° C to remove the surfactants. Afterwards, the surface is functionalized with a toluene-hexamethyldisilazane solution and rinsed in acetone. The resulting mesoporous coating has pore sizes in the order of $\sim$ 5 to 10 nm, and has a uniform thickness.

The coating has shown to be sensitive, with limits of detection in the 3-7 ppm range when using IR absorbance measurements [42], and within the 50-500 ppm range when using on-chip Raman spectroscopy measurements [36]. With our refractive index sensing method, the limit of detection is pushed down to the low ppb range.

The adsorption and desorption of VOCs inside the coating is completely reversible. The amount of adsorption can be modelled with the Langmuir model of monolayer adsorption or the Freundlich model of multilayer adsorption [41]. In general, the Freundlich model results in a better fit and is described in equation 5.40, which is a modified version of equation 5.11. q_e is the amount of adsorbed analyte, K_F is the Freundlich affinity constant, c is the gas concentration inside the gas chamber during measurements and n is a unitless constant. This model is thus used to fit the measurement results discussed in section 5.4.2.

$$q_e = K_F \cdot c^{1/n} \tag{5.40}$$
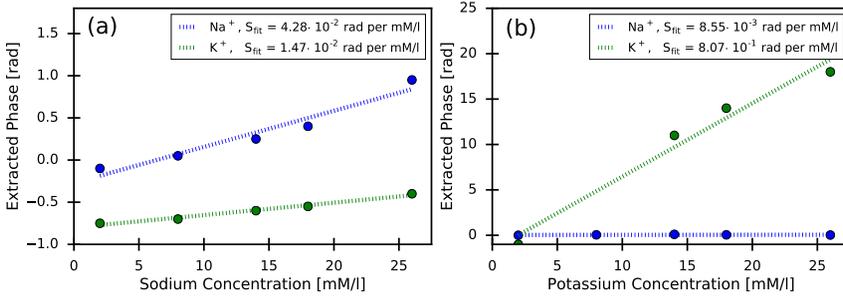
Figure 5.18: Unwrapped coherent phase response of the dual-analyte sensor with sodium and potassium sensitive coatings, under varying concentrations of (a) sodium and (b) potassium. The difference in S_Φ is attributed to the different spiral lengths of each sensor.

5.4 Measurement results of MZI Δn sensors

In this section the measurement results of both sensors are discussed. Only a limited data set is available for the ion-sensor, due to the aforementioned issues of adhesion, stability and wettability. The main focus therefore lays on the VOC sensor.

5.4.1 Ion sensor

The ion-sensor was measured with a fixed wavelength laser diode (Thorlabs DBR825S). The laser is used to monitor the power-phase response of the three-output MZI as described in section 5.2.1. The benchtop fluidic setup connected sodium and potassium concentrations to a water reservoir. By mixing the flowrate of the concentrated ion-solutions with a pure water reservoir, discrete concentrations levels (2-6-8-12 mM/l) of either sodium or potassium covered the target area of the PIC. These concentration levels cover the relevant biological range between 2 and 25 mM/l.

The measured power levels are converted into the elliptical S-signal. After calibration, the phase is unwrapped to account for changes that exceed the 2π range. The results are shown in Figure 5.18-(a) and -(b) for a PIC coated with Na^+- and K^+-sensitive coatings. The respective sensitivities of the coatings are $4.28 \cdot 10^{-2}$ and $8.07 \cdot 10^{-1}$ rad per mM/l, as indicated by the slopes of the linear fit on the figures. The difference in sensitivity is partially attributed to the different arm lengths of the various MZIs at 1550 and 2980 µm for the sodium and potassium sensor, respectively. Similarly, the cross-sensitivity of the potassium sensor is higher than for the sodium sensor at $1.47 \cdot 10^{-2}$ and $8.55 \cdot 10^{-3}$ rad per mM/l.

Due to the instability of the coating, it was difficult to assess an accurate value
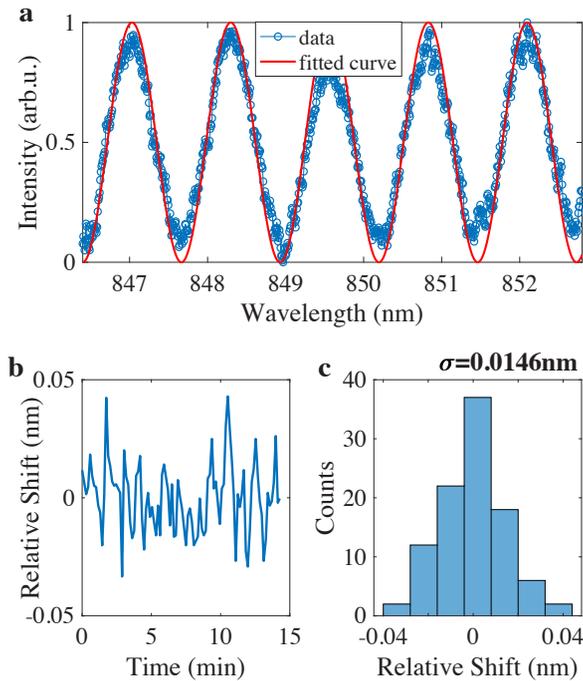
Figure 5.19: (a) Reference measurement spectrum from the OSA, normalized to the maximum transmission and with a cosine fit shown in red. (b) Shows the instrumental signal drift of the resonance wavelength (fitted) over a 15 minute time period. (c) A histogram of this relative wavelength drift of the time measurement, with a σ of 0.0146 nm.

of the limit of detection. The time response of the coating is in the minute time range. While this may be perceived as slow, the ion concentrations are not expected to change at higher frequencies in a biological environment (e.g. sweat sensor).

5.4.2 VOC sensor

The discussion is limited to the wavelength-tuning read-out of method (3). The setup consisted of the PIC inside a gas cell, kept at ambient temperature. The gas chamber has a transparent sapphire cover, allowing optical coupling to the chip using single mode fibers and on-chip grating couplers. The optical coupling is optimized with a polarization controller. Broadband light is coupled in from a supercontinuum laser (SC). Subsequently, an agilent OSA (86140B) is used to read-out a 6 nm spectrum around 850 nm, with a 500 ms exposure time. The different gas concentrations are generated with a gas generator, VICI Metronics Model 505. The concentrations range from 0.1 ppb to 100 ppm. Figure 5.19-(a)
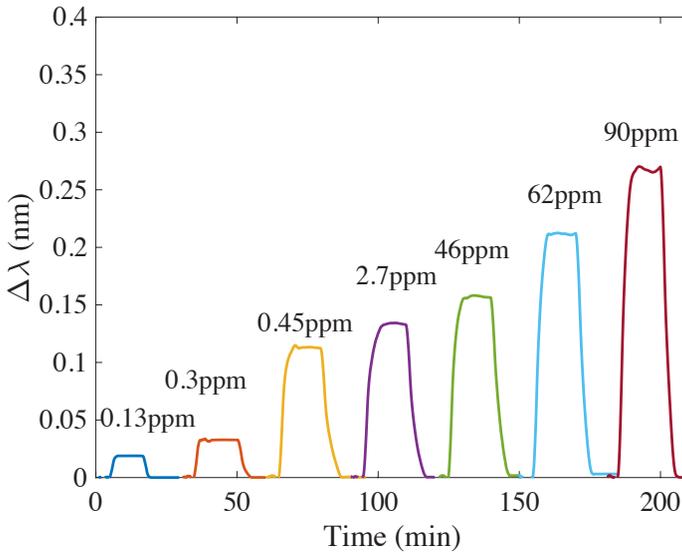
Figure 5.20: Adsorption and desorption curves for different acetone vapor concentrations, represented by the resonant wavelength shift $\Delta\lambda_{res}$ of the MZI sensor.

shows an output spectrum of the MZI, after normalization to the maximum power. The data is fitted to a cosine function shown in red. The resonance wavelength of this function is tracked over a 15 minute time duration, leading to more than 100 independent measurements. The instrumentel noise of the configured setup can be determined from the time trace in Figure 5.19-(b). A histogram of the relative shift is plotted in Figure5.19-(c), showing a standard deviation of $\sigma = 0.0146$ nm for the current exposure time of 500 ms. This is the reference LOD for the sensor consisting of the setup and PIC.

The sensor response to a gas concentration is characterized in adsorption/desorption measurements, like the one shown in Figure 5.20 for acetone concentrations. The relative wavelength shift $\Delta\lambda_{res}$, extracted from the cosine-fit of the normalized measurement spectrum, is plotted against time. Initially the chamber was conditioned with a steady flow of air diluent. Afterwards, the gas inlet is opened and a specified gas concentration enters the gas cell. It then flows over the PIC for a duration of 15 minutes, to ensure that the steady-state regime of the adsorption cycle is reached. Afterwards, air diluent is again inserted into the measurement gas cell for 15 minutes, this time to ensure a complete desorption of the coating. The MZI spectrum is collected every second, to accurately track the wavelength shift over time.
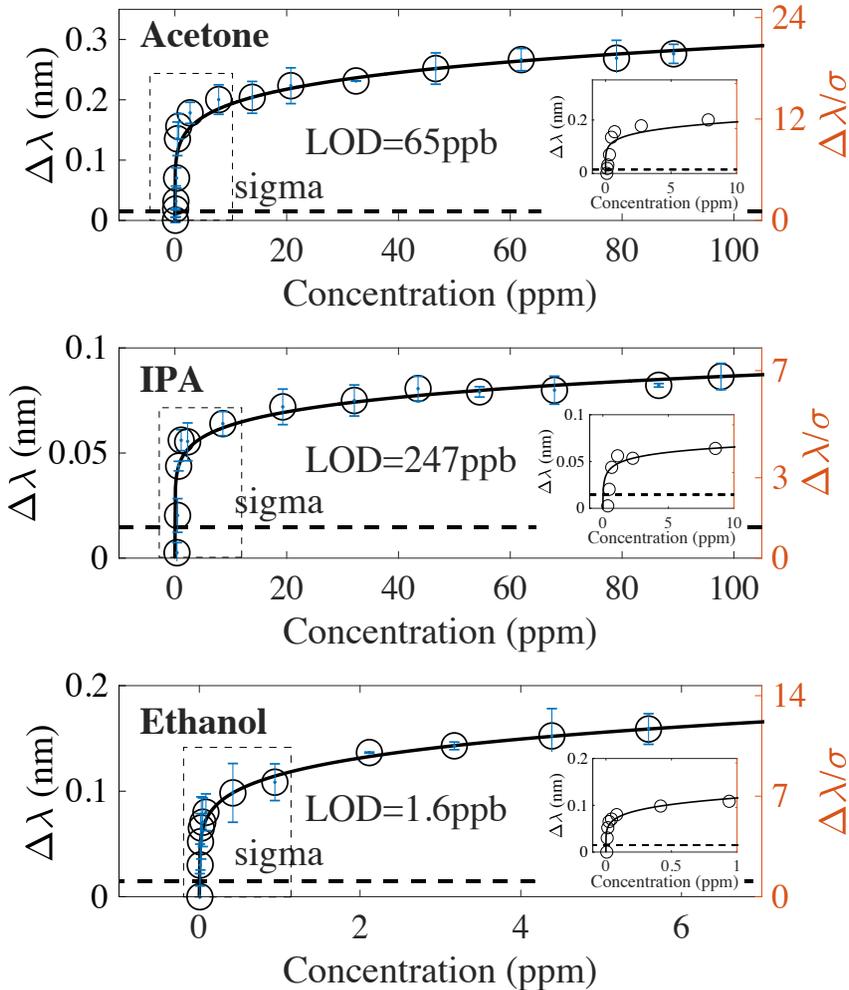
Figure 5.21: Relative wavelength shift of the MZI response is shown on the left axis, obtained from fitting the interference fringes for the different adsorption-desorption measurements. The right axis shows the relative wavelength shift-to-setup noise ratio, with the 1-σ value indicated as a dashed line. The response follows the nonlinear Freundlich behavior, with a fit to this model shown in black ($R^2 > 0.9$). The limit of detection is estimated on the small-concentration linear regime (shown in inset), with values of 65, 247 and 1.6 ppb for acetone, IPA and ethanol respectively. The error bars indicate the standard deviation of the wavelength shift over time, once the adsorption cycle is complete.

The results show a clear and defined wavelength shift for gas concentrations below 1 ppm, even down to 0.13 ppm for acetone. It is immediately clear that the adsorption and desorption process is completely reversible, with the resonance wavelength returning back to the original wavelength . The resonant wavelength shifts are also well above the noise-baseline. A small time dependent swing of the signal remains present during this steady-state adsorbed regime, as is most clearly visible for the 90 ppm case. The wavelength shifts for each concentration level are plotted again in Figure 5.21, along with the standard deviation of the wavelength shift on top of the adsorption cycle as error bars [18]. These fluctuations determine the accuracy, and arise from fluctuations in temperature inside the bubbler, and are shown in the time trace in Figure 5.20.

Figure 5.21 analyses the sensor response for acetone, IPA and ethanol. The left axis is the resonant wavelength shift, the same as before. The right axis illustrates the ratio of the resonant wavelength over the noise floor of the sensor and setup. The behavior for each vapor follows standard non-linear adsorption models, where a strong response is present at low concentrations when the monolayer is formed, and with a dampened response once the monolayer binding sites are all occupied. At this point, multilayers are formed, but less efficiently as the monolayer. The data points are fitted to the Freundlich model of equation 5.40, with a $R^2 > 0.9$ for each of three vapors. From this model, the limit of detection is found to be: $LOD_{acetone} = 65$ ppb, $LOD_{IPA} = 247$ ppb and $LOD_{ethanol} = 1.6$ ppb. Using the instrumental noise figure for the wavelength shift and the LOD values, the sensitivity in the linear regime at low concentrations is derived as $S = \sigma/LOD$, resulting in: $S_{acetone} = 0.22$ nm/ppm, $S_{IPA} = 0.06$ nm/ppm and $S_{ethanol} = 9.12$ nm/ppm. The differences in the LOD between the different vapors can be due to (1) differences in affinity to the binding site, and (2) due to the differences in vapor pressure.

To ensure that the observed wavelength shifts are indeed due to changes in gas vapor concentrations, a study is done on the influence of the gas generator operation. Figure 5.22-(a) shows the gas generator setup. The gas vapors are created in a permeation chamber, with a heater permeation tube inside. The control software controls the heating of the permeation tube and the mixing ratio between the diluent and the vapor gas to obtain the desired concentration. Figure 5.22-(b) shows a time trace of the resonant wavelength shift of the sensor to the baseline operation of the gas generator. There, it can be noticed that an influence is present, likely due to the cyclic heating of the permeation tube. The generated signal is small in comparison to the response under the presence of different gas vapor concentrations. This cyclic signal is incorporated into the standard deviation of the measurements in Figure 5.21.
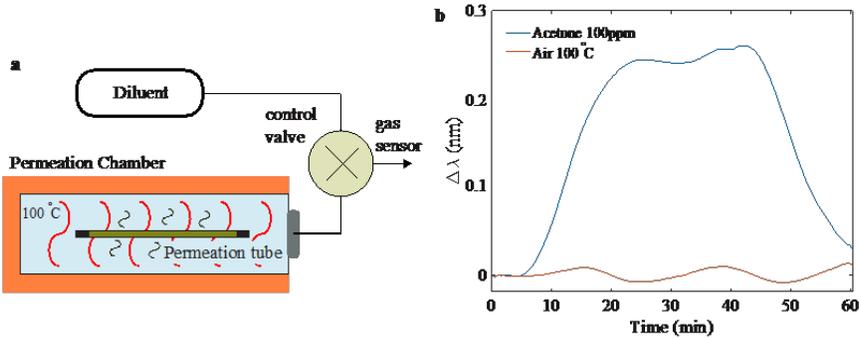
Figure 5.22: (a) The gas generator creates the desired gas concentration by heating a permeation tube inside the permeation chamber within 0.1 °C, and by mixing the gas with a diluent. (b) Shows the system response for a flow setting of heated air (100 °C) and for 100 ppm acetone concentration. The hot airflow has an effect on the sensor, albeit minimal, in comparison with the response of an actual gas concentration (100 ppm acetone).
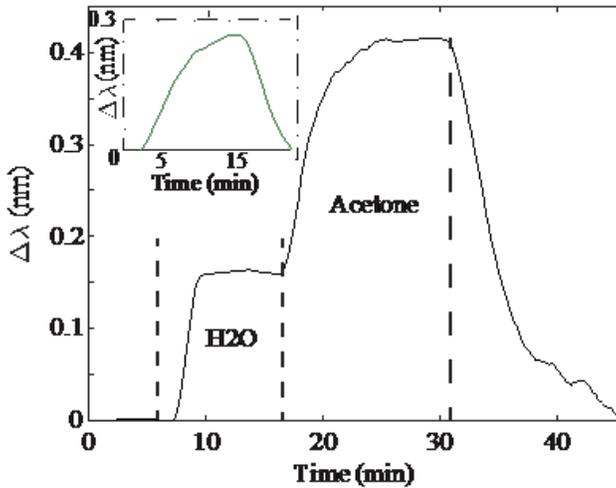
Figure 5.23: Influence of relative humidity on the sensor response. Approximately 50 μl of H_2O is placed into the permeation chamber. The sensor has a non-negligible response. Although, when acetone is added, the sensor response increases once again.

Figure 5.23 shows the influence of the relative humidity on the sensor response. A 50 μl vial of DI-water is placed inside the permeation chamber. It can be seen that the presence of water sets a new baseline level for the sensor operation, but without influencing the capability of the sensor to still adsorb VOCs. The inset shows the sensor response to acetone without the presence of the water in the dilution chamber. The response is stronger without the presence of water, indicating that the coating is not entirely hydrophobic as expected. Using non-coated reference sensors, which are expected to react more strongly to changes in moisture than VOCs, allows one to disentangle these two effects.

The demonstrated Δn sensor lacks the selectivity that Raman spectroscopy has. There are different coating types that function on a key-lock binding mechanism [3], similar to antibody based sensing, that have a higher inherent selectivity that the adsorption based operation of the demonstrated VOC-sensing coating. Nevertheless, the sensitivity and limit of detection of refractive index sensors are unparalleled, further proving the viability of the MZI as an ideal transducer.

5.5   Conclusions

In this chapter, the field of optical refractive index sensors is studied. A brief comparison is made between MZIs and ring-based transducers such as APF, ADD or Vernier filters. It is shown that the APF and ADD have limited freedom in the design of their sensitivity. Moreover, they require a high-resolution tunable laser to interrogate the ring spectrum. Vernier filters are better, with an adjustable sensitivity. However, they usually require the same costly, high resolution tunable laser, and they have lower signal-to-noise ratio than MZIs.

Then, a study was done on the different interrogation methods of MZIs as transducer. The two measurement types are fixed-wavelength and spectral. For the fixed wavelength lasers it is required to have a 90° or a 120° hybrid coupler with multiple outputs to do a full phase extraction. For the spectral measurements, it is shown that the tunable laser approach of an integrated VCSEL would outperform a broadband light source with an on-chip interrogator simply due to the higher spectral sampling capability of the laser, the lower cross talk and the easier signal recording.

Afterwards, the principle of operation of a single MZI-sensor was demonstrated with an ion-sensing coating that could detect sodium and potassium within the relevant biological range. However, the investigation has been put on hold due to time stability and durability issues. A switch was made with a VOC-sensitive coating, developed by TU Vienna. The sensor, consisting of the VOC-sensitive

coating on a MZI transducer, showcased an extremely sensitive response to acetone, IPA and ethanol. The limits of detection were in the mid to low ppb range.

References

[1] E. Ryckeboer, R. Bockstaele, M. Vanslembrouck, and R. Baets. *Glucose sensing by waveguide-based absorption spectroscopy on a silicon chip*. Biomedical Optics Express, 5(5):1636, 2014.

[2] Jacob T. Robinson, Long Chen, and Michal Lipson. *On-chip gas detection in silicon optical microcavities*. Optics InfoBase Conference Papers, 16(6):4296–4301, 2008.

[3] Rozalia Orghici, Peter Lützow, Jörg Burgmeier, Jan Koch, Helmut Heidrich, Wolfgang Schade, Nina Welschoff, and Siegfried Waldvogel. *A microring resonator sensor for sensitive detection of 1,3,5-trinitrotoluene (TNT)*. Sensors, 10(7):6788–6795, 2010.

[4] Vittorio M.N. Passaro, Francesco Dell'Olio, and Francesco De Leonardis. *Ammonia optical sensing by microring resonators*. Sensors, 7(11):2741–2749, 2007.

[5] Nebiyu A. Yebo, Petra Lommens, Zeger Hens, and Roel Baets. *An integrated optic ethanol vapor sensor based on a silicon-on-insulator microring resonator coated with a porous ZnO film*. Optics Express, 18(11):11859, 2010.

[6] Nebiyu Adello Yebo, Wim Bogaerts, Zeger Hens, and Roel Baets. *On-chip arrayed waveguide grating interrogated silicon-on-insulator microring resonator-based gas sensor*. IEEE Photonics Technology Letters, 23(20):1505–1507, 2011.

[7] Nebiyu A. Yebo, Sreeprasanth Pulinthanathu Sree, Elisabeth Levrau, Christophe Detavernier, Zeger Hens, Johan A. Martens, and Roel Baets. *Selective and reversible ammonia gas detection with nanoporous film functionalized silicon photonic micro-ring resonator*. Optics Express, 20(11):11855, 2012.

[8] T. H. Stievater, S. A. Holmstrom, D. A. Kozak, R. A. McGill, M. W. Pruessner, N. Tyndall, W. S. Rabinovich, and J. B. Khurgin. *Trace-gas Raman spectroscopy using functionalized waveguides*. 2016 Conference on Lasers and Electro-Optics, CLEO 2016, 3(8), 2016.

[9] Daan Martens. *Photonic Biosensors in Silicon Nitride with an On-Chip Spectral Filter Read Out by a Broadband Light Source*. PhD thesis, Ghent University, 2018.

[10] Tom Claes, Wim Bogaerts, and Peter Bienstman. *Experimental characterization of a silicon photonic biosensor consisting of two cascaded ring resonators based on the Vernier-effect and introduction of a curve fitting method for an improved detection limit*. Optics Express, 18(22):22747, 2010.

[11] Tom Claes, Wim Bogaerts, and Peter Bienstman. *Vernier-cascade label-free biosensor with integrated arrayed waveguide grating for wavelength interrogation with low-cost broadband source*. Optics Letters, 36(17):3320, 2011.

[12] Daan Martens and Peter Bienstman. *Comparison between Vernier-cascade and MZI as transducer for biosensing with on-chip spectral filter*. Nanophotonics, 6(4):703–712, 2017.

[13] N. Fabricius, G. Gauglitz, and J. Ingenhoff. *A gas sensor based on an integrated optical Mach-Zehnder interferometer*. Sensors and Actuators: B. Chemical, 7(1-3):672–676, 1992.

[14] D. Celo, E. Post, M. Summers, T. Smy, M. J. Brett, and J. Albert. *Interferometric sensing platform with dielectric nanostructured thin films*. Optics Express, 17(8):6655, 2009.

[15] Firehun Tsige Dullo, Susan Lindecrantz, Jana Jágerská, Jørn H. Hansen, Magnus Engqvist, Stian Andre Solbø, and Olav Gaute Hellesø. *Sensitive on-chip methane detection with a cryptophane-A cladded Mach-Zehnder interferometer*. Optics Express, 23(24):31564, 2015.

[16] Souvik Ghosh and B. M.A. Rahman. *A Compact Mach-Zehnder Interferometer Using Composite Plasmonic Waveguide for Ethanol Vapor Sensing*. Journal of Lightwave Technology, 35(14):3003–3011, 2017.

[17] V. Rochus, R. Jansen, B. Figeys, F. Verhaegen, R. Rosseel, P. Merken, S. Lenci, and X. Rottenberg. *Double MZI Micro-Opto-Mechanical Pressure Sensors for increased sensitivity and pressure range*. TRANSDUCERS 2017 - 19th International Conference on Solid-State Sensors, Actuators and Microsystems, pages 954–957, 2017.

[18] D. Martens, P. Ramirez-Priego, M. S. Murib, A. A. Elamin, A. B. Gonzalez-Guerrero, M. Stehr, F. Jonas, B. Anton, N. Hlawatsch, P. Soetaert, R. Vos, A. Stassen, S. Severi, W. Van Roy, R. Bockstaele, H. Becker, M. Singh, L. M. Lechuga, and P. Bienstman. *A low-cost integrated biosensing platform based on SiN nanophotonics for biomarker detection in urine*. Analytical Methods, 10(25):3066–3073, 2018.

[19] Konstantinos Misiakos, Eleni Makarona, Marcel Hoekman, Romanos Fyrogenis, Kari Tukkiniemi, Gerhard Jobst, Panagiota Sotirios Petrou, Sotirios Elias Kakabakos, Alexandros Salapatas, Dimitrios Goustouridis, Mikko Harjanne, Paivi Heimala, and Ioannis Raptis. *All-Silicon Spectrally Resolved Interferometric Circuit for Multiplexed Diagnostics: A Monolithic Lab-on-a-Chip Integrating All Active and Passive Components*. ACS Photonics, 6(7):1694–1705, 2019.

[20] Mohammed Sharif Murib, Daan Martens, and Peter Bienstman. *Label-free real-time optical monitoring of DNA hybridization using SiN Mach–Zehnder interferometer-based integrated biosensing platform*. Journal of Biomedical Optics, 23(12):1, 2018.

[21] A. Densmore, M. Vachon, D.-X. Xu, S. Janz, R. Ma, Y.-H. Li, G. Lopinski, A. Delâge, J. Lapointe, C. C. Luebbert, Q. Y. Liu, P. Cheben, and J. H. Schmid. *Silicon photonic wire biosensor array for multiplexed real-time and label-free molecular detection*. Optics Letters, 34(23):3598, 2009.

[22] R. Halir, L. Vivien, X. Le Roux, D. X. Xu, and P. Cheben. *Direct and sensitive phase readout for integrated waveguide sensors*. IEEE Photonics Journal, 5(4), 2013.

[23] Giuseppe Antonacci, Jeroen Goyvaerts, Haolan Zhao, Bettina Baumgartner, Bernhard Lendl, and Roel Baets. *Ultra-sensitive refractive index gas sensor with functionalized silicon nitride photonic circuits*. APL Photonics, 5(8), 2020.

[24] K. Misiakos, I. Raptis, E. Makarona, A. Botsialas, A. Salapatas, P. Oikonomou, A. Psarouli, P.S. Petrou, S.E. Kakabakos, Kari Tukkiniemi, M. Sopanen, and G. Jobst. *All-silicon monolithic Mach-Zehnder interferometer as a refractive index and bio-chemical sensor*. Optics Express, 22(22):26803, 2014.

[25] Karthik Reddy, Yunbo Guo, Jing Liu, Wonsuk Lee, Maung Kyaw Khaing Oo, and Xudong Fan. *Rapid, sensitive, and multiplexed on-chip optical sensors for micro-gas chromatography*. Lab on a Chip, 12(5):901–905, 2012.

[26] R. Bruck, E. Melnik, P. Muellner, R. Hainberger, and M. Lämmerhofer. *Integrated polymer-based Mach-Zehnder interferometer label-free streptavidin biosensor compatible with injection molding*. Biosensors and Bioelectronics, 26(9):3832–3837, 2011.

[27] Muzammil Iqbal, Martin A Gleeson, Bradley Spaugh, Frank Tybor, William G Gunn, Michael Hochberg, Tom Baehr-jones, Ryan C Bailey, and L Cary Gunn. *Label-Free Biosensor Arrays Based on Silicon*. IEEE Journal of Selected Topics in Quantum Electronics, 16(3):654–661, 2010.

[28] Tom Claes, Jordi Gironès Molera, Katrien De Vos, Etienne Schacht, Roel Baets, and Peter Bienstman. *Label-free biosensing with a slot-waveguide-based ring resonator in silicon on insulator*. IEEE Photonics Journal, 1(3):197–204, 2009.

[29] Kirill Zinoviev, Laura G. Carrascosa, José Sánchez Del Río, Borja Sepúlveda, Carlos Domínguez, and Laura M. Lechuga. *Silicon photonic biosensors for lab-on-a-chip applications*. Advances in Optical Technologies, 2008, 2008.

[30] Katrien De Vos, Irene Bartolozzi, Etienne Schacht, Peter Bienstman, and Roel Baets. *Silicon-on-Insulator microring resonator for sensitive and label-free biosensing*. Optics Express, 15(12):7610, 2007.

[31] Albrecht Brandenburg, Rainer Edelhäuser, Tobias Werner, Huarui He, and Otto S. Wolfbeis. *Ammonia detection via integrated optical evanescent wave sensors*. Mikrochimica Acta, 121(1-4):95–105, 1995.

[32] L. Tombez, E. J. Zhang, J. S. Orcutt, S. Kamlapurkar, and W. M. J. Green. *Methane absorption spectroscopy on a silicon photonic chip*. Optica, 4(11):1322, 2017.

[33] Xiaoning Jia, Joris Roels, Roel Baets, and Gunther Roelkens. *On-chip non-dispersive infrared CO2 sensor based on an integrating cylinder†*. Sensors (Switzerland), 19(19):1–14, 2019.

[34] Crawford Massie, George Stewart, George McGregor, and John R. Gilchrist. *Design of a portable optical sensor for methane gas detection*. Sensors and Actuators, B: Chemical, 113(2):830–836, 2006.

[35] H. Guo, S. C. Lee, L. Y. Chan, and W. M. Li. *Risk assessment of exposure to volatile organic compounds in different indoor environments*. Environmental Research, 94(1):57–66, 2004.

[36] Haolan Zhao, Bettina Baumgartner, Ali Raza, Andre Skirtach, Bernhard Lendl, and Roel Baets. *Multiplex volatile organic compound Raman sensing with nanophotonic slot waveguides functionalized with a mesoporous enrichment layer*. Optics Letters, 45(2):447, 2020.

[37] Todd H. Stievater, Marcel W. Pruessner, Doewon Park, William S. Rabinovich, R. Andrew McGill, Dmitry A. Kozak, Robert Furstenberg, Scott A. Holmstrom, and Jacob B. Khurgin. *Trace gas absorption spectroscopy using functionalized microring resonators*. Optics Letters, 39(4):969, 2014.

[38] Bettina Baumgartner, Jakob Hayden, and Bernhard Lendl. *Mesoporous silica films for sensing volatile organic compounds using attenuated total reflection spectroscopy*. Sensors and Actuators, B: Chemical, 302(September 2019):127194, 2020.

[39] Radim Halir and Jan Flusser. *Numerically Stable Direct Least Squares Fitting Of Ellipses*. 1998.

[40] Sarvagya Dwivedi, Herbert D'Heer, and Wim Bogaerts. *A compact all-silicon temperature insensitive filter for WDM and bio-sensing applications*. IEEE Photonics Technology Letters, 25(22):2167–2170, 2013.

[41] Bettina Baumgartner, Jakob Hayden, Andreas Schwaighofer, and Bernhard Lendl. *In Situ IR Spectroscopy of Mesoporous Silica Films for Monitoring Adsorption Processes and Trace Analysis*. ACS Applied Nano Materials, 1(12):7083–7091, 2018.

[42] Bettina Baumgartner, Jakob Hayden, Jérôme Loizillon, Sophia Steinbacher, David Grosso, and Bernhard Lendl. *Pore Size-Dependent Structure of Confined Water in Mesoporous Silica Films from Water Adsorption/Desorption Using ATR-FTIR Spectroscopy*. Langmuir, 35(37):11986–11994, 2019.

6

Conclusions and outlook

This final chapter reviews the obtained results and whether the earlier specified goals are achieved. It also includes which additional development is still required for transfer-print compatible GaAs opto-electronic components and their use in low-cost, low-power, photonic integrated sensors.

6.1   Conclusions

The market for silicon (Si) and silicon nitride (SiN_x) photonics is growing rapidly. While SiN_x offers several application based advantages over Si, the integration of active components on the SiN_x platform is more challenging. In contrast to Si platforms, there are no high speed detectors or modulators available for SiN_x waveguide platforms. It is for this reason that hybrid and heterogeneous integration is of special interest for SiN_x photonics and the topic of this dissertation.

For the different devices, several release layer systems were studied for the GaAs opto-electronic components: AlAs for the MSM PD, InAlP for the PIN PD, and InGaP for the VCSEL. The best and most flexible layer system for transfer-printing is when the epi-vendor can grow high-quality crystalline layers on top of an InAlP release layer. If that is not possible, the next relevant question is whether the AlAs oxidation can be mitigated. AlAs is very prone to oxidation and this
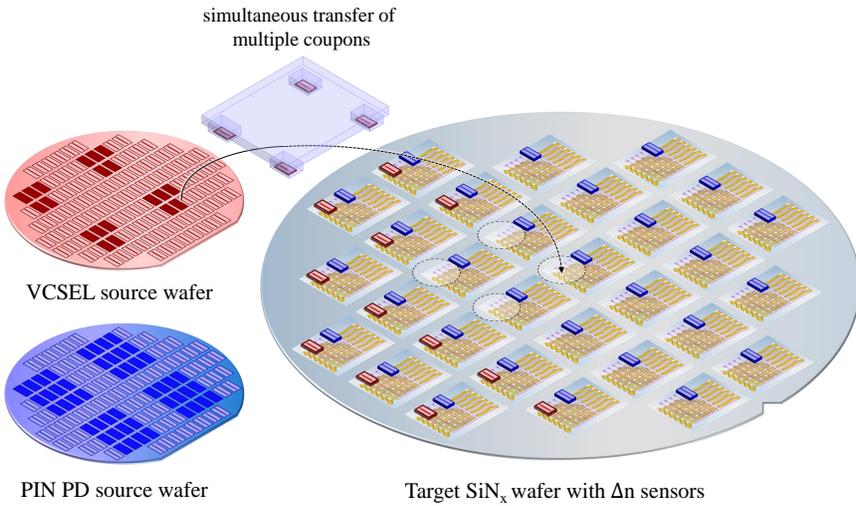
Figure 6.1: Illustration of the studied Micro-Transfer-Printing method for integrating GaAs based opto-electronic components onto a biopix - 300 nm SiN_x application wafer.

can impact the processing yield. However, with proper etch control, passivation layers and expertise in prevention of oxidation, as is expected with a commonly used material such as GaAs, AlAs is the second most suitable candidate. Compared to AlAs, InGaP can provide excellent etch control, without the risk of oxidation. The main downside is the low etch rate, requiring high-concentration HCl etchants, which further complicate the processing and passivation of the devices.

In chapter 2, an investigation was done on transfer-print integration of high-speed MSM photodetectors. High-speed PDs on SiN_x PICs are especially relevant for photonic interposers. Our standalone PDs had nA-range dark currents and a bandwidth of up to 19 GHz, with a path towards obtaining larger bandwidths. With this bandwidth, a signal read-out of up to 40 Gbps is possible. Both fiber-interfacing and waveguide-interfacing PDs were transfer-printed.

Besides the high-speed MSM PD, a sensitive PIN PD is studied in chapter 3. A thicker GaAs absorption layer ($\sim$ 2.5 μm) is used to collect as much light as possible. This improves the waveguide-based external quantum efficiency, resulting in a waveguide-referred quantum efficiency of just below 50% for a single-etch SiN_x grating coupler. A demonstration is made for array printing of multiple devices onto the output grating couplers of an on-chip arrayed waveguide grating/spectrometer. Very low dark currents ($<$ 10 pA) are measured, which are important for integrated optical sensors.

In chapter 4, transfer-print integration of vertical cavity surface emitting lasers

is investigated. The VCSELs couple to in-plane SiN_x waveguides via a diffraction grating. The chosen approach for the bottom-emitting VCSEL compromises between performance on one side, and cost and ease of fabrication on the other side. Through optimization of the process flow, high device yield, release yield and print yield are obtained. Moreover, the results are comparable or best-in-class for 850 nm VCSELs-on-SiN_x PICs. The waveguide-coupled VCSELs have a double-sided power coupling of about 100 μW. With the aid of the diffraction grating, a SMSR close to 50 dB is measured. The VCSILs can operate in environments of up to 85 °C. A tuning range of 4 to 5 nm is attainable within the 90 % roll-over regime, maintained up to 50% at scan frequencies exceeding 1 MHz.

Combining the WG-coupled power of the VCSEL with the low-dark current of the PIN PDs, a massively parallel refractive index sensing platform that uses VCSELs as light sources and PIN PDs as detectors is within reach. It is for this reason that a study was done in chapter 5 on such a specific narrowband refractive index sensor. The different options of MZI-based interrogation with lasers and broadband sources were studied and compared. From this, the 120° hybrid and resonance wavelength tracking read-out methods were chosen as the architectures for fixed wavelength operation and scanning wavelength operation, respectively. Together with external partners, Bosch & TU Vienna, proof-of-concept demonstrators were made. The Bosch sweat-sensor was capable of detecting ions in the relevant concentration range of human sweat (mMol/l), while the TU Vienna gas sensor showcased record low limits of detection in the low ppb concentration range for volatile organic compounds. With this, all individual building blocks have been developed and proven to work separately. The integration of all individual building blocks into a single system is left for future work.

6.2   Outlook

The presented set of devices, a near infrared MSM PD - PIN PD - VCSEL, are very promising, as they allow for active near infrared photonics integrated circuits that can be realized at wafer-scale and at low cost. At the same time, they match competitive products in terms of bandwidth, dark current and WG-coupled power. However, improvements can still be found. With the knowledge gained in the course of this work, the following areas are identified for further research in improving the device and application performance.

For the MSM PDs, the current bandwidth limitations are associated with the resolution of the lithography used in defining the metal interdigitated contact fingers. Improving the finger spacing will lead to an increase in the bandwidth of the PDs.

With the PIN PDs, the aim has always been to provide a solution for on-chip sensing applications in combination with a VCSEL light source. For this purpose, future improvements should aim to increase the responsivity of the PD-on-GC system. The most straightforward enhancements can be found by increasing the directionality of the SiN_x grating coupler used underneath the PIN PD. Switching to dual-etch grating can impede yield for fiber-coupling applications, as small variations can shift the out-coupling angle. However, this constraint is less relevant for the bottom-illuminated PIN PD. Additional progress in the directionality can be achieved by introducing higher index materials into the platform layerstack.

As mentioned at the end of chapter 4, there are several points to be investigated for enhancing the waveguide-coupled power in the VCSIL. In essence, the presented version of the PIC is a first design version design. Improvements can be found by reducing external back reflections or reducing the fringes on the LI curves. On the III-V side, an argument can be made for increasing the single-mode output power by introducing a mode filter on top of the GaAs DBR. This requires a review of the cost vs. benefit of additional processing. Another area of focus is the use of a BCB planarization layer, and to integrate this in a process flow compatible with coating the refractive index sensor. One option is to use photosensitive BCB, another is to use a thin BCB bonding layer and transfer-print measure-ready devices with wirebond pads on the III-V coupon.

Combining the VCSEL with the high-speed PD is especially relevant for low-cost photonic interposers. An important roadblock is that more on-chip optical power is required for large signal data rate measurements between the VCSEL and the MSM PDs. This requires a change in the coupling structure, to boost the coupling efficiency. With the current, standard platform, only a medium index contrast is attainable. Combining SiN_x waveguides with metal diffraction gratings, could pave the way for coupling efficiencies exceeding well over 50 %.

For the sensors, the relevant individual sensor architectures have been discussed. We also reviewed larger architectural points of the sensor, that aim to combine varying degrees of sensitivity with unambiguous signal reconstruction from the measurements. The performance of each individual building block suffices for the target application, with the VCSEL having a wavelength tuning range of over 4 nm. The VCSEL, in combination with the low dark current PIN PD, creates the ideal platform for a multi-parameter sensor array. The outlook in this work is the combination of the different building blocks developed that can amount to a fully integrated refractive index sensing platform for bio-applications in the near infrared.